# **Staggered Synthetic Aperture Radar**

Zur Erlangung des akademischen Grades eines

#### **DOKTOR-INGENIEURS**

an der Fakultät für Elektrotechnik und Informationstechnik des Karlsruher Instituts für Technologie (KIT)

genehmigte

#### **DISSERTATION**

von

Michelangelo Villano, M.Sc. geb. in Vallo Della Lucania (SA), Italien

Tag der mündlichen Prüfung: Hauptreferent:

Korreferenten:

23.02.2016
Prof. Dr.-Ing. habil. Alberto Moreira
Prof. Dr. Pierfrancesco Lombardo
Prof. Dr.-Ing. Dr. h.c. Dr.-Ing. E.h. mult. Werner Wiesbeck

## Acknowledgements

This thesis describes research carried out between 2011 and 2015 at the Microwaves and Radar Institute of the German Aerospace Center (DLR) in Oberpfaffenhofen, Germany. This work could not have been carried out without the help of many people, to all of whom I am deeply indebted.

I would like to express my special appreciation and thanks to my advisor Prof. Alberto Moreira, who has been an excellent mentor for me. I would like to thank him for encouraging my research at every stage and for his extremely useful advice. I would also like to thank my co-advisors Prof. Werner Wiesbeck and Prof. Pierfrancesco Lombardo for their valuable feedbacks.

A special acknowledgement goes to my supervisor Dr. Gerhard Krieger for his expert guidance and continual support. Working with him has been both a privilege and a pleasure.

I would also like to thank all my colleagues past and present for always helping out and making this experience so much more enjoyable. Special thanks go to Dr. Sigurd Huber for providing the antenna pattern of the reflector used for the design examples in Section 5, Marc Jäger for providing the F-SAR processing tools for the experiment described in Section 6.1, Ulrich Steinbrecher for commanding the TerraSAR-X satellite for the experiment described in Section 6.2, Dr. Marc Rodriguez-Cassola for processing the TerraSAR-X staggered SAR data, Vincenzo Del Zoppo, who spent six months at DLR working on data volume reduction under my supervision, and Michele Martone for contributing to the analysis of the joint effects of Doppler filtering and quantization, described in Section 7.5.

I am very grateful to all of my friends for being supportive throughout my PhD experience. Last but not least I would like to express my deepest gratitude to my parents, to whom this thesis is dedicated.

Oberpfaffenhofen, March 2016

Michelangelo Villano

# Contents

Zus	samme	enfassu	ing	v
Ab	stract			vii
Acı	ronym	s and S	Symbols	ix
1	Intr	oductio	on	1
	1.1	State	of the Art: Spaceborne SAR Sensors	2
	1.2	Motiv	vation, Objectives, and Structure of the Thesis	5
2	SAF	R Remo	ote Sensing	9
	2.1	Geom	netry and Acquisition Process	9
	2.2	Signal	l Processing	11
		2.2.1	The Range Dimension	11
		2.2.2	The Azimuth Dimension	14
	2.3	Syster	m Performance	17
		2.3.1	Resolution and Sidelobes	17
		2.3.2	Distributed Scatterers and Speckle	17
		2.3.3	Noise Equivalent Sigma Zero	18
		2.3.4	Azimuth Ambiguities	18
		2.3.5	Range Ambiguities and Nadir Returns	20
3	Hig	h-Reso	lution Wide-Swath Imaging	23
	3.1	Azimı	uth Resolution and Swath Width	23
	3.2	Digita	al Beamforming and Multiple Receive Subapertures	26
		3.2.1	Multi-Channel Processing	28
	3.3	New A	Architectures and Concepts	30

<u>ii</u> Contents

		3.3.1	Multi-Channel ScanSAR	30
		3.3.2	Multiple Elevation Beams	30
4	Stag	ggered (	SAR	33
	4.1	Conce	pt	33
		4.1.1	Processing Strategies	34
	4.2	Design	n of Sequences of PRIs	35
		4.2.1	Slow PRI Change	36
		4.2.2	Fast PRI Change	38
		4.2.3	More Elaborated Sequences	46
		4.2.4	Sequences for Fully Polarimetric SAR Systems	47
	4.3	Interp	olation Methods	49
		4.3.1	Two-Point Linear Interpolation	50
		4.3.2	Multi-Channel Reconstruction	50
		4.3.3	Best Linear Unbiased (BLU) Interpolation	53
5	Per	forman	ce Analysis and Design Examples	55
	5.1	Input 1	Parameters and Performance Measurements	55
	5.2	Impac	t on Performance of the Features Peculiar of a Staggered SAR System	64
		5.2.1	Impact of the Sequence of PRIs on Performance	64
		5.2.2	Impact of the Interpolation Method on Performance	70
		5.2.3	Impact of the Processing Strategy on Performance	71
	5.3	Syster	n Design Considerations	73
		5.3.1	Mean PRF on Transmit	73
		5.3.2	Processed Doppler Bandwidth	76
		5.3.3	Duty Cycle	77
		5.3.4	Fully Polarimetric SAR Systems	78
	5.4	C-Ban	nd Design Examples Based on a Planar Antenna	80
6	Exp	erimen	ts with Real Data	87
	6.1	F-SAI	R Experiment	87
		6.1.1	Generation of Equivalent Staggered SAR Data	87
		6.1.2	Performance Assessment on Raw Data	92
		6.1.3	Data Focusing and Impulse Response Analysis	94
	6.2	Terras	SAR-X Experiment	106
		6.2.1	Characteristics of TerraSAR-X and Experiment Definition	106
		6.2.2	TerraSAR-X Data Processing and Analysis of the Results	114

Contents

7	Dat	a Volume Reduction	119
	7.1	HRWS Systems and Azimuth Oversampling	119
	7.2	On-Board Doppler Filtering and Decimation	120
	7.3	FIR Filter Design	122
	7.4	Performance Analysis	125
	7.5	Joint Effects of Doppler Filtering and Quantization	129
8	Stag	ggered SAR with Displaced Phase Centers	133
	8.1	Concept	133
	8.2	System Design	134
9	Con	nclusions	141
	9.1	Discussion	141
	9.2	Summary of Results	143
	9.3	Outlook	145
Bibli	iogra	phy	147
A	Sph	nerical SAR Geometry	157
Curi	riculı	um Vitae	161

iv Contents

# Zusammenfassung

Fernerkundung mittels Radar mit synthetischer Apertur (SAR) ermöglicht hochauflösende Aufnahmen, unabhängig von Wetter oder Sonneinstrahlung und ist somit ideal für die systematische Beobachtung von dynamischen Prozessen auf der Erdoberfläche geeignet. Allerdings sind konventionelle SAR-Systeme dahingehend limitiert, dass eine große Streifenbreite nur durch eine Verschlechterung der Azimut-Auflösung realisiert werden kann. Diese Einschränkung kann durch Systeme mit mehreren Empfangs-Subaperturen, die in Flugrichtung versetzt sind, überwunden werden. In diesem Fall wird jedoch eine sehr lange Antenne für große Streifenbreiten benötigt. Falls eine relativ kurze Antenne mit nur einer Apertur in Flugrichtung vorhanden ist, ist es trotzdem möglich große Flächen abzubilden: Mehrere Streifen können simultan durch digitales Beamforming in Elevation abgebildet werden. Nachteil dieser Methode sind jedoch "blinde Entfernungen" zwischen benachbarten Streifen, da das Radar während dem Sendevorgang keine Signale empfangen kann. Staggered-SAR löst das Problem der blinden Entfernungen, indem das Puls-Wiederhol-Intervall (pulse repetition interval, PRI) kontinuierlich variiert wird. Eine passende Wahl der PRIs, in Verbindung mit Überabtastung in Azimut, ermöglicht eine akkurate Interpolation der unregelmäßig abgetasteten Rohdaten in ein regelmäßiges Raster, wodurch die neu abgetasteten Daten mit einem konventionellen SAR-Prozessor fokussiert werden können. Daher wird durch dieses Konzept die hochauflösende Aufnahme von breiten kontinuierlichen Streifen ohne eine lange Antenne mit mehreren Empfangs-Subaperturen möglich. Ein zusätzlicher Vorteil ist die Verteilung der Energie von Azimut- und Entfernungsmehrdeutigkeiten über große Gebiete: Dadurch beeinträchtigen Mehrdeutigkeiten die Aufnahme eher wie ein Rauschen und nicht wie klar abgrenzbare Artefakte. Im Rahmen dieser Arbeit wird der Einfluss der ausgewählten PRI-Sequenz, der angepassten Interpolationsmethode und der Prozessierungsstrategie auf die eizielbare Abbildungsleistung dargestellt. Entwürfe für mono-, dual- und vollpolarimetrische Staggered-SAR-Systeme werden, sowohl für Planar- als auch Reflektorantennen, jeweils im L- und C-Band, gezeigt. Zusätzlich wird der Einfluss des Staggered-SAR-Konzeptes auf die Bildqualität durch Experimente mit realen Daten evaluiert. Zunächst wurden stark überabgetastete flugzeuggestützte F-SAR-Aufnahmen verwendet, um äquivalente Staggered-SAR-Daten zu erzeugen und die Bildqualität für verschiedene Überabtastungsraten auszuwerten. In einem weiteren Schritt wurde der deutsche Satellit TerraSAR-X dahingehend gesteuert, dass er Daten im Staggered-SAR-Modus über dem Bodensee aufgenommen hat. Die Ergebnisse mit diesen Daten vi Zusammenfassung

zeigten eine sehr gute Übereinstimmung mit simulierten Werten. Darüber hinaus wurde eine Strategie zur Reduzierung des Datenvolumens, basierend auf einem on-board Doppler-Filter und einer Datendezimierung, entwickelt, um die erhöhte Azimutüberabtastung des Staggered-SAR zu kompensieren. Abschließend wird eine patentierte Erweiterung des Staggered-SAR-Konzeptes präsentiert, in der durch eine kontinuierliche Variation der Phasenzentren erreicht wird, dass gleichmäßig abgetastete Daten ohne die Notwendigkeit eines Interpolationsschrittes unter der Verwendung einer veränderten Reihenfolge von *PRIs* aufgenommen werden können. Für Tandem-L, ein Vorschlag für eine polarimetrische und interferometrische satellitengestützte SAR-Mission zur Beobachtung dynamischer Prozesse der Erdoberfläche mit bisher unerreichter Genauigkeit und Auflösung, wird das Staggered-SAR-Konzept derzeit als der Standardaufnahmemodus in Betracht gezogen.

#### **Abstract**

Synthetic aperture radar (SAR) remote sensing allows high-resolution imaging independently of weather conditions and sunlight illumination and is therefore very attractive for the systematic observation of dynamic processes on the Earth's surface. However, conventional SAR systems are limited in that a wide swath can only be imaged at the expense of a degraded azimuth resolution. This limitation can be overcome by using systems with multiple receive subapertures displaced in along-track, but a very long antenna is required to map a wide swath. If a relatively short antenna with a single aperture in along-track is available, it is still possible to map a wide area: Multiple subswaths can be, in fact, simultaneously imaged using digital beamforming in elevation, but "blind ranges" are present between adjacent swaths, as the radar cannot receive while it is transmitting. Staggered SAR overcomes the problem of blind ranges by continuously varying the pulse repetition interval (PRI). A proper selection of the PRIs, together with an average oversampling in azimuth, allows an accurate interpolation of the non-uniformly sampled raw data on a uniform grid, so that resampled data can be then focused with a conventional SAR processor. This concept therefore allows high-resolution imaging of a wide continuous swath without the need for a long antenna with multiple subapertures. As an additional benefit, the energy of range and azimuth ambiguities is spread over large areas: Ambiguities therefore appear in the image as a noise-like disturbance rather than localized artifacts. In this thesis, the impact on performance of the selected sequence of PRIs, the adopted interpolation method and the processing strategy are addressed. Design examples for single-, dual-, and fully-polarimetric staggered SAR systems are presented, based on both planar and reflector antennas, in L-band and C-band. The impact of staggered SAR operation on image quality is furthermore assessed with experiments using real data. As a first step, highly oversampled F-SAR airborne data have been used to generate equivalent staggered SAR data sets and evaluate the performance for different oversampling rates. Moreover, the German satellite TerraSAR-X has been commanded to acquire data over the Lake Constance in staggered SAR mode. Measurements on data show very good agreement with predictions from simulations. Furthermore, a data volume reduction strategy, based on on-board Doppler filtering and decimation, has been developed to cope with the increased azimuth oversampling of staggered SAR. Finally, a patented extension of the staggered SAR concept is provided, where the phase centers are continuously varied as well, so that it is possible to transmit pulses according to a sequence of different PRIs and acquire uniformly samviii Abstract

pled data without the need of any interpolation. The staggered SAR concept is currently being considered as the baseline acquisition mode for Tandem-L, a proposal for a polarimetric and interferometric spaceborne SAR mission to monitor dynamic processes on the Earth's surface with unprecedented accuracy and resolution.

# Acronyms and Symbols

In this work identical notation is used for real and complex quantities.

#### **List of Constants**

$c_0$	speed of light in free space	$2.99792458 \cdot 10^8 \text{ m/s}$
$k_B$	Boltzmann constant	$1.38064852 \cdot 10^{-23} \mathrm{J/K}$
$\pi$	ratio of a circle's circumference to its diameter	3.141592
e	Euler's number	2.71828
$R_E$	mean Earth's radius	$6.371 \cdot 10^6 \mathrm{m}$

### **Mathematical Notations, Symbols and Functions**

```
imaginary unit ( j = \sqrt{-1} )
j
cos(x)
                    cosine function
\exp(x)
                    natural exponential function
rect((t-t_0)/\tau)
                    rectangular window function of width \tau centered in t_0
sin(x)
                    sine function
                    cardinal sine function (sinc(x) = sin(\pi x)/(\pi x))
sinc(x)
sign(x)
                    sign of x
                    Kronecker delta
\delta(\cdot)
                    expected value of a random variable or process
E\{\cdot\}
\Sigma
                    sum
                    approximately equal
\cong
                    relates single element with corresponding set of values
\in
                    element-wise multiplication of matrices
```

\* complex conjugate of a scalar or vector quantity

|·| absolute value of a quantity

 $\lceil \cdot \rceil$  ceiling function  $\lfloor \cdot \rfloor$  floor function

denotes transpose of vector quantity

estimated value of a quantity

#### **Acronyms**

Italic letters indicate that the acronym is also used as a variable.

1-D one-dimensional

2-D two-dimensional

AASR Azimuth Ambiguity-to-Signal Ratio

APC Azimuth Phase Coding
ASI Italian Space Agency

ASR Ambiguity-to-Signal Ratio

AWGN Additive White Gaussian Noise

A/D Analog-to-Digital (Converter)

BAQ Block Adaptive Quantization

BLU Best Linear Unbiased

CEBRAS Cross Elevation Beam Range Ambiguity Suppression

CSA Canadian Space Agency
DBF Digital Beamforming
DEM Digital Elevation Model
DLR German Aerospace Center

DoA Direction of Arrival

ESA European Space Agency
FIR Finite Impulse Response
FFT Fast Fourier Transform

HH horizontal transmit and horizontal receive polarizationHV vertical transmit and horizontal receive polarization

HRWS High-Resolution Wide-Swath IRE Institute of Radio Engineering

IRF Impulse Response Function

ISLR Integrated Sidelobe Ratio

JAXA Japan Aerospace Exploration Agency

JPL Jet Propulsion Laboratory

LCMV Linear Constrained Minimum Variance

LEO Low Earth Orbit

LFM Linear Frequency Modulated

MVDR Minimum Variance Distortionless Response

NASA National Aeronautics and Space Administration

NRL Naval Research Laboratory

NESZ Noise Equivalent Sigma Zero

PBW Processed Doppler Bandwidth

PolSAR Polarimetric SAR

PRF Pulse Repetition Frequency
 PRI Pulse Repetition Interval
 PSD Power Spectral Density
 PSF Point Spread Function

*PSLR* Peak Sidelobe Ratio

radar Radio Detection and Ranging

RASR Range Ambiguity-to-Signal Ratio

RCM Range Cell Migration

RX Receive

SAR Synthetic Aperture Radar

SCORE Scan On Receive

SNR Signal-to-Noise Ratio

SRTM Shuttle Radar Topography Mission
TAXI TanDEM-X Interferometric Processor

T/R transmit/receive module

TOPS Terrain Observation with Progressive Scan

TX Transmit

USA United States of America

VH horizontal transmit and vertical receive polarization
VV vertical transmit and vertical receive polarization

### **Lower Case Letters**

	Unit	
$b_{mk}$		with reference to multi-channel reconstruction of staggered SAR data, com-
		plex coefficient associated to the transfer function $H_{mk}(f)$
c(x)		azimuth raw signal received from a point-like scatterer
dc		duty cycle
f	Hz	frequency
$f_0$	Hz	radar carrier frequency
$f_{0,\mathrm{m}}$	Hz	with reference to multi-channel reconstruction, center frequency of a sub-band
$f_D$	Hz	Doppler frequency
$f_{DC}$	Hz	Doppler centroid frequency
$f_S$	Hz	range sampling frequency
$g_{qs}$		with reference to BLU interpolation, mutual correlation between two available samples at times $t_q$ and $t_s$
h(t)		impulse response of the matched filter
$\mathbf{h}_{\mathrm{DVR}}$		vector containing the coefficients of the filter for data volume reduction
$h_i(t)$ $h_S$	m	impulse response of the <i>i</i> -th linear system, used in the representation of a SAR system with multiple receive subapertures sensor (orbit) height above ground
$n_S$ $n(t)$	111	signal representing the noise contribution added at the receiver
$p_k(t)$		impulse response of the $k$ -th post-filter (reconstruction filter) in a SAR sys-
$P_{k}(i)$		tem with multiple receive subapertures
r		with reference to BLU interpolation, vector containing the correlations $r_q$
r(t)		received echo from a point-like scatterer after coherent demodulation
$r_q$		with reference to BLU interpolation, correlation between an available sample at time $t_q$ and the sample to be estimated
$\mathbf{r}_{\mathbf{u}\mathbf{s}}$		correlation vector of the useful signal, used to compute the coefficient of the Wiener filter for data volume reduction
s(t)		baseband waveform radiated after modulation by the radar antenna
t	S	time coordinate
$t_{int}$	S	with reference to BLU interpolation, time at which the raw azimuth signal has to be estimated
$t_q$	S	with reference to BLU interpolation, time at which a sample of the raw azimuth signal, correlated with the sample to be estimated, is available
u		vector containing the available samples of the raw azimuth signal to be used in BLU interpolation

u(t)		raw azimuth signal, characterized as zero-mean complex random process
$u(t_{int})$		with reference to BLU interpolation, true value of the raw azimuth signal at
		the time $t_{int}$ at which it has to be estimated
$u(t_q)$		with reference to BLU interpolation, value of an available sample of the raw
( D)		azimuth signal correlated with the sample to be estimated
u(x, R)		2-D IRF (or PSF) of the SAR
u[q,p]		with reference to the F-SAR experiment, raw data before removal of the Doppler centroid
$u_{dem}[q,p]$		with reference to the F-SAR experiment, raw data after removal of the Dop-
		pler centroid (demodulated raw data)
v(x)		output of the matched filter
$v_g$	m/s	speed of the radar beam on ground
$v_r$	m/s	effective speed
$v_{\rm S}$	m/s	platform speed
$W_{km}$		with reference to multi-channel reconstruction of staggered SAR data, complex coefficients, used to weight the different subbands
X	m	azimuth coordinate
x[p]	m	with reference to the F-SAR experiment, azimuth coordinate for the $p$ -th transmitted pulse (used for removal of the Doppler centroid)
y(t)		output of the matched filter
$Z_{mk}$		with reference to the multi-channel reconstruction of staggered SAR data, ratio of the coefficients $w_{mk}$ and $b_{mk}$

# **Capital Letters**

	Unit	
$\boldsymbol{A}$		multiplicative factor accounting for attenuation
В		matrix containing the coefficients $b_{mk}$
B	Hz	chirp bandwidth
$B_D$	Hz	Doppler bandwidth
$B_p$	Hz	processed Doppler bandwidth
<i>C</i> ( <i>f</i> )		amplitude weighting of the Doppler spectrum applied in the processing to compensate for the distortion of the data volume reduction filter
F		noise figure
$\mathbf{G}$		with reference to BLU interpolation, matrix of the mutual correlations $g_{qs}$
$G_{TX}$		transmit antenna gain
$G_{RX}$		receive antenna gain

$G^2(\theta)$		two-way antenna power pattern as a function of the elevation angle
$G^2(f)$		two-way antenna power pattern as a function of the Doppler frequency
$G^2(\theta,f)$		two-way antenna power pattern as a function of the elevation angle and the Doppler frequency
<b>H</b> ( <i>f</i> )		matrix, which collects the transfer functions $H_i(f)$ in a SAR system with multiple receive subapertures
$H_{DVR}(f)$		transfer function of the filter used for data volume reduction
$H_i(f)$		transfer function of the <i>i</i> -th linear system, used in the representation of a SAR system with multiple receive subapertures
$H_{mk}(f)$		element of the matrix $\mathbf{H}(f)$
$I_1$	Hz	with reference to multi-channel reconstruction, frequency interval which delimits a subband
L	m	length of the radar antenna
$L_{\rm s}$	m	extent of the antenna footprint in azimuth, extent of the synthetic aperture length on ground
$L_{ m tot}$		total losses
M		number of PRIs of a sequence of PRIs
$M_{ m min}$		minimum number of <i>PRIs</i> in a sequence with fast <i>PRI</i> change necessary to ensure that two consecutive azimuth samples are never missed
$N_{az}$		number of azimuth samples of a data set
$N_b$		number of bursts in a ScanSAR system
$N_L$		number of looks
$N_{sub}$		number of subapertures in a SAR system with multiple receive subapertures
P		number of coefficients (or taps) of the FIR filter for data volume reduction
$\mathbf{P}(f)$		matrix containing the reconstruction filter functions $P_k(f)$
$P_k(f)$		transfer function of the $k$ -th post-filter (reconstruction filter) in a SAR system with multiple receive subapertures
$P_{km}(f)$		element of the matrix $P(f)$
$P_{TX}$	W	radiated power
$P_u(f)$		PSD of $u(t)$
$PRF_{mean\ eff}$		mean effective PRF of a staggered SAR system
$PRF_{mean\ TX}$	Hz	mean PRF on transmit of a staggered SAR system
$PRI_{max}$	S	maximum PRI of a sequence of PRIs
$PRI_{\min}$	S	minimum PRI of a sequence of PRIs
Q		number of samples used to estimate a sample in BLU interpolation

Q(f)		amplitude weighting of the Doppler spectrum applied in the processing
R	m	slant range coordinate
R(x)	m	slant range as a function of the azimuth position
$R_0$	m	minimum slant range distance (closest approach)
$R_{0 \text{ max}}$	m	maximum slant range of the imaged swath
$R_{0 \mathrm{\ min}}$	m	minimum slant range of the imaged swath
$R_d$		correlation matrix of the disturbance signal, used to compute the coefficient of the MVDR filter for data volume reduction
$R_d[n]$		with reference to data volume reduction, correlation of the disturbance signal at $\log n$
$R_g$	m	ground range coordinate
$\mathbf{R}_{\mathrm{s}}$		correlation matrix of the overall signal, used to compute the coefficient of the Wiener filter for data volume reduction
$R_s[n]$		with reference to data volume reduction, correlation of the overall signal at $lag n$
$R_u(\xi)$		autocorrelation function of the azimuth raw signal $u(t)$
$R_{un}(\xi)$		autocorrelation function of the azimuth raw signal $u(t)$ in presence of noise
$R_{us}[n]$		with reference to data volume reduction, correlation of the useful signal at $lag n$
S		number of sequences with fast <i>PRI</i> change used to form a more elaborated sequence
T	S	time during which a scatterer is in the radar beam (synthetic aperture time)
$T_S$	K	receiver temperature
$T_{sw}$	S	period of a sequence of PRIs (i.e., sum of the M PRIs of the sequence)
U(f)		spectrum of the raw azimuth signal $u(t)$
$\mathbf{W}$		matrix containing the coefficients $w_{km}$
W	m	height of the radar antenna
$W_g$	m	swath width on ground
$W_k(f)$		with reference to multi-channel reconstruction of staggered SAR data, filter which provides complex weighting of the subbands
$W_{ m s}$	m	swath width in the slant range direction
$\mathbf{Z}$		matrix containing the coefficients $z_{km}$

# **Greek Symbols**

	Unit	
α		coefficient of the generalized Hamming window
$\alpha_L$	rad	look angle
β		estimation bias in the interpolation of F-SAR raw data
γ	rad	angle formed by the line segments connecting the Earth's center to the radar and the point scatterer
$\delta f_D$	Hz	Doppler frequency resolution
$\delta R$	m	slant range resolution
$\delta R_g$	m	ground range resolution
$\delta x$	m	azimuth resolution
$\varepsilon$		relative estimation error (energy) in the interpolation of F-SAR raw data
η	rad	incidence angle
$\theta$	rad	elevation angle
κ	S	with reference to the design of more elaborated sequences, difference (absolute value) of the maximum <i>PRIs</i> of two subsequent sequences with fast <i>PRI</i> change
λ	m	radar wavelength
$\sigma^0(\eta)$		backscatter as a function of the incidence angle
τ	S	pulse length
$\varphi$	rad	azimuth angle
$arphi_{sq}$	rad	squint angle
Δ	S	difference between two consecutive <i>PRIs</i> in a sequence with linear <i>PRI</i> variation
$\Delta_{az,m}$	m	relative displacement in azimuth of the $m$ -th order azimuth ambiguity
$\Delta_{ m min}$	S	minimum difference between two consecutive <i>PRIs</i> in a sequence with fast <i>PRI</i> change necessary to ensure that two consecutive azimuth samples are never missed
$\Delta_{rg,m}$	m	relative displacement in slant range of the m-th order azimuth ambiguity
$\Delta R_{0blind}$	m	width in slant range of each blind range area
$\Delta x$	m	distance between two adjacent subapertures in a SAR system with multiple receive subapertures
$\Delta x_i$	m	distance between the transmitter and the phase center of the <i>i</i> -th subaperture in a SAR system with multiple receive subapertures
Φ		SNR scaling factor

### 1 Introduction

Nearly 130 years have passed since Heinrich Hertz demonstrated the basic principle of radar¹ detection, showing that radio waves could be reflected by metallic and dielectric bodies, as suggested in James C. Maxwell's seminal work on electromagnetism [1], [2]. The German engineer Christian Hülsmeyer foresaw the application of this principle for obstacle detection in ship navigation and obtained a patent in 1904 [3], [4]. Experiments with detection of ships were also conducted at that time in Italy by Guglielmo Marconi, who pointed out the potentials of radar technology in a speech before the Institute of Radio Engineering (IRE) in 1922, and by Albert H. Taylor, Leo C. Young, and Lawrence A. Hyland at the Naval Research Laboratory (NRL), United States of America (USA) [5], [6]. In none of these cases, however, the relevance of the work was properly recognized. Radar mainly developed just prior to World War II in several countries, among which the USA, Germany, France, the Soviet Union, Japan, Netherlands, Italy, and Great Britain, where the valuable contribution of Sir Robert Watson-Watt deserves a mention. While the early developments were mainly concerned with military applications, the measurement of the height of the ionosphere by Gregory Breit and Merle A. Tuve in 1925 can probably be regarded as the first remote sensing application of radar [7].

A major milestone for radar remote sensing was the conception of the synthetic aperture radar (SAR) principle by Carl A. Wiley in 1951, which allows high-resolution radar imaging independently of the range distance, as explained in Chapter 2 [8]-[10]. Further developments of this concept led the Jet Propulsion Laboratory (JPL) of the National Aeronautics and Space Administration (NASA) to the launch of the first civilian SAR satellite, Seasat, in 1978 [11]. A number of SAR satellites were launched in the 90s, namely ERS-1/2 by the European Space Agency (ESA), JERS-1 by the Japan Aerospace Exploration Agency (JAXA), Radarsat-1 by the Canadian Space Agency (CSA), and SIR-C/X-SAR, the first spaceborne SAR system with fully-polarimetric and multi-frequency capability, realized in a cooperation between the NASA/JPL, the German Aerospace Center (DLR) and the Italian Space Agency (ASI) [12]-[15]. Other spaceborne SAR sensors, launched in the 2000s and no longer in operation, are the Shuttle Radar Topography Mission (SRTM), ENVISAT/ASAR and ALOS-PALSAR [16]-[18].

<sup>&</sup>lt;sup>1</sup> Radar is an acronym for "radio detection and ranging."

2 1 Introduction

In the meanwhile, new techniques were developed, which involved the joint exploitation of multiple SAR images, acquired in different polarizations (cf. polarimetric SAR or PolSAR), from slightly different observation angles (cf. SAR interferometry, polarimetric SAR interferometry, and SAR tomography), and/or at different times (cf. differential and permanent scatterer interferometry) [19]-[26]. In that respect, airborne SAR systems played a significant role by allowing early demonstrations of these techniques, which have later been implemented in spaceborne missions. The DLR's E-SAR sensor, predecessor of the F-SAR sensor, is an example [27], [28].

### 1.1 State of the Art: Spaceborne SAR Sensors

Table 1 provides an overview of the civilian spaceborne SAR sensors currently in operation [29]. As is apparent, they were all launched within the last decade and their frequency bands range from L-band to X-band. While the frequency bands have remained the same as for the previous sensors of the same institution (e.g., L-band for JAXA's sensors, C-band for CSA's and ESA's sensors, where data continuity was indeed the main goal of the Sentinel-1 mission), current sensors are characterized by a spatial resolution or level of detail at least one order of magnitude higher than the sensors of the previous generation. Moreover, most of them offer a much higher flexibility in that several acquisition modes can be selected for different trade-offs between resolution and coverage [30]-[35].

A prominent example is TerraSAR-X, whose main acquisition modes are summarized in Table 2 together with their characteristics in terms of resolution, swath width, and polarization: A resolution of 1 m is achieved in (sliding) spotlight mode, while a 100 km swath width can be imaged in ScanSAR mode [30], [36], [37]. Moreover, experimental modes allow an even higher resolution (0.2 m in staring spotlight mode), a wider swath (up to 260 km in wide ScanSAR mode), as well as dual- and fully-polarimetric acquisitions [38]-[41].

Sensor	Launch	Frequency band	Institution, Country	
TerraSAR-X/TanDEM-X	2007, 2010	X	DLR/Airbus, Germany	
Radarsat-2	2007	C	CSA, Canada	
Cosmo-SkyMed-1/4	2007 2010	X	ASI, Italy	
RISAT-1	2012	С	ISRO, India	
HJ-1C	2012	S	CRESDA/CAST/NRSCC, China	
Kompsat-5	2013	X	KARI, Korea	
Sentinel-1a	2014	С	ESA, Europe	
ALOS-2	2014	L	JAXA, Japan	

Table 1. Civilian spaceborne SAR sensors currently in operation [29].

Mode	Resolution	Swath width	Polarization
ScanSAR	16 m	100 km	Single
Stripmap	3 m	30 km	Single
(Sliding) spotlight	1 m	10 km	Single

Table 2. Main acquisition modes of TerraSAR-X and their characteristics in terms of resolution, swath width, and polarization.

TerraSAR-X data, acquired in different acquisition modes, have been used to demonstrate several applications of SAR to environmental monitoring. Fig. 1 shows a SAR image acquired over the Drygalski glacier on the Antarctic Peninsula. Thirty images were acquired by TerraSAR-X over the same area between October 2007 and October 2008 to show how the glacier was pushed out into the area formerly occupied by an ice shelf at a speed of up to 2 km/year (a time-lapse video is available online) [42]. Fig. 2 shows a ScanSAR image acquired over Mato Grosso, Brazil, where logging has been particularly extensive in recent years. Because of their different reflection characteristics, clearings appear in the radar image as rectangular, relatively dark zones within the otherwise homogeneous surface of the forest. In contrast, covering large areas with optical cameras mounted on satellites is problematic in tropical regions due to the dense cloud layers [43]. Fig. 3 shows a further example of application concerning the mapping of a flood of the Mississippi River, USA, while Fig. 4 shows how the ground in Mexico City, Mexico, has sunk in some areas by as much as 10 cm in four months as a result of the water extraction [44], [45].



Fig. 1. TerraSAR-X image acquired over the Drygalski Glacier on the Antarctic Peninsula [42].

1 Introduction

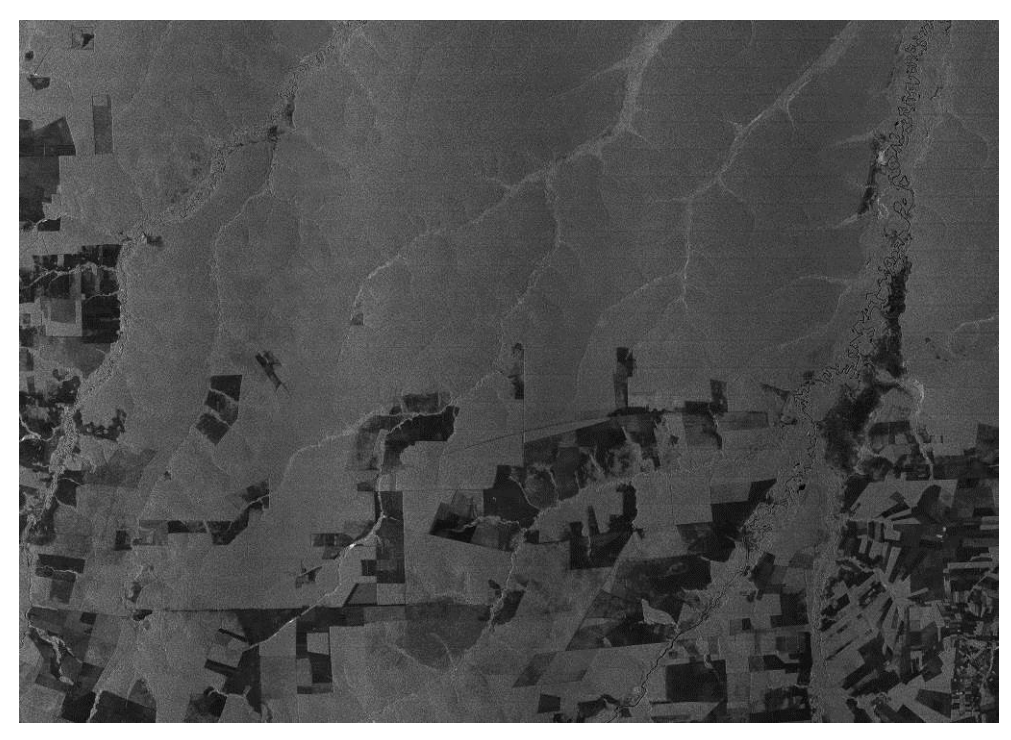


Fig. 2. TerraSAR-X image acquired over Mato Grosso, Brazil, where logging has been particularly extensive [43].

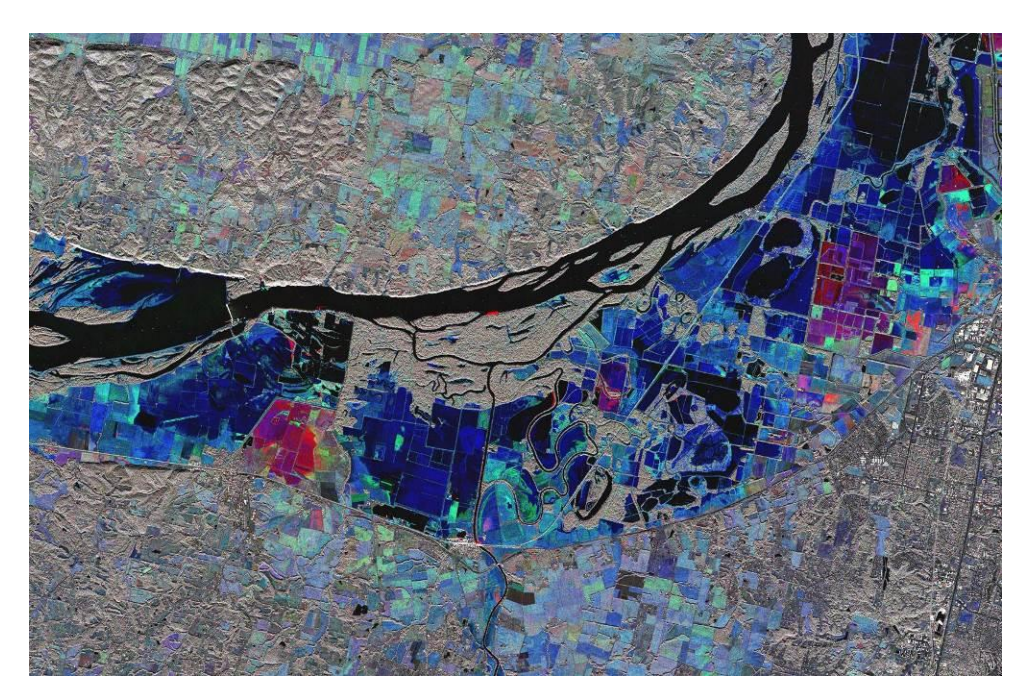


Fig. 3. Example of application of TerraSAR-X to map a flood of the Mississippi River, USA [44].



Fig. 4. Ground sinking in Mexico City, Mexico. The red areas correspond to a sinking of 10 cm in 4 months [45].

While very powerful and flexible, TerraSAR-X can map in stripmap mode only 2% of the Earth's landmass during its 11 days repeat cycle, due to its relatively small orbit duty cycle (the satellite can only operate 3 minutes per orbit) and its 30 km swath width [36]. This limitation also posed a challenge in the design of the TanDEM-X mission, which required one year for one global interferometric acquisition of the Earth's landmass [46].

More recently launched sensors, such as Sentinel-1a and ALOS-2, are still characterized by comparable mapping capabilities at that resolution [34], [35]. As it will be clarified in Section 3.1, this limitation is not due to technology development, but is inherent to the SAR acquisition principle [47], [48]. A brute force solution to this problem consists of flying a constellation of satellites on the same orbit, as done for Cosmo-SkyMed and planned for Sentinel-1 [33], [34]. This solution allows increasing the mapping capability by a factor equal to the number of satellites of the constellation, but becomes costly or even unfeasible, if the mapping capability has to be boosted by one or even two orders of magnitude.

#### 1.2 Motivation, Objectives, and Structure of the Thesis

In recent years there has been increased interest in the scientific community in understanding and quantifying dynamic processes within the Earth system occurring in different spatial and temporal scales as well as their interdependency and interaction. Many of these processes are currently inadequately researched and understood. An important reason for this is the lack of suitable observation data for analyzing these interactions [49]-[52].

The imaging performance and/or measurement resolution and accuracy of existing remote sensing configurations are often inadequate to draw reliable conclusions on the dynamics of 6 1 Introduction

large-scale processes. The measurement of dynamic processes requires a continuous, extended and systematically planned observation strategy in order to detect changes and quantify them with sufficient accuracy. Depending on the processes to be observed, changes have to be measured on variable spatial and temporal scales and then related to one another. The combination of short revisit times and extended acquisitions over several years is required when it comes to monitor fast developing, highly-dynamic processes, such as the relaxation following an earthquake, as well as slowly developing processes (e.g., the inter-annual variation of forest biomass), with the necessary accuracy and resolution.

SAR represents the ideal candidate to provide answers to these questions, but spaceborne SAR sensors currently in operation do not have the resolution and mapping capability needed to meet these scientific requirements. In particular, a SAR sensor is required, capable of mapping the whole Earth's surface twice per week, in fully-polarimetric mode and with a spatial resolution below 10 m (this corresponds to a mapping capability two orders of magnitude better than that of TerraSAR-X) [49]. In response to these needs, a proposal for a highly innovative L-band SAR mission, Tandem-L, was started at DLR with a pre-phase A study in 2013 and is currently undergoing a phase-A study [50]-[52].

While increasing the orbit duty cycle contributes to some degree to extend the mapping capability, this is still not enough to reach the desired requirements. New radar techniques have therefore to be employed, which allow boosting the mapping capability at a given resolution beyond the aforementioned inherent limitation. These techniques are mainly based on digital beamforming (DBF) and multiple subaperture signal recording [53]-[63]. As presented in detail in Section 3, two distinct SAR architectures can be identified:

- A system with multiple subapertures, displaced in the flight direction, which uses in addition DBF on receive in elevation to increase the sensitivity;
- A system, where DBF allows forming multiple elevation beams, which simultaneously map multiple subswaths.

The two architectures have important implications on the required size of the radar antenna: For the same resolution and swath width, in fact, the former architecture requires a much longer antenna, while the latter architecture asks for a much shorter, but higher antenna. The system with multiple azimuth subapertures is preferable, if a resolution of the order of 1 m has to be achieved over a swath of the order of 80 km, while the architecture with multiple elevation beams is better suited for a resolution of the order of 5 to 10 m over an even wider swath (350 to 400 km), as required for the aforementioned mission aiming at monitoring dynamic processes on Earth's surface<sup>2</sup>. The problem of the architecture with multiple elevation beams is that the wide mapped swath is not continuous, but "blind ranges" are present between the different subswaths.

Staggered SAR allows getting rid of the "blind ranges" in a system with multiple elevation beams and imaging a wide continuous swath. The core idea is the continuous variation of the

<sup>&</sup>lt;sup>2</sup> As discussed in Section 3.3.1, a system with multiple subapertures can also achieve a resolution in the order of 5 to 10 m over a swath in the order of 350 to 400 km with an antenna of reasonable length, if used in combination with ScanSAR, but this has other drawbacks related to interferometric applications.

pulse repetition interval (*PRI*), the time distance between consecutive transmitted pulses, together with an average oversampling of the signal in azimuth [61]-[74]. If the *PRI* is continuously varied, the ranges, from which the echoes are not received, because the radar is transmitting, will be different for each transmitted pulse. A proper selection of the *PRIs*, i.e., imposing that two consecutive samples in azimuth are never missed, together with an average oversampling of the signal in azimuth allows an accurate interpolation of the non-uniformly sampled raw data on a uniform grid, so that they can be then focused with a conventional SAR processor. Staggered SAR is currently being considered as the baseline acquisition mode of the Tandem-L mission, but represents an appealing option for the next generation of Sentinel sensors as well [50].

This thesis defines an established staggered SAR concept, based on the following main contributions:

- Optimized design of the sequence of *PRIs* to be employed in relation to the other system parameters;
- Definition of an optimal interpolation method and a novel processing strategy for the acquired data, which are particularly effective in combination with the optimized sequences of *PRIs*;
- Thorough performance analysis with special attention to range and azimuth ambiguities, including several design examples (mainly for the Tandem-L mission, but also for the next generation of Sentinel sensors) and experiments with real data;
- On-board data volume reduction strategy able to cope with the increased amount of data, due to the required oversampling of the signal in azimuth.

The thesis is structured as follows. Section 2 provides a short review of SAR remote sensing: The basic SAR principle is presented together with a high-level description of the required signal processing and an overview of the main performance parameters of a SAR system. Section 3 highlights the contradicting requirements imposed by swath width and resolution in conventional SAR systems and describes the novel SAR architectures for high-resolution wide-swath (HRWS) imaging.

The staggered SAR concept is then presented in Section 4, followed by a detailed description of the procedure for the design of optimized sequences of *PRIs* and the interpolation methods. Section 5 explains how the relevant performance measurements can be evaluated and are influenced by the different input parameters. It also shows through several design examples the outstanding performance achievable by a staggered SAR system for different frequency bands and antenna types, even in fully-polarimetric mode. Section 6 describes the experiments with real data: Staggered SAR data have been simulated from highly-oversampled F-SAR airborne data and the TerraSAR-X satellite has been operated in staggered SAR mode.

Section 0 considers a strategy for reducing the volume of data to be downloaded, which represents an integral part of the staggered SAR concept, while Section 1 introduces an extension of the staggered SAR concept, where the phase centers continuously change as well, for which a patent is pending. Finally, conclusions are drawn in Section 9, where an outlook for further research is also provided.

8 1 Introduction

# 2 SAR Remote Sensing

SAR is an active microwave remote sensing technique that can provide high-resolution images independently of sunlight illumination. Moreover, because clouds, fog, and precipitation do not have a significant effect on microwaves, all-weather imaging is possible. Because of the coherent reception of the radar echoes, an effective long "synthetic" antenna can be generated by signal processing and exploited to achieve high resolution. These peculiarities make SAR very attractive for the systematic observation of dynamic processes on Earth's surface [8], [75]-[81].

#### 2.1 Geometry and Acquisition Process

Fig. 5 shows a simplified geometry of a SAR. A platform moving with constant speed  $v_S$  in a straight line at constant height  $h_S$  carries a side-looking radar antenna. The length and height of the antenna are L and W, respectively. The direction of travel of the platform is known as the azimuth (or along-track) direction; distance from the radar track is measured in the slant range (or cross-track) direction, while distance from the nadir track is measured in the ground range direction.

The radar transmits pulses of electromagnetic radiation downwards to the surface to be imaged at a constant pulse repetition frequency (PRF). The radiated pulses spread out as growing shells of thickness  $c_0\tau$ , where  $c_0$  is the speed of light in free space and  $\tau$  is the pulse length. A point-like scatterer P whose slant range is  $R_0$  will therefore return echoes of duration  $\tau$  that will arrive back at the radar with a time delay  $2R_0/c_0$  after transmission.

The power per unit area received at each point on the surface depends on the radiated power, the antenna pattern, i.e., the angular distribution of the power from the antenna, and the slant range, according to an inverse-square law. Most of the power is directed to the footprint, i.e., the area illuminated by the radar beam, whose extent in ground range and azimuth is given by

$$W_g = \frac{\lambda R_0}{W \cos \eta} \tag{1}$$

and

$$L_s = \frac{\lambda R_0}{L} \tag{2}$$

respectively, where  $\eta$  is the incidence angle and  $\lambda$  is the radar wavelength, which is related to the radar carrier frequency  $f_0$  by

$$\lambda f_0 = c_0 \tag{3}$$

The strip on ground covered by the footprint as the platform moves is known as the swath.

The electromagnetic radiation interacts with the surface, which affects the characteristics of the scattered wave (power, phase, polarization), and propagates back to the radar. The radar samples the returning echoes coherently, i.e., it retains both amplitude and phase, and stores the data for future processing.

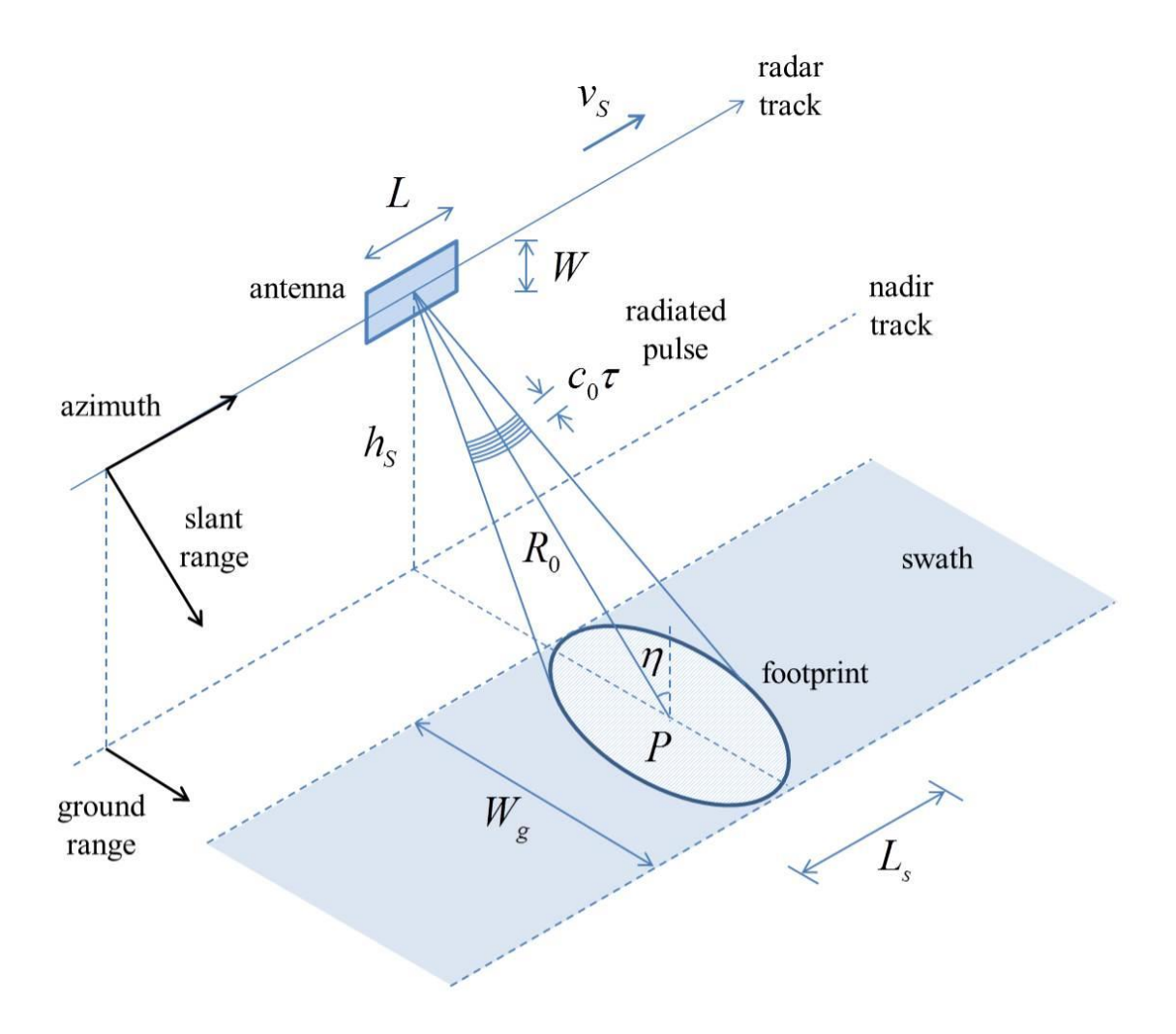


Fig. 5. Simplified geometry of a SAR.

Fully-polarimetric SAR systems employ two orthogonal wave polarizations (e.g., horizontal and vertical) on both transmit and receive. On transmit the antenna alternately radiates pulses with horizontal and vertical polarizations, while on receive echoes are simultaneously recorded using two separate channels with horizontal and vertical polarizations, respectively. Four data sets are therefore obtained for each acquisition, corresponding to four polarimetric channels. A polarimetric channel and the corresponding data set is usually identified by two letters, e.g. HV, where the first letter indicates the polarization on receive and the second the polarization on transmit and where H and V stand for horizontal and vertical, respectively. The four data sets are independently processed and then jointly exploited to retrieve additional information on the scatterers of the imaged area [19], [20].

A spherical Earth model rather than a flat Earth one is usually used for the design of space-borne SAR systems. The relationships between the main parameters of the spherical Earth model are summarized in Appendix A.

#### 2.2 Signal Processing

The echoes corresponding to each radiated pulse (henceforth also referred to as the raw data) are arranged side-by-side in a two-dimensional matrix with coordinates time delay and pulse number, corresponding to slant range and azimuth, respectively. The raw data that look like noise are then processed to obtain a focused SAR image, a two-dimensional map of the surface backscatter, where the features of the imaged scene can be recognized. Fig. 6 shows the raw data and the corresponding focused SAR image acquired by DLR's F-SAR airborne sensor over the calibration test site of Kaufbeuren, Germany [28].

SAR processing consists essentially of two separate linear filtering operations along the range and azimuth dimensions.

#### 2.2.1 The Range Dimension

Let s(t) be the baseband waveform radiated after modulation by the radar antenna and let us assume that the received echo r(t) from a point-like scatterer at slant range  $R_0$  after coherent demodulation is the sum of a delayed, attenuated, and phase-shifted version of s(t) and an additive white Gaussian noise (AWGN) contribution n(t), added at the receiver

$$r(t) = As\left(t - \frac{2R_0}{c_0}\right) \exp\left(-j\frac{4\pi R_0}{\lambda}\right) + n(t)$$
(4)

where the factor A accounts for the attenuation and j is the imaginary unit.

Under these assumptions, it can be shown that the linear, time invariant filter h(t), which maximizes the output signal-to-noise ratio (SNR), i.e., the ratio of the signal power to the noise power, while locating the scatterer at the correct slant range  $R_0$ , is the "matched filter" with impulse response h(t) given by

$$h(t) = s^*(-t) \tag{5}$$

where \* denotes complex conjugation [76].

A main concern is the resolution of the radar system, i.e., the minimum distance by which two scatterers can still be distinguished. The output y(t) of the matched filter in (5) for a rectangular input waveform

$$s(t) = \operatorname{rect}\left(\frac{t}{\tau}\right) = \begin{cases} 1, & |t| \le \tau/2\\ 0, & |t| > \tau/2 \end{cases}$$
(6)

is given by

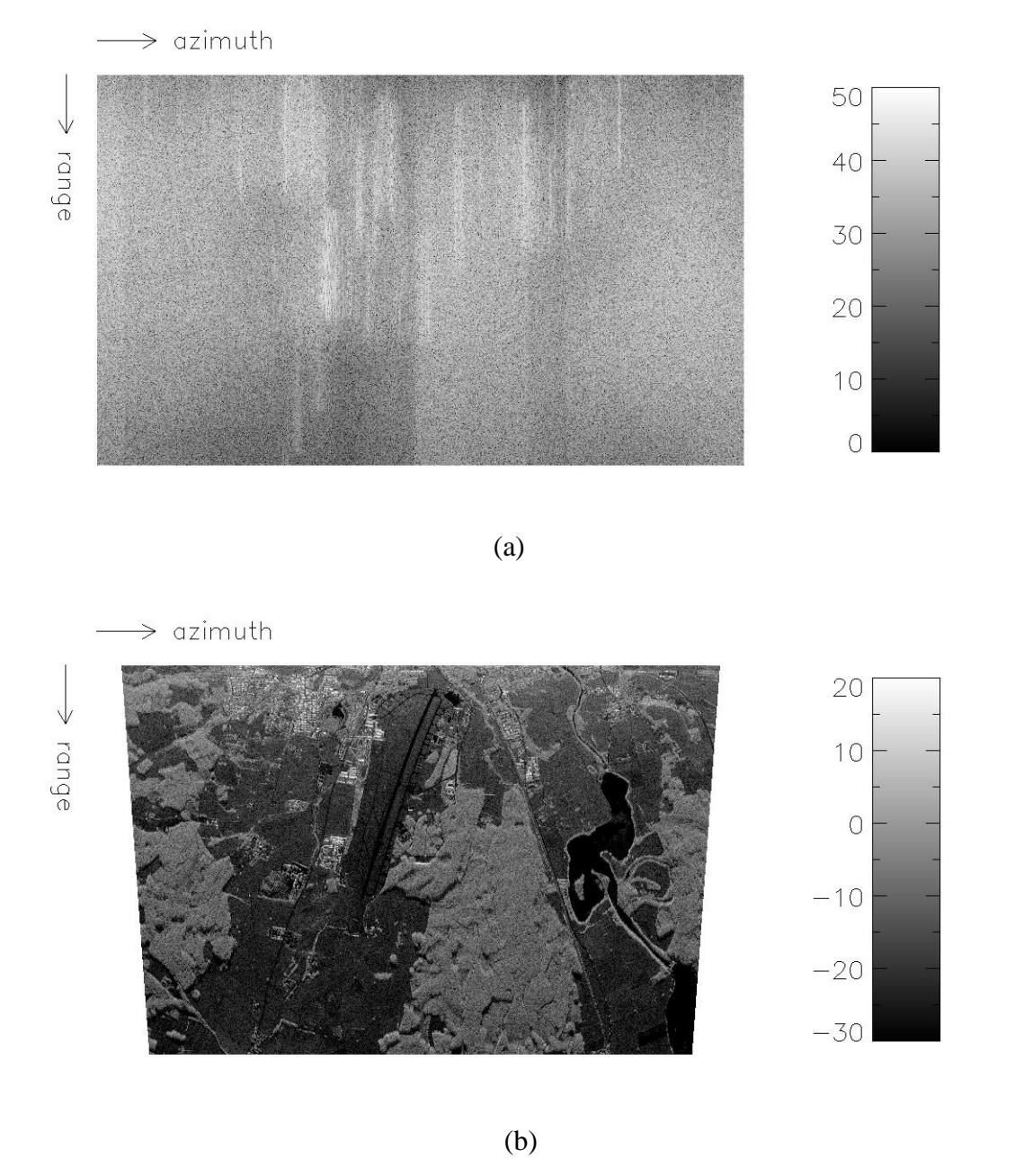


Fig. 6. SAR data acquired by the DLR's F-SAR sensor over the calibration test site of Kaufbeuren, Germany. (a) Raw data (log-intensity). (b) Focused SAR image (log-intensity).

$$y(t) = \begin{cases} \tau \left( 1 - \frac{|t|}{\tau} \right), & t \le |\tau| \\ 0, & \text{otherwise} \end{cases}$$
 (7)

and the attainable resolution in the slant range direction  $\delta R$  is approximately given by the width of  $|y(t)|^2$  (of the order of the pulse length  $\tau$ ) times half the speed of light in free space  $c_0$ 

$$\delta R \cong \frac{c_0 \tau}{2} \tag{8}$$

i.e., the shorter the pulse, the higher the resolution. However, as the radiated energy and hence the SNR after matched filtering is proportional to the pulse length  $\tau$ , the higher the resolution, the lower the SNR.

To overcome this problem, many radar systems adopt a linear frequency-modulated (LFM) waveform, also known as "chirp", of the form

$$s(t) = \exp\left(j\pi B \frac{t^2}{\tau}\right) \operatorname{rect}\left(\frac{t}{\tau}\right) \tag{9}$$

i.e., characterized by constant amplitude and quadratic phase variation across the pulse profile, where B is the chirp bandwidth. The output y(t) of the matched filter in (5) for the LFM input waveform of (9) and for a large time-bandwidth product  $B\tau$  can be written to a good approximation as

$$y(t) \cong \tau \operatorname{sinc}(Bt) \tag{10}$$

where sinc(t) denotes the cardinal sine, defined as

$$\operatorname{sinc}(t) = \frac{\sin(\pi t)}{\pi t} \tag{11}$$

and the attainable slant range resolution  $\delta R$  is approximately given by the reciprocal of the chirp bandwidth B times half the speed of light in free space  $c_0$ 

$$\delta R \cong \frac{c_0}{2B} \tag{12}$$

The ground range resolution  $\delta R_g$  is related to the slant range resolution  $\delta R$  by

$$\delta R_g = \frac{\delta R}{\sin \eta} \tag{13}$$

and therefore varies across the swath.

As illustrated in Fig. 7, a relatively long waveform is radiated that conveys a large amount of energy, while a waveform characterized by a sharp peak that leads to high resolution and high *SNR* is obtained after the matched filtering operation, hence also known as pulse compression or range compression.

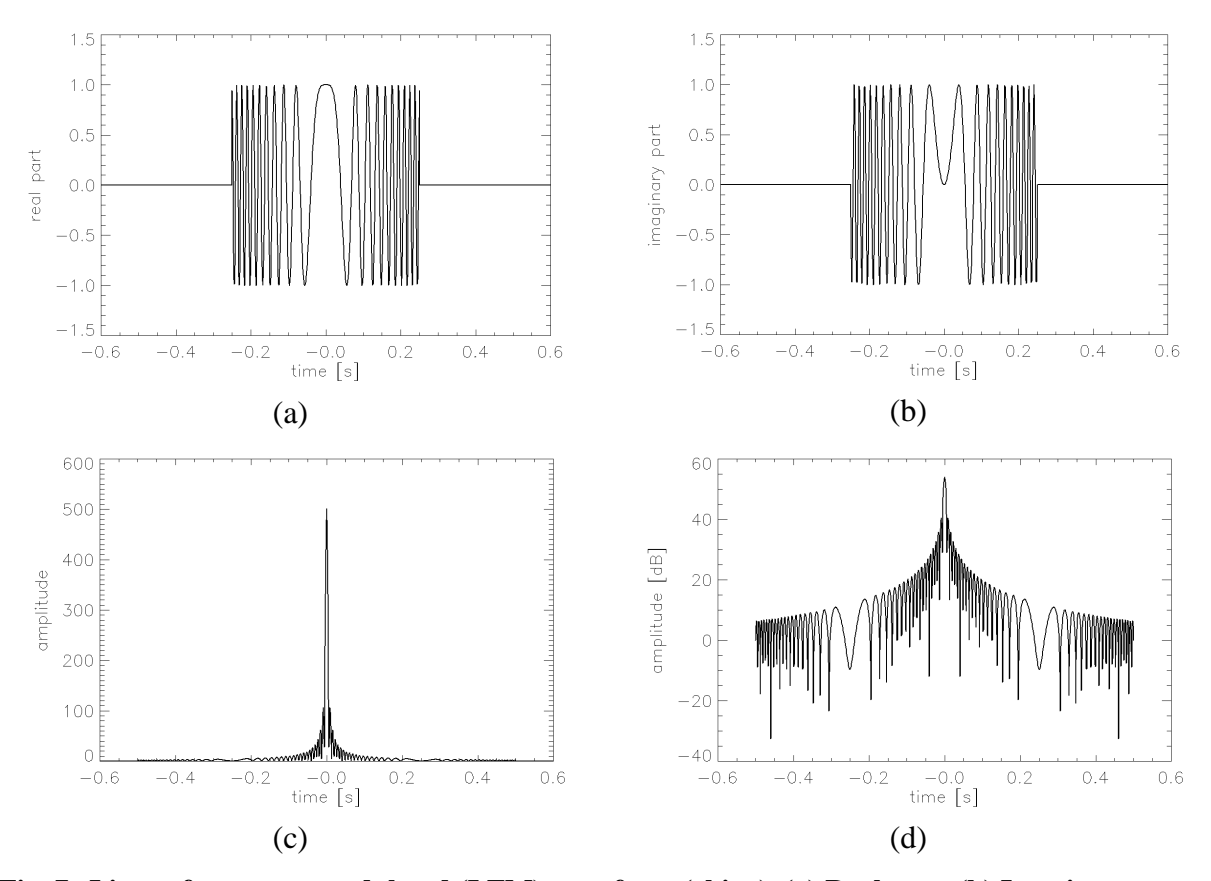


Fig. 7. Linear frequency-modulated (LFM) waveform (chirp). (a) Real part. (b) Imaginary part. (c) Amplitude after compression. (d) Amplitude after compression in dB.

In practice, the received echoes are sampled at a range sampling frequency  $f_S$  and conveniently quantized, therefore the filtering operation is inherently performed on digital signals and often in the frequency domain in order to reduce the computational burden. The data after range compression are often referred to as the range-compressed data.

#### 2.2.2 The Azimuth Dimension

Each sample of the range compressed data contains a contribution from scatterers in an azimuthally extended strip of width  $L_s$  given by (2). If no further processing is performed, the resolution of the system in the azimuth direction  $\delta x$  is also given by the extent of the radar beam in azimuth  $L_s$ , leading to a rather poor resolution at microwave wavelength. As an example, TerraSAR-X with an antenna length L=4.8 m and a wavelength  $\lambda=0.03$  m at a slant range  $R_0=650$  km would attain an azimuth resolution of only  $\delta x=4$  km.

The basic principle of SAR, which leads to a drastically improved azimuth resolution, dates back to 1951 and is due to Carl A. Wiley [9], [10], [76]. He noticed that scatterers at different azimuth angles  $\varphi$  (see Fig. 8) with respect to the radar track return echoes with distinct instantaneous Doppler frequency shifts  $f_D$  relative to the transmitted frequency, given by

$$f_D = \frac{2v_S \sin \varphi}{\lambda} \cong \frac{2v_S x}{\lambda R_0} \tag{14}$$

2.2 Signal Processing

where x is the azimuth coordinate of the scatterer and where the small angle assumption for  $\varphi$  is made. The analysis of the Doppler frequency spectrum of the return echoes therefore allows location of the scatterer in the azimuth direction, hence the name "Doppler beam sharpening".

The best attainable azimuth resolution  $\delta x$  can be obtained from the Doppler frequency resolution  $\delta f_D$  using (14), where  $\delta f_D$  is equal to the reciprocal of the time T during which the scatterer is in the radar beam. As is apparent from the sketch of Fig. 8, it holds

$$T = \frac{L_s}{v_S} = \frac{\lambda R_0}{v_S L} \tag{15}$$

and therefore

$$\delta x = \frac{\lambda R_0}{2v_s} \delta f_D = \frac{\lambda R_0}{2v_s} \frac{1}{T} = \frac{\lambda R_0}{2v_s} \frac{v_s L}{\lambda R_0} = \frac{L}{2}$$
(16)

i.e., the best attainable azimuth resolution  $\delta x$  is half the antenna length L.

From a different point of view, the signal c(x) received from a point-like scatterer as the platform moves along the azimuth coordinate x under the simplified assumption of a rectangular antenna pattern in azimuth and after coherent demodulation is given by

$$c(x) = \exp\left(-j\frac{4\pi R(x)}{\lambda}\right) \operatorname{rect}\left(\frac{x}{L_s}\right)$$
(17)

where (see Fig. 8)

$$R(x) = \sqrt{R_0^2 + x^2} \cong R_0 + \frac{x^2}{2R_0}$$
(18)

i.e., c(x) has a nearly quadratic phase variation. The normalized output v(x) of a matched filter in the azimuth direction can be written for large values of  $L_x/L$  to a good approximation as

$$v(x) \cong \operatorname{sinc}\left(\frac{2L_s}{\lambda R_0}x\right) = \operatorname{sinc}\left(\frac{2}{L}x\right)$$
 (19)

and the attained resolution in the azimuth direction, given by the width of  $|v(x)|^2$ , is approximately  $\delta x = L/2$ , i.e., the same as obtained in (16).

In analogy with the chirp bandwidth in the range direction a Doppler bandwidth  $B_D$  can be defined as

$$B_D = \frac{2v_S}{L} \tag{20}$$

so that the azimuth resolution  $\delta x$  can be expressed as a function of the Doppler bandwidth as

$$\delta x \cong \frac{v_S}{B_D} \tag{21}$$

The matched filtering in the azimuth direction coherently adds the echoes received at different locations over a very long aperture  $L_s$ , the synthetic aperture, as in a phased array. A very sharp equivalent azimuth beam is therefore generated by signal processing means, which leads to high azimuth resolution.

As the range to the scatterer changes along the synthetic aperture according to (18), the response from a fixed scatterer in the range-compressed data is curved and spreads over different range cells (see Fig. 8). Moreover, the curvature of the response changes with range. This is the phenomenon of range cell migration (RCM). Several algorithms have been developed for accu-

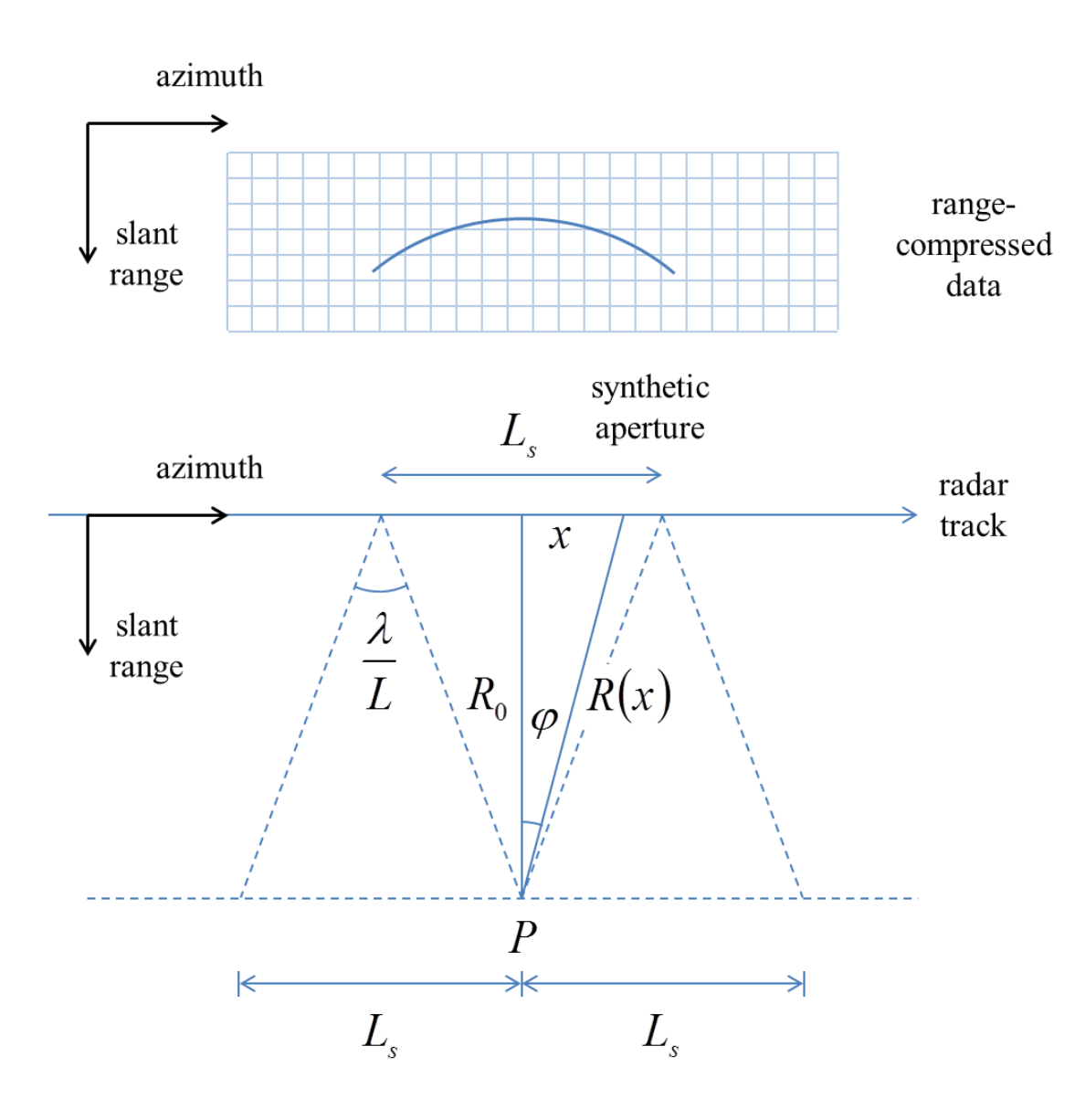


Fig. 8. Synthetic aperture and range cell migration.

rate and efficient correction of RCM, among which the most commonly used are those based on the range-Doppler, the chirp scaling, and the  $\omega$ -k approaches [81].

## 2.3 System Performance

This section reviews the main system performance parameters for a SAR, most of which can be derived from the two-dimensional (2-D) impulse response function (IRF) or point spread function (PSF) of the SAR, i.e., the response obtained, if only a point-like scatterer is present in the scene.

The 2-D IRF u(x, R) can be written to a first approximation as the normalized product of the matched filter outputs y(t) and v(x), given by (10) and (19), respectively, where the slant range variable R has been substituted to the time variable t:

$$u\left(x, R = \frac{c_0}{2}t\right) \cong \operatorname{sinc}\left(\frac{2B}{c_0}R\right) \operatorname{sinc}\left(\frac{2}{L}x\right)$$
 (22)

#### 2.3.1 Resolution and Sidelobes

The 2-D IRF u(x, R) presents a mainlobe centered in (x, R) = (0, 0), whose half-power widths in slant range and azimuth define the slant range and azimuth resolution, respectively.

The 2-D IRF u(x, R) also presents sidelobes, which impair the image quality and may mask weak scatterers. Two relevant parameters are the peak sidelobe ratio (PSLR), defined as the ratio of the peak intensity of the most prominent sidelobe to the mainlobe peak intensity, and the integrated sidelobe ratio (ISLR), defined as the ratio of the energy of all sidelobes to the mainlobe energy. A range/azimuth PSLR and ISLR can be similarly defined for the range/azimuth main cut of the impulse response.

The *PSLR* and the *ISLR* can be reduced by applying an amplitude weighting to the transfer function of the matched filters in range and azimuth in the processing. This however degrades the resolution [82].

### 2.3.2 Distributed Scatterers and Speckle

In focused SAR images a large variability of the intensity can be observed over neighboring resolution cells of the same region (e.g. a field). This phenomenon is known as speckle and can be explained by assuming that a large number of scatterers are present in each resolution cell, i.e., that the scatterer is distributed. The complex value recorded by the radar for each resolution cell is the coherent sum of the contributions from all scatterers and can be characterized as a realization of a statistical process. A simple but convenient model leads to a negative exponential distribution for the observed scatterer intensity (or backscatter) with standard deviation equal to the mean value of the intensity itself [79].

The standard deviation of the backscatter measurement can be reduced by a factor  $\sqrt{N_L}$ , if the intensities of  $N_L$  independent resolution cell of the same region – and therefore characterized

by the same statistical process – are averaged (multilooking). This however degrades the resolution by a factor  $N_L$ , which is also known as the number of looks. Several adaptive despeckling algorithms have been developed, able to preserve resolution at the edges of the regions or in presence of point-like scatterers, while removing the speckle in uniform regions [79].

### 2.3.3 Noise Equivalent Sigma Zero

As already noted, the matched filtering maximizes the output SNR, which is a relevant parameter. As the SNR depends on the backscatter and changes spatially within the scene, while the noise level of the system is constant, the noise equivalent sigma zero (NESZ), defined as the backscatter that leads to SNR = 1, is usually adopted to characterize the sensitivity of a SAR system. The NESZ of a SAR is given by

$$NESZ = \frac{256 \,\pi^3 R^3 \,v_S \sin \eta \,k_B \,T_s \,B \,F \,L_{tot}}{P_{TX} \,G_{TX} \,G_{RX} \,\lambda^3 \,c_0 \,\tau \,PRF}$$
(23)

where  $k_B$  is the Boltzmann constant,  $T_s$  is the receiver temperature, F is the noise figure,  $L_{tot}$  accounts for the total losses (e.g. atmosphere, system, processor),  $P_{TX}$  is the radiated power, and  $G_{TX}$  and  $G_{RX}$  are the transmit (TX) and receive (RX) antenna gain, respectively [46], [76].

### 2.3.4 Azimuth Ambiguities

The azimuth pattern of a real antenna – and therefore the Doppler spectrum – is not rectangular, as assumed for simplicity in (17), but has sidelobes. Due to the finite sampling of the Doppler spectrum at the PRF, the signal components outside the frequency interval [-PRF/2, PRF/2] fold back into the main part of the spectrum, giving rise to azimuth ambiguities, i.e., ambiguous signals displaced from the true location of the scatterer [76], [83]-[88].

The relative displacement in azimuth and slant range of the m-th order azimuth ambiguity for a scatterer at slant range  $R_0$  is approximately given by

$$\Delta_{az,m} \approx m \frac{\lambda PRF R_0}{2v_S} \tag{24}$$

and

$$\Delta_{rg,m} \approx \sqrt{R_0^2 + \Delta_{az,m}^2} - R_0 \tag{25}$$

respectively. Fig. 9 shows the 2-D IRF of a SAR with azimuth ambiguities up to the fourth order. As is apparent, azimuth ambiguities are not just displaced replicas of the main response; on the contrary, they spread over several range cells, because RCM is wrongly compensated for in the processing.

Azimuth ambiguities are mainly observed in images that have high backscatter regions adjacent to low backscatter regions (e.g., urban area next to a lake). The ratio of the azimuth ambiguous signal power to the main signal power for a uniform backscatter scene is referred to as the azimuth ambiguity-to-signal ratio (AASR) and can be estimated as

$$AASR \approx \frac{\sum_{\substack{m=-\infty\\m\neq 0}}^{\infty} \int_{f=-B_p/2}^{B_p/2} G^2(f+mPRF)Q^2(f)df}{\int_{f=-B_p/2}^{B_p/2} G^2(f)Q^2(f)df}$$
(26)

where  $G^2(f)$  is the two-way antenna power pattern as a function of the Doppler frequency, Q(f) accounts for the amplitude weighting of the Doppler spectrum applied in the processing, and  $B_p$  (< PRF) is the processed Doppler bandwidth (PBW), i.e., an azimuth low-pass filter of width  $B_p$  can be applied to the focused SAR data to meet the AASR requirement, but this also degrades the azimuth resolution, which becomes

$$\delta x \cong \frac{v_S}{B_p} \tag{27}$$

If the normalized azimuth pattern remains unchanged with the elevation angle, the AASR is constant across the swath.

As most of the scenes are not characterized by uniform backscatter, a local AASR can be de-

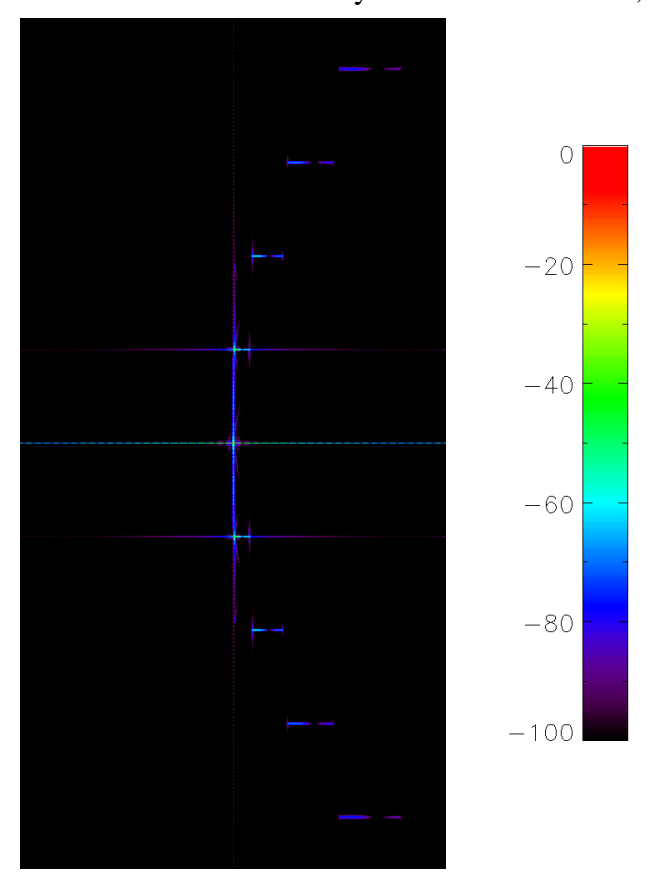


Fig. 9. Two-dimensional impulse response of a SAR (log-intensity) with azimuth ambiguities up to the fourth order. The horizontal and vertical axes represent slant range (0.7 km) and azimuth (36.9 km), respectively.

fined as the ratio of the ambiguous signal's local power to the main signal's local power. A method for the estimation of the local *AASR* from SAR images is described in [86]. Fig. 10 shows a SAR image, acquired by the German satellite TerraSAR-X over the Franz Josef Land, Russia, and the corresponding estimated local *AASR* in dB.

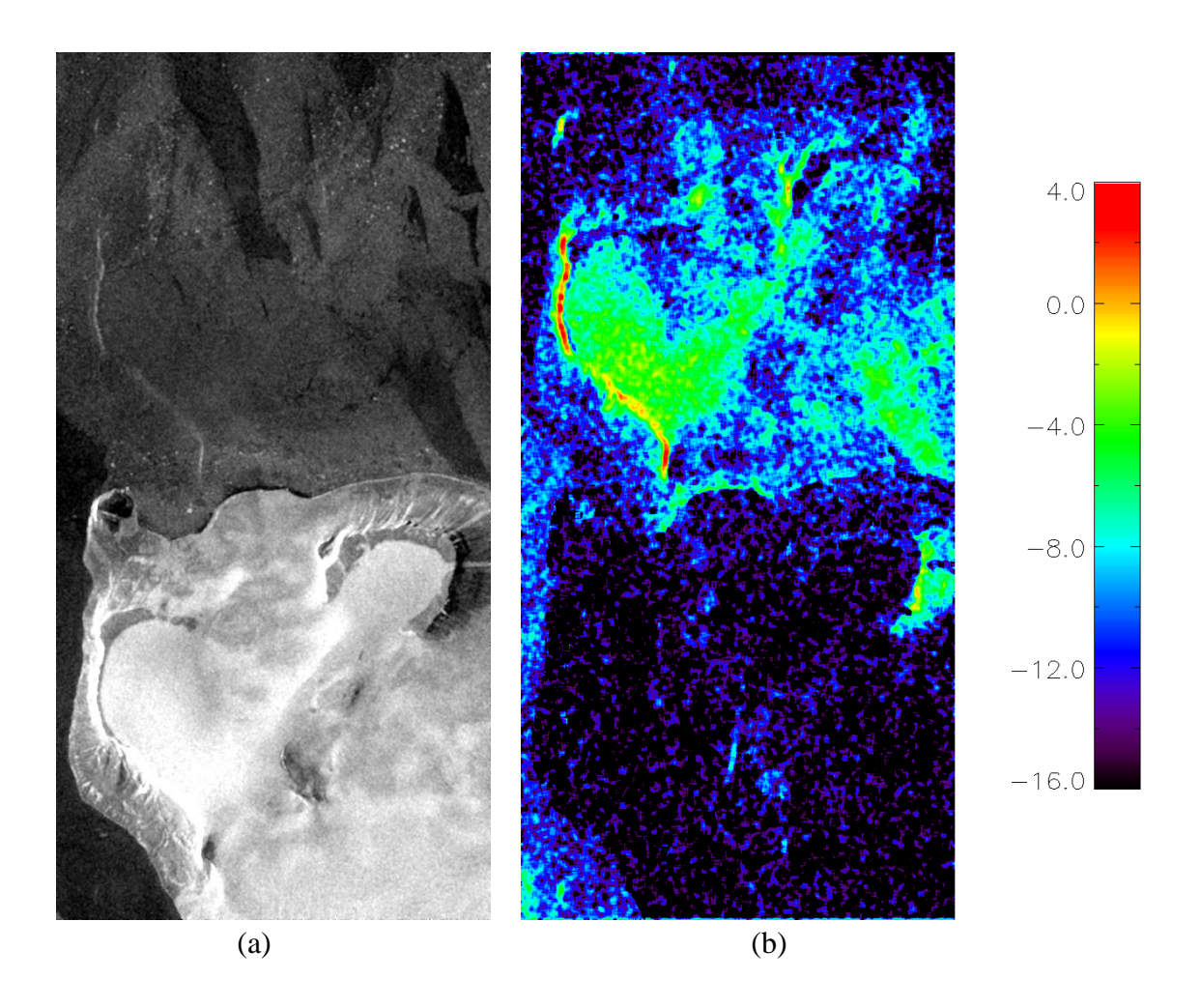


Fig. 10. (a) TerraSAR-X image acquired over the Franz Josef Land, Russia. The horizontal and vertical axes represent slant range (2.8 km) and azimuth (9.2 km), respectively. (b) Estimated local *AASR* in dB using the method proposed in [86].

### 2.3.5 Range Ambiguities and Nadir Returns

Range ambiguities arise from preceding and succeeding echoes arriving back at the radar simultaneously with the desired return [76]. This phenomenon is mainly relevant for spaceborne SAR, where several pulses are transmitted after a given pulse before receiving its echo.

A range ambiguity-to-signal ratio (*RASR*) is defined as the ratio of the range ambiguous signal power to the main signal power and can be estimated as

$$RASR \cong \frac{\sum_{j=1}^{N_A} \frac{\sigma^0(\eta_j) G^2(\theta_j)}{R_j^3 \sin \eta_j}}{\frac{\sigma^0(\eta_{main}) G^2(\theta_{main})}{R_{main}^3 \sin \eta_{main}}}$$
(28)

where  $\sigma^0(\eta)$  is the backscatter as a function of the incidence angle and  $G^2(\theta)$  is here the two-way antenna power pattern in elevation. The subscript "main" refers to the desired return, while the subscripts j,  $j = 1..N_A$ , to the  $N_A$  ambiguous (preceding and succeeding) returns. Equation (28) assumes that for each elevation angle the azimuth pattern is, but for a multiplicative constant, the same. While this assumption holds for planar antennas, where the 2-D pattern can be written as the product of an azimuth pattern and an elevation pattern, (28) may lead to inaccurate RASR evaluation for reflector antennas. In the latter case, for each elevation angle of interest the energy of the return is obtained by integrating the two-way azimuth power pattern over the PBW  $B_p$  and accounting for the amplitude weighting of the Doppler spectrum applied in the processing Q(f)

$$RASR \approx \frac{\sum_{j=1}^{N_{A}} \frac{\sigma^{0}(\eta_{j}) \int_{f=-B_{p}/2}^{B_{p}/2} G^{2}(\theta_{j}, f) Q^{2}(f) df}{R_{j}^{3} \sin \eta_{j}}}{\sigma^{0}(\eta_{main}) \int_{f=-B_{p}/2}^{B_{p}/2} G^{2}(\theta_{main}, f) Q^{2}(f) df}$$

$$\frac{\sigma^{0}(\eta_{main}) \int_{f=-B_{p}/2}^{B_{p}/2} G^{2}(\theta_{main}, f) Q^{2}(f) df}{R_{main}^{3} \sin \eta_{main}}$$
(29)

A model for the backscatter decay as a function of incidence angle is needed along with the geometry, for which a spherical Earth is usually assumed [89]. Unlike the AASR, the RASR may significantly vary across the swath and has therefore to be evaluated at each slant range within the swath.

In fully-polarimetric SAR systems, the ambiguous echoes from some of the preceding and succeeding pulses correspond to radiated pulses with different polarizations. This has to be taken into account, when evaluating the *RASR* in (28) or (29), by using the proper value of  $\sigma^0$  for each contribution. The *RASR* will be different for each polarimetric channel and in particular could be critical for the cross-polarized channels, i.e., those characterized by a different polarization on transmit and receive, as some of the ambiguous echoes are characterized by the same polarization on transmit and receive and therefore by higher backscatters.

Among the ambiguous returns the echo arriving back at the radar from the nadir has to be carefully considered. Due to the shorter slant range R and the null incidence angle  $\eta$ , this contribution can be significant and is difficult to quantify. The SAR system designer can select the PRF of the system, so that the nadir return arrives back while the radar is transmitting, and/or control the antenna pattern in the elevation direction, so that the nadir return is strongly attenuated.

# 3 High-Resolution Wide-Swath Imaging

Azimuth resolution and swath width impose conflicting requirements on the *PRF* of a SAR. SAR systems are therefore limited in that a wide swath can only be imaged at the expense of a degraded azimuth resolution. This limitation can be overcome by using systems with multiple receive subapertures, displaced in along-track, which simultaneously acquire multiple samples for each transmitted pulse, in combination with DBF on receive. However, a very long antenna is required to map a wide swath. If a relatively short antenna with a single aperture in along-track is available, it is still possible to map a wide area: DBF in elevation, in fact, allows simultaneous imaging of multiple subswaths through multiple elevation beams, but "blind ranges" are present between adjacent subswaths.

## 3.1 Azimuth Resolution and Swath Width

In a SAR the swath width constrains the *PRF*: To control range ambiguities, i.e., to avoid that ambiguous echoes arrive back at the radar from within the swath, the reciprocal of the *PRF*, i.e., the *PRI*, must be larger than the time it takes to collect returns from the entire illuminated swath

$$PRI = \frac{1}{PRF} > \frac{2W_s}{c_0} \tag{30}$$

where  $W_s$  is the swath width in the slant range direction, given by

$$W_s = W_g \sin \eta \tag{31}$$

Moreover, as the radar cannot receive, while it is transmitting, once the PRI is fixed, the echoes coming back at the radar from some ranges cannot be received. The continuous time interval, where the radar echo can be received is upper bounded by the time distance between the end of a transmitted pulse and the beginning of the next one, that is by  $PRI - \tau$ . Neglecting guard intervals, we have therefore intervals of duration  $PRI - \tau$ , where the radar echo is received, separated by intervals of duration  $\tau$ , where the radar echo cannot be received, because the radar is transmitting.

In order to image a scatterer with full range resolution, however, the echo of the full transmitted pulse of duration  $\tau$  has to be received for that scatterer and convolved with a conjugated replica of the transmitted signal. This means that only scatterers included within intervals of duration  $PRI - 2\tau$ , centered in the aforementioned intervals of duration  $PRI - \tau$ , can be imaged with full range resolution. After range compression, there will therefore be intervals of duration  $PRI - \tau$ , where scatterers can be imaged with full range resolution, separated by intervals of duration  $2\tau$ , where scatterers can be only imaged with degraded range resolution, as only part of the echo of the transmitted pulse is received for those scatterers. The maximum value of the slant range swath width  $W_s$  is therefore obtained by multiplying the interval duration  $PRI - 2\tau$  by  $c_0/2$ 

$$W_s \le \frac{c_0 \left( PRI - 2\tau \right)}{2} \tag{32}$$

The blind areas, where targets can be only imaged with degraded range resolution, also known as "blind ranges", are characterized by slant ranges  $R_0$  comprised between

$$\frac{c_0}{2} \left( kPRI - \frac{\tau}{2} \right) \le R_0 \le \frac{c_0}{2} \left( kPRI + \frac{3\tau}{2} \right), \quad k = 1, 2...$$
 (33)

while the width in slant range  $\Delta R_{0 \, blind}$  of each blind range area is given by

$$\Delta R_{0blind} = c_0 \tau \tag{34}$$

Blind ranges can be represented as a function of the PRF in a timing diagram, which shows for each PRF the available swaths, whose widths satisfy the inequality in (32). Fig. 11 shows a timing diagram, where blind ranges are marked in black and three of the available swaths for PRF = 1600 Hz are highlighted in green.

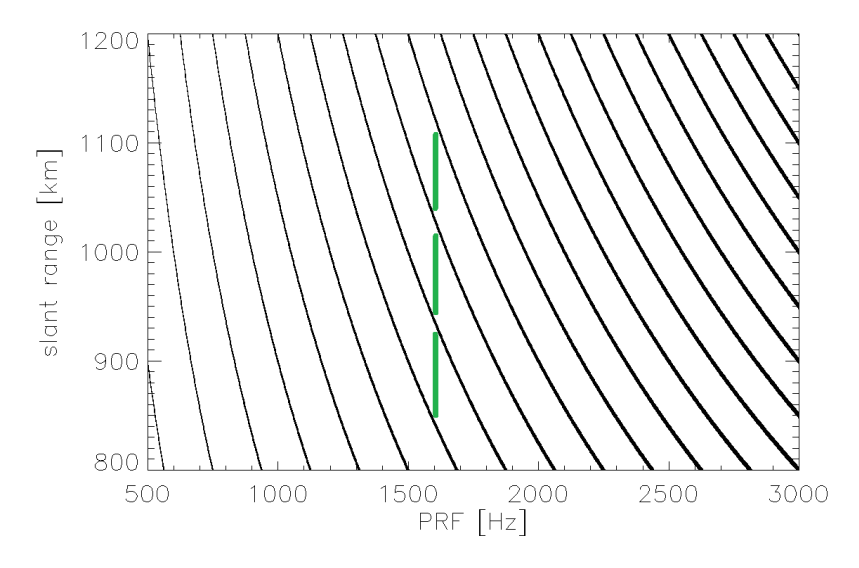


Fig. 11. Timing diagram for a pulse length  $\tau = 20~\mu s$ . Three of the available swaths for PRF = 1600 Hz are highlighted in green.

If, on the one hand, a low PRF allows the imaging of a wide swath, on the other hand, to avoid significant azimuth ambiguity levels, a low PRF, or equivalently a large PRI, also implies the adoption of a small PBW  $B_p$ , which limits the attainable azimuth resolution. Neglecting the pulse length, the condition that the PRF has to be greater than the PBW  $B_p$ , whose expression can be derived from (27), together with (30), leads to an upper bound to the ratio between the swath width in slant range  $W_s$  and the azimuth resolution  $\delta x$ 

$$\frac{W_s}{\delta x} < \frac{c_0}{2v_S} \tag{35}$$

where the right side of (35) is nearly constant at 20,000 for typical satellites in low Earth orbit (LEO), i.e., once fixed the azimuth resolution (e.g.  $\delta x = 3$  m), the swath width in slant range cannot be larger than 20,000 times the azimuth resolution, that is  $W_s < 60$  km [76]. A smaller swath is usually selected, in order to account for the pulse length as well and to impose that given AASR and RASR requirements are met.

If the highest azimuth resolution is to be attained, the antenna length L has to be selected so that the PRF is greater or equal than the Doppler bandwidth  $B_D$ , given by (20), leading to

$$L \ge \frac{2v_s}{PRF} \tag{36}$$

or even, substituting (30) in (36), to

$$L > \frac{4v_s}{c_0}W_s \tag{37}$$

i.e., the wider the swath, the longer the required antenna. In practice, a further margin factor (greater than 1) is usually introduced by the SAR system designer on the right side of (37) to meet the ambiguity requirement.

The SAR acquisition mode so far described is known as stripmap, because a strip on ground is imaged as the platform moves along the radar track (Fig. 12 (a)). Additional SAR acquisition modes allow for wider swath (ScanSAR) or higher resolution (spotlight) [90], [91].

In the ScanSAR acquisition mode the time T during which the scatterer is in the radar beam is divided into  $N_b + 1$  intervals or bursts, where the radar observes  $N_b$  different subswaths by cyclically steering the radar beam to different elevation directions (Fig. 12 (b)) [90]. The swath width therefore increases by a factor  $N_b$ , but as the observation time is now  $N_b + 1$  times smaller, the azimuth resolution degrades by a factor  $N_b + 1$ . A variant of ScanSAR is Terrain Observation by Progressive Scans (TOPS) [92].

In the spotlight observation mode, in contrast, the beam is steered in the azimuth direction to a fixed point to increase the time during which the scatterer is in the radar beam (Fig. 12 (c)) [91]. This leads to higher azimuth resolution, but the imaged area is no longer a strip, but only a patch.

An inherent limitation therefore exists, for which widening the swath results in degradation of the azimuth resolution and, vice versa, increased azimuth resolution results in a smaller imaged area.

For dual-polarimetric SAR systems, where the two polarizations are characterized by the same polarization on transmit, the same swath width and azimuth resolution as single-polarimetric systems can be achieved, provided that two separate channels are employed on receive to record the two distinct polarizations. Fully-polarimetric SAR systems instead imply a further reduction of the swath width, if the same azimuth resolution has to be achieved [93]. As explained in Section 2.1, fully-polarimetric SAR systems employ two orthogonal wave polarizations (e.g., horizontal and vertical) on both transmit and receive. On transmit the antenna alternately radiates pulses with horizontal and vertical polarizations, while on receive echoes are simultaneously recorded by two separate antennas with horizontal and vertical polarizations, respectively. In this case, in order to keep the same azimuth resolution of the single-polarimetric system, the same time span between two consecutive pulses transmitted in the same polarization has to be kept. This means that the effective *PRF* of the system becomes double, as the pulses from the other orthogonal polarization have to be transmitted as well, and the imaged swath is therefore halved. In addition, following the considerations in Section 2.3.5, a demanding requirement on the *RASR* of the cross-polarized channels may further limit the imaged swath.

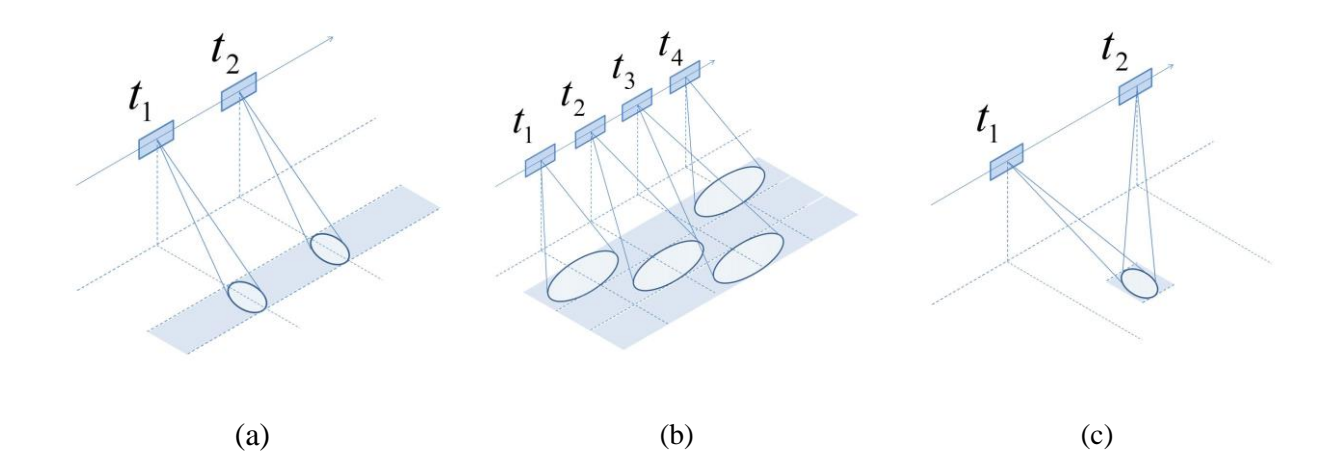


Fig. 12. SAR acquisition modes. (a) Stripmap. (b) ScanSAR. (c) Spotlight.

# 3.2 Digital Beamforming and Multiple Receive Subapertures

To overcome this limitation, new radar techniques have been developed, which allow for the acquisition of spaceborne high-resolution SAR images without the classical swath limitation imposed by range and azimuth ambiguities. These techniques are mainly based on DBF and multiple subaperture signal recording [53]-[59].

In conventional radar systems with phased-array technology the scattered wave is received by several subapertures; the received signals are individually amplified, phase-shifted and then superimposed in an analog beamforming network; only the sum of the received signals is therefore digitized and stored for future processing. In modern radar systems with DBF capability, in contrast, the signal received by each receive subaperture is individually amplified and digitized; the beamforming is therefore performed using the digital values in software, hence the name "digital beamforming". This architecture enables not only the steering of the radar beam in real time, but also the formation of multiple beams, which simultaneously point in different elevation directions.

In side-looking radar geometry (Fig. 5), the echo corresponding to a given radiated pulse arrives back at the radar with increasing delays from increasing elevation angles. DBF can be therefore exploited on receive to steer in real-time a narrow beam towards the direction of arrival (DoA) of the radar echo from the ground, thereby exploiting the one-to-one relationship between the radar pulse travel time and its DoA (this is also referred to as scan-on-receive (SCORE) [58] or Sweep-SAR [59]). A large receiving antenna can hence be used to improve the sensitivity of the system without narrowing the swath width. As the unambiguous swath width is limited by the antenna length according to (37), a long antenna has to be deployed to map a wide swath.

Moreover, to improve the azimuth resolution, the receive antenna can be divided into multiple subapertures, mutually displaced in the along-track direction and connected to individual receive channels. By this, multiple samples of the synthetic aperture can be acquired for each transmitted pulse. If  $N_{sub}$  is the number of subapertures, the equivalent PRF is equal to  $N_{sub}$  times the employed PRF. The coherent combination of all signals in a dedicated multi-channel processor enables the generation of a HRWS SAR image [94]-[96]. The described architecture is depicted in Fig. 13.

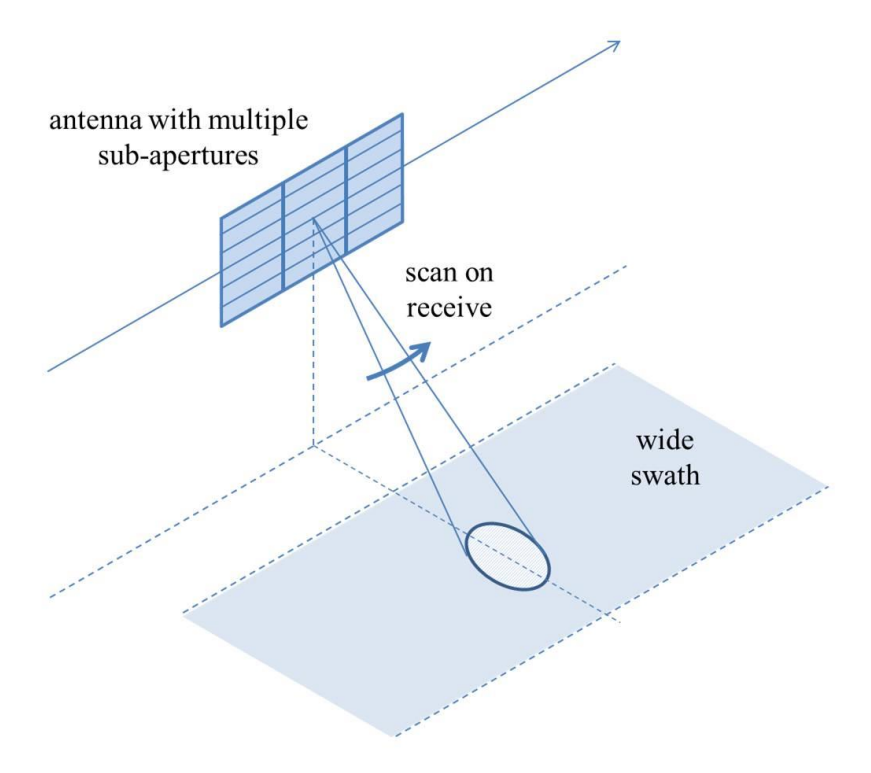


Fig. 13. SAR system with scan-on-receive and multiple receive subapertures in azimuth.

A prominent example of such a system is the HRWS SAR, currently under development at Airbus with support from the DLR [55]. This system will provide a stripmap resolution of 1 m for a 70 km wide swath, by this increasing the stripmap resolution of TerraSAR-X by a factor of three and the swath width by a factor of more than two.

The need for a very long antenna represents the main limitation of the mentioned system: A 40 m antenna is, in fact, required to map a 350 km swath width on ground in stripmap imaging mode.

## 3.2.1 Multi-Channel Processing

Let us consider a system, which for each transmitted pulse collects samples at  $N_{sub}$  uniformly displaced subapertures, and let  $\Delta x_{sub}$  be the distance between two adjacent subapertures. In order to obtain a uniformly sampled signal in the azimuth direction, a specific PRF is required, given by

$$PRF = \frac{2v_S}{N_{sub}\Delta x_{sub}} \tag{38}$$

where  $N_{sub} \Delta x_{sub}$  is also the total antenna length, i.e., the radar has to move half the total antenna length between subsequent transmitted pulses. If a different PRF is selected, e.g., to image ranges which would otherwise be blind or to improve the AASR, the signal is not anymore uniformly sampled in the azimuth direction.

A uniformly sampled signal can be however recovered from the recurrent non-uniform one using a technique, known as multi-channel reconstruction, firstly suggested in [94] and based on the generalized sampling expansion [97].

The generalized sampling theorem states that a band-limited signal is uniquely determined in terms of the samples of the responses of N linear systems  $h_i(t)$ , i = 1...N, with input the signal itself, sampled at 1/N the Nyquist rate [97]. Moreover, the band-limited signal can be obtained by means of N post-filters  $p_k(t)$ , k = 1...N, whose transfer functions  $P_k(f)$ , k = 1...N, are related to the transfer functions  $H_i(f)$ , i = 1...N, of the linear systems  $h_i(t)$  [98]. In particular, the transfer functions  $P_k(f)$  are given by

$$P_{k}(f) = \sum_{m=1}^{N} P_{km}(f) \operatorname{rect}\left(\frac{f - f_{0,m}}{PRF}\right), f_{0,m} = \left(-\frac{N}{2} + m - \frac{1}{2}\right) PRF, k = 1..N$$
(39)

where  $P_{km}(f)$ , k = 1...N, m = 1...N, are the elements of the matrix  $\mathbf{P}(f)$ , given by

$$\mathbf{P}(f) = N \cdot \mathbf{H}^{-1}(f) = \begin{bmatrix} P_{11}(f) & P_{12}(f + PRF) & \cdots & P_{1N}(f + (N-1)PRF) \\ P_{21}(f) & P_{22}(f + PRF) & \cdots & P_{2N}(f + (N-1)PRF) \\ \vdots & \vdots & \ddots & \vdots \\ P_{N1}(f) & P_{N2}(f + PRF) & \cdots & P_{NN}(f + (N-1)PRF) \end{bmatrix}$$
(40)

and  $\mathbf{H}(f)$  is the matrix, which collects the transfer functions  $H_i(f)$ , given by

$$\mathbf{H}(f) = \begin{bmatrix} H_{1}(f) & H_{2}(f) & \cdots & H_{N}(f) \\ H_{1}(f+PRF) & H_{2}(f+PRF) & \cdots & H_{N}(f+PRF) \\ \vdots & \vdots & \ddots & \vdots \\ H_{1}(f+(N-1)PRF) & H_{2}(f+(N-1)PRF) & \cdots & H_{N}(f+(N-1)PRF) \end{bmatrix}$$
(41)

As is apparent from (39), the post-filters  $P_k(f)$ , k = 1...N, can be interpreted as a composition of N pass-band filters. A block diagram of the multi-channel reconstruction is sketched in Fig. 14.

In the special case of systems with multiple subapertures on receive, where a common transmitter is employed and adopting the quadratic phase approximation of (18), the linear systems  $h_i(t)$  only consist of a time delay and a phase shift and the transfer function  $H_i(f)$  can be expressed as [96]

$$H_i(f) = \exp\left(-j\frac{\pi\Delta x_i}{2\lambda R_0}\right) \exp\left(-j\frac{\pi\Delta x_i}{v_S}f\right), i = 1..N$$
(42)

where  $\Delta x_i$  is the distance between the transmitter and the phase center of the *i*-th subaperture.

As the received azimuth signal is not strictly band-limited, a reconstruction error will be present, as the signal components outside the above mentioned frequency band fold back to the main part of the spectrum and disturb the reconstruction of the signal itself. In particular, the *AASR* can be evaluated as described in [96], [99].

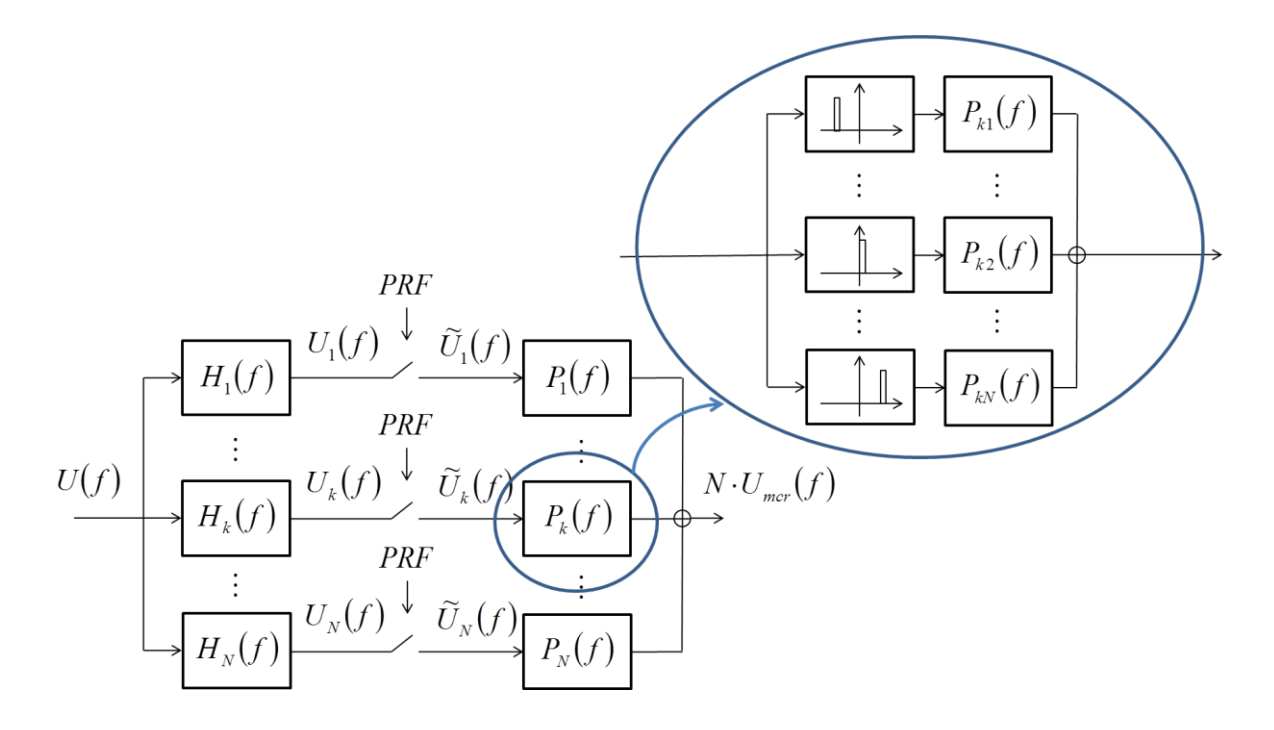


Fig. 14. Block diagram of multi-channel reconstruction with interpretation of the post-filters as a composition of bandpass filters.

Moreover, the reconstruction filters may amplify the noise. Depending on the distribution of the samples and the PBW  $B_p$ , a *SNR* scaling factor can be evaluated [96].

Additional algorithms for multi-channel processing have been recently proposed, based on different criteria, such as the minimization of the ambiguous signal power coming from some frequency bands, the maximization of the signal power after reconstruction, the maximization of the signal to ambiguity plus noise ratio, and the minimization of the mean square error in the reconstruction [100]-[101].

## 3.3 New Architectures and Concepts

In order to keep the antenna length down, several new instrument architectures and modes have been proposed [60]-[62].

### 3.3.1 Multi-Channel ScanSAR

One example is the combination of multiple subapertures in azimuth with ScanSAR or TOPS mode (Fig. 15 (a)). As in classical ScanSAR, azimuth bursts are used to map several swaths. The associated resolution loss from sharing the synthetic aperture among different swaths is compensated by collecting radar echoes with multiple displaced azimuth subapertures [60]-[61]. The peculiarities of the multi-channel ScanSAR processing and their impact on system performance have been analyzed in [102], [103]. A possible drawback of multi-channel ScanSAR or TOPS approaches is the rather high Doppler centroid for some of the imaged targets, in case high resolution is desired. Moreover, high squint angles may also challenge co-registration in interferometric applications [104].

### 3.3.2 Multiple Elevation Beams

Besides multi-channel ScanSAR, of great interest are concepts based on simultaneous recording of echoes of different pulses, transmitted by a wide beam illuminator and coming from different directions. This enables an increase of the coverage area without the necessity to either lengthen the antenna or to employ burst modes [60]-[62]. Fig. 15 (b) provides an illustration, where three narrow receive beams follow the echoes from three simultaneously mapped image swaths that are illuminated by a broad transmit beam. With reference to the timing diagram of Fig. 11, the three swaths highlighted in green can be simultaneously imaged. A sufficiently high antenna is needed to separate the echoes from the different swaths by digital beamforming on receive, while a wide beam can either be accomplished by a separate small transmit antenna or a combined transmit-receive antenna together with tapering, spectral diversity on transmission or sequences of subpulses [105], [106].

An interesting alternative to a planar antenna is a reflector, fed by a multi-channel array, as illustrated in Fig. 15 (c). A parabolic reflector focuses an arriving plane wave on one or a small subset of feed elements. As the swath echoes arrive as plane waves from increasing look angles,

one needs hence to only read out one feed element after the other to steer a high-gain beam in concert with the arriving echoes.

A drawback of the multi-beam mode is the presence of blind ranges across the swath, as the radar cannot receive while it is transmitting.

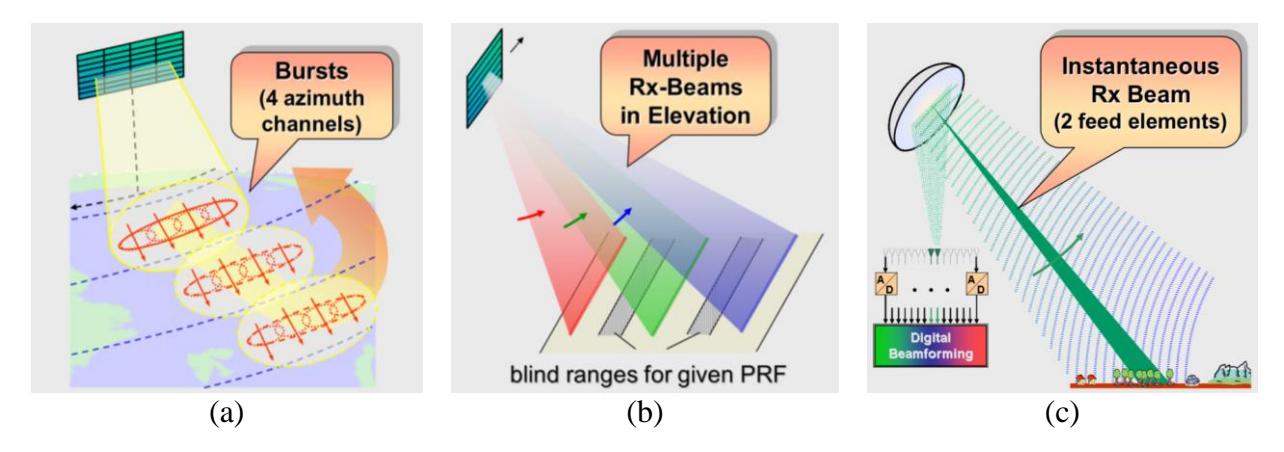


Fig. 15. Advanced concepts for HRWS imaging. (a) Multi-channel ScanSAR. (b) SAR with multiple elevation beams (planar antenna). (c) SAR with multiple elevation beams (reflector antenna).

Staggered SAR overcomes the problem of blind ranges by continuously varying the *PRI*. If the *PRI* is continuously varied, there will still be ranges, from which the echoes are not received, because the radar is transmitting, but they will be different for each transmitted pulse. A proper selection of the *PRIs*, i.e., imposing that two consecutive samples in azimuth are never missed, together with an average oversampling in azimuth allows an accurate interpolation of the non-uniformly sampled raw data on a uniform grid, so that they can be then focused with a conventional SAR processor. This concept therefore allows high-resolution imaging of a wide continuous swath without the need for a long antenna with multiple subapertures [61]-[74].

# 4.1 Concept

DBF in elevation allows the simultaneous mapping of multiple subswaths, but blind ranges are present between adjacent subswaths [60]-[62]. If the PRI is uniform, blind ranges remain unchanged along azimuth (Fig. 16 (a)). After compression in azimuth, the image will therefore contain blind strips of width  $\Delta R_{0 \text{ blind}}$ , given by (34).

If, in place of a constant *PRI*, a sequence of *M* distinct *PRIs*, which then repeat periodically, is employed, there will still be blind ranges. The width of the blind range areas will be still given by (34), but the locations of the blind ranges will no longer be given by (33). In general, the locations of the blind ranges will be different for each transmitted pulse, as they are related to the time distances to the preceding transmitted pulses (Fig. 16 (b)). If the overall synthetic aperture is considered, it turns out that at each slant range only some of the transmitted pulses are missing.

In particular, if a sequence of PRIs is chosen such that the blind range areas are almost uniformly distributed across the swath, it can be shown that the percentage of missing samples in the raw data is approximately equal to the mean duty cycle, i.e., the ratio of the uncompressed pulse length  $\tau$  to the mean PRI. Following the discussion of Section 3.1, the percentage of samples in the range-compressed data, where scatterers are only imaged with degraded range resolution, is instead approximately equal to twice the mean duty cycle.

If a relatively small percentage of pulses is missing, it is still possible to focus the data and obtain a SAR image over a wide continuous swath: The presence of large gaps in the raw azi-

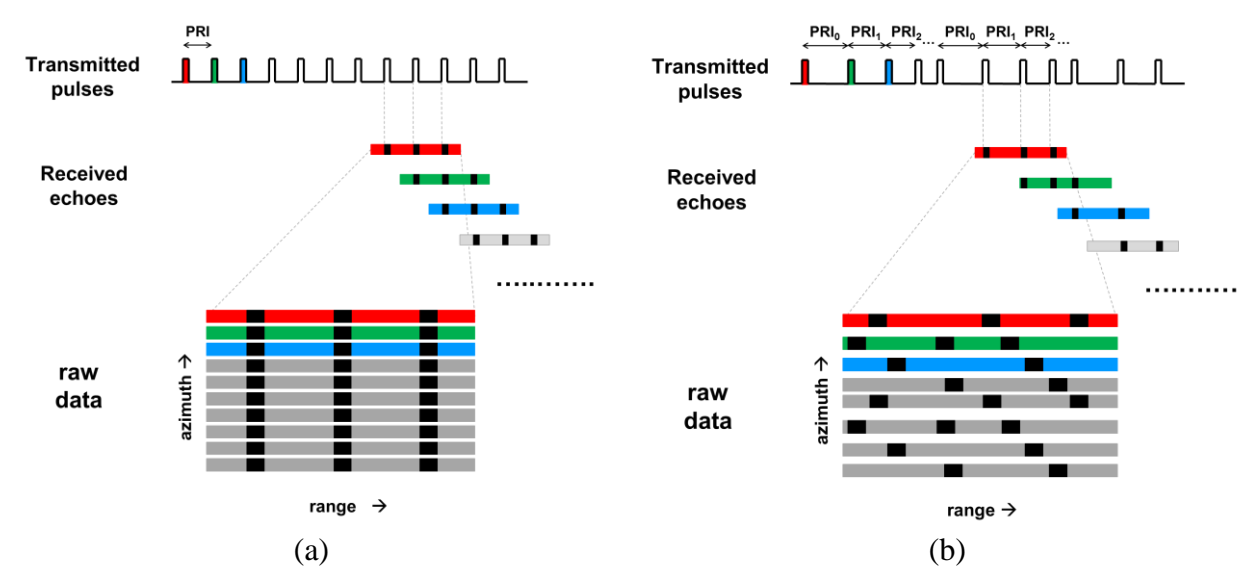


Fig. 16. Location of blind ranges. (a) Constant PRI SAR. (b) Staggered SAR.

muth signal, however, will determine the presence of rather high sidelobes in the azimuth impulse response [107], [108].

Another possibility is to design the sequence of *PRIs* such that two consecutive samples in azimuth are never missed in the raw data. In this case, if the mean pulse repetition interval is decreased, i.e., if the signal is averagely oversampled, it is possible to accurately interpolate the data on a uniform grid, so avoiding the high sidelobes in the azimuth impulse response. As a lower mean *PRI* is used, it will be necessary to increase the antenna height in order to keep the same *RASR*.

The use of a variable *PRI* to image a large continuous swath has been first suggested in [64] and later independently discovered by DLR [61]. Further work on the subject can be found in [65]. This thesis presents a robust and optimized concept of staggered SAR; moreover, it introduces novel sequences of *PRIs*, interpolation methods, and processing strategies, which allow a staggered SAR system to meet outstanding ambiguity requirements with state-of-the-art antenna technology. A detailed analysis of range and azimuth ambiguities is furthermore presented, which allows an understanding of the impact of the different system parameters on the SAR imaging performance [66]-[74], [93].

## 4.1.1 Processing Strategies

As sequences of *PRIs* are employed and the lost pulses are different for each slant range, the raw data recorded by a staggered SAR system are inherently non-uniformly sampled. In principle, non-uniformly sampled raw data can be processed focusing each pixel independently, i.e., in time domain. For efficient implementation, however, the data can be at some point resampled to a uniformly spaced grid and then further processed with a conventional SAR processor. Fig. 17 shows the block diagrams for two different processing strategies: The processing strategy of Fig. 17 (a), alluded in [66], consists of performing range compression on the raw staggered SAR data, then resampling the range-compressed staggered SAR data on a uniformly spaced grid and finally performing azimuth compression, while the strategy of Fig. 17 (b), proposed in [67], consists

of resampling the raw data on a uniformly-spaced grid and then performing range and azimuth compression. The advantages of the latter approach in combination with some sequences of *PRIs* will become clear in the following.

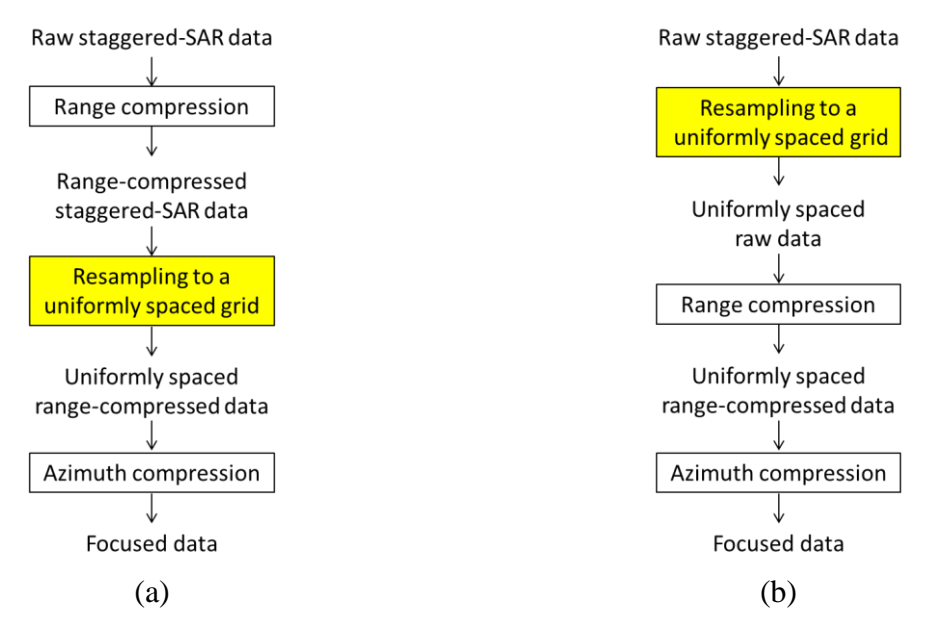


Fig. 17. Block diagrams for different processing strategies for staggered SAR data. (a) Strategy based on the resampling of range-compressed data. (b) Strategy based on the resampling of raw data.

# 4.2 Design of Sequences of PRIs

Let us assume that a sequence of M distinct PRIs, which then repeat periodically, is employed. Let us indicate the M PRIs as  $PRI_m$ , m = 0..M - 1 and let us define  $PRI_{min}$  and  $PRI_{max}$  as the minimum and the maximum of the M PRIs, respectively.  $PRI_{min}$  has to be kept large enough to control range ambiguities, while  $PRI_{max}$  has to be kept small enough to ensure proper sampling in the azimuth direction: Moreover, in case the sequence of PRIs is designed such that in the raw azimuth signal two consecutive samples are never missed,  $PRI_{max}$  imposes an upper bound to the maximum gap width, which is always smaller than 2  $PRI_{max}$ .

In principle, the M PRIs can be arbitrarily (or even randomly) chosen in the interval  $[PRI_{min}, PRI_{max}]$ . However, as it will be clear in the following, a linear PRI trend has the advantage of letting the system designer optimize the choice of the PRIs in relation to other system parameters (slant ranges of interest, uncompressed transmitted pulse length) and control in a straightforward way the location and/or the width of the resulting gaps. A sequence, where the PRI has a linear trend, is defined as

$$PRI_{m} = PRI_{m-1} - \Delta = PRI_{0} - m\Delta, \quad m = 1..M - 1$$
 (43)

where  $\Delta$  is the difference between two consecutive *PRIs* and *M* is the number of *PRIs* of the sequence. Without loss of generality, we will consider the case  $\Delta > 0$ , i.e., decreasing *PRI*. It goes without saying that sequences with increasing *PRI* ( $\Delta < 0$ ) can be used as well.

### 4.2.1 Slow PRI Change

It has been already noted that, for a constant PRI, blind range areas are located at fixed slant range along azimuth. If a long sequence of PRIs with a linear slowly-changing trend is employed, it can be observed that blind range areas are no longer strips parallel to the along-track axis, but they are instead tilted, where the tilt angle increases, as the PRI span increases. Moreover, for a given PRI span, it can be observed that the tilt slightly increases with range. Fig. 18 shows the location of blind ranges for different PRI spans. In all four cases the maximum PRI is set to 0.72 ms, while the minimum PRI spans from 0.72 ms (constant PRI) to 0.66 ms. The pulse length is set to  $\tau = 30$  µs and the number of PRIs of the sequence to M = 250. Two cycles of PRI variation are shown in the diagrams, while an orbit height  $h_S = 745$  km has been considered for the plots, i.e., to convert slant range into ground range according to the spherical Earth model of Appendix A.

As a limited PRI span has the advantage to ensure proper sampling in the azimuth direction, without significantly impacting range and azimuth ambiguities, a reasonable criterion to design sequences of PRIs is to choose the minimum PRI span such that blind ranges are almost uniformly distributed over the slant range of interest. This means that the blind areas are tilted such that at far range they span over a slant range equal to the distance of two consecutive blind ranges in a uniform PRI case, i.e., PRI times half the speed of light in free space  $c_0/2$ . As the tilt is slightly smaller at closer ranges, the other blind areas will span over a slightly smaller slant range and there will be some ranges, where all samples are received.

With reference to the timing diagram of Fig. 19, where the blind ranges are displayed as a function of 1/PRI, the above mentioned minimum span of 1/PRI is given by the horizontal distance between two adjacent blind ranges at the maximum slant range of interest  $R_{0\text{max}}$ 

$$\frac{1}{PRI_{\min}} - \frac{1}{PRI_{\max}} \ge \frac{c_0}{2R_{0\max}} \tag{44}$$

It has to be noted that  $PRI_{min}$  and  $PRI_{max}$  can be arbitrarily chosen, as long as the difference of their reciprocals is given by (44): The reciprocals of  $PRI_{min}$  and  $PRI_{max}$  must not necessarily correspond to blind ranges at  $R_{0max}$ . If the span of PRI is selected according to (44), as the PRI spans between  $PRI_{min}$  and  $PRI_{max}$ , it can be observed that a large gap, i.e., a gap made of several consecutive missing samples, and a very short gap occur at each slant range [65].

Assuming a linear PRI trend, a sequence of PRIs is defined, if the number of PRIs of the sequence M is given in addition to  $PRI_{min}$  and  $PRI_{max}$ . In order to avoid that the resulting azimuth impulse response is strongly dependent on target position, M has to be chosen such that the period  $T_{sw}$  of the sequence of PRIs, i.e., the sum of the M PRIs, is much smaller than the shortest illumination time T, i.e., the illumination time at near range  $T(R_{0 \text{ min}})$ , given by (15). In [65] it is shown that a sequence with  $T_{sw} = T(R_{0 \text{ min}})$  is still characterized by an azimuth impulse response

strongly dependent on target position, while for a sequence with  $T_{sw} = T(R_{0 \text{ min}})/5$  the dependence is no longer significant. On the other hand, as M decreases, the distribution of blind ranges becomes less and less uniform.

Fig. 20 shows, for a sample sequence with slow PRI change, the PRI trend, the location of missing samples in the raw data, the percentage of missing samples and the maximum, mean and minimum pulse separation ( $PRI_{max} = 0.38$  ms,  $PRI_{min}$  has been computed using (44) with  $R_{0max} = 1031.9$  km, M = 250,  $\tau = 14.81$  µs,  $h_S = 745$  km). From Fig. 20 (b) it is also apparent that, even though tilted, blind ranges divide the swath of interest into multiple subswaths. The echoes from these different subswaths are simultaneously collected using multiple beams by employing DBF in elevation.

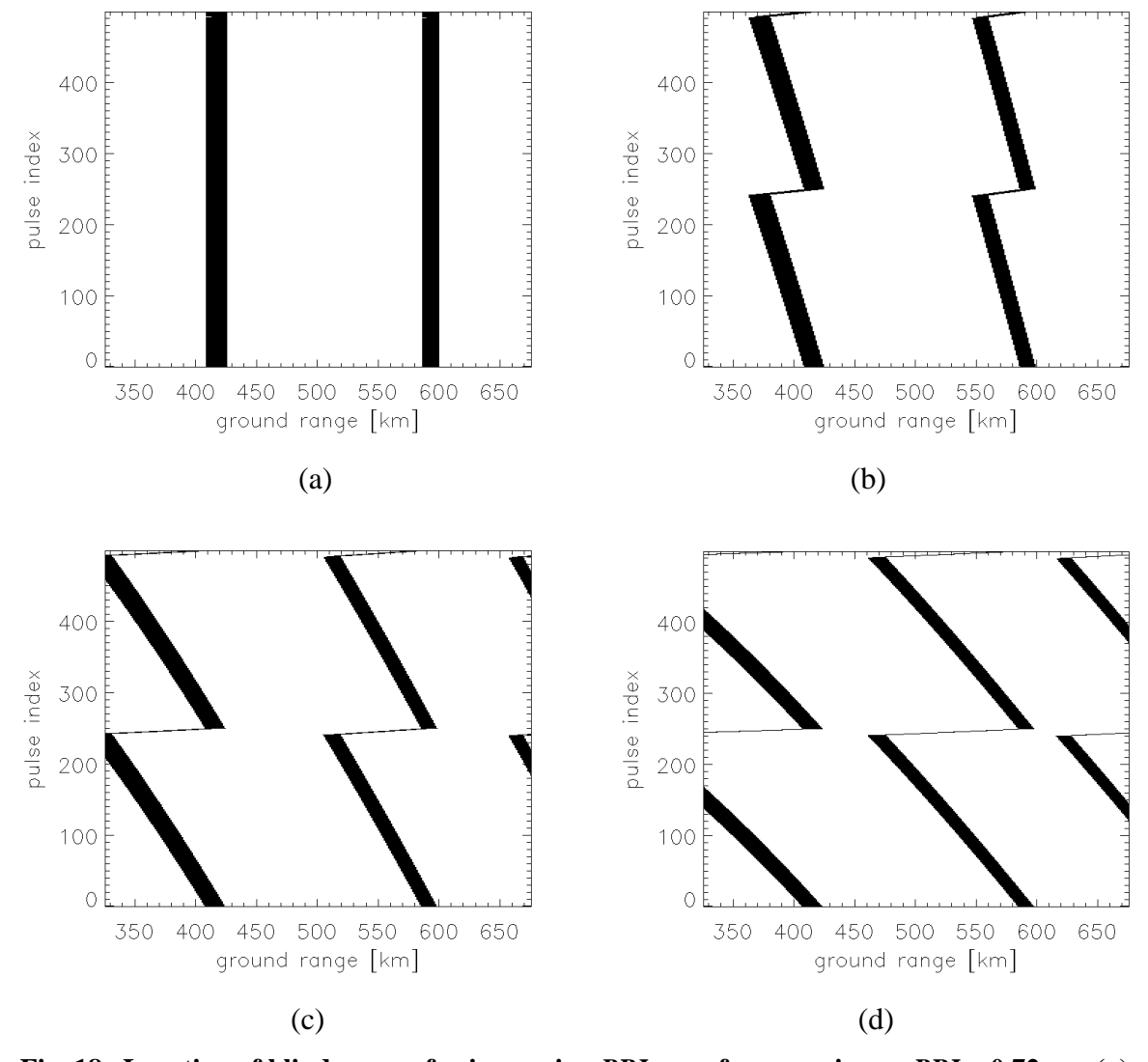


Fig. 18. Location of blind ranges for increasing PRI span for a maximum PRI = 0.72 ms. (a) Minimum PRI = 0.72 ms (constant PRI). (b) Minimum PRI = 0.70 ms. (c) Minimum PRI = 0.68 ms. (d) Minimum PRI = 0.66 ms.

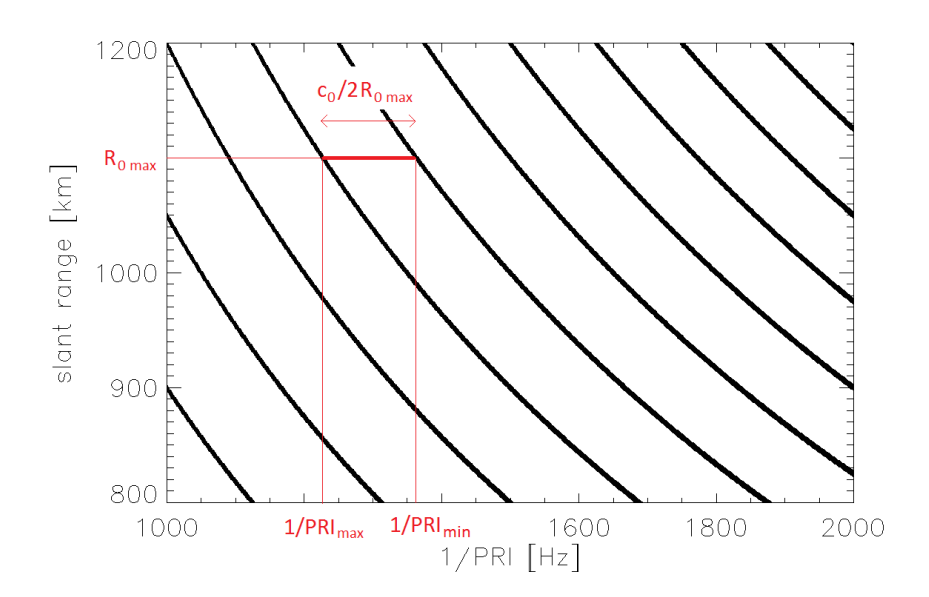


Fig. 19. Timing diagram as a function of 1/PRI and minimum span of 1/PRI.

If on the one hand sequences of PRIs, characterized by a slowly-changing PRI trend, have the advantage of relatively large values of  $PRI_{min}$ , their main drawback is that large gaps are present in the raw azimuth signal. As a consequence, after azimuth focusing, high sidelobes are present in the azimuth impulse response in the vicinity of the mainlobe, as shown in Section 5.

As already noticed in [60], the different azimuth bursts, separated by the large gaps, can be processed independently, so avoiding the high sidelobes associated to the gaps and obtaining several independent low resolution images, which can then be multi-looked and used to either enhance the radiometric resolution or to reduce interferometric phase errors.

### 4.2.2 Fast *PRI* Change

An alternative criterion to design sequences of *PRIs* is to require that two consecutive samples in azimuth are never missed in the raw data for all slant ranges of interest. The idea of optimizing the sequence of *PRIs* by imposing that two consecutive samples in azimuth (although in the range-compressed data) are never missed has been suggested in [61]. In case linear *PRI* trends are considered, this criterion leads to shorter sequences with a much faster *PRI* change, compared to the previously described criterion [66], [67], [70].

With reference to (43), assuming that  $PRI_0 = PRI_{max}$  is given,  $\Delta$  and M have to be determined. If the above mentioned requirement is satisfied over intervals of  $\Delta$  and M, the minimum values of  $\Delta$  and M have to be chosen to maximize  $PRI_{min}$  and therefore achieve better performance in terms of range ambiguities. It is assumed that the minimum and maximum slant ranges,  $R_{0min}$  and  $R_{0max}$ , as well as the uncompressed transmitted pulse length  $\tau$ , are known.

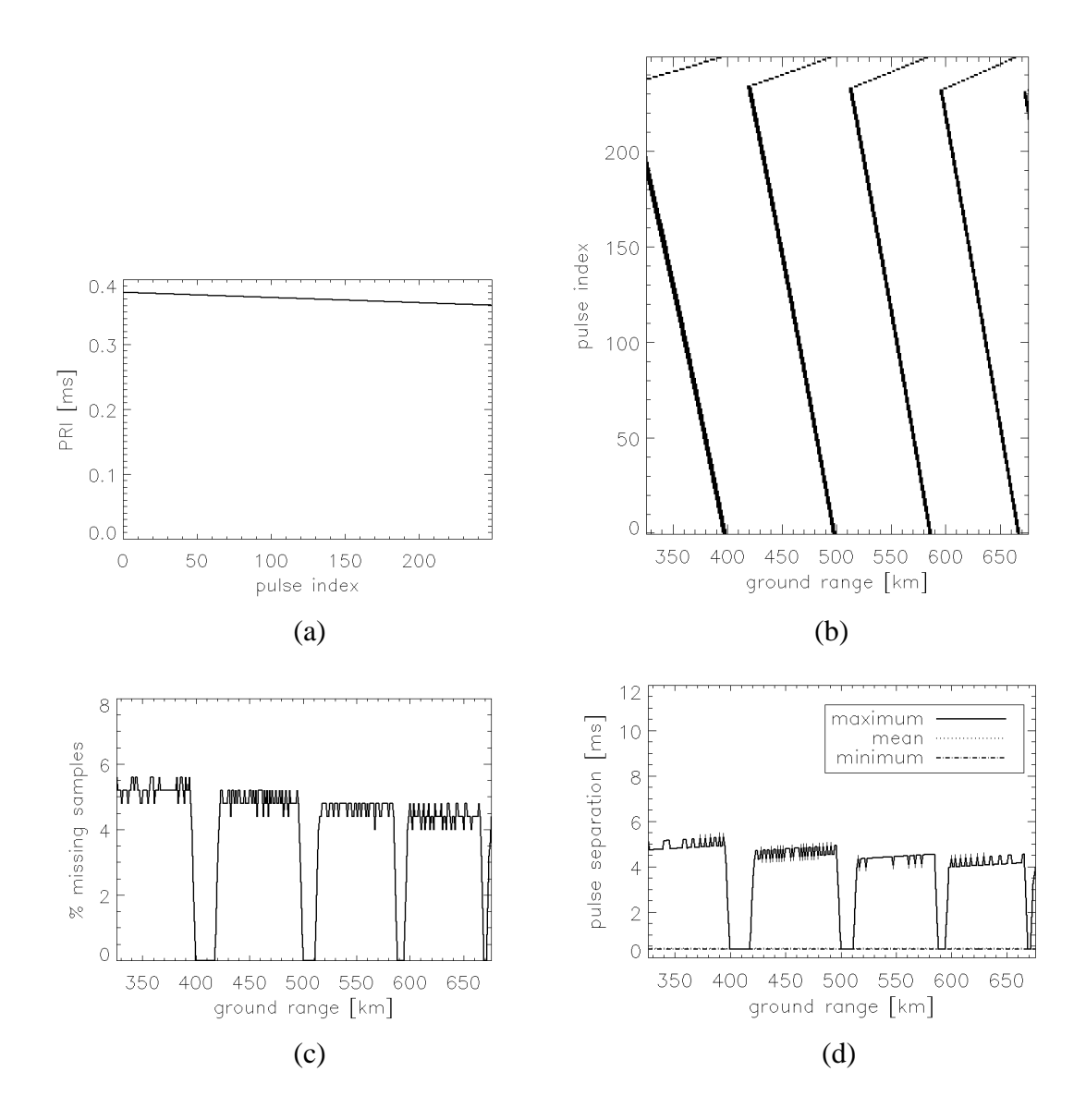


Fig. 20. Example of sequence of *PRIs* with slow *PRI* change ( $PRI_{max} = 0.38$  ms,  $PRI_{min}$  has been computed using (44) with  $R_{\theta max} = 1031.9$  km, M = 250,  $\tau = 14.81$  µs). (a) *PRI* trend. (b) Location of missing samples in the raw data. (c) Percentage of missing samples in the raw data versus ground range. (d) Maximum, mean and minimum pulse separation versus ground range. The minimum and mean pulse separations are not well visible, as they are very small compared to the maximum pulse separation.

Fig. 21 (a) shows the sequence of transmitted pulses and the sequence of received pulses for slant range  $R_0$ . The received pulses are therefore shifted by  $t_0 = 2 R_0/c_0$  with respect to the transmitted pulses. The pulse marked by the blue arrow cannot be fully received, as another pulse is being transmitted at the same time.

In order to avoid that two consecutive azimuth samples are lost in the raw data, the time separation of the first two pulses of the sequence (i.e., the largest PRI of the sequence, denoted as  $PRI_0$ ) must be at least  $\tau$  larger than the separation  $PRI_{k^*}$  of the pulses transmitted while the two first pulses are received from a range  $R_{0\min}$ . This first condition is depicted in Fig. 21 (b) and can be formally expressed as

$$PRI_0 \ge PRI_{\nu^*} + \tau \tag{45}$$

where  $k^*$  is the maximum value such that

$$\sum_{m=0}^{k^*-2} PRI_m \le \frac{2R_{0\min}}{c_0} - \Delta \tag{46}$$

The separation of the pulses transmitted while the first two pulses are received from farther ranges, in fact, will be even smaller. Moreover, it is enough to impose this condition on the first two pulses, because the linear *PRI* trend guarantees a constant difference between consecutive *PRIs*.

Substituting (43) in (45) one obtains

$$\Delta \ge \Delta_{\min} = \frac{\tau}{k^*} \tag{47}$$

Expanding (46) and substituting in place of  $\Delta$  its minimum possible value  $\Delta_{\min}$  given in (47), the maximum value of  $k^*$ , which satisfies

$$\sum_{m=0}^{k^{*}-2} PRI_{m} \leq \frac{2R_{0\min}}{c_{0}} - \Delta \Leftrightarrow \\ (k^{*}-1)PRI_{0} - \frac{(k^{*}-1)(k^{*}-2)}{2} \Delta \leq \frac{2R_{0\min}}{c_{0}} - \Delta \Leftrightarrow \\ (k^{*}-1)PRI_{0} - \frac{(k^{*}-1)(k^{*}-2)}{2} \frac{\tau}{k^{*}} \leq \frac{2R_{0\min}}{c_{0}} - \frac{\tau}{k^{*}} \Leftrightarrow \\ (k^{*}-1)PRI_{0} - \frac{\tau}{2} k^{*} + \frac{3\tau}{2} \leq \frac{2R_{0\min}}{c_{0}} \Leftrightarrow \\ k^{*} \left( PRI_{0} - \frac{\tau}{2} \right) \leq \frac{2R_{0\min}}{c_{0}} + PRI_{0} - \frac{3\tau}{2}$$

$$(48)$$

is obtained, where

$$k^* = \left| \frac{\frac{2R_{0\,\text{min}}}{c_0} + PRI_0 - \frac{3\tau}{2}}{PRI_0 - \frac{\tau}{2}} \right| \tag{49}$$

and  $\lfloor \cdot \rfloor$  denotes the floor function, i.e., the largest integer not greater than the argument of the function. This value of  $k^*$  can then be substituted in (47) to obtain  $\Delta_{\min}$ . Slightly larger values of  $\Delta$  could be used to build up more elaborated sequences, as justified in Section 4.2.3. In that case, it is anyway necessary to compute  $k^*$  again, as it is needed in the following to obtain M. This can be done by substituting the desired value of  $\Delta$  in (46) and finding the maximum value of  $k^*$  which satisfies it. One obtains

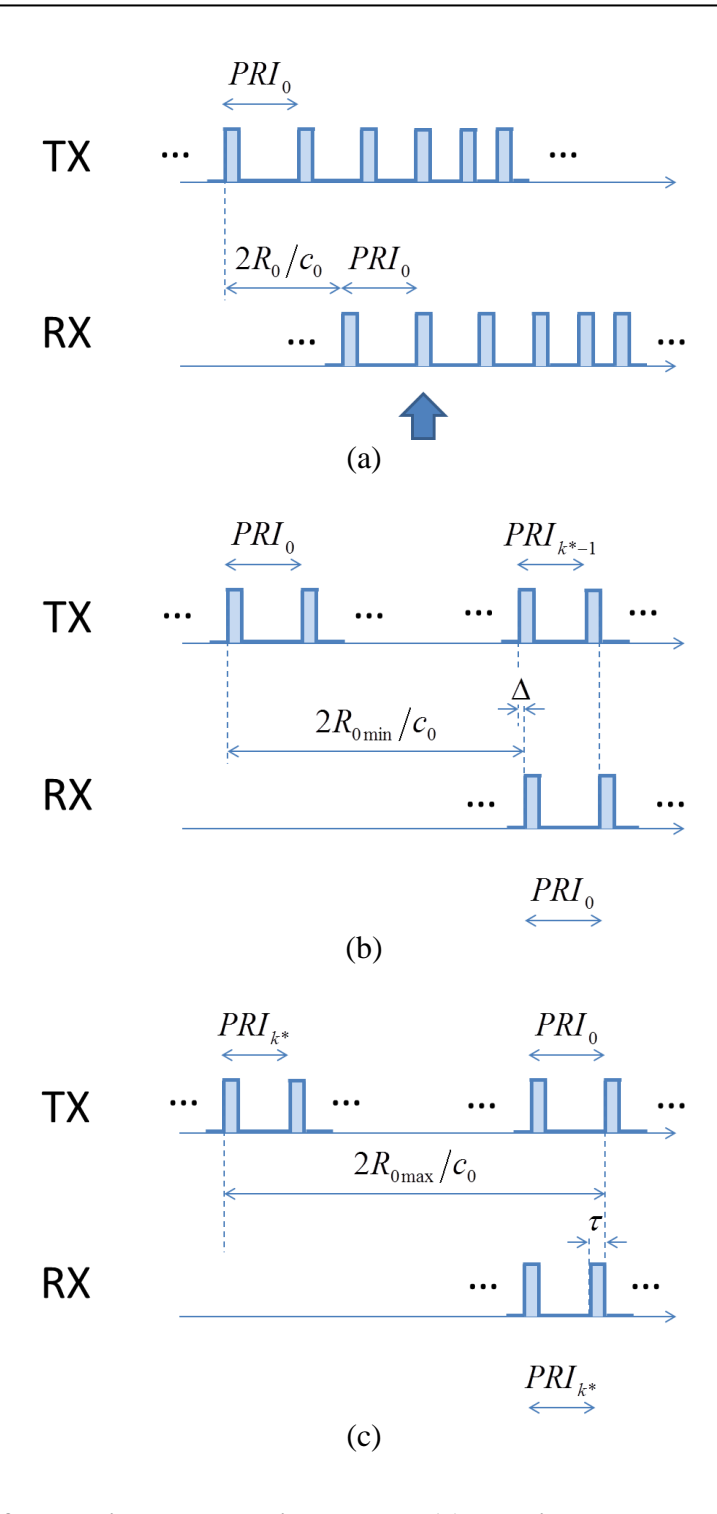


Fig. 21. Diagram of transmitted and received pulses. (a) Relative delay between transmitted and received pulses. The pulse highlighted by a blue arrow cannot be fully received. (b) Graphical representation of the first condition to avoid that two consecutive azimuth samples are missing in the raw data, i.e., the time separation of the first two pulses of the sequence must be at least  $\tau$  larger than the separation of the pulses transmitted while the two first pulses are received from a range  $R_{0\min}$ . (c) Graphical representation of the second condition to avoid that two consecutive azimuth samples are missing in the raw data, i.e., when the pulses, whose separation is  $PRI_{k^*}$ , are received from a range  $R_{0\max}$ , all the pulses of the period must have have been already transmitted.

$$k^* = \frac{\left(PRI_0 + \frac{3\Delta}{2}\right) - \sqrt{\left(PRI_0 + \frac{3\Delta}{2}\right)^2 - 2\Delta\left(\frac{2R_{0\min}}{c_0} + PRI_0\right)}}{\Delta}$$
 (50)

Once  $\Delta$  has been determined, M has to be determined as well. In this case, in order to avoid that two consecutive samples are missing in the raw data, M must be large enough that, when the pulses, whose separation is  $PRI_{k*}$ , are received from a range  $R_{0\text{max}}$ , all the pulses of the period have been already transmitted, i.e., the radar is transmitting the first two pulses of the next period. This second condition is depicted in Fig. 21 (c) and can be formally expressed as

$$\sum_{m=k^{*}}^{M-1} PRI_{m} + PRI_{0} - \tau \ge \frac{2R_{0\max}}{c_{0}}$$
(51)

From (45), in fact,  $PRI_{k^*}$  is at least  $\tau$  smaller than the separation of the first two pulses. If a smaller M were used, two consecutive pulses would be lost, when the two first pulses are transmitted.

The minimum possible value  $M_{min}$ , which satisfies (51), is obtained

$$\sum_{m=k^{*}}^{M-1} PRI_{m} \ge \frac{2R_{0\text{max}}}{c_{0}} - PRI_{0} + \tau \Leftrightarrow$$

$$\left(M - k^{*}\right) PRI_{0} - \frac{M^{2} - k^{*2} - \left(M - k^{*}\right)}{2} \Delta \ge \frac{2R_{0\text{max}}}{c_{0}} - PRI_{0} + \tau \Leftrightarrow$$

$$\frac{\Delta}{2} M^{2} - \left(PRI_{0} + \frac{\Delta}{2}\right) M + \frac{2R_{0\text{max}}}{c_{0}} + \left(k^{*} - 1\right) \left(PRI_{0} - \frac{\Delta}{2}k^{*}\right) + \tau \le 0 \Leftrightarrow$$

$$M \ge M_{\text{min}} = \left[\frac{\left(PRI_{0} + \frac{\Delta}{2}\right) - \sqrt{\left(PRI_{0} + \frac{\Delta}{2}\right)^{2} - 2\Delta \left(\frac{2R_{0\text{max}}}{c_{0}} + \left(k^{*} - 1\right) \left(PRI_{0} - \frac{\Delta}{2}k^{*}\right) + \tau\right)}{\Delta}\right]$$
(52)

where  $\lceil \cdot \rceil$  denotes the ceiling function, i.e., the smallest integer not less than the argument of the function.

As it will be shown in Section 5, if two consecutive samples are never missed in the raw data and the mean *PRI* is decreased, i.e., if the signal is averagely oversampled in azimuth, it is possible to accurately interpolate the data on a uniform grid, so avoiding the high sidelobes in the azimuth impulse response. Additional advantages derive from the use of sequences with fast *PRI* change in combination with the processing strategy based on the resampling of the raw data, as discussed in the following.

In the left-hand part of Fig. 22 some range lines of a raw staggered SAR data set, where two consecutive samples in azimuth are never missed, are sketched. Blind areas, where data are missing, as the radar is transmitting, are marked in black. The width in slant range of each blind area

is given by the pulse length  $\tau$  times half the speed of light in free space  $c_0$ . In the right-hand part of Fig. 22 the corresponding range-compressed staggered SAR data, obtained by correlating each range line with a replica of the transmitted waveform, are sketched. The shaded areas represent data where targets are not imaged with full range resolution, as only part of the echo of the transmitted pulse is received. The width in slant range of each of the latter areas is given by the pulse length  $\tau$  times the speed of light in free space  $c_0$ , i.e., twice the width of the blind area in the raw data. If LFM waveforms are employed, the shaded areas correspond to data for which only a portion of the range spectrum is available. As these data cannot be straightforwardly used to recover the samples on a uniformly spaced grid, they were discarded in [66], although pointing out that this information could have been exploited. In the following, it is shown that this information can be exploited, if the strategy based on the resampling of the raw data is used [67].

As apparent from Fig. 22, the first advantage of the strategy based on the resampling of the raw data is that the percentage of missing samples in the raw data is equal to the mean duty cycle, while for the strategy, based on the resampling of the range-compressed data, the percentage of discarded samples was equal to twice the mean duty cycle.

Furthermore, the processing strategy impacts the design of the sequence of PRIs. The values of  $\Delta$  and M obtained, requiring that in the range-compressed data there are never two consecutive azimuth samples, where targets are imaged with degraded range resolution, are given by

$$\Delta \ge \Delta_{\min} = \frac{2\tau}{k^*} \tag{53}$$

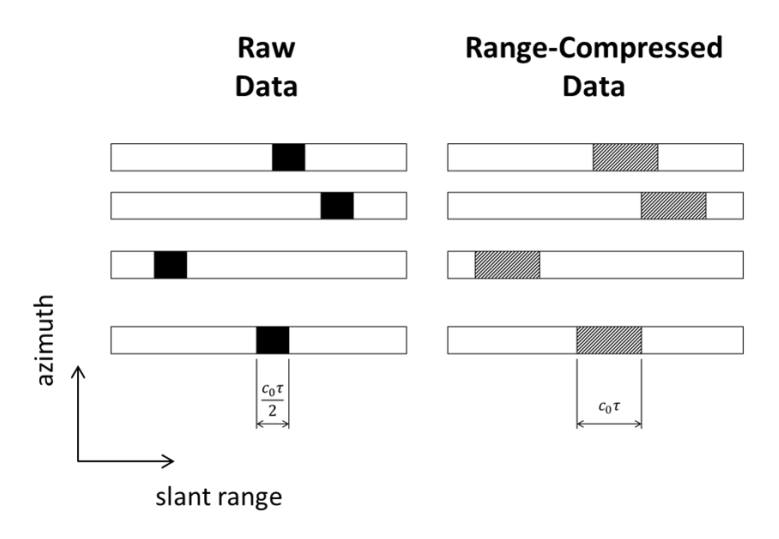


Fig. 22. Raw (left) and range-compressed (right) staggered SAR data. Blind areas, where data are missing, are marked in black. The shaded areas represent data, where targets are not imaged with full range resolution.

$$M \ge M_{\min} = \left[ \frac{\left( PRI_0 + \frac{\Delta}{2} \right) - \sqrt{\left( PRI_0 + \frac{\Delta}{2} \right)^2 - 2\Delta \left( \frac{2R_{0\max}}{c_0} + \left( k^* - 1 \right) \left( PRI_0 - \frac{\Delta}{2} k^* \right) + \tau \right)}{\Delta} \right]$$
(54)

respectively, where

$$k^* = \left| \frac{\frac{2R_{0\,\text{min}}}{c_0} + PRI_0 - 2\tau}{PRI_0 - \tau} \right|$$
 (55)

Let us assume that  $PRI_0$ ,  $\tau$ ,  $R_{0\text{min}}$  and  $R_{0\text{max}}$  are fixed. Fig. 23 shows the PRI trends of the sequences obtained for the two different strategies, i.e., using (47), (52), and (49) for the strategy based on the resampling of the raw data and (53), (54), and (55) for the strategy based on the resampling of the range-compressed data, for  $PRI_0 = 0.386$  ms,  $\tau = 14.81$  µs,  $R_{0\text{min}} = 820.7$  km,  $R_{0\text{max}} = 1031.9$  km, while in Table 3 some parameters of the two sequences are summarized. The mean PRF on transmit  $PRF_{mean\ TX}$  is defined as the reciprocal of the mean PRI of the sequence, while the mean effective  $PRF\ PRF_{mean\ eff}$  is defined as the reciprocal of the mean PRI of the available data, i.e., data where missing or discarded samples are not considered. The following relation between  $PRF_{mean\ TX}$  and  $PRF_{mean\ eff}$  holds

$$PRF_{mean\ eff} = (1 - i \cdot dc)PRF_{mean\ TX}$$
(56)

where i is equal to 1 and 2 for the strategy based on the resampling of raw and range-compressed data, respectively. As apparent, for the same maximum PRI, the processing strategy based on the resampling of the raw data leads to a sequence with approximately equal mean effective PRF, but with a larger minimum PRI and a lower mean PRF on transmit. If the same antenna pattern in elevation is used, therefore, the strategy based on the resampling of the raw data will lead to a better RASR.

From a different point of view, if the minimum PRI of the sequence is fixed and sequences are designed so that two consecutive azimuth samples are never missed, the processing strategy based on the resampling of the raw data allows the use of a much longer transmitted pulse. For this example, fixing a minimum PRI equal to 0.315 ms, the strategy based on the resampling of the range-compressed data allows a maximum pulse length  $\tau_{max} = 14.81$  µs, corresponding to a mean duty cycle of 4.22%, while the strategy based on the resampling of the raw data allows a maximum pulse length  $\tau_{max} = 29.62$  µs, corresponding to a mean duty cycle of 8.44%, i.e., it has doubled with respect to the former strategy. As the NESZ of the SAR system is inversely proportional to the length of the transmitted pulse, the latter strategy can be also exploited to improve the NESZ of the system by 3 dB with respect to a system where the data are resampled after range compression, keeping approximately constant the RASR.

The processing strategy based on the resampling of the raw data therefore allows much more flexibility in designing the staggered SAR system in compliance with ambiguities and *NESZ* requirements. Note that in a conventional SAR with DBF in elevation using a constant *PRI* and multiple elevation beams, the increase of the transmitted pulse length would also imply the enlargement of the gaps between the multiple swaths.

Fig. 24 shows for a sample sequence with fast PRI change the PRI trend, the location of missing samples in the raw data, the percentage of missing samples and the maximum, mean and minimum pulse separation ( $PRI_{max} = 0.386$  ms,  $R_{Omin} = 820.7$  km,  $R_{Omax} = 1031.9$  km,  $\tau = 14.81$   $\mu$ s,  $h_S = 745$  km).

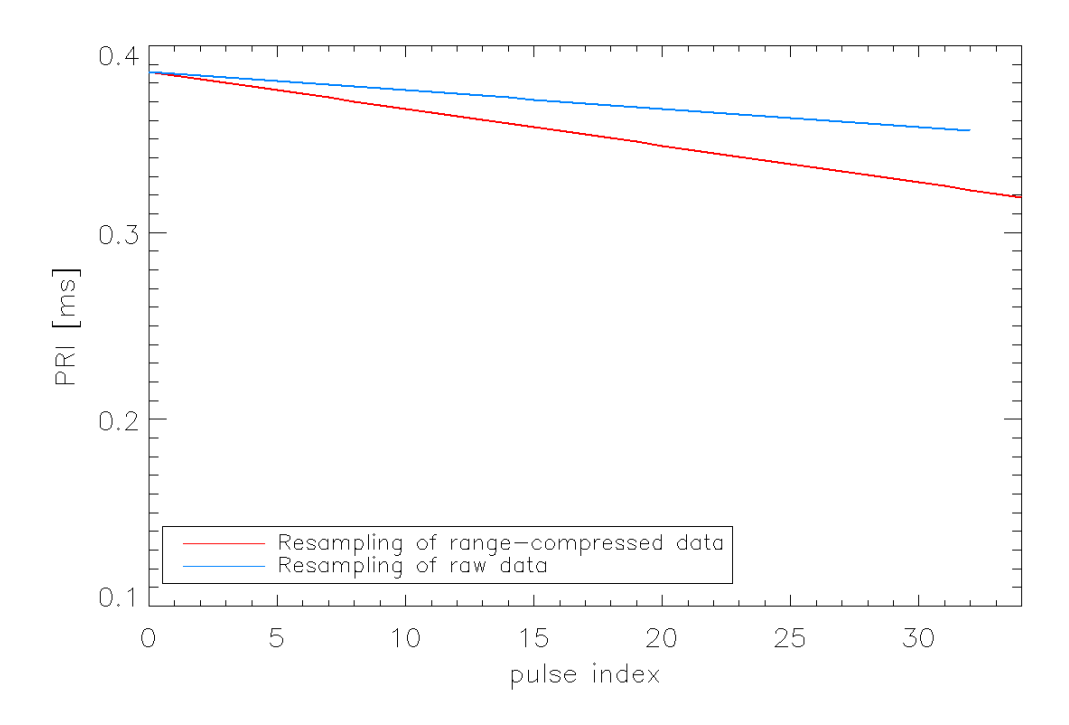


Fig. 23. *PRI* trends of the sequences obtained for the two different strategies, for  $PRI_0 = 0.386$  ms,  $\tau = 14.81$  µs,  $R_{0min} = 820.7$  km,  $R_{0max} = 1031.9$  km.

Parameter	Resampling of	Resampling of raw
	range-compressed data	data
Minimum PRI	0.318 ms	0.354 ms
Mean <i>PRF</i> on transmit	2837 Hz	2701 Hz
Mean effective <i>PRF</i>	2598 Hz	2593 Hz

Table 3. Parameters of the two sequences of *PRIs*.

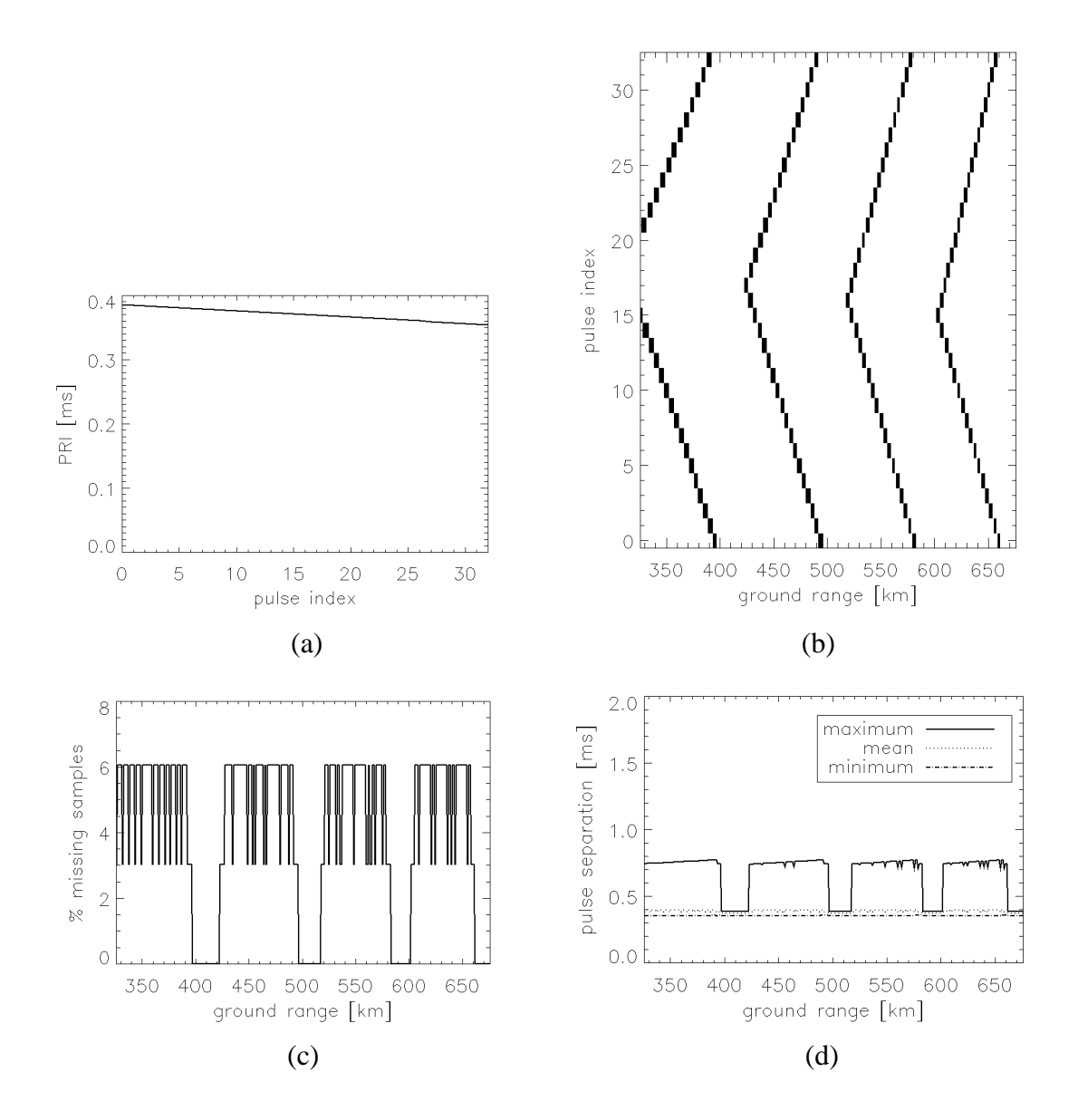


Fig. 24. Example of sequence of *PRIs* with fast *PRI* change ( $PRI_{max} = 0.386$  ms,  $R_{\theta min} = 820.7$  km,  $R_{\theta max} = 1031.9$  km,  $\tau = 14.81$  µs). (a) *PRI* trend. (b) Location of missing samples in the raw data. (c) Percentage of missing samples in the raw data versus ground range. (d) Maximum, mean and minimum pulse separation versus ground range.

### 4.2.3 More Elaborated Sequences

Sequences of *PRIs* with fast *PRI* change have the advantage of the limited maximum pulse separation, which allows the recovery of missing samples by interpolation. In contrast to sequences with slow *PRI* change, no high sidelobes are present in the azimuth impulse response in the vicinity of the mainlobe. However, due to the periodicity of the gaps, more distant sidelobes are anyway present in the azimuth impulse response. The energy of such sidelobes can be spread along azimuth introducing some irregularity in the sequence of *PRIs*.

One possibility is to concatenate S sequences of PRIs with fast PRI change. Let us denote the S sequences with the index s = 0...S-1 and let us assume that the (S-1)-th sequence has been computed, as explained in Section 4.2.2. In particular, for that sequence,  $PRI_0$ ,  $k^*$ ,  $\Delta$ , and M are known and will be indicated as  $PRI_0(S-1)$ ,  $k(S-1)^*$ ,  $\Delta(S-1)$ , and M(S-1), respectively. For all the other S-1 sequences,  $PRI_0(s)$ ,  $k(s)^*$ ,  $\Delta(s)$ , and M(s), s = 0...S-2, can be computed as follows

$$\Delta(s) = \Delta(S-1) = \Delta 
\kappa = \frac{PRI_0(S-1) - PRI_{M-1}(S-1) + \Delta}{S-1} 
PRI_0(s) = PRI_0(S-1) - (S-1-s)\kappa 
k^*(s) = \frac{\left(PRI_0(s) + \frac{3\Delta}{2}\right) - \sqrt{\left(PRI_0(s) + \frac{3\Delta}{2}\right)^2 - 2\Delta\left(\frac{2R_{0\min}}{c_0} + PRI_0(s)\right)}}{\Delta} 
M(s) = \frac{\left(PRI_0(s) + \frac{\Delta}{2}\right) - \sqrt{\left(PRI_0(s) + \frac{\Delta}{2}\right)^2 - 2\Delta\left(\frac{2R_{0\max}}{c_0} + \left(k^*(s) - 1\right)\left(PRI_0(s) - \frac{\Delta}{2}k^*(s)\right) + \tau\right)}}{\Delta}$$
(57)

The *S* sequences of *PRIs* repeat then periodically. If the described procedure is used, two consecutive azimuth samples are never missing in the raw azimuth data. Fig. 25 shows for such a more elaborated sequence the *PRI* trend, the location of missing samples in the raw data, the percentage of missing samples and the maximum, mean and minimum pulse separation (S = 7,  $PRI_{max}(S-1) = 0.405$  ms,  $R_{0min} = 820.7$  km,  $R_{0max} = 1031.9$  km,  $\tau = 14.81$  µs,  $h_S = 745$  km). In this case the percentage of lost samples in the raw data is minimized and kept below 6% over the swath width.

The same considerations on the processing strategies of Sections 4.1.1 and 4.2.2 also apply to the more elaborated sequences of *PRI*s.

### 4.2.4 Sequences for Fully Polarimetric SAR Systems

Several applications of SAR require or at least benefit from full polarimetry. The staggered SAR concept can be also used to design fully polarimetric SAR systems, which image a wide continuous swath with high resolution.

As on transmit the antenna alternately radiates pulses with horizontal and vertical polarizations, while on receive echoes are simultaneously recorded using two separate channels with horizontal and vertical polarizations, the sequence of *PRIs* has to be designed such that two consecutive azimuth samples are never missed in the raw data for each of the four data sets, corresponding to the four polarimetric channels.

A straightforward way to obtain such a sequence is to design a sequence of *PRIs*, as explained in Sections 4.2.2 and 4.2.3, and then repeat each *PRI* of the sequence twice. Fig. 26 shows for a sample sequence of *PRIs* the *PRI* trend, the location of missing samples in the raw data for each polarimetric channel, and the percentage of missing samples for each polarimetric channel. A 175 km continuous ground swath is considered in this example.

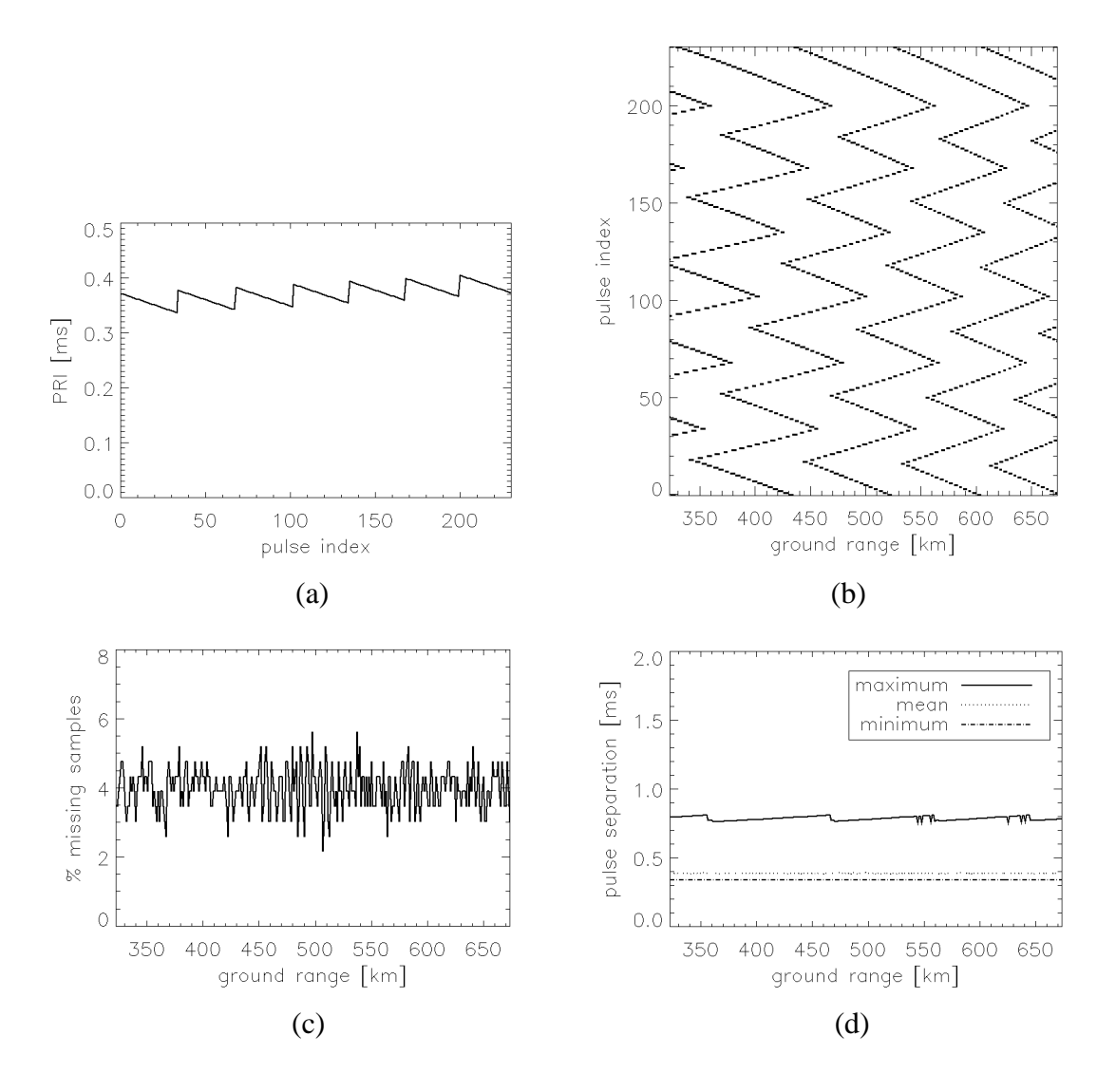


Fig. 25. Example of a more elaborated sequence of *PRIs*. (a) *PRI* trend. (b) Location of missing samples in the raw data. (c) Percentage of missing samples in the raw data versus ground range. (d) Maximum, mean and minimum pulse separation versus ground range.

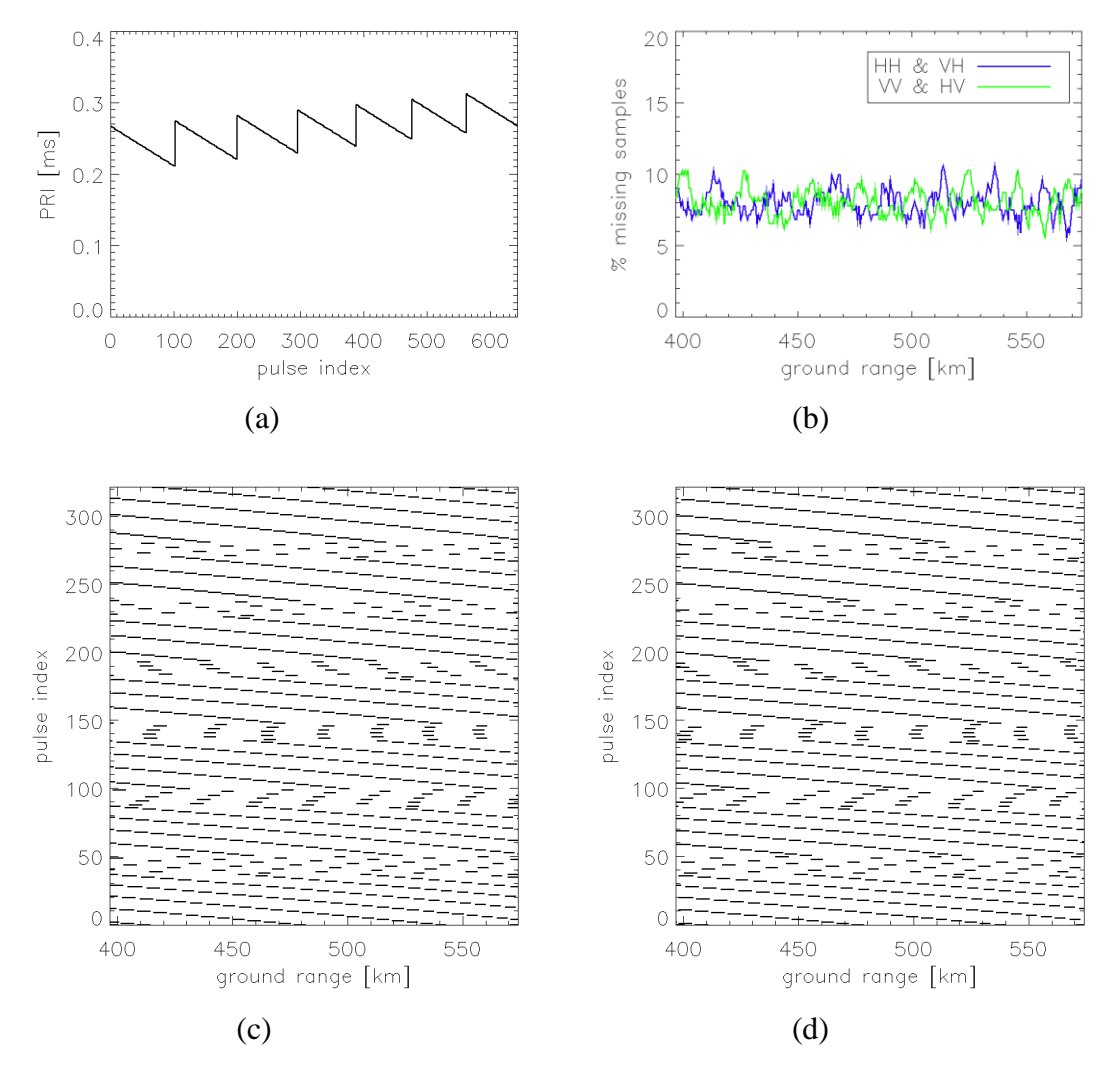


Fig. 26. Example of a sequence of *PRIs* for fully polarimetric staggered SAR. (a) *PRI* trend. (b) Percentage of missing samples versus ground range for the different polarimetric channels. (c) Location of missing samples in the raw data for the polarimetric channels HH and VH. (d) Location of missing samples in the raw data for the polarimetric channels HV and VV.

# 4.3 Interpolation Methods

In this section some resampling methods are discussed, which allow recovering uniformly sampled data from staggered SAR raw data, which are inherently non-uniformly sampled. The recovered uniformly sampled raw data are then focused using a conventional SAR processor.

The effects of RCM and their implications on the 2-D signal reconstruction are also a concern. This problem has been dealt with in [95] with reference to multiple subaperture (separation between receivers of the order of 10 m) and multiple platform (separation between receivers of the order of 250 m) systems. In particular, it has been shown that, while the differential range curvature can be neglected in both multiple subaperture and multiple platform systems, the relative range offset is negligible only in the multiple subaperture case, while it has to be compensated for in the multiple platform case. In the staggered SAR case, all samples received from the

same range have the same range curvature, as they are acquired in monostatic geometry. As far as the range offset is concerned, the time difference between the samples in the non-uniform and uniform grids is of the order of tenths of a millisecond (equivalent spatial difference of the order of few meters). The range offset is therefore comparable or even smaller than in the multiple subaperture case and can hence be neglected.

### 4.3.1 Two-Point Linear Interpolation

The simplest way to resample a non-uniformly sampled signal to a uniform grid is to use a two-point linear interpolator. Each complex sample of the uniform grid is obtained by a weighted average of the closest preceding and succeeding complex samples. The computational cost is small.

#### 4.3.2 Multi-Channel Reconstruction

As the raw azimuth signal is non-uniformly sampled, but at the same time the non-uniform sampling is recurrent, an alternative approach to the resampling is the use of multi-channel reconstruction, described in Section 3.2.1 for systems with multiple receive subapertures.

If for a given range, N out of the M samples of the sequence of PRIs are available, i.e., M-N samples are missing, the samples of the non-uniformly sampled azimuth signal can be divided into N streams, where the i-th stream contains the i-th received (non-missing) sample of each sequence. The N streams are therefore uniformly sampled signals, characterized by a PRI equal to the period of the sequence  $T_{sw}$ , and can be interpreted as filtered versions of the uniformly sampled azimuth signal, subsampled by a factor of N. For the i-th stream, the linear filter consists of a mere time shift and its transfer function is given by

$$H_i(f) = \exp(j2\pi t_i f), i = 1..N$$
(58)

where  $t_i$ , i=1..N, is the time at which the i-th (non-missing) pulse is begun to be received. Unlike the linear filter for the multiple subaperture case, given in (42), the phase term coming from the bistatic geometry of the system with multiple subapertures is missing in the staggered SAR case.

In the special case, where all linear filters consist of mere time shifts, the expression of the post-filters can be further simplified. In particular, the k-th post-filter  $P_k(f)$  is given by the cascade of a filter  $H_k*(f)$ , that is the complex conjugate of  $H_k(f)$ , and a second filter, which consists of a complex weighting of the N subbands.

The elements  $H_{mk}(f)$ , m = 1..N, k = 1..N, of the matrix  $\mathbf{H}(f)$ , defined in (41) and here considered using the reciprocal of  $T_{sw}$  in place of the PRF of the multiple subaperture system, in fact, become

$$H_{mk}(f) = \exp(j2\pi t_k (f + (m-1)/T_{sw})) = \exp(j2\pi t_k f) \exp(j2\pi t_k (m-1)/T_{sw}) = b_{mk} \exp(j2\pi t_k f), m = 1..N, k = 1..N$$
(59)

i.e.,  $H_{mk}(f)$  can be decomposed into the product of a frequency variant component and a complex coefficient  $b_{mk}$ , defined as

$$b_{mk} = \exp(j2\pi t_k (m-1)/T_{sw}), m = 1..N, k = 1..N$$
(60)

As  $\mathbf{H}(f)$  and  $\mathbf{P}(f)$  are related by (40), for the matrix multiplication rule, it has to hold

$$\begin{cases}
\sum_{k=1}^{N} H_{mk}(f) P_{km}(f + (m-1)/T_{sw}) = N, m = 1..N \\
\sum_{k=1}^{N} H_{mk}(f) P_{kq}(f + (q-1)/T_{sw}) = 0, m = 1..N, q = 1..N, m \neq q
\end{cases}$$
(61)

In particular, the two equations in (61) have to hold for all frequencies f in the interval  $I_I$ , defined as

$$I_{1} = \left[ -\frac{N}{2T_{sw}}, -\frac{N}{2T_{sw}} + \frac{1}{T_{sw}} \right]$$
 (62)

therefore  $P_{km}(f+(m-1)/T_{sw})$  in the first equation of (61) has to contain a frequency variant component, which cancels out the one in  $H_{mk}(f)$ .  $P_{km}(f+(m-1)/T_{sw})$  can be therefore written as

$$P_{km}(f + (m-1)/T_{sw}) = w_{km} \exp(-j2\pi t_k (f + (m-1)/T_{sw})), m = 1..N, k = 1..N$$
(63)

Recalling the definition of the post-filter  $P_k(f)$ , given in (39), and considering the expression of the functions  $P_{km}(f)$  given in (63), it is apparent that, in the staggered SAR case,  $P_k(f)$  consists of a cascade of a filter  $H_k*(f)$ , complex conjugate of  $H_k(f)$ , and a second filter, which provides complex weighting of the N subbands by the coefficients  $w_{km}$ , m=1..N.

The coefficients  $w_{km}$ , k=1..N, m=1..N, can be computed by solving the set of equations obtained by substituting (59) and (63) in (61)

$$\begin{cases}
\sum_{k=1}^{N} w_{km} = N, m = 1..N \\
\sum_{k=1}^{N} w_{kq} \exp(j2\pi t_{k}(m-q)f) = 0, m = 1..N, q = 1..N, m \neq q
\end{cases}$$
(64)

The set of equations can be solved by introducing the coefficients  $z_{km}$ , k=1..N, m=1..N

$$z_{km} = w_{km} \exp(-j2\pi t_k (m-1)/T_{sw}) = w_{km}/b_{mk}, m = 1..N, k = 1..N$$
(65)

and substituting them in (64)

$$\begin{cases}
\sum_{k=1}^{N} b_{mk} z_{km} = N, m = 1..N \\
\sum_{k=1}^{N} b_{mk} z_{kq} = 0, m = 1..N, q = 1..N, m \neq q
\end{cases}$$
(66)

The coefficients  $z_{km}$ , k=1..N, m=1..N, are therefore the elements of the matrix **Z**, which is related to the elements  $b_{km}$ , k=1..N, m=1..N, of the matrix **B** by

$$\mathbf{Z} = N \cdot \mathbf{B}^{-1} \tag{67}$$

The coefficients  $w_{km}$ , k=1..N, m=1..N, are finally obtained from (65). They can also be seen as elements of a matrix **W**, which can be written in a compact form as

$$\mathbf{W} = \mathbf{Z} \cdot \mathbf{B}^{\mathrm{T}} = N \cdot \mathbf{B}^{-1} \cdot \mathbf{B}^{\mathrm{T}} \tag{68}$$

where the symbol .\* stands for element-wise multiplication of matrices and the apex <sup>T</sup> denotes matrix transposition (without conjugation).

In the special case of non-uniformly sampled signals, therefore, the following expression for  $P_k(f)$  holds

$$P_{k}(f) = H_{k}^{*}(f)W_{k}(f), k = 1..N$$
(69)

where  $W_k(f)$  is a filter, which provides complex weighting of the subbands

$$W_{k}(f) = \sum_{m=1}^{N} w_{km} \operatorname{rect}((f - f_{0,m})T_{sw}), f_{0,m} = \left(-\frac{N}{2} + m - \frac{1}{2}\right) \frac{1}{T_{sw}}, k = 1..N$$
(70)

Fig. 27 shows the equivalent block diagram of multi-channel reconstruction for the special case of staggered SAR. It is also highlighted how the filter  $W_k(f)$  weights the N subbands.

Even in the staggered SAR case, as the received azimuth signal is not strictly band-limited, a reconstruction error will be present, as the signal components outside the above mentioned frequency band fold back to the main part of the spectrum and disturb the reconstruction of the signal itself [96], [99]. As it will be shown in Section 5, for very large N, such signal components may be significantly amplified, making the reconstruction of the signal no longer possible.

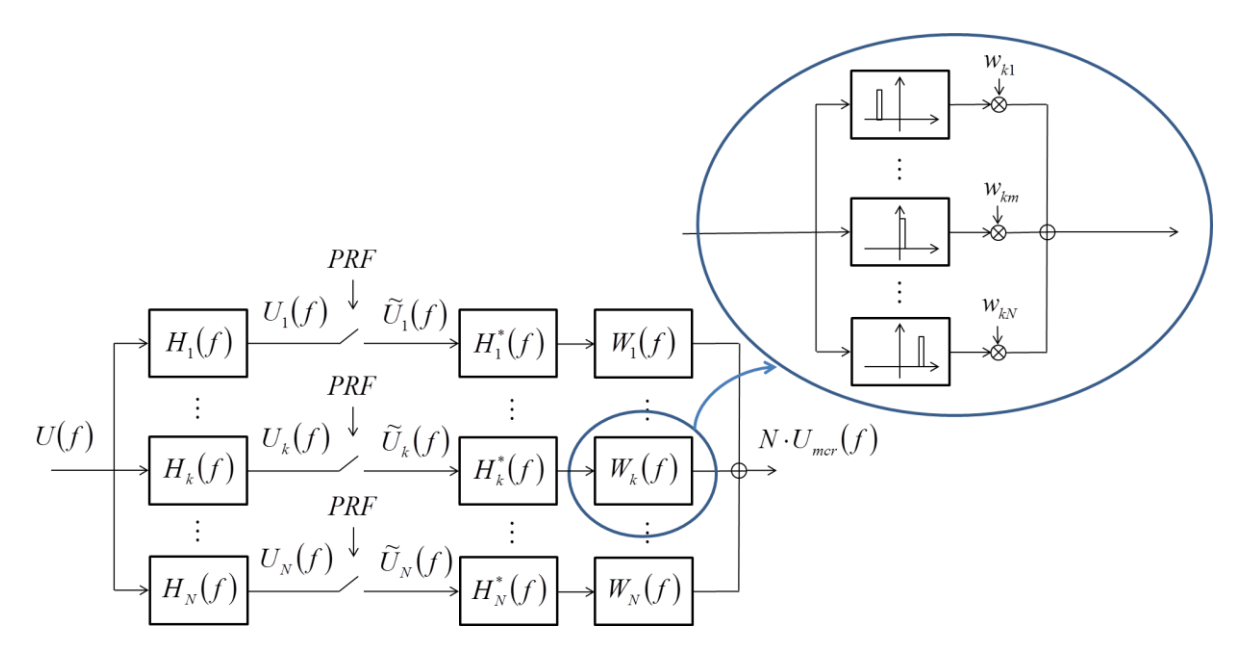


Fig. 27. Block diagram for multi-channel reconstruction for the staggered SAR case, where the post-filters consist of a cascade of a filter  $H_k*(f)$ , complex conjugate of  $H_k(f)$ , and a second filter, which provides complex weighting of the N subbands.

Moreover, the reconstruction filters may amplify the noise. Depending on the distribution of the samples and the PBW, a *SNR* scaling factor can be evaluated [96]. The *SNR* scaling factor is here defined as the ratio of the noise power in the focused staggered SAR image to the noise power in the focused image of a reference system with a constant *PRI*, equal to the mean effective *PRI* of the considered staggered SAR system.

Some investigations concerning the use of multi-channel reconstruction in systems with continuously varied *PRI* have been reported in [73].

#### 4.3.3 Best Linear Unbiased (BLU) Interpolation

The best way to account for the statistical properties of the raw azimuth signal is to make use of the knowledge of its power spectral density (PSD) to obtain the best linear unbiased estimates of the signal itself at the desired locations [109].

Let u(t) be the raw azimuth signal, which can be characterized as a zero-mean complex random process. If a uniformly illuminated rectangular azimuth aperture of length L is used in transmission as well as in reception, neglecting the range variation, the PSD of u(t), denoted as  $P_u(f)$ , is proportional to the antenna power pattern and given (but for a real constant) by [110]

$$P_{u}(f) = U(f)U^{*}(f) = \sin^{4}\left(\pi \frac{L}{2v_{s}}f\right) / \left(\pi \frac{L}{2v_{s}}f\right)^{4}$$

$$(71)$$

where U(f) is the spectrum of u(t).

The normalized autocorrelation function  $R_u(\xi)$  of the complex random process u(t) is proportional to the inverse Fourier transform of  $P_u(f)$  and can be expressed in closed form as

$$R_{u}(\xi) = E\left\{u^{*}(t)u(t+\xi)\right\}/E\left\{|u(t)|^{2}\right\} = \left(\frac{v_{s}}{L}\right)^{3}\left[6\xi^{3}\operatorname{sign}(\xi) + \left(\xi - \frac{L}{v_{s}}\right)^{3}\operatorname{sign}\left(\xi - \frac{L}{v_{s}}\right) + 4\left(-\xi + \frac{L}{2v_{s}}\right)^{3}\operatorname{sign}\left(\xi - \frac{L}{2v_{s}}\right) - 4\left(\xi + \frac{L}{2v_{s}}\right)^{3}\operatorname{sign}\left(\xi + \frac{L}{2v_{s}}\right) + \left(\xi + \frac{L}{v_{s}}\right)^{3}\operatorname{sign}\left(\xi + \frac{L}{v_{s}}\right)\right]$$

$$(72)$$

The expression of (71) can be written as the product of two squared cardinal sine functions, whose Fourier transforms are given by triangular functions. The Fourier transform of the expression of (71) can be therefore obtained by taking the convolution of two triangular functions.

It can be noticed that

$$R_{u}(\xi) = 0, |\xi| \ge \frac{L}{v_{s}} \tag{73}$$

In the presence of AWGN, the autocorrelation function of the contaminated complex random process  $u_n(t)$ , now denoted as  $R_{un}(\xi)$ , is given by

54 4 Staggered SAR

$$R_{un}(\xi) = \frac{1}{SNR} \delta(\xi) + \frac{SNR - 1}{SNR} R_u(\xi)$$
(74)

where  $\delta(\cdot)$  is the Kronecker delta.

The interpolation problem can be formalized as follows: We would like to estimate  $u(t_{int})$ , using Q values  $u(t_q)$ , q = 1...Q. As far as Q is concerned, Q is the number of available samples, whose distance from  $t_{int}$  is less than  $L/v_S$ . Samples that are more distant than that, in fact, are uncorrelated with  $u(t_{int})$ , as apparent from the property given in (73), which was directly derived from the expression of the autocorrelation itself.

Let **u** be a column vector collecting the samples  $u(t_q)$ , q = 1..Q, let **r** be a column vector, whose elements are given by

$$r_q = R_{un}(t_{int} - t_q), q = 1..Q$$
 (75)

and let G be a matrix, whose elements are given by

$$g_{qs} = R_{un}(t_q - t_s), q = 1..Q, s = 1..Q$$
 (76)

The best linear estimate of  $u(t_{int})$  is given by [109]

$$\hat{u}(t_{\text{int}}) = \mathbf{u}^{\mathsf{T}} \mathbf{G}^{-1} \mathbf{r} \tag{77}$$

Moreover, the relative variance is given by [109]

$$E\left\{\left|\hat{u}(t_{\text{int}}) - u(t_{\text{int}})\right|^{2}\right\} / E\left\{\left|u(t_{\text{int}})\right|^{2}\right\} = 1 - \mathbf{r}^{\mathsf{T}}\mathbf{G}^{-1}\mathbf{r}$$
(78)

In order to avoid the *SNR* estimation, a suboptimal approach for high *SNR* is to use  $R_u(\xi)$  in place of  $R_{un}(\xi)$  in (75) and (76) and then evaluate the resulting *SNR* scaling.

In case the rectangular aperture is not uniformly illuminated or a different kind of aperture is used, e.g. a reflector, the PSD of the raw azimuth signal is no longer given by (71) and it is not always possible to express the autocorrelation function in closed form. In this case, the autocorrelation function has to be evaluated numerically. Moreover, as for each of the samples to be estimated the distances to its Q closest samples change, a fitting of the numerically evaluated autocorrelation function to an adequate closed-form expression would allow a much faster implementation.

Compared to two-point linear interpolation, the computational cost of best linear unbiased interpolation is significantly increased. A clever implementation is therefore required, especially if the processing has to be performed on-board. As better discussed in Section 0, performing the interpolation on-board allows a considerable reduction of the data volume to be transferred to the ground segment.

# 5 Performance Analysis and Design Examples

The performance of staggered SAR is discussed and compared to that of a SAR system with constant *PRI* and multiple elevation beams through an L-band design example based on a reflector antenna with multiple feeds. The attained range and azimuth resolutions are the same as for a system with constant *PRI*, while a wide continuous swath is imaged rather than several subswaths divided by blind areas. Outstanding ambiguity performance is obtained, provided that a high mean *PRF* on transmit is employed, i.e., data have to be oversampled in azimuth. As an additional benefit, the energy of range and azimuth ambiguities is spread over large areas: Ambiguities therefore appear in the image as a noise-like disturbance rather than localized artifacts. The impact on performance of the selected sequence of *PRIs*, the adopted interpolation method and the processing strategy are also addressed. The implications of full polarimetry are discussed and a C-band design example based on a planar antenna is presented as well.

## **5.1** Input Parameters and Performance Measurements

The performance of a system based on the staggered SAR concept depends on several system and processing parameters. Some of them are typical of a conventional SAR system, such as the orbit height, the wavelength, the antenna characteristics, the transmitted chirp bandwidth and duration, the processed bandwidth, the employed processing windows and so on. Other parameters are instead peculiar of a staggered SAR system, namely the selected sequence of *PRIs*, the adopted resampling method, and the processing strategy, i.e., whether the resampling is performed on raw data or range-compressed data.

An exemplary set of system and processing parameters is provided in Table 4. Among the system parameters there are the radar wavelength, related to the radar carrier frequency through (3), the wave polarization (or polarizations), and the parameters related to the geometry, i.e., the orbit height and the minimum and maximum incidence angles, which – for this exemplary set of parameters – correspond to a swath width on ground of approximately 350 km, according to the spherical-Earth model of Appendix A. Then the main characteristics of the antenna are listed, including the tilt angle, i.e., the angle between the nadir direction and the pointing direction of the antenna. In this example, a reflector antenna, whose diameter, focal length and offset are specified, is considered. The antenna has thirty-two feeds in elevation and six feeds in azimuth,

where the six feeds in azimuth are pairwise combined to form three azimuth channels. For each group of six azimuth feeds a transmit/receive (T/R) module is used, whose power is divided between the three azimuth channels according to fixed weights. On transmit, all feeds are activated to illuminate the full swath. A set of phase-only weights is applied to the thirty-two groups of six azimuth feeds to optimize the shape of the elevation pattern on transmit. On receive, different groups of five adjacent elevation feeds and all six azimuth feeds are activated to steer multiple high-gain beams in concert with the arriving echoes, as already described in Section 3.3.2. For each group of six azimuth feeds, the signals received by the three azimuth channels are combined according to fixed weights, while for each elevation beam the five signals received by five groups of six azimuth feeds are combined on-board through real-time beamforming, as described in [111]. In particular, the weights are selected according to the minimum variance distortionless response (MVDR) or Capon beamformer, assuming an AWGN disturbance [112]. It has to be stressed that this is not a system with multiple azimuth subapertures, as only a linear combination of the received signals is digitized and stored for future processing.

Parameter	Value
Radar wavelength	0.2384 m (L-band)
Wave polarization	НН
Orbit height	745 km
Minimum incidence angle	26.3°
Maximum incidence angle	46.9°
Tilt angle	32.4°
Antenna type	Reflector
Antenna diameter	15 m
Focal Length	13.5 m
Offset	9 m
Feed elements in azimuth	6
Feed elements in elevation	32
Mean duty cycle	4%
Chirp bandwidth	80 MHz
Range sampling frequency	88 MHz
Mean PRF on TX	2700 Hz
Sequence of <i>PRIs</i>	More elaborated sequence
Number of concatenated sequences	7
Resampling method	BLU on raw data (before range
	compression)
Processed Doppler bandwidth	780 Hz
Azimuth processing window	Generalized Hamming with $\alpha = 0.6$
Compensation of the azimuth pattern	Yes
Range processing window	Generalized Hamming with $\alpha = 0.6$
Backscatter model	D'Aria [114]

Table 4. Exemplary set of system and processing parameters of a staggered SAR system.

Fig. 28 shows the normalized transmit and receive antenna patterns in elevation (at near range) as a function of the elevation angle, while Fig. 29 shows the normalized transmit and receive antenna patterns in azimuth at near range (worst case, i.e., wider patterns) as a function of the azimuth angle. The antenna patterns have been computed using the GRASP software [113].

Further parameters present in the table are the mean duty cycle, i.e., the ratio of the uncompressed pulse length to the mean *PRI*, the chirp bandwidth, and the range sampling frequency, which is usually selected to be slightly higher than the chirp bandwidth. Furthermore, the sequence of *PRIs* is specified; in this example the sequence of Fig. 25 is adopted, characterized by a mean *PRF* on transmit equal to 2700 Hz and a mean effective *PRF* equal to 2588 Hz.

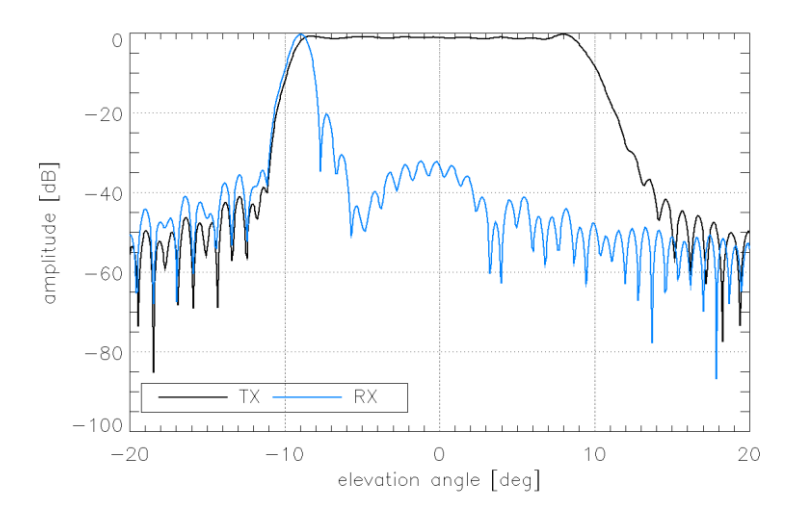


Fig. 28. Normalized transmit and receive antenna patterns in elevation at near range vs. elevation angle for the reflector antenna with multiple feeds.

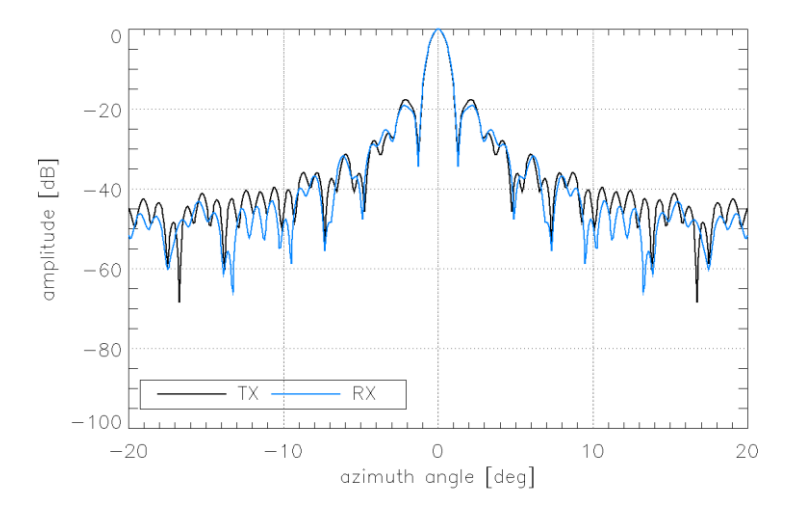


Fig. 29. Normalized transmit and receive antenna patterns in azimuth at near range vs. elevation angle for the reflector antenna with multiple feeds.

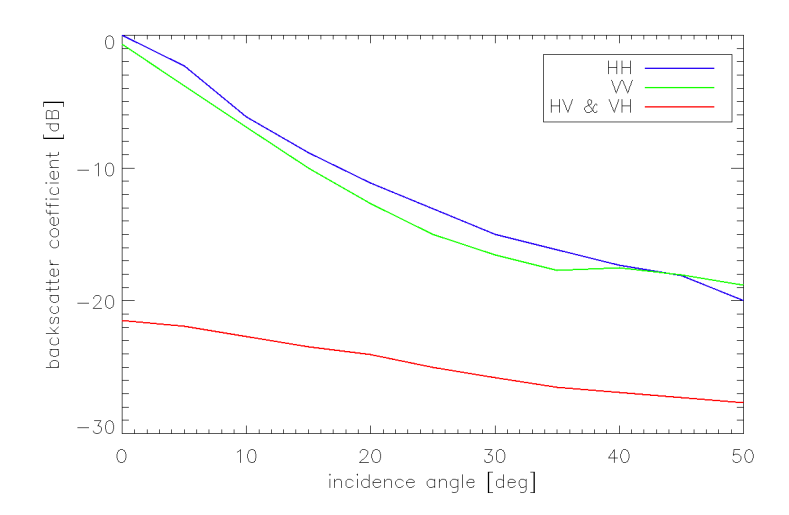


Fig. 30. Backscatter coefficient as a function of the incidence angle for different polarizations at L-band according to the model of D'Aria [114].

Among the processing parameters, in addition to the interpolation method, used to resample the non-uniformly sampled signal to a uniform grid, the PBW has to be specified, together with the amplitude weighting (or processing windows) used in range and azimuth to reduce the *PSLR* and the *ISLR*. An additional azimuth processing window, which compensates for the azimuth antenna pattern within the PBW, is sometimes applied to obtain similar shapes of the PSDs of the SAR signal in range and azimuth. Finally, a model for the backscatter decay as a function of the incidence angle has to be assumed to evaluate the *RASR*. The backscatter decay as a function of the incidence angle used for the L-band design examples is taken from [114] and depicted in Fig. 30 for the different polarization channels.

The main advantage of a staggered SAR over a SAR system with constant PRI and multiple elevation beams is the possibility to image a wide continuous swath rather than several subswaths divided by blind areas. As already pointed out in Section 4.2, the design of the sequences of PRIs may require information concerning the swath as an input: For sequences of PRIs with slow PRI change, the minimum span of 1/PRI in fact has to be selected on the basis of the maximum slant range  $R_{0max}$ , according to (44); for sequences of PRIs with fast PRI change and more elaborated sequences, the sequence has to be designed taking into account the minimum and maximum slant ranges  $R_{0min}$  and  $R_{0max}$ , so that two consecutive azimuth samples are never missed in the raw data for all slant ranges of interest.

As for a SAR system with constant PRI, the attained slant range, ground range, and azimuth resolutions are roughly given by (12), (13), and (27), respectively. More accurate expressions should include a factor 0.886 related to the "sinc" shape of the IRF and a resolution broadening factor (greater than 1) due to the amplitude weighting for sidelobe suppression. As far as the range and azimuth PSLR are concerned, as for a constant PRI SAR, they are equal to -13.3 dB, if no amplitude weighting is applied in the processing, while they become better than -30 dB, after a weighting with a generalized Hamming window with  $\alpha = 0.6$ . This is also the amplitude weighting applied in the operational TerraSAR-X/TanDEM-X processor.

The *NESZ* is the same as for a constant *PRI* SAR with multiple elevation beams, same input parameters, and *PRF* equal to the mean *PRF* on transmit of the staggered SAR system, but for a possible *NESZ* degradation, due to the amplification of the noise within the resampling operation, already mentioned in Sections 3.2.1 and 4.3.2 with regard to multi-channel reconstruction and denoted as *SNR* scaling

$$NESZ = \frac{256 \,\pi^3 R^3 \,v_S \sin \eta \,k_B \,T_s \,B \,F \,L_{tot} \Phi}{P_{TX} \,G_{TX} \,G_{RX} \,\lambda^3 \,c_0 \,\tau \,PRF_{mean \,TX}}$$
(79)

where  $\Phi$  denotes the *SNR* scaling factor, i.e., the *SNR* (or *NESZ*) degradation due to the resampling, which can be assessed by simulation, as explained in the following, and is expected to vary across the swath, as different samples are missing at different ranges.

Staggered SAR operation has significant effects on range and azimuth ambiguities, which deserve a dedicated analysis. In a SAR system with constant PRI, during the acquisition of the raw data, the range ambiguous echoes of a scatterer are located at the same ranges along the whole synthetic aperture. This is due to the constant time distance to preceding and succeeding pulses and causes, after azimuth focusing, the presence of ghost targets in the SAR image, because the ambiguous energy is integrated along azimuth, even though the range migration is not fully matched, as for the scatterer. In a staggered SAR system, the range ambiguities are located at different ranges for different range lines, as the time distance to the preceding and succeeding pulses continuously varies. The ambiguous energy is therefore incoherently integrated and spread almost uniformly across the Doppler spectrum. If the mean PRF on transmit of the system  $PRF_{mean}$  is much larger than the PBW  $B_p$ , a significant amount of the ambiguous energy is therefore filtered out during the SAR processing. Moreover, the residual ambiguous energy of a scatterer is spatially almost uniformly distributed over the whole synthetic aperture and over a range equal to the PRI span times half the speed of light. The same applies to nadir echoes, which result from the same phenomenon.

These peculiarities, as well as the specific sequence of PRIs, have to be taken into account for the evaluation of the RASR. In particular, for a given sequence of PRIs, the RASR has to be evaluated for each of the M transmitted pulses of the sequence. Due to the uniform distribution of the ambiguous energy, the RASR is then obtained for each slant range by averaging the RASR obtained for the M transmitted pulses. Moreover, the amplitude weighting of the Doppler spectrum applied in the processing Q(f) has to be accounted for. The RASR can be then expressed as

$$RASR \cong \frac{\frac{1}{M} \sum_{m=0}^{M-1} \sum_{j=1}^{N_{A_{m}}} \frac{\sigma^{0}(\eta_{jm}) \frac{f = -B_{p}/2}{PRF_{mean}} \int_{f = -PRF_{mean}/2}^{PRF_{mean}/2} \int_{f = -PRF_{mean}/2}^{Q^{2}(\theta_{jm}, f) df} \frac{1}{R_{jm}^{3} \sin \eta_{jm}} \frac{\int_{f = -B_{p}/2}^{Q^{2}(\theta_{main}, f) Q^{2}(f) df}{R_{main}^{3} \sin \eta_{main}}$$
(80)

where the subscripts m, m = 0..M-1, refers to the transmitted pulse of the sequence and j,  $j = 1..N_{Am}$ , to the  $N_{Am}$  ambiguous (preceding and succeeding) returns and where the azimuth ambiguities of the range ambiguities have been neglected [69]. The same formula can be also used for the fully polarimetric case, taking into account that the ambiguous echoes from some of the preceding and succeeding pulses correspond to radiated pulses with different polarizations and using the proper value of  $\sigma^0(\eta)$  for each contribution. Fig. 31 shows the RASR in dB for a staggered SAR with the parameters of Table 4, evaluated using (80), and a constant PRI SAR with a PRF equal to the mean PRF on transmit of the staggered SAR, evaluated using (29). As apparent, the RASR is up to 5.7 dB better in the staggered SAR case, due to the aforementioned incoherent integration of the range ambiguous echoes.

It should be also mentioned that for SAR systems with multiple elevation beams, either with constant *PRI* or staggered SAR, the wide antenna elevation pattern on transmit represents a drawback for range ambiguity suppression. While a conventional SAR with a single elevation beam typically benefits from both transmit and receive antenna elevation patterns for range ambiguity suppression, a SAR with multiple elevation beams has to rely on the receive beams alone. The most prominent range ambiguous returns, in fact, are typically illuminated by almost the same antenna elevation pattern on transmit as the desired return. To improve the range ambiguity suppression, one has therefore to decrease the beam width in elevation, which corresponds to an increase of the antenna height. Another option could be the employment of on-board null-steering techniques like the linear constrained minimum variance (LCMV) beamforming [115], analyzed in [111].

As far as azimuth ambiguities are concerned, for a staggered SAR system it is not always straightforward to evaluate the *AASR* using the azimuth antenna pattern as for a constant *PRI* SAR, i.e., using (26), because the resampling operation may change the shape of the azimuth spectrum of the signal. In order to assess the impact of azimuth ambiguities, however, the acquisition process and the signal processing can be simulated, assuming that only a point-like scatterer is present in the scene. The focused data obtained from the simulation correspond to the 2-D IRF of the system, from which several performance parameters – and in particular the *ISLR* – can be then evaluated.

A good estimate of the *AASR* can be obtained as the difference of the attained *ISLR* and the *ISLR* of a constant *PRI* SAR with *PRF* equal to the mean *PRF* on transmit of the staggered SAR system  $PRF_{mean\ TX}$ , same values for the other system and processing parameters as the staggered SAR, and an azimuth antenna pattern equal to zero outside the interval [-*PRF*<sub>mean\ TX</sub>/2,  $PRF_{mean\ TX}/2$ ] [69]. Fig. 32 shows for a constant *PRI* SAR with the parameters of Table 4 and a *PRF* equal to the mean *PRF* of the staggered SAR the estimated *AASR* using the azimuth antenna pattern, i.e. (26), and the difference of the *ISLRs*. As is apparent, the method based on the difference of the *ISLRs* provides a very accurate estimate of the *AASR* even for very low *AASR* levels.

Fig. 33 shows for the parameters of Table 4 and a slant range  $R_0 = 820.7$  km (near range) the raw data with gaps and the raw data after resampling, Fig. 34 shows the focused data, while Fig. 35 shows the focused data for a system with constant *PRI* with a *PRF* equal to the mean *PRF* on transmit of the staggered SAR system. The comparison of the 2-D IRFs of Fig. 34 (a) and Fig. 35 (a) highlights a peculiarity of staggered SAR: Not only range ambiguities, but also azimuth ambiguities appear smeared in the staggered SAR 2-D IRF, where some additional ambiguous energy is however present within 20 km distance from the mainlobe. As discussed in Section 5.3, in order to limit this additional ambiguous energy and meet the *AASR* requirement, the mean *PRF* on transmit of the staggered SAR system has to be higher than the *PRF* of a constant *PRI* SAR with the same antenna characteristics.

From the 2-D IRF the slant range and azimuth resolutions, the range and azimuth PSLRs, and the ISLR can be evaluated. The ground range resolution is computed from the slant range resolution, using (13), while the AASR is estimated from the difference of the ISLRs, as explained above. The SNR scaling factor is instead evaluated by simulations as described in the following. Noise-only raw data, i.e., the AWGN contribution, are generated for both the staggered SAR raw data and the reference raw data with constant PRF equal to the mean PRF on transmit of the staggered SAR. Noise-only raw data are then processed as the noise-free raw data (i.e., resampling to a uniform grid, conventional SAR processing). The SNR scaling factor  $\Phi$  is therefore evaluated as the ratio of the ratios of the output and input SNRs of the staggered SAR data

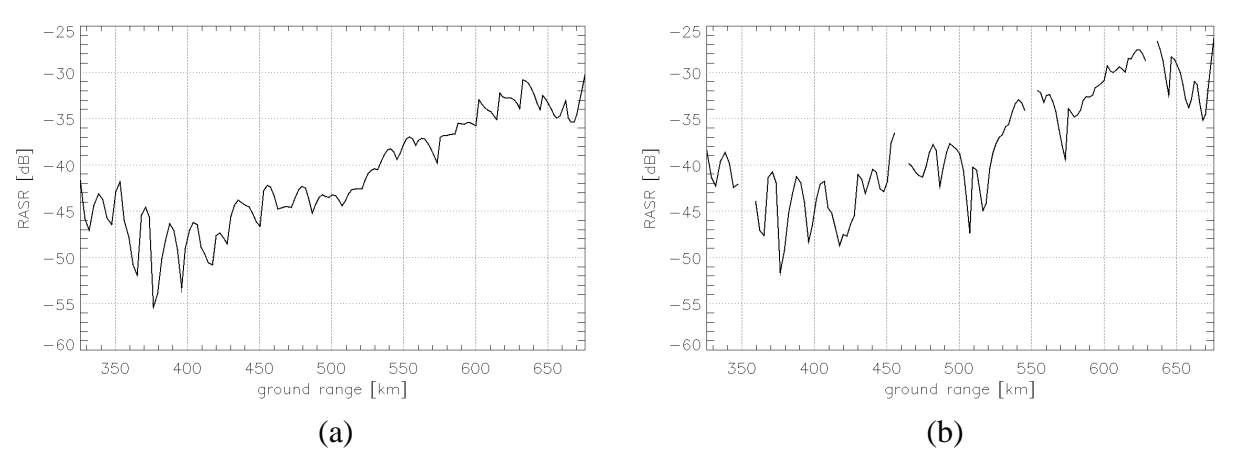


Fig. 31. *RASR* in dB. (a) Staggered SAR with the parameters of Table 4. (b) Constant *PRI* SAR with *PRF* equal to the mean *PRF* on transmit of the staggered SAR system.

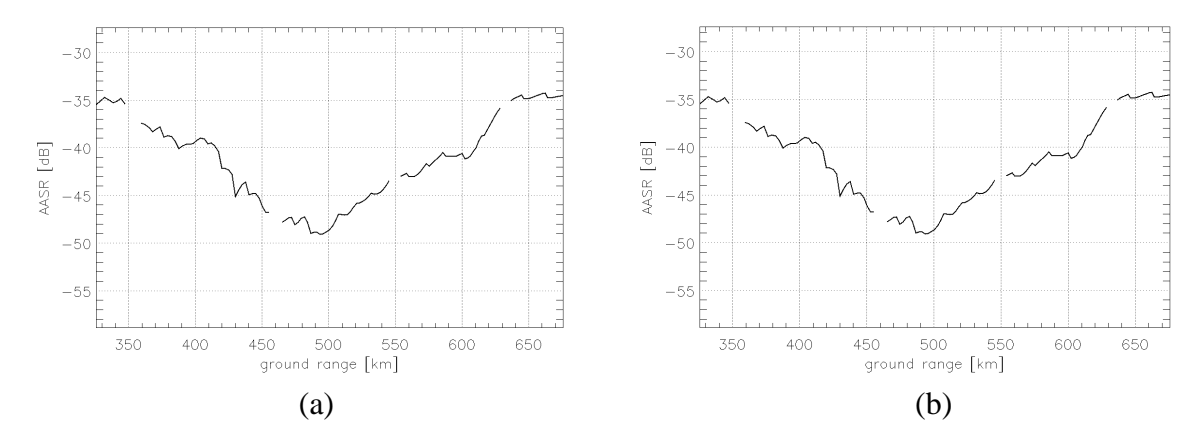


Fig. 32. Estimated AASR for a constant PRI SAR. (a) Using the azimuth antenna pattern and (26). (b) Using the method based on the difference of the ISLRs.

and the reference data with constant *PRF*. In agreement with (79), the *SNR* scaling factor describes the degradation of the *NESZ* for a staggered SAR system with reference to a constant *PRI* system with the same mean *PRF* on transmit. All these performance measurements for a staggered SAR with the parameters of Table 4 are displayed as a function of ground range in Fig. 36.

There are two main reasons why 2-D simulations have been preferred to 1-D (azimuth) simulations: First, 1-D simulations do not provide the correct absolute levels of azimuth ambiguities for a point-like scatterer, as the defocusing of azimuth ambiguities is not accounted for [83]-[85]; furthermore, possible effects related to the two-dimensional spatial distribution of the missing samples within the pulse extension would be neglected. However, it can be observed that a 1-D (azimuth) simulation still provides a good estimate for the *AASR* from the difference of the 1-D (azimuth) *ISLRs*, while requiring a considerably smaller computational time.

Fig. 37 shows for the parameters of Table 4 and a slant range  $R_0 = 820.7$  km (near range) the raw azimuth signal data with gaps and the raw azimuth signal after resampling, Fig. 38 shows the focused azimuth signal, while Fig. 39 shows the focused azimuth signal for a system with constant PRI with a PRF equal to the mean PRF on transmit of the staggered SAR system. Fig. 40 (a) shows the AASR estimated by a 1-D simulation, which slightly differs from the AASR estimated by a 2-D simulation, displayed in Fig. 36 (g). The difference of the AASRs estimated by 1-D and 2-D simulations, which can be interpreted as the estimation error for a 1-D simulation, is displayed in Fig. 40 (b) and is smaller than -45 dB. 1-D simulation can be therefore very useful to quickly assess the impact of one or more input parameters on the AASR.

<sup>&</sup>lt;sup>3</sup> The part of the raw data responsible for the azimuth ambiguities, i.e., the area illuminated by the azimuth sidelobes of the antenna pattern, spreads over several range cells. RCM is not properly compensated for those data, nor is the azimuth filter matched to the phase variation of those data. As a consequence, ambiguous echoes of point-like scatterers appear therefore defocused in range and azimuth. This phenomenon is more significant at longer wavelengths.

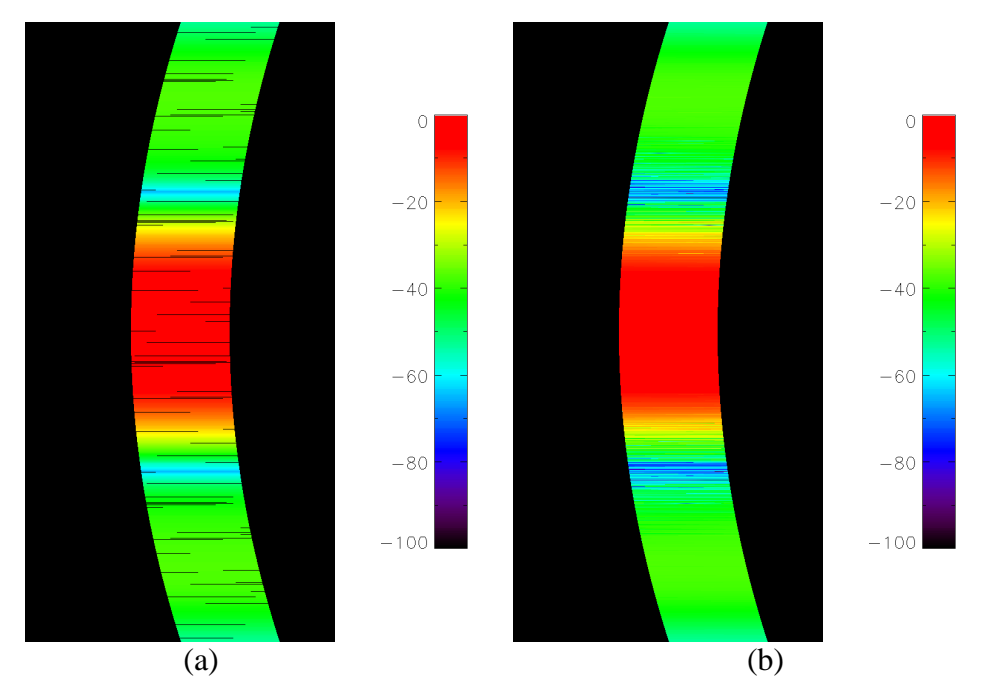


Fig. 33. Two-dimensional simulation for a staggered SAR system. The horizontal and vertical axes represent slant range and azimuth, respectively. The sizes (slant range  $\times$  azimuth) are specified for each plot. (a) Amplitude of the raw data with gaps in dB (7 km  $\times$  81.3 km). (b) Amplitude of the raw data after resampling in dB (7 km  $\times$  81.3 km).

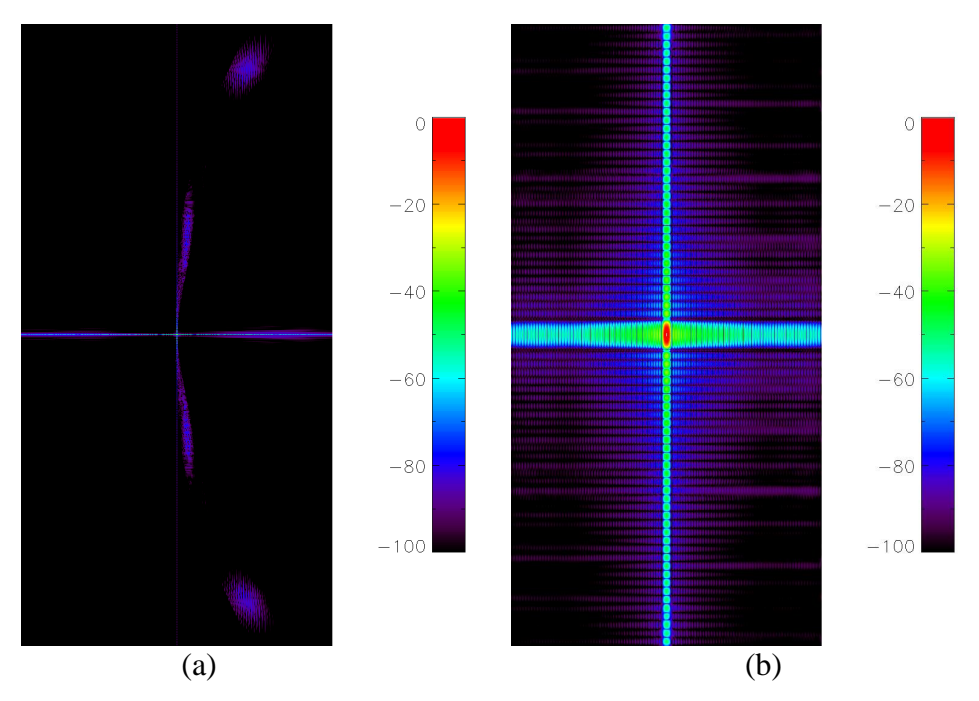


Fig. 34. Two-dimensional simulation for a staggered SAR system. The horizontal and vertical axes represent slant range and azimuth, respectively. The sizes (slant range  $\times$  azimuth) are specified for each plot. (a) Amplitude of the focused data in dB (3.5 km  $\times$  81.3 km). (b) Amplitude of the focused data in dB (zoom in the vicinity of the mainlobe, 218 m  $\times$  635 m).

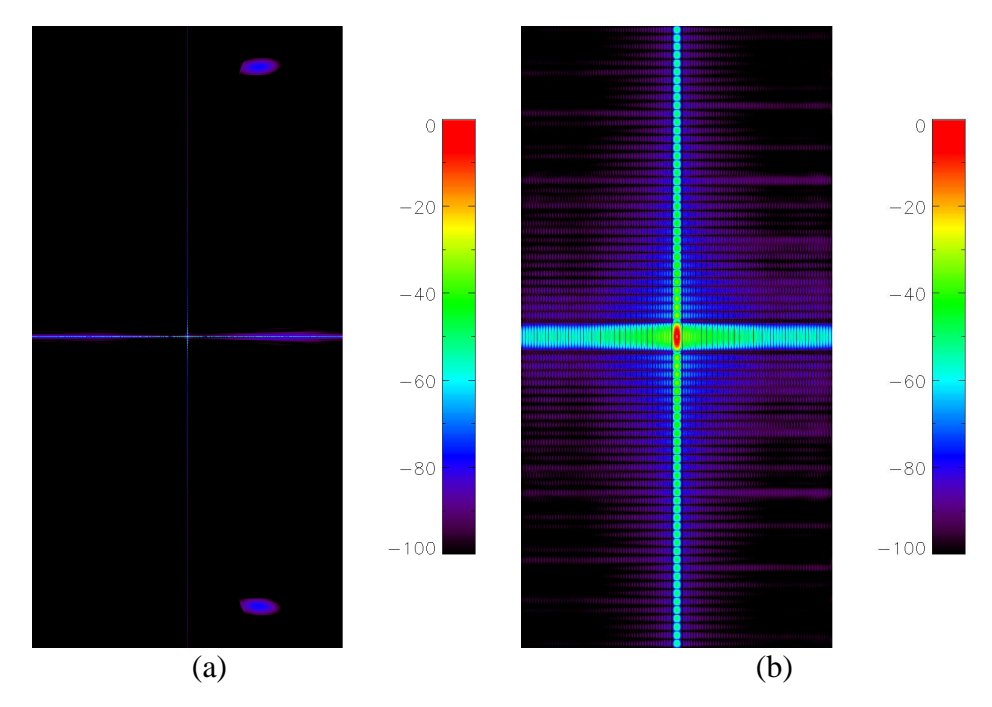


Fig. 35. Two-dimensional simulation for a SAR system with constant PRI. The horizontal and vertical axes represent slant range and azimuth, respectively. The sizes (slant range  $\times$  azimuth) are specified for each plot. (a) Amplitude of the focused data in dB (3.5 km  $\times$  81.3 km). (b) Amplitude of the focused data in dB (zoom in the vicinity of the mainlobe, 218 m  $\times$  635 m).

# 5.2 Impact on Performance of the Features Peculiar of a Staggered SAR System

In the following the impact on performance of the features peculiar of a staggered SAR system, namely the selected sequence of *PRIs*, the adopted resampling method, and the processing strategy, is considered.

#### 5.2.1 Impact of the Sequence of *PRIs* on Performance

Different options for the selection of the sequence of PRIs have been presented in Section 4.2, among which sequences with slow PRI change, sequences with fast PRI change, and more elaborated sequences. Furthermore, three sample sequences, one for each of the three aforementioned design options, have been shown in Fig. 20, Fig. 24, and Fig. 25, respectively. All three sequences are characterized by the same mean PRF on transmit and have been designed to map a 350 km ground swath, defined by the minimum and maximum slant range  $R_{0min} = 820.7$  km and  $R_{0max} = 1031.9$  km.

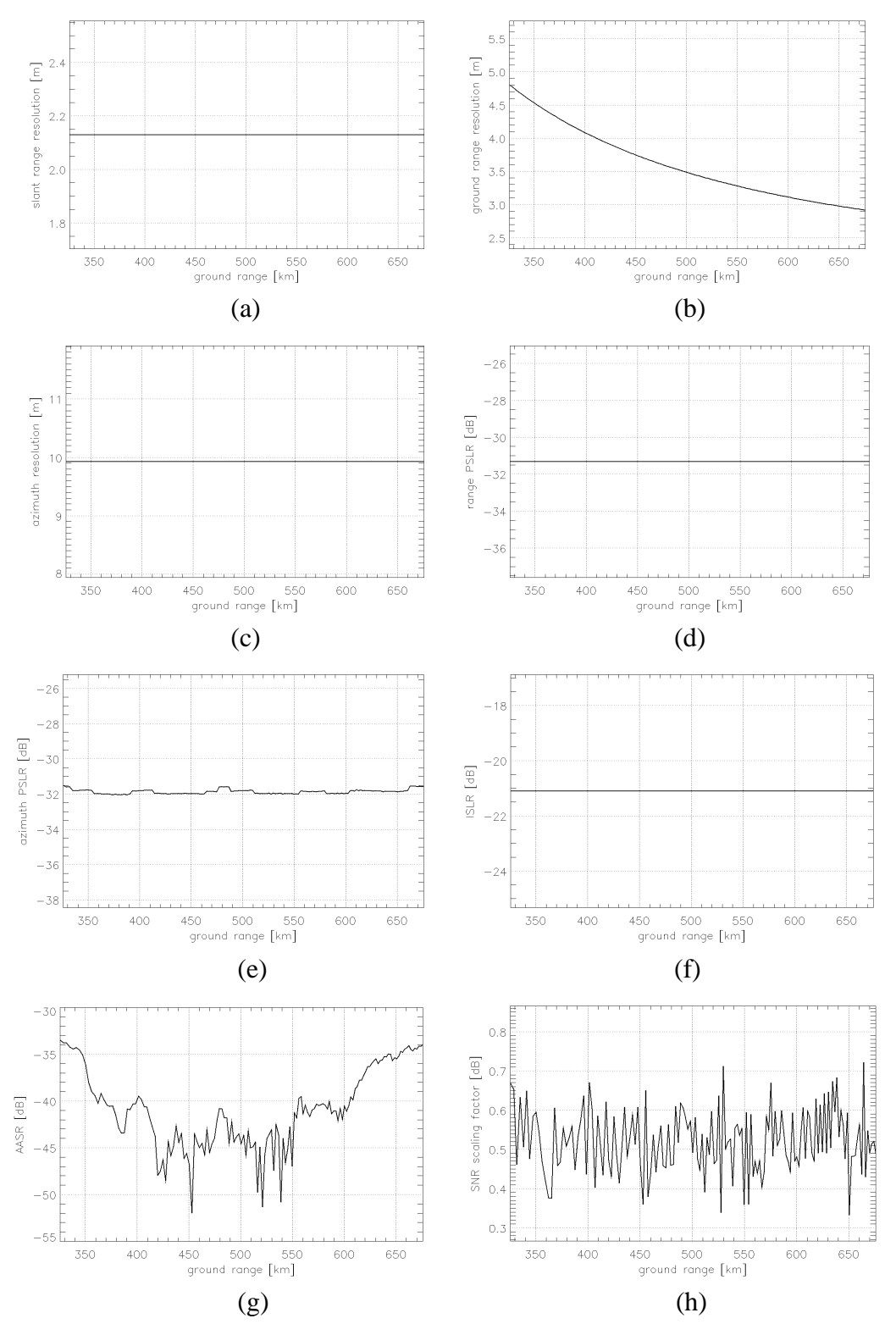


Fig. 36. Performance measurements obtained by simulation for a staggered SAR with the parameters of Table 4 as a function of ground range. (a) Slant range resolution. (b) Ground range resolution. (c) Azimuth resolution. (d) Range *PSLR*. (e) Azimuth *PSLR*. (f) *ISLR*. (g) *AASR*. (h) *SNR* scaling factor.

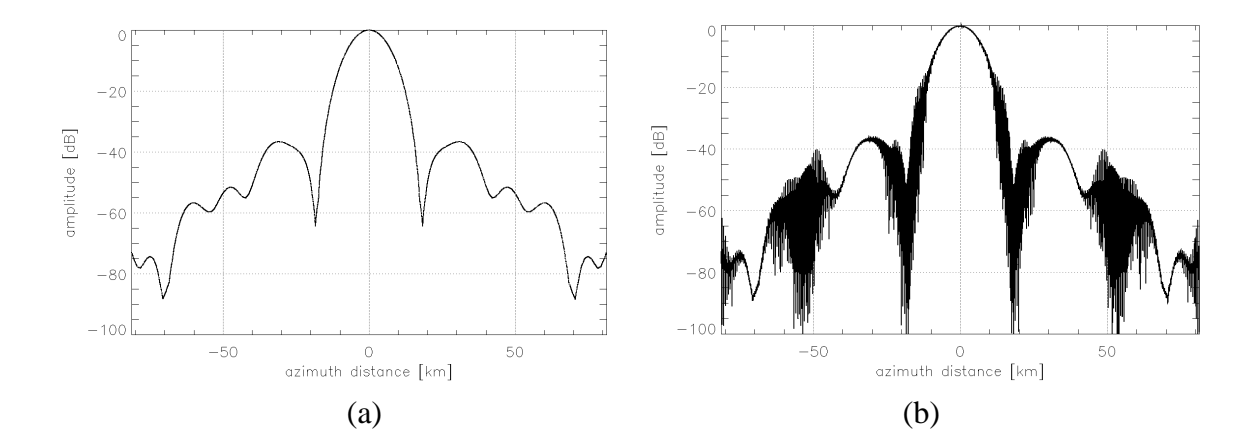


Fig. 37. One-dimensional simulation for a staggered SAR system. (a) Amplitude of the raw azimuth signal with gaps in dB. (b) Amplitude of the raw azimuth signal after resampling in dB.

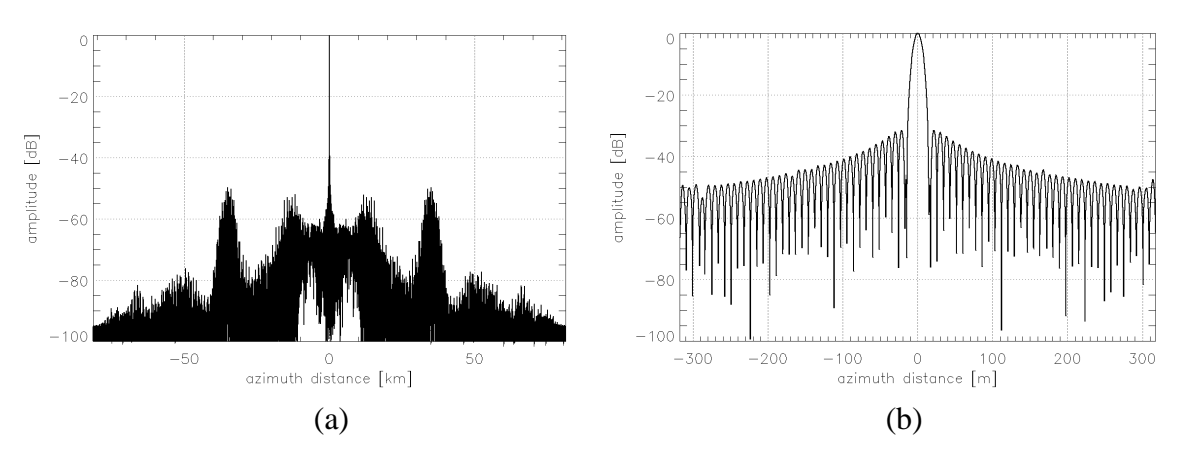


Fig. 38. One-dimensional simulation for a staggered SAR system. (a) Amplitude of the focused azimuth signal in dB. (b) Amplitude of the focused azimuth signal in dB (zoom in the vicinity of the mainlobe).

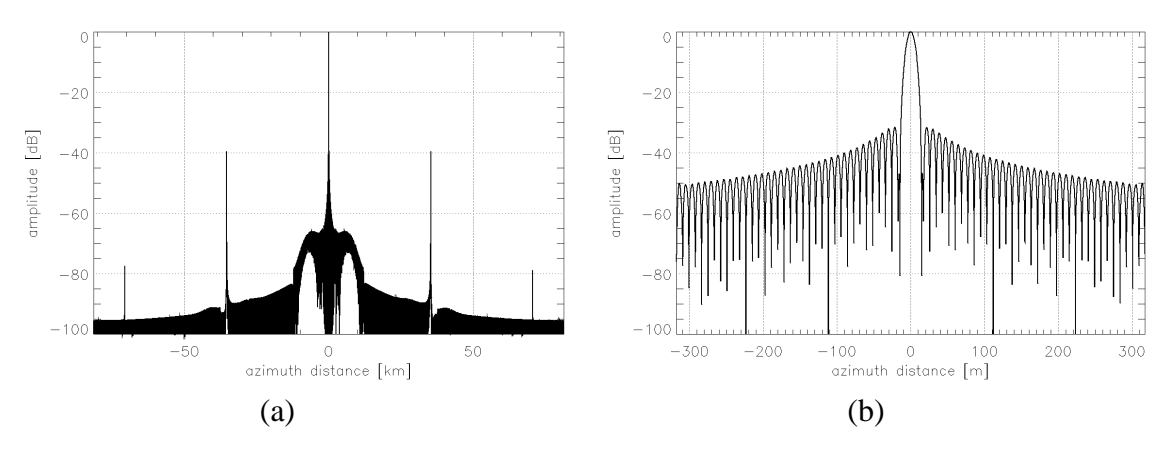


Fig. 39. One-dimensional simulation for a SAR system with constant *PRI*. (a) Amplitude of the focused azimuth signal in dB. (b) Amplitude of the focused azimuth signal in dB (zoom in the vicinity of the mainlobe).

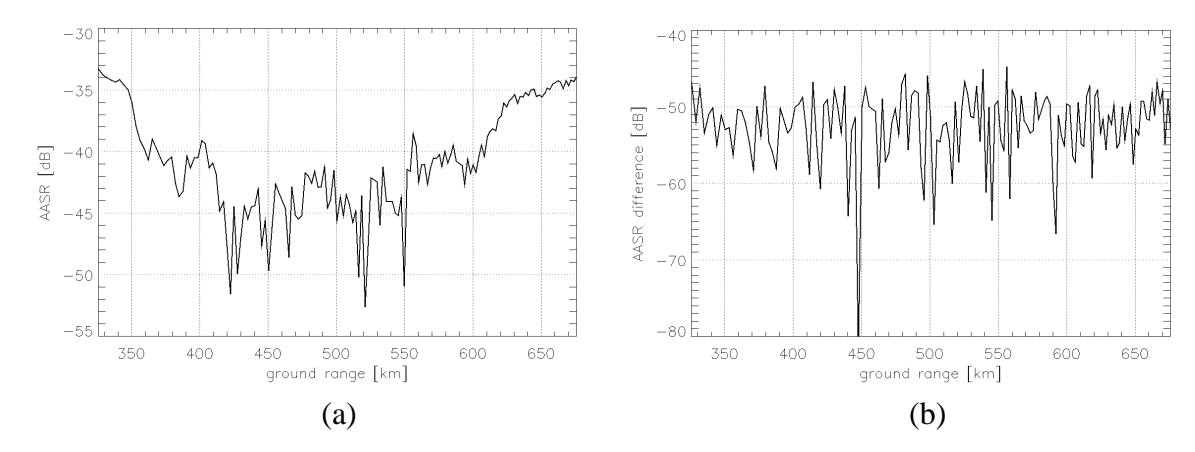


Fig. 40. (a) AASR of the staggered SAR system with the parameters of Table 4, as estimated with a 1-D simulation. (b) Difference of the AASRs estimated by 1-D (Fig. 40 (a)) and 2-D (Fig. 36 (g)) simulations.

The performance for the more elaborated sequences of Fig. 25 has been already considered in Section 5.1 for the system parameters of Table 4. In the following the impact of the sequence of *PRIs* on performance is shown, evaluating and comparing the performance obtained for the sample sequences of Fig. 20 (slow *PRI* change) and Fig. 24 (fast *PRI* change). The same system parameters as in Table 4 are assumed.

Fig. 41 and Fig. 42 show the 2-D IRFs (including a zoom in the vicinity of the mainlobe) for a slant range  $R_0 = 820.7$  km (near range) and the sample sequences of Fig. 20 (slow *PRI* change) and Fig. 24 (fast *PRI* change), respectively, which can be compared to the 2-D IRF of Fig. 34.

As already anticipated in Section 4.2.1 and apparent in Fig. 41 (b), high sidelobes are present in the vicinity of the mainlobe of the 2-D IRF for the sequence with slow *PRI* change. This is due to the fact that the raw signal cannot be recovered where the large azimuth gaps are present (see also the diagram with the location of missing samples in the raw data in Fig. 20 (b)). The 2-D IRF for the sequence with fast *PRI* change is instead very similar to the one obtained for the more elaborated sequence, but, while in the former distinct sidelobes are visible (Fig. 42 (a)), in the latter the sidelobes are smeared.

Fig. 43 shows the performance in terms of azimuth resolution, *RASR*, *AASR*, and *SNR* scaling factor for the three sample sequences as a function of ground range. As is apparent in Fig. 43 (a), the achieved azimuth resolution is the same for the three sequences. The achieved *RASR*, shown in Fig. 43 (b), is similar for the three sequences, as expected from sequences with the same mean *PRF* on transmit. The *AASR* obtained using the sequence with slow *PRI* change reaches -13 dB and is therefore not compliant with typical requirements. The *AASR* is instead better than -33 dB for the sequence with fast *PRI* change and the more elaborated sequence.

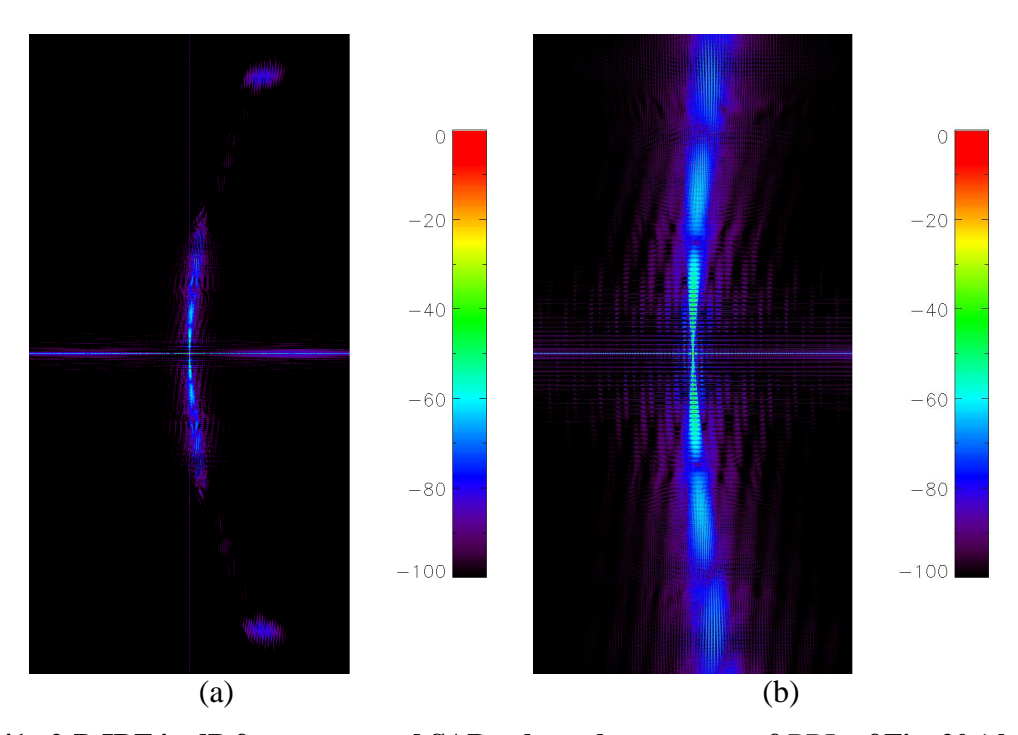


Fig. 41. 2-D IRF in dB for a staggered SAR, where the sequence of *PRIs* of Fig. 20 (slow *PRI* change) is used. The horizontal and vertical axes represent slant range and azimuth, respectively. The sizes (slant range  $\times$  azimuth) are specified for each plot. (a) 2-D IRF with first order azimuth ambiguities visible (3.5 km  $\times$  81.3 km). (b) Zoom in the vicinity of the mainlobe (218 m  $\times$  635 m).

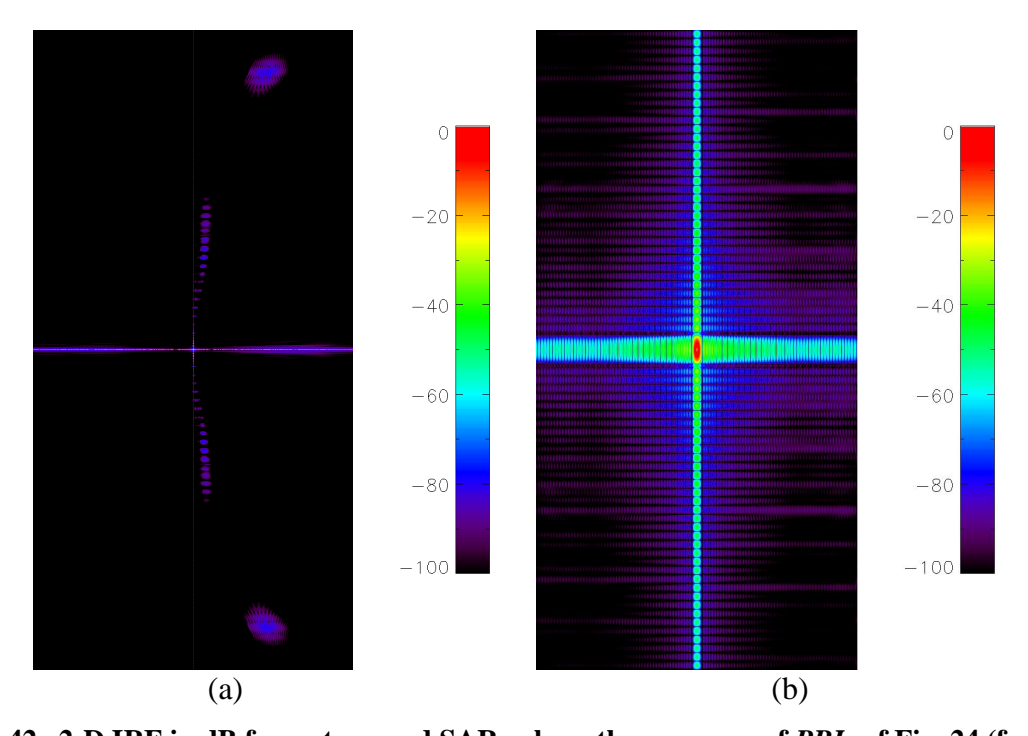


Fig. 42. 2-D IRF in dB for a staggered SAR, where the sequence of *PRIs* of Fig. 24 (fast *PRI* change) is used. The horizontal and vertical axes represent slant range and azimuth, respectively. The sizes (slant range  $\times$  azimuth) are specified for each plot. (a) 2-D IRF with first order azimuth ambiguities visible (3.5 km  $\times$  81.3 km). (b) Zoom in the vicinity of the mainlobe (218 m  $\times$  635 m).

It can be also noticed that very good values of *AASR* are achieved for the sequences with slow *PRI* change and fast *PRI* change in correspondence of the ground ranges, where no samples are missed. The *SNR* scaling factor, displayed in Fig. 43 (d), is slightly better and more uniform for the more elaborated sequence, but also for the other two sample sequences is smaller than 1.1 dB. The abrupt changes in *AASR* and *SNR* scaling factor for the sequences with slow and fast *PRI* change could be visually seen in the image. This is however not the case for the more elaborated sequences.

On the basis of the AASR performance, sequences with fast PRI change and more elaborated sequences have to be preferred to sequences with slow PRI change, if high-resolution single-look SAR images are required. If the images have to be then multi-looked to either enhance the radiometric resolution or to reduce interferometric phase errors, sequences with slow PRI change can be used by independently processing the different azimuth bursts, as already pointed out in Section 4.2.1. More elaborated sequences might be preferred to sequences with fast PRI change, as they are characterized by smeared sidelobes and a better worst value of SNR scaling factor. However, if the staggered SAR system has to be used in combination with an on-board filter for data volume reduction (see Section 0), the use of sequence with fast PRI change allows a drastic reduction of the coefficients to be stored.

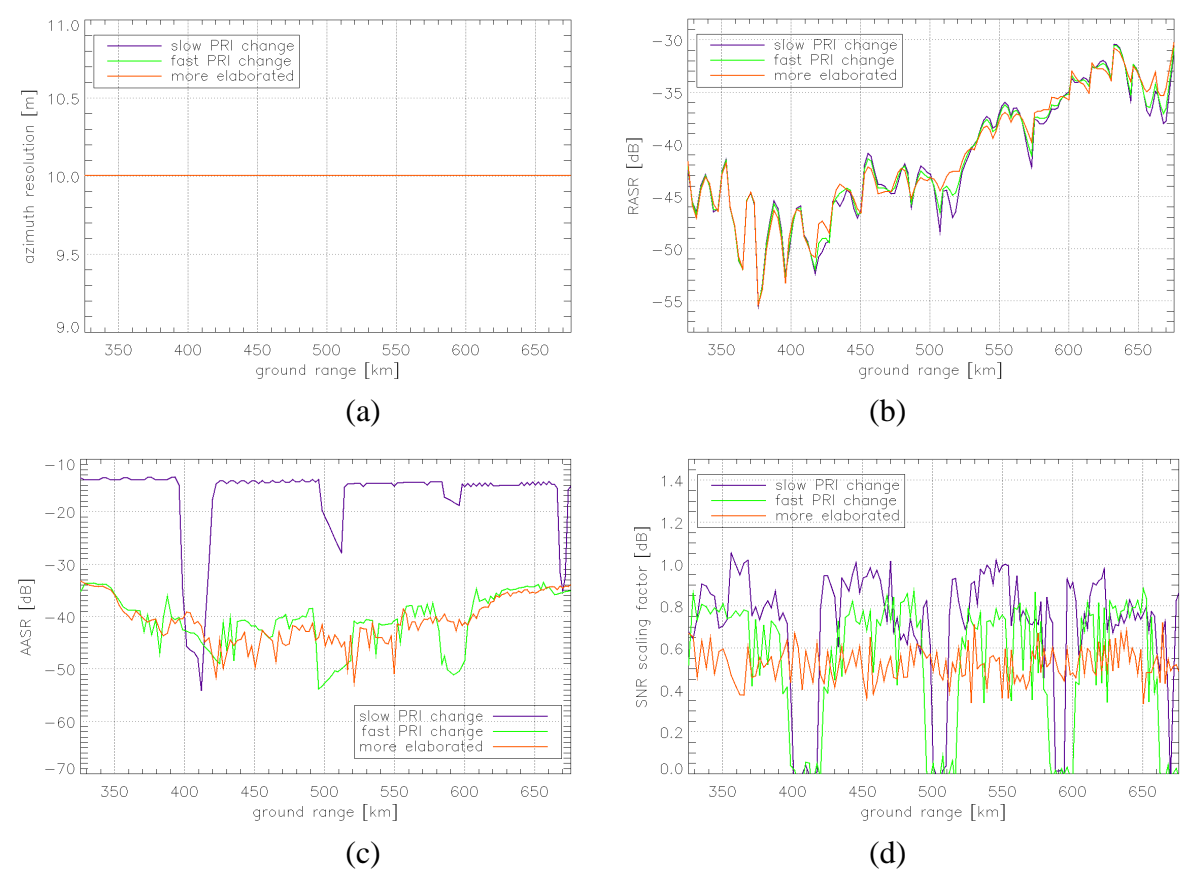


Fig. 43. Performance comparison for different sequences of *PRIs* obtained by simulation for a staggered SAR with the parameters of Table 4 as a function of ground range. (a) Azimuth resolution. (b) *RASR*. (c) *AASR*. (d) *SNR* scaling factor.

#### **5.2.2** Impact of the Interpolation Method on Performance

Different resampling methods have been discussed in Section 4.3, which allow the recovering of a uniformly sampled data set from the staggered SAR raw data, which are inherently non-uniformly sampled. It has been observed that BLU interpolation accounts for the statistical properties of the signal to be interpolated and is therefore expected to lead to better performance than two-point linear interpolation. This is visible by comparing the 2-D IRF in Fig. 44, obtained using the parameters of Table 4 and a slant range  $R_0 = 820.7$  km (near range) for the two aforementioned interpolation methods. As is apparent, the energy of the sidelobes is much lower, if BLU interpolation is used.

Fig. 45 shows the azimuth resolution, the AASR, and the SNR scaling factor for different interpolation methods as a function of ground range, for the parameters of Table 4, using the more elaborate sequence of Fig. 25 (plots on the left side) and the sequence with fast PRI change of Fig. 24 (plots on the right side). The RASR is not shown, as it is not influenced by the interpolation method, i.e., it is the same for all interpolation methods and is given for the different sequences in Fig. 43 (b). In the case of the more elaborate sequence of Fig. 25 multi-channel reconstruction is not able to recover the uniformly sampled signal, due to the high number of equivalent channels (i.e., number of PRIs of the sequence), while in the case of the sequence with fast PRI change the performance for multi-channel reconstruction is provided as well, although the significant level of SNR scaling factor, due to the distribution of the available non-uniform samples, suggests that this technique is not well suited for staggered SAR.

For both sequences of *PRIs*, BLU interpolation leads to much better *AASR* levels (better than -33 dB) compared to two-point linear interpolation (better than -26 dB), slightly better resolution and slightly worse *SNR* scaling factor, therefore it has to be preferred to the other interpolation methods.

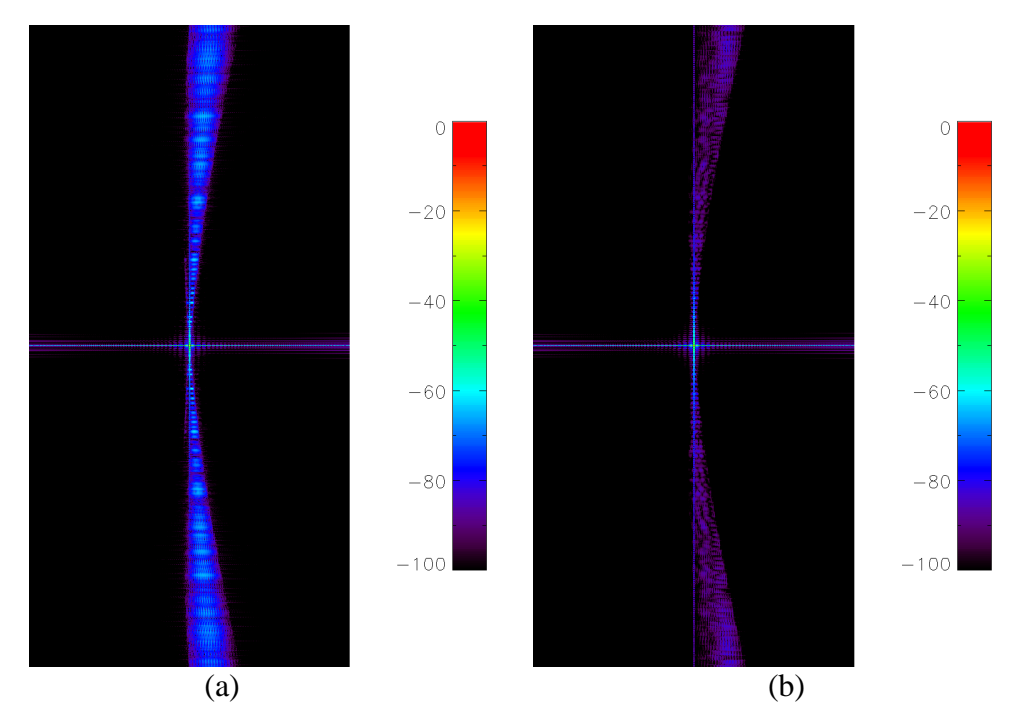


Fig. 44. 2-D IRF in dB for a staggered SAR, where the more elaborated sequence of PRIs of Fig. 25 is used. The horizontal and vertical axes represent slant range and azimuth, respectively. The size (slant range  $\times$  azimuth) is 0.9 km  $\times$  20.3 km. (a) Using two-point linear interpolation. (b) Using best linear unbiased (BLU) interpolation.

#### 5.2.3 Impact of the Processing Strategy on Performance

Two different processing strategies have been described in Section 4.1.1 and illustrated through block diagrams in Fig. 17. In Section 4.2.2 it has been pointed out that the processing strategy based on the resampling of raw data leads to better performance than the one based on the resampling of the range-compressed data, if used in combination with sequences, where two consecutive azimuth samples are never missed, i.e., sequences with fast PRI change or more elaborated sequences. Fig. 46 compares the 2-D IRF obtained using the parameters of Table 4 in combination with the sequence of PRIs of Fig. 24 for a slant range  $R_0 = 820.7$  km (near range) and the two aforementioned processing strategies. The achieved AASRs are equal to -22 dB and -33 dB for the strategy based on the resampling of range-compressed and raw data, respectively.

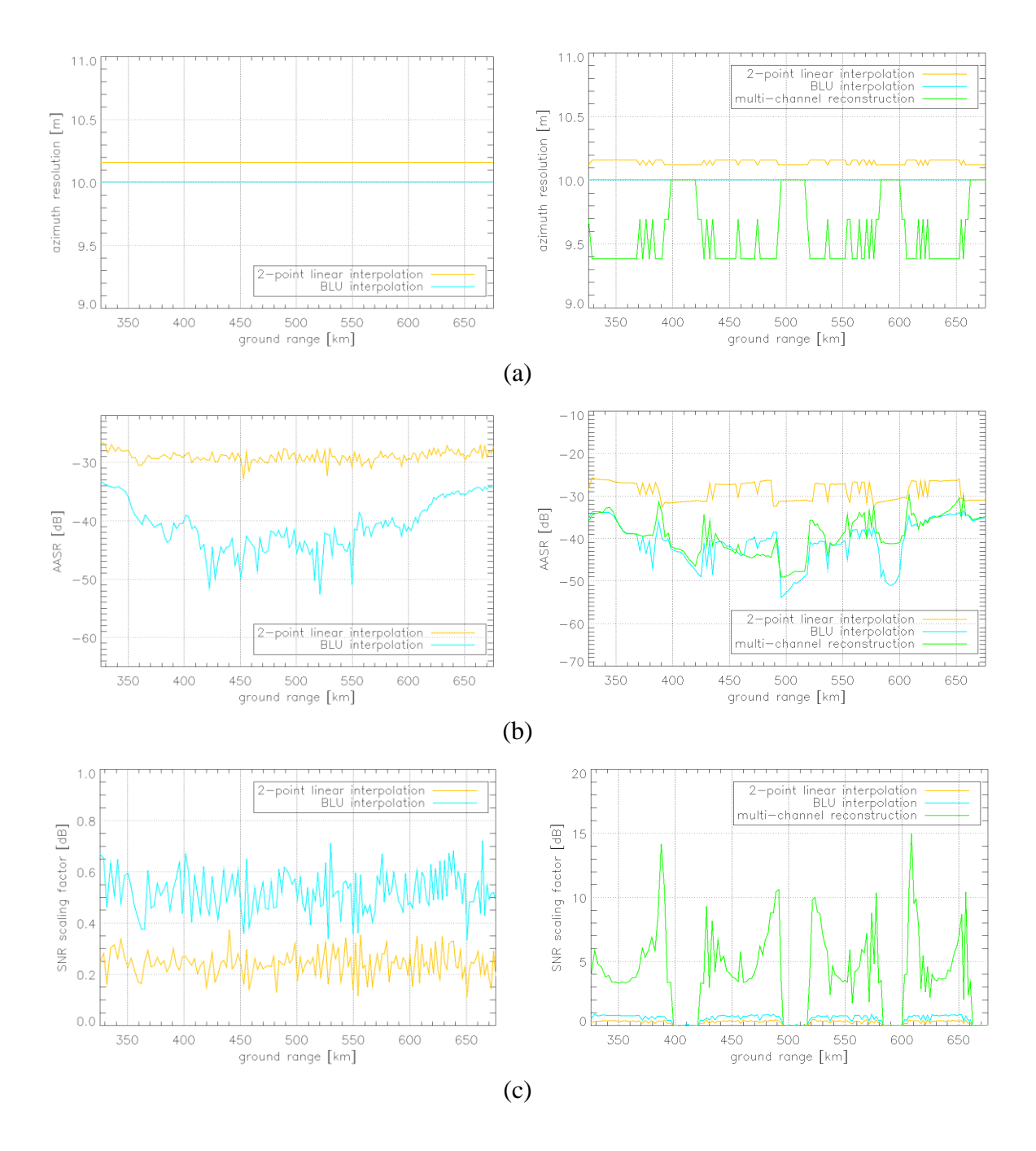


Fig. 45. Performance comparison for different interpolation methods obtained by simulation for a staggered SAR with the parameters of Table 4 as a function of ground range for the sequences of Fig. 25 (left) and Fig. 24 (right). (a) Azimuth resolution. (b) AASR. (c) SNR scaling factor.

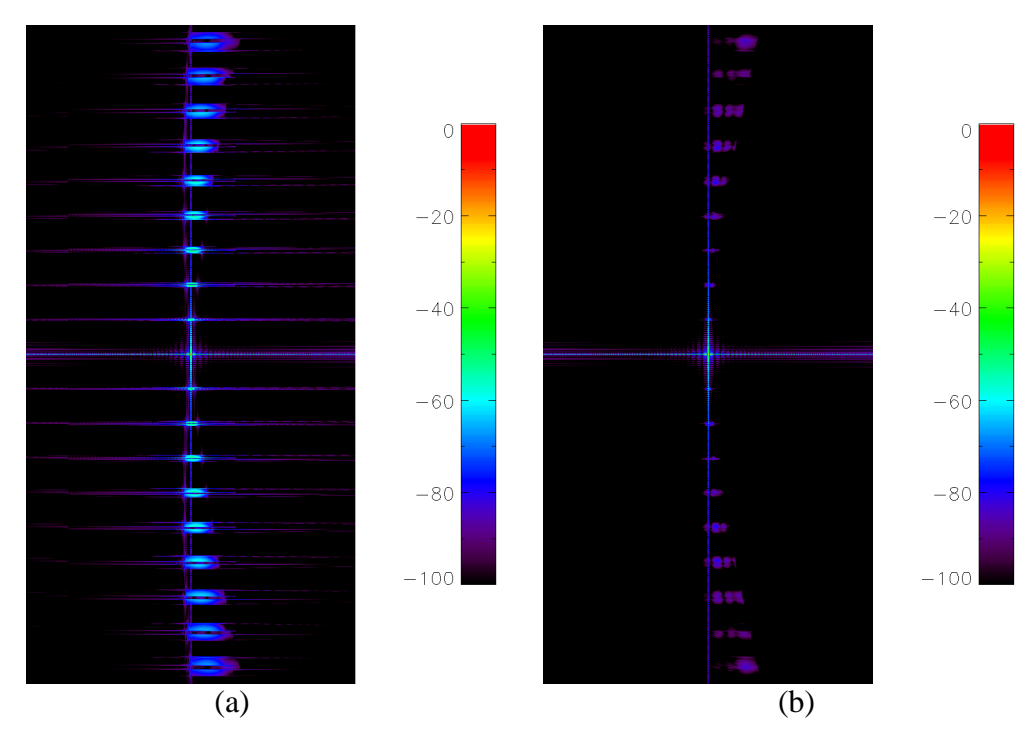


Fig. 46. 2-D IRF in dB for a staggered SAR, where the sequence with fast PRI change of Fig. 24 is used. The horizontal and vertical axes represent slant range and azimuth, respectively. The size (slant range × azimuth) is 0.9 km × 20.3 km. (a) Using the processing strategy based on resampling of range-compressed data. (b) Using the processing strategy based on resampling of raw data.

## 5.3 System Design Considerations

In the following the impact on performance of some system and processing parameters, i.e., the mean *PRF* on transmit, the PBW, and the duty cycle, is analyzed. The reference case of a SAR system with constant *PRI* and multiple elevation beams is considered as well. The aim of this section is to show how a staggered SAR system can meet different requirements, in terms of azimuth resolution, ambiguity, and *NESZ*, by properly selecting some system parameters.

#### 5.3.1 Mean *PRF* on Transmit

The mean PRF on transmit  $PRF_{mean\ TX}$  of a staggered SAR system has to be selected to comply with RASR and AASR requirements. As the PRF or the mean PRF on transmit increases, the AASR improves, while the RASR degrades. Fig. 47 shows the AASR, the RASR, and the SNR scaling factor for the system and processing parameters of Table 4 as a function of ground range for different values of the mean PRF on transmit  $PRF_{mean\ TX}$ . The SNR scaling factor is slightly better for the higher mean PRF on transmit, as the gaps are smaller. The comparison of the AASR and RASR trends of Fig. 47 (a) and (b) with the trends of Fig. 48, which shows the performance of a SAR with constant PRI and multiple elevation beams, reveals that the effect on ambiguities of the mean PRF on transmit in a staggered SAR system is similar to the effect on ambiguities of the PRF in a SAR with constant PRI. In both cases AASR trends can be observed, where the AASR

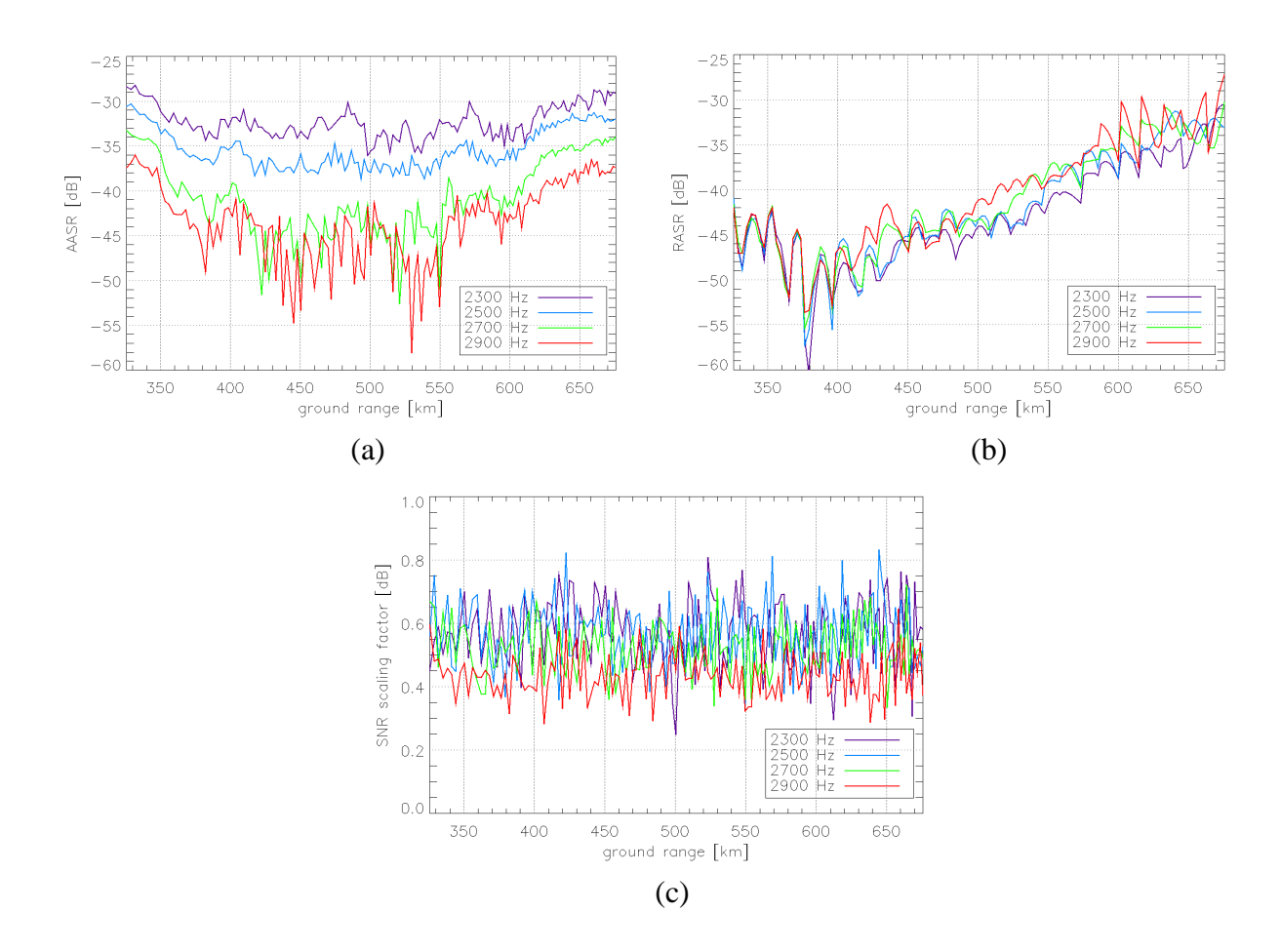


Fig. 47. Performance vs. ground range for the staggered SAR system with the parameters of Table 4 for different values of the mean *PRF* on transmit. (a) *AASR*. (b) *RASR*. (c) *SNR* scaling factor.

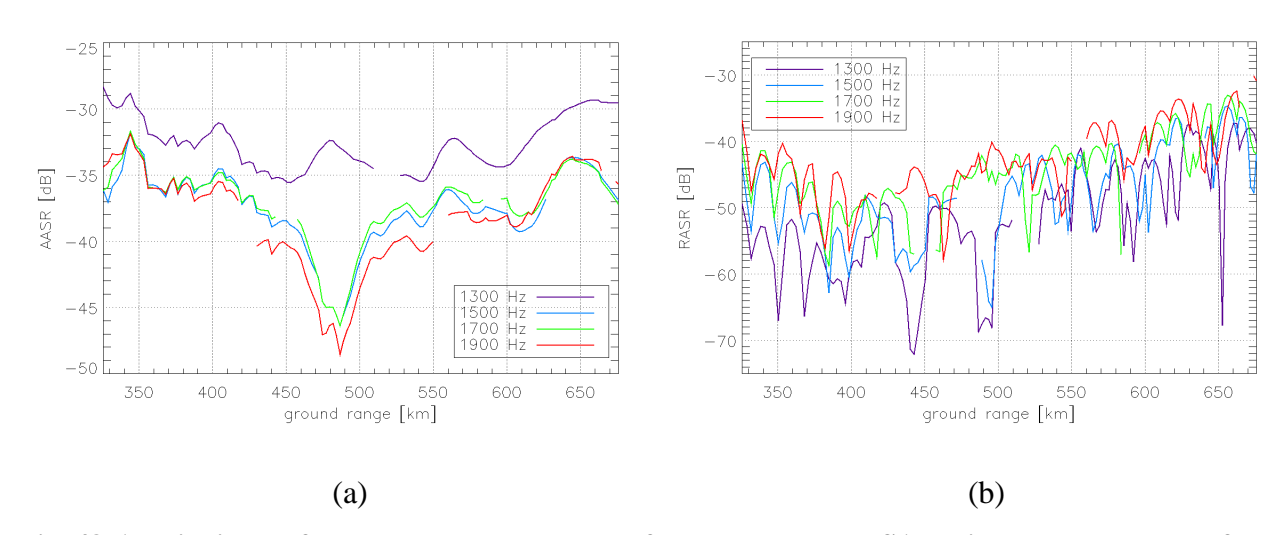


Fig. 48. Ambiguity performance vs. ground range for a constant *PRI* SAR with the parameters of Table 4 and different values of the *PRF*. (a) *AASR*. (b) *RASR*.

degrades at near range and far range, due to the worse azimuth patterns of the reflector in correspondence of those elevation angles. The worst values of the *RASR* occur at far range, as the ambiguous returns from near range are characterized by shorter range and higher backscatter than the main return at far range. In order to meet the ambiguity requirements with the worst value within the swath, a careful design of the antenna is therefore required.

Fig. 49 shows the worst values of the AASR, the RASR, and the ambiguity-to-signal ratio (ASR), defined as the sum of AASR and RASR, for a staggered SAR system and a SAR with constant PRI as a function of the (mean) PRF. These plots allow the selection of the mean PRF on transmit or the PRF on the basis of the ambiguity requirements, which depend on the application. As is apparent in Fig. 49 (a), an optimal selection of the mean PRF on transmit, i.e., around 2600 Hz, allows keeping the sum of AASR and RASR, i.e. the ASR, under -29 dB. In a SAR system with constant PRI and multiple elevation beams, with the same antenna, an optimal selection of the PRF (i.e., around 1600 Hz, as apparent in Fig. 49 (b)) leads to a worst value of the ASR better than -31.5 dB. Although the staggered SAR system cannot reach the same level as a system with constant PRI and multiple elevation beams, it allows imaging of a wide continuous swath instead of multiple disconnected subswaths. Moreover, as range and azimuth ambiguities are smeared, i.e., their energy is spread over a large area, in most of the scenarios and in particular for strong localized scatterers, ambiguities are likely to be less visible in the staggered SAR case, even if the ASR is worse by 2.5 dB.

Moreover, although the requirements are often to be met by the worst value within the swath, as apparent from most of the previous plots, the ambiguity performances are likely to be much better in average. The plots of Fig. 50 show the mean values of the AASR, the RASR, and the ASR across the swath as a function of the mean PRF on transmit and the PRF, for a staggered SAR system and a system with constant PRI, respectively.

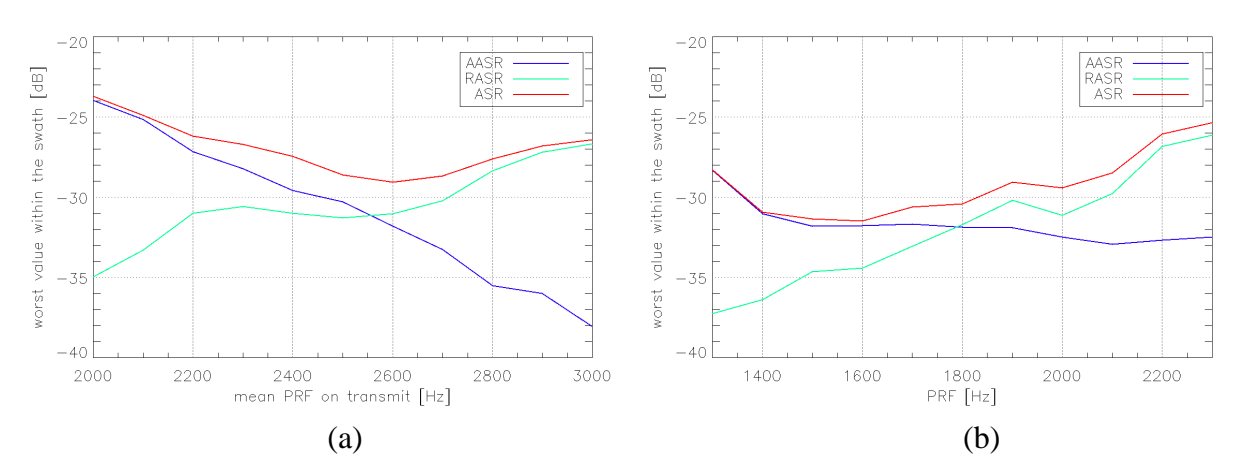


Fig. 49. (a) Worst value of the AASR, the RASR, and the ASR within the swath vs. mean PRF on transmit for the staggered SAR system with the parameters of Table 4. (b) Worst value of the AASR, the RASR, and the ASR within the swath vs. PRF for a constant PRI SAR with the parameters of Table 4.

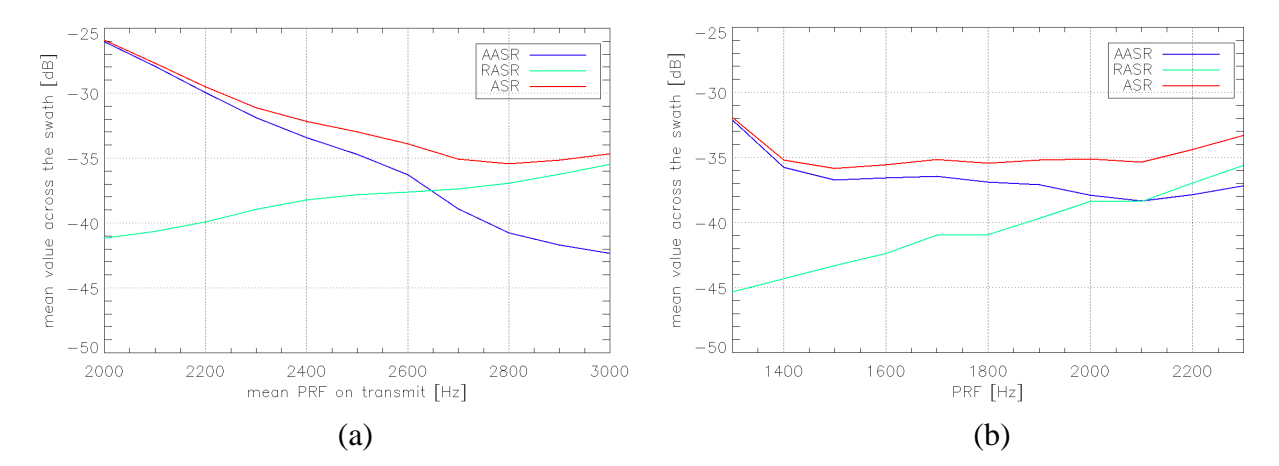


Fig. 50. (a) Mean value of the AASR, the RASR, and the ASR across the swath vs. mean PRF on transmit for the staggered SAR system with the parameters of Table 4. (b) Mean value of the AASR, the RASR, and the ASR across the swath vs. PRF for a constant PRI SAR with the parameters of Table 4.

The selection of the optimal mean PRF on transmit in the staggered SAR case, i.e., the one which allows keeping the ASR under a given threshold, leads to much higher values than in the constant PRI case, where the optimal PRF is already much higher than the PBW  $B_p$ . This has an implication for the volume of data to be downlinked, which can be anyway significantly reduced by an on-board Doppler filter, as described in Section 0.

#### **5.3.2** Processed Doppler Bandwidth

In Section 2.3.4 the relation between PBW, azimuth resolution and AASR in a SAR with constant PRI has been discussed: the PBW can be reduced to improve the AASR, but this determines a degradation of the azimuth resolution, according to (26) and (27), respectively. In a constant PRI SAR the change of the PBW has only a very slight (in most of the cases negligible) impact on the RASR and only if the RASR is computed using the two-way azimuth power patterns, i.e., the expression in (29).

While the relation between PBW and resolution still holds in the staggered SAR case, the impact of the PBW on the AASR can be only assessed by simulation, evaluating the AASR as difference of ISLRs, as explained in Section 5.1. Fig. 51 shows the AASR and the RASR for two different PBWs, i.e., 780 Hz and 1110 Hz, which correspond to 10 m and 7.5 m azimuth resolution, respectively. A mean PRF on transmit of 2700 Hz has been selected for the staggered SAR system (Fig. 51 (a)) and a PRF equal to 1800 Hz for the SAR with constant PRI (Fig. 51 (b)). As apparent, improving the azimuth resolution from 10 m to 7.5 m results in an acceptable AASR degradation for both the constant PRI case and the staggered SAR case (less than 1 dB on the worst value), where also a very slight RASR degradation (approximately 0.5 dB) occurs.

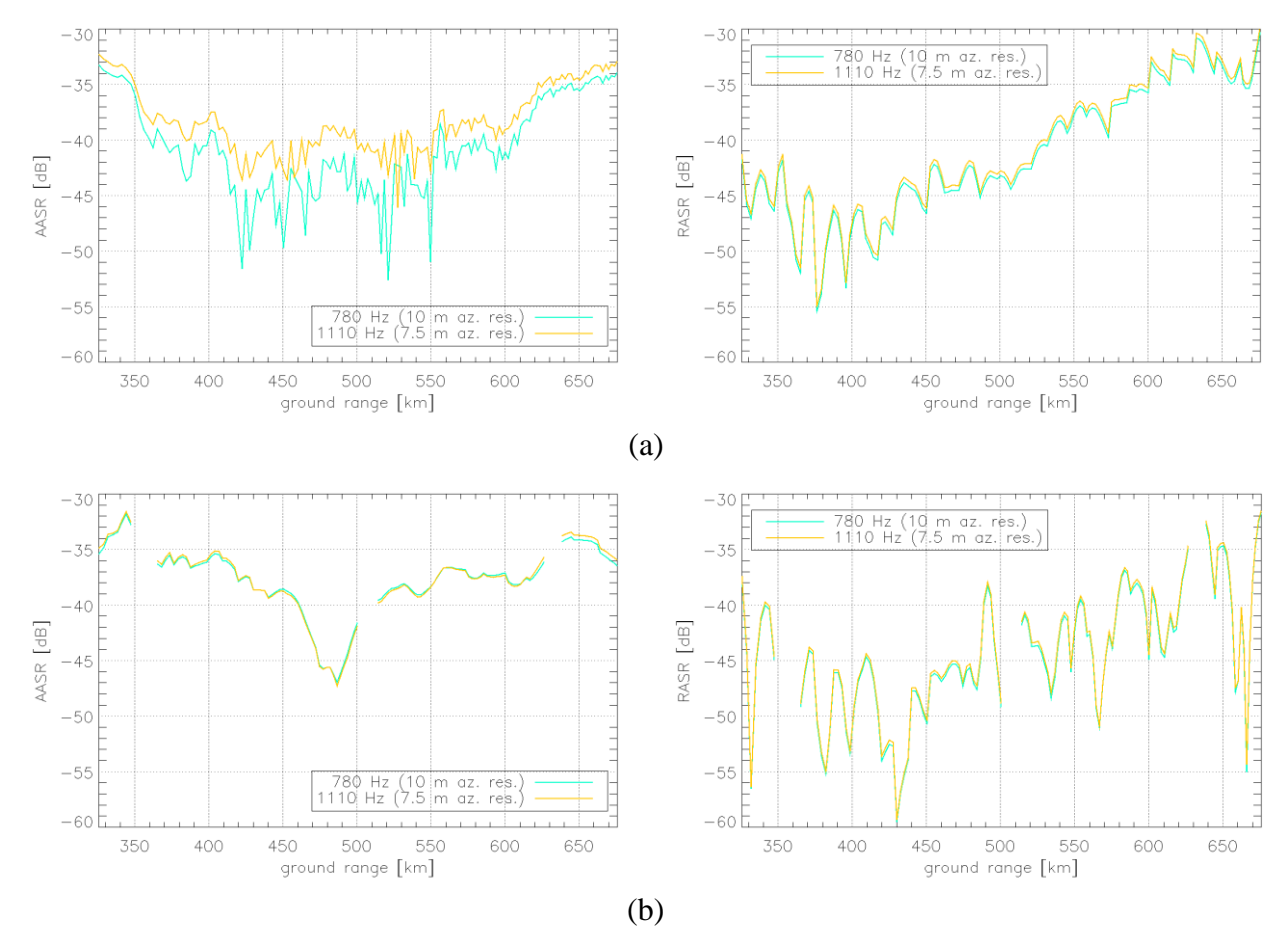


Fig. 51. AASR (left) and RASR (right) for two different PBWs and the parameters of Table 4. (a) Staggered SAR system with  $PRF_{mean\ TX} = 2700\ Hz$  (b) SAR system with constant PRI and multiple elevation beams with  $PRF = 1800\ Hz$ .

#### 5.3.3 Duty Cycle

Another important performance parameter is the *NESZ*, given for a staggered SAR system by (79). The *NESZ* is significantly influenced by the radiated power  $P_{TX}$ , which depends on the number and power of T/R modules, which are chosen to meet the *NESZ* requirement for a given orbit. The system designer, however, can also influence the *NESZ* through an appropriate selection of the duty cycle, i.e., the pulse length for a given mean *PRF* on transmit. The longer is the pulse length, the better will be the achieved *NESZ*.

While in a SAR with constant *PRI* and multiple elevation beams, once the *PRF* is fixed, an increase of the pulse length leads to larger gaps between the multiple subswaths, according to (34), but has no impact on range and azimuth ambiguities, in the staggered SAR case, the increase of the pulse length influences the design of the sequence of *PRIs* (see Section 4.2) with a consequent degradation of the *AASR*, the *RASR*, and the *SNR* scaling factor. An example is provided in Fig. 52, where the duty cycle of a staggered SAR system with the parameters of Table 4 is gradually increased from 4% to 12%.

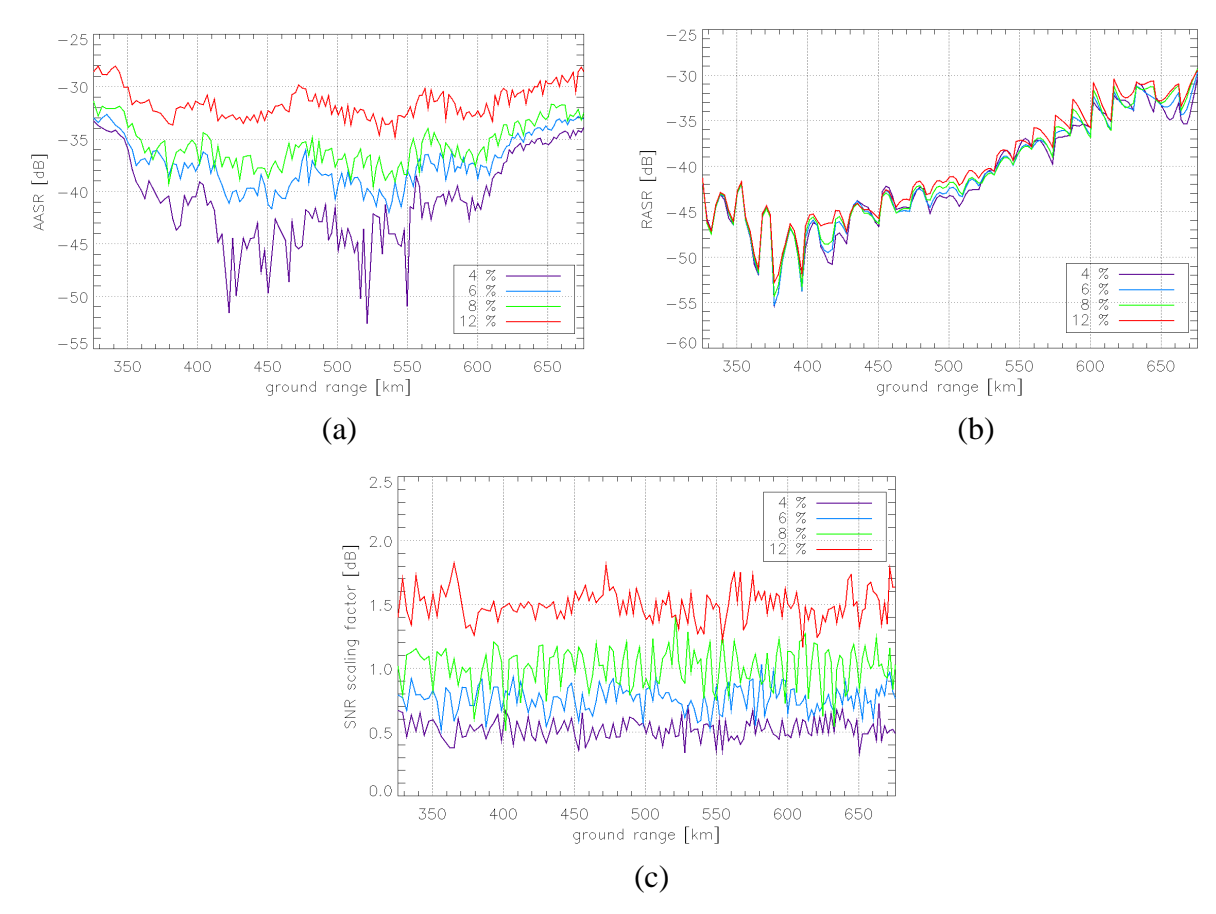


Fig. 52. Impact of the mean duty cycle on the performance for a staggered SAR with the parameters of Table 4. (a) AASR. (b) RASR. (c) SNR scaling factor.

With reference to the design example based on the parameters of Table 4, the ambiguity performance for a duty cycle equal to 4% is outstanding. It is therefore possible to remain within acceptable ambiguity requirements even by increasing the duty cycle. It has to be noted that increasing the duty cycle by a factor k (k > 1) does not lead to an improvement of the *NESZ* by a factor k, because an increased duty cycle leads to an increased *SNR* scaling factor, as more samples are missing. In the considered example the average *SNR* scaling factor increases from 0.5 dB to 1.5 dB, if the duty cycle is increased from 4% to 12% (see Fig. 52 (c)). If we also account for the noise scaling, increasing the duty cycle from 4% to 12% (i.e., by a factor of 3 or 4.8 dB) implies an improvement of the *NESZ* by "only" 3.8 dB.

#### **5.3.4** Fully Polarimetric SAR Systems

As already mentioned, the staggered SAR concept can be also adopted in combination with polarimetry. As far as dual-polarimetric SAR systems are concerned, it is still possible to keep the same performance as a single-polarimetric system, i.e., the one provided for the design examples in Sections 5.3.1, 5.3.2, and 5.3.3, provided that two separate channels are employed on receive to record two distinct polarizations at the same time.

The design of fully polarimetric staggered SAR systems, for which specific sequences of *PRIs* have been proposed in Section 4.2.4, is instead much more challenging. If the same antenna

designed for the single- and dual-polarimetric case is used, much worse ambiguity performance is expected and typical ambiguity requirements are likely to be met only over a smaller swath. In order to keep the same *AASR* for each of the four polarimetric channels, in fact, the mean *PRF* on transmit has to be doubled, with a consequent degradation of the *RASR*. As already pointed out in Section 2.3.5 with reference to a SAR with constant *PRI*, the *RASR* is usually critical for the cross-polarized channels, i.e., those characterized by a different polarization on transmit and receive, as some of the ambiguous echoes are characterized by the same polarization on transmit and receive and therefore by higher backscatters.

Fig. 53 shows the performance in terms of AASR, RASR, and SNR scaling factor, for a fullypolarimetric staggered SAR, which images a 175 km continuous ground swath, using the sequence of PRIs of Fig. 26. The same reflector antenna described in Section 5.1 is considered, where only sixteen out of the thirty-two groups of six azimuth feeds are activated on transmit<sup>4</sup>. A set of phase-only weights is applied to the sixteen groups of six azimuth feeds to optimize the shape of the elevation pattern on transmit. On receive, for each elevation beam five adjacent elevation feeds and all six azimuth feeds are activated and combined as described in Section 5.1. The minimum and maximum incidence angle are given by 31.2° and 41.8°, respectively, the mean PRF on transmit is equal to  $2 \times 1900$  Hz, the duty cycle is equal to 8%, while the other system and processing parameters are the same as given in Table 4. The idea is that the same system can be used within the same mission for different acquisition modes, i.e., single- and dual-polarimetric modes with 350 km continuous ground swath and a fully polarimetric mode with 175 km continuous ground swath. The ambiguity performance is worse compared to the singleand dual-polarimetric case: An AASR and a RASR better than -22 dB can be achieved, which can be considered satisfactory for many applications, considering that range and azimuth ambiguities are smeared. As is apparent in Fig. 53 (b), the RASR of the cross-polarized channels is much worse than the RASR of the co-polarized channels, as for the cross-polarized channels some of the ambiguous returns are characterized by a backscatter higher than that of the desired return (cf. Fig. 30).

The design of a fully polarimetric HRWS SAR system is challenging for a system with constant *PRI* and multiple elevation beams as well, as even in that case the considerations on the doubling of the *PRF* and the critical *RASR* for the cross-polarized channels hold. However, in the constant *PRI* case azimuth phase coding (APC) can contribute to a significant improvement of the *RASR* [116]-[117]. APC is unfortunately not straightforwardly applicable to the staggered SAR case, because the range ambiguous echoes are located at different ranges for different azimuth samples.

<sup>&</sup>lt;sup>4</sup> For fully polarimetric operation two T/R modules are used for each group of six azimuth feeds.

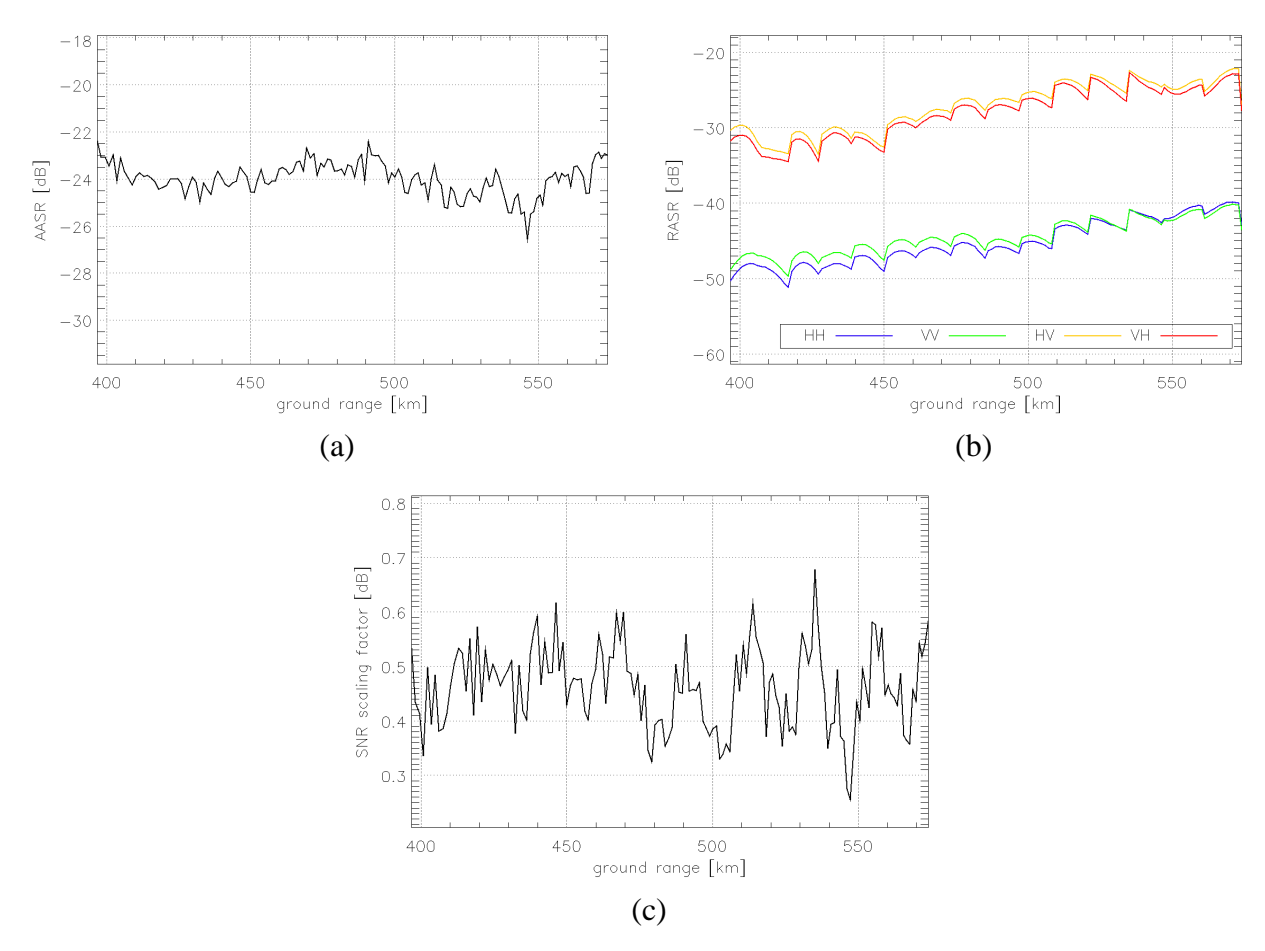


Fig. 53. Performance of a fully polarimetric staggered SAR, which images a 175 km continuous ground swath. (a) AASR. (b) RASR. (c) SNR scaling factor.

# 5.4 C-Band Design Examples Based on a Planar Antenna

In the following further staggered SAR design examples are provided, where the radar carrier frequency lies in the C-band portion of the electromagnetic spectrum, i.e., it is approximately 4 times larger than for the previous L-band examples.

A prominent C-band SAR mission, Sentinel-1, consisting of a constellation of two satellites, is currently operated by the ESA, as part of the Copernicus programme, to provide continuity of data from the former C-band ERS and Envisat missions [34]. The operational modes of Sentinel-1 include a stripmap mode, able to map a 80 km ground swath with a 5 m azimuth resolution, an interferometric wide-swath mode, able to map a 250 km ground swath with 20 m azimuth resolution, and an extra wide swath mode, able to map a 400 km ground swath with 40 m azimuth resolution, where TOPS is used in the latter two modes to achieve a wide swath at the expenses of a degraded azimuth resolution. Due to the inherent limitation described in Section 3.1, however, Sentinel-1 is not able to map a wide ground swath, e.g., 400 km, with a high azimuth resolution, e.g., 5 m. Moreover, its polarimetric capability is limited, as only single- and dual-polarimetric data can be acquired in the aforementioned modes.

In 2008 ESA has commissioned DLR to undertake a study for a HRWS C-band SAR instrument, able to map a 400 km ground swath with a 5 m azimuth resolution in single- and dual-polarimetric modes and a 280 km ground swath with a 5 m azimuth resolution in fully-polarimetric mode [118]. The sum of *AASR* and *RASR*, i.e., the *ASR*, is required to be better than -22 dB. The outcome of the study was that these requirements could be fulfilled using a 12.8 m × 1.18 m planar antenna in combination with a multi-channel ScanSAR concept, described in Section 3.3.1, where 4 subswaths are mapped using 8 azimuth channels [118]. As already pointed out, a possible drawback of this approach is the rather high Doppler centroid for some of the imaged targets, in case high resolution is desired. Moreover, high squint angles may also challenge co-registration in interferometric applications [104].

The aforementioned requirements, however, can be also met using a staggered SAR with a planar antenna of comparable size and without the need of 8 azimuth channels. Table 5 shows a possible set of system and processing parameters for a 400 km ground swath, 5 m azimuth resolution, single- and dual-polarimetric staggered SAR system.

Parameter	Value
Radar wavelength	0.0555 m (C-band)
Orbit height	700 km
Minimum incidence angle	17°
Maximum incidence angle	44.3°
Tilt angle	27°
Antenna type	Planar
Antenna size	$10 \text{ m (length)} \times 1.5 \text{ m (height)}$
Antenna elements in elevation	22
Mean duty cycle	6%
Mean <i>PRF</i> on TX	2800 Hz
Sequence of PRIs	More elaborated sequence
Number of concatenated sequences	7
Resampling method	BLU on raw data (before range
	compression)
Processed Doppler bandwidth	1200 Hz
Azimuth processing window	Uniform
Compensation of the azimuth pattern	Yes
Range processing window	Uniform
Backscatter model	Fig. 55

Table 5. System and processing parameters for a single- and dual-polarimetric C-band staggered SAR with a planar antenna, able to map a 400 km swath with 5 m azimuth resolution.

In particular, a  $10 \text{ m} \times 1.5 \text{ m}$  planar antenna with 22 elements in elevation has been considered for the single- and dual-polarimetric case. Fig. 54 shows the normalized transmit and receive antenna patterns in elevation (at near range) as a function of the elevation angle, while in

the azimuth direction the "sinc-like" pattern obtained for a uniform illumination of the 10 m antenna has been considered. For the purpose of this analysis a "rectangular-like" transmit pattern in elevation has been assumed by amplitude tapering of the 22 elements with a sinc function, while the receive patterns in elevation are obtained by Hamming tapering ( $\alpha = 0.54$ ) of the 22 elements and phase shifting in the desired direction. Unlike for the previously presented L-band design examples, patterns have not been optimized and further performance improvements can be achieved as a consequence of pattern optimization.

The same backscatter decay as a function of the incidence angle used for the HRWS C-band study, depicted in Fig. 55 for the different polarizations, has been used.

Fig. 56 shows the AASR, the RASR, and the ASR for the single- and dual- polarimetric design example. As is apparent in Fig. 56 (c), an ASR better than -22 dB is achieved. In comparison with the design examples, where a reflector is used, a much lower variability of the AASR is observed,

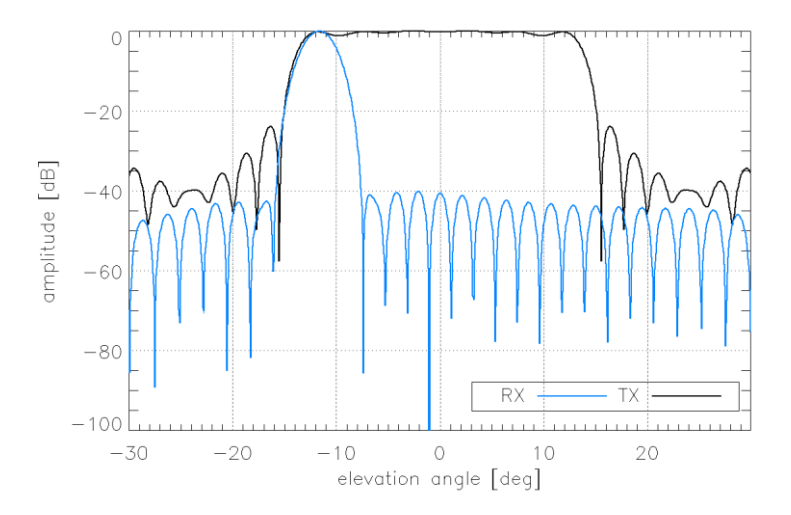


Fig. 54. Normalized transmit and receive antenna patterns in elevation at near range vs. elevation angle for the planar antenna with multiple elevation elements.

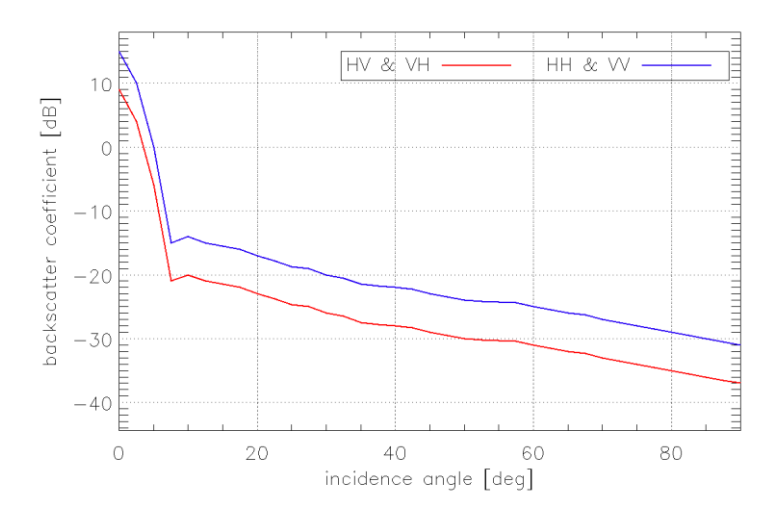


Fig. 55. Backscatter coefficient as a function of the incidence angle for different polarizations at C-band.

as the azimuth antenna pattern of a planar antenna is the same for all elevation angles and the *AASR* variation is only due to the different number and location of missing samples at different ranges, i.e., it would be constant for a SAR with constant *PRI*.

Table 6 shows the system parameters for the fully polarimetric design example, where a 280 km ground swath is mapped with 5 m azimuth resolution. Only the parameters which differ from the ones in Table 5 are specified. In this case, a higher antenna (2.6 m) with a 36 elements in elevation has to be used. The ambiguity performance is summarized for this design example in Fig. 57, where it can be observed that an *ASR* better than -22 dB is achieved in this case as well.

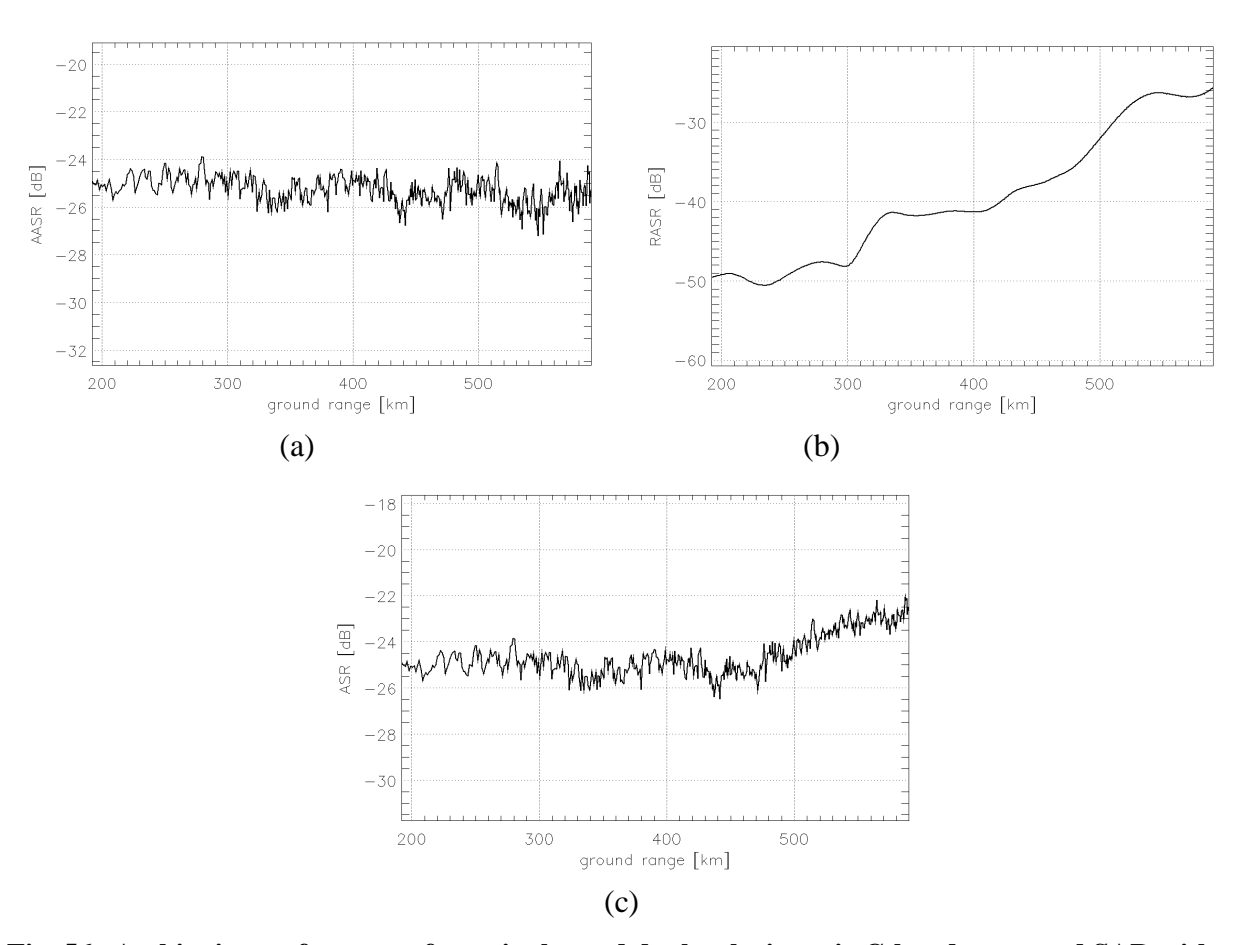


Fig. 56. Ambiguity performance for a single- and dual-polarimetric C-band staggered SAR with a planar antenna, able to map a 400 km ground swath with 5 m azimuth resolution. (a) AASR. (b) RASR. (c) ASR.

Parameter	Value
Minimum incidence angle	17°
Maximum incidence angle	37.5°
Tilt angle	24°
Antenna type	Planar
Antenna size	$10 \text{ m (length)} \times 2.6 \text{ m (height)}$
Antenna elements in elevation	36
Mean duty cycle	12%
Mean PRF on TX	5400 Hz

Table 6. System parameters for a fully polarimetric C-band staggered SAR with a planar antenna, able to map a 280 km swath with 5 m azimuth resolution.

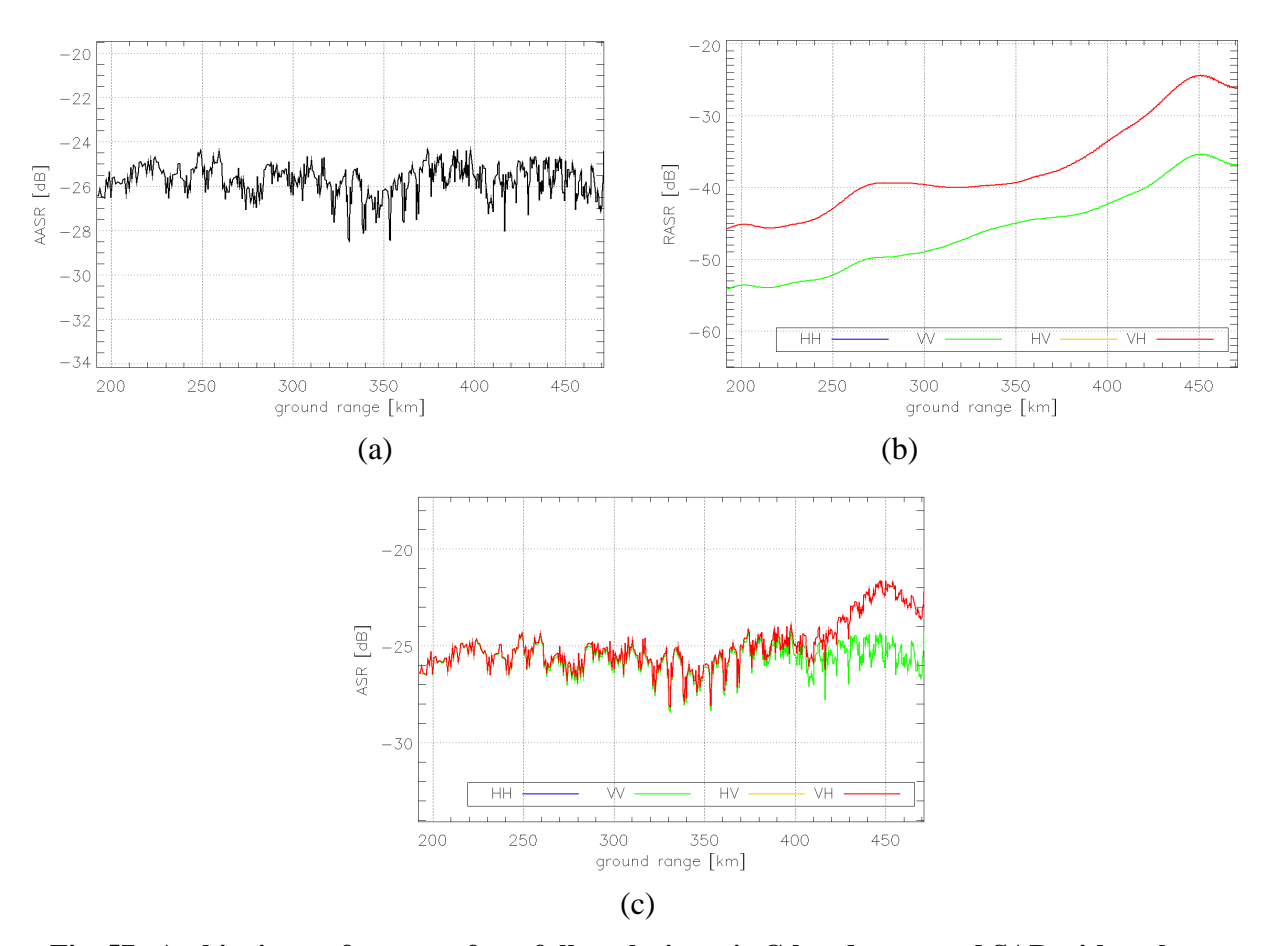


Fig. 57. Ambiguity performance for a fully polarimetric C-band staggered SAR with a planar antenna, able to map a 280 km ground swath with 5 m azimuth resolution. (a) AASR. (b) RASR. (c) ASR.

The latter system, designed to map a 280 km ground swath in fully polarimetric mode, can be also used to map a 400 km ground swath in single- and dual-polarimetric modes with outstanding ambiguity performance. As shown in Fig. 58, an *ASR* better than -30.5 dB is achieved.

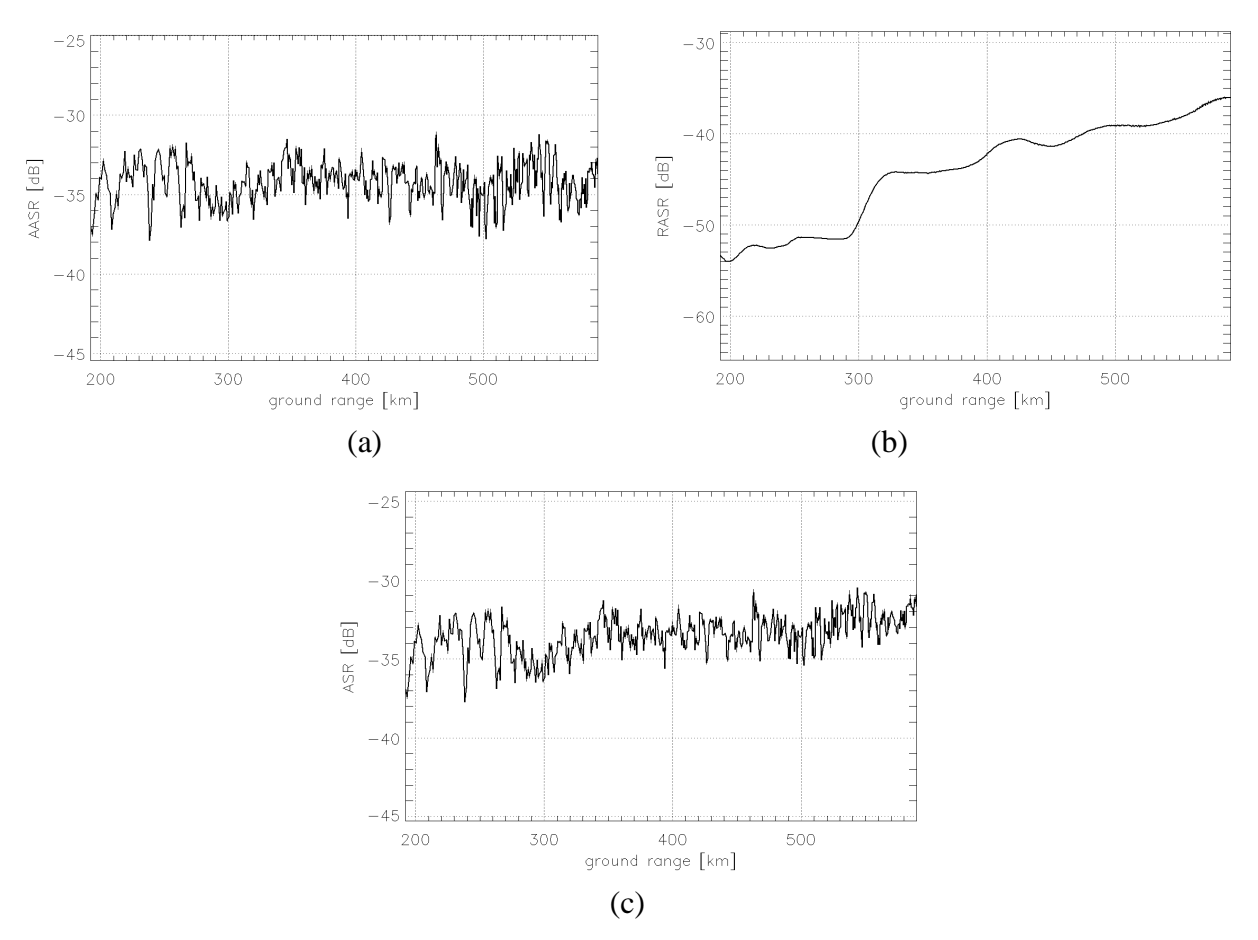


Fig. 58. Ambiguity performance for single- and dual-polarimetric modes of the system designed to map a 280 km ground swath in fully polarimetric mode. (a) AASR. (b) RASR. (c) ASR.

# 6 Experiments with Real Data

The impact of staggered SAR operation on image quality is furthermore assessed with experiments using real data. As a first step, highly oversampled F-SAR airborne data have been used to generate equivalent staggered SAR data sets and evaluate the performance for different sequences of *PRIs* and interpolation methods. Then, the German satellite TerraSAR-X has been commanded to acquire data over the Lake Constance in staggered SAR mode. Measurements on these data show very good agreement with predictions from simulations.

### **6.1** F-SAR Experiment

In order to better understand the implications of staggered SAR operation on image quality, airborne data with a *PRF* much larger than their Doppler bandwidth, i.e., highly oversampled in azimuth, are firstly used. From the highly oversampled raw data, it is possible to extract raw data as they would have been received by a staggered SAR system with arbitrary sequences of *PRIs*. These data can be then resampled to a uniform grid, using the different algorithms described in Section 4.3, such as two-point linear interpolation or BLU interpolation, allowing an assessment of the reconstruction error on raw data. Furthermore, conventional SAR processing can be performed and the image quality can be assessed for different sequences of *PRIs* and resampling algorithms, especially if several corner reflectors are present in the scene. For that reason, airborne data have been acquired by DLR's F-SAR sensor over the calibration test site of Kaufbeuren, Germany [28].

#### 6.1.1 Generation of Equivalent Staggered SAR Data

The raw data used for this analysis, uniformly sampled in time, are displayed in Fig. 59. The scene includes twelve trihedral corner reflectors near the center of the azimuth trajectory at different slant range distances. Simulated data for a scene with the same acquisition geometry, where only the corner reflectors are present, have been generated and are displayed in Fig. 60. The relevant system parameters for the considered F-SAR data set are summarized in Table 7.

Due to the non-vanishing squint angle  $\varphi_{sq}$ , the data are characterized by a Doppler centroid frequency  $f_{DC}$ , which can be evaluated using the well-known relationship between Doppler fre-

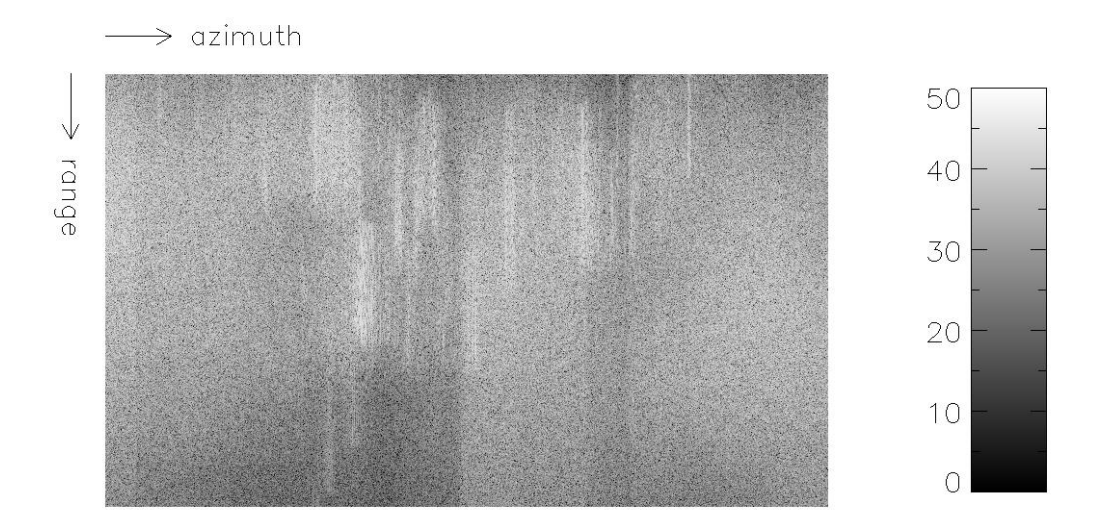


Fig. 59. Raw data (log-intensity) acquired by the F-SAR airborne sensor over the calibration test site of Kaufbeuren, Germany.

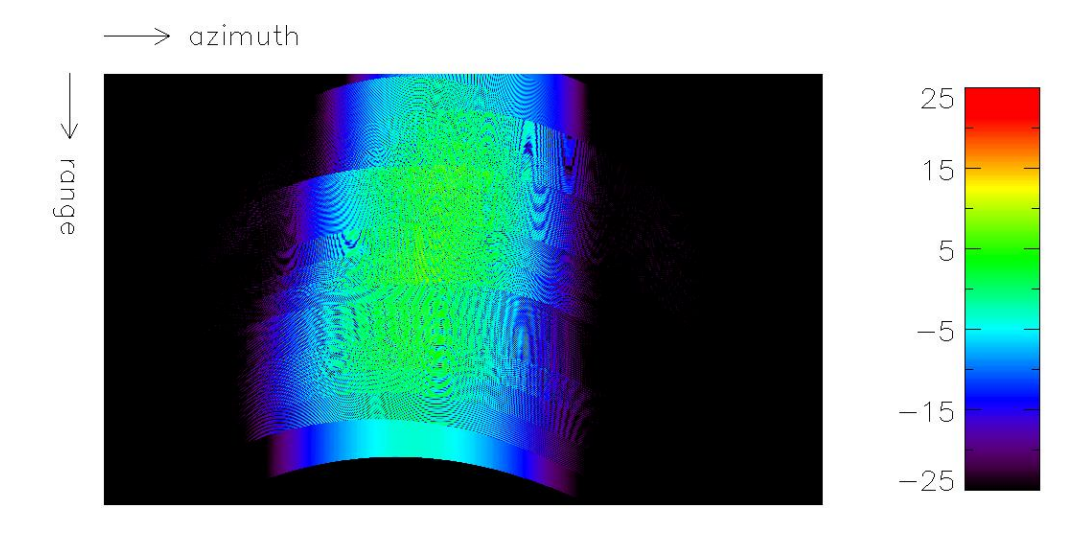


Fig. 60. Simulated raw data (log-intensity), assuming that only the twelve corner reflectors are present in the scene.

quency  $f_D$  and azimuth angle  $\varphi$ , given in (14). For this data set, the Doppler centroid frequency is equal to  $f_{DC} = -37.45$  Hz. As the spatial coordinate in the flight direction x[p],  $p = 0..N_{az} - 1$  is known for each pulse transmission time, the Doppler centroid can be removed by demodulating the original data u[q,p] as follows

$$u_{dem}[q, p] = u[q, p] \exp\left\{-j \frac{4\pi \sin \varphi_{sq}}{\lambda} x[p]\right\}$$
(81)

Parameter	Value
Carrier frequency	1.275 GHz (L-band)
Polarization	НН
Sensor velocity	90.897780 m/s
PRF	3048.7805 Hz
Chirp bandwidth	50 MHz
Range sampling frequency	125 MHz
Minimum slant range	2118.3346 m
Maximum slant range	4572.3417 m
Transmitted pulse duration	5 μs
Squint angle	-2.7757023°
Number of range lines	208896
Number of azimuth lines	3136

Table 7. System parameters for the considered F-SAR data set.

Fig. 61 shows the two-way azimuth antenna pattern as a function of the Doppler frequency, which is related to the azimuth angle through (14). In particular, the Doppler frequency corresponding to targets coming from an angle  $\varphi=\pm90^\circ$  can be evaluated using (14) and for this acquisition is equal to  $f_D=\pm773$  Hz. As the *PRF* is equal to 3048.7805 Hz, there is therefore no signal component characterized by a Doppler frequency outside the frequency interval [-*PRF*/2, *PRF*/2], which would fold back into the main part of the spectrum, leading to azimuth ambiguities. The absence of these types of artifacts implies that the value of the complex signal can be recovered at arbitrary azimuth locations with very good accuracy, as the estimation is only limited by thermal noise. Since the *NESZ* for this data set is better than -38 dB, this allows a highly accurate generation of an equivalent staggered SAR data set <sup>5</sup>.

Before generating the staggered SAR data set, it is nevertheless of interest to evaluate an upper bound for the error in the estimation of a complex sample at an arbitrary azimuth location. In particular, with reference to an azimuth line of the data set, it is possible to estimate the value of each sample using neighboring samples by means of two-point linear interpolation or BLU interpolation. As the true value of the sample  $u_{dem}[q,p]$  is known, a relative measurement of the error can be obtained by the ratio of the energy of the error to the energy of the true value

$$\varepsilon = \frac{\sum_{p=0}^{N_{az}-1} |\hat{u}_{dem}[q,p] - u_{dem}[q,p]|^2}{\sum_{p=0}^{N_{az}-1} |u_{dem}[q,p]|^2}$$
(82)

<sup>&</sup>lt;sup>5</sup> As fully polarimetric data are available for this acquisition, the *NESZ* can be estimated from the focused data of the two cross-polarized channels as explained in [119].

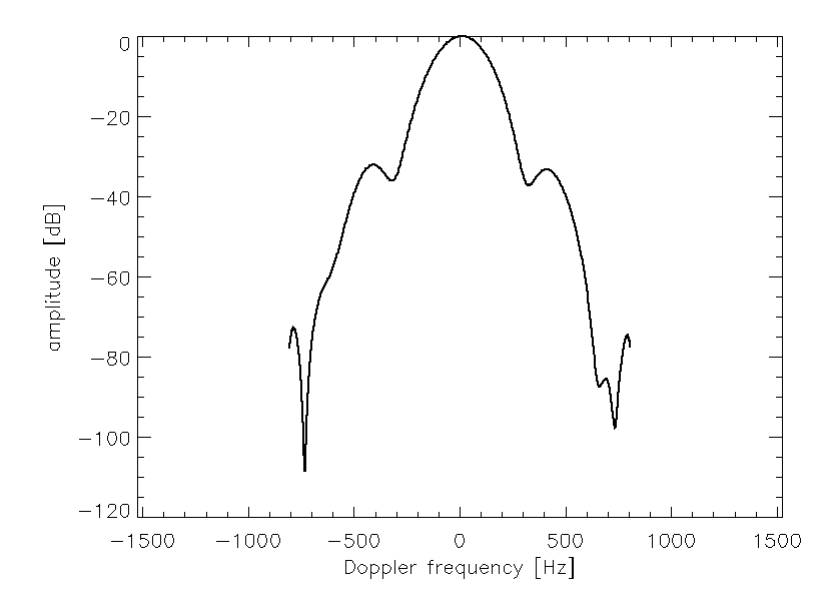


Fig. 61. Two-way azimuth antenna pattern as a function of Doppler frequency.

where  $\hat{u}_{dem}[q,p]$  is the estimated value of the sample. This error has to be clearly considered as an upper bound, as in this case, the time difference between the closest previous and subsequent samples is 2/PRF, while, when generating the staggered SAR data set, the corresponding time difference is 1/PRF. The relative error  $\varepsilon$ , as defined in (82), is displayed in logarithmic scale in Fig. 62 for each valid<sup>6</sup> azimuth line of the data set and for different interpolation methods, while the autocorrelation function used within BLU interpolation and estimated from the whole data set is displayed in Fig. 63.

Fig. 62 shows that BLU interpolation generally performs better than two-point linear interpolation, even when only two samples are used. This has been expected, as BLU interpolation makes use of the spectral characteristics of the data. However, even in the worst case of two-point linear interpolation, the significant oversampling of the data leads to errors smaller than -26 dB. For the present purposes, these can be considered negligible, as satellite data are often characterized by a thermal noise variance much larger than the variance of this estimation error.

In order to generate the equivalent staggered SAR data set, some reference sequences of *PRIs* have to be considered. As shown in Section 5.2.1, better ambiguity performance is achieved, if sequences of *PRIs* are used in which two consecutive azimuth samples are never missed. For our analysis we considered two sample sequences of *PRIs*, taken from a typical satellite design example, namely the sequence with fast *PRI* change of Fig. 24, from now on referred to as sequence 1, and the more elaborated sequence of Fig. 25, from now on referred to as

<sup>&</sup>lt;sup>6</sup> As is apparent from Table 7 the number of azimuth lines is equal to 3136, although azimuth lines comprised between 0 and 410 and between 2759 and 3135 are considered invalid, as the compression in range is partial. Invalid azimuth lines are not displayed in Fig. 59 and Fig. 60.

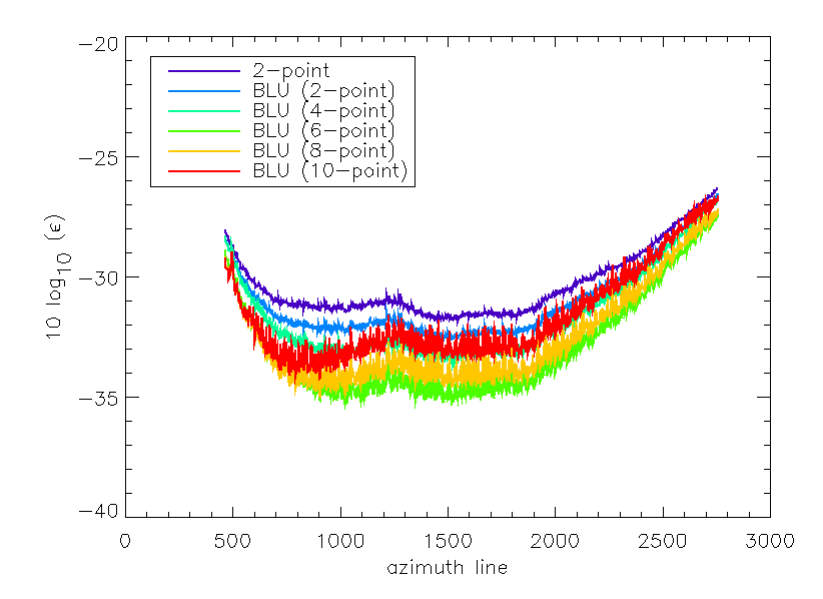


Fig. 62. Relative error ε, as defined in (82), in logarithmic scale for each valid azimuth line of the data set and for different interpolation methods.

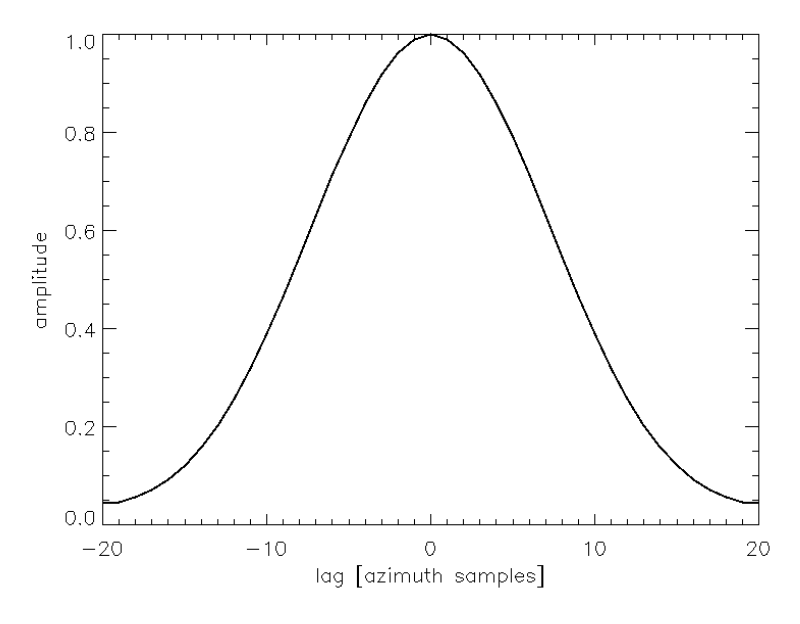


Fig. 63. Autocorrelation function used within BLU interpolation and estimated from the whole data set.

sequence 2. For each slant range some of the pulses (but never two consecutive ones) are lost depending on the duration of the uncompressed transmitted pulse.

In order to account for the different 3-dB Doppler bandwidths of the actual F-SAR system and the satellite design example of Section 5, the *PRIs* of the two aforementioned sequences have to be scaled: As the 3-dB Doppler bandwidth in the satellite design example (855 Hz at near range, where the worst *AASR* performance is achieved) is 4.5 times larger than in the F-SAR data set (190 Hz), the sampling times for the F-SAR data needs to be 4.5 times larger than for the design example. A mean *PRF* on transmit of 2700 Hz in the satellite design example therefore

corresponds to a mean PRF on transmit of 2700/4.5 = 600 Hz in the F-SAR example. This case will be from now on referred to as high azimuth oversampling. In order to observe the impact of lower mean PRFs on transmit on image quality, scaling factors equal to 6 and 7.5 are considered as well. Sequences of PRIs are therefore obtained with mean PRFs on transmit equal to 450 Hz and 360 Hz, corresponding to mean PRFs on transmit equal to 2025 Hz and to 1620 Hz in the satellite design example at near range, and referred to as medium and low azimuth oversampling, respectively. For the sake of simplicity, the equivalent staggered SAR data set has been generated using two-point linear interpolation.

Once the non-uniformly sampled data have been generated, missing samples can be introduced by blanking portions of some range lines corresponding to the length of the transmitted pulse of the F-SAR system, i.e., 5 µs. In order to obtain a raw staggered SAR data set as it would have been received by a wide-swath satellite system, the same pattern of missing samples of a 50 km slant range portion of a wide swath is mapped to the 3.7 km slant range swath of F-SAR. Fig. 64 shows for the two aforementioned sequences a portion (namely 375 range lines) of the raw staggered SAR data, where the periodic pattern of missing samples is visible.

Finally, in order to compare the results with a reference, uniformly sampled data set with an oversampling rate representative of a typical staggered SAR system, i.e., much lower than the oversampling rate of the F-SAR data set, for which azimuth ambiguities are no longer negligible, a further data set has been created, where data have been downsampled (decimated) in the azimuth direction by a factor of seven and then upsampled by a factor of seven by means of zero-padding of the fast Fourier transform (FFT). With reference to the SAR system with constant PRI and multiple elevation beams of Section 5, this correspond to a PRF of 3048 Hz / 7 × 4.5 = 1960 Hz in the satellite design example at near range. Equivalent staggered SAR data sets, as well a reference uniformly sampled data set, have been generated for the simulated data displayed in Fig. 60 as well.

#### 6.1.2 Performance Assessment on Raw Data

Once the equivalent staggered SAR data sets have been generated, the latter can be resampled to a uniform grid. The relative error  $\varepsilon$ , as defined in (82), is displayed in logarithmic scale in Fig. 65 for each valid azimuth line of the data set, for the two sequences of *PRIs*, the two interpolation methods (two-point linear interpolation and BLU) and the three considered mean *PRFs* on transmit. As expected, the error becomes smaller, as the oversampling rate increases. Moreover, for the same oversampling rate, BLU interpolation performs better than two-point linear interpolation and the more elaborated sequence (sequence 2) leads to smaller errors than the one with fast *PRI* change (sequence 1), except for the ranges where no samples are missing in the sequence with fast *PRI* change.

Further comparisons between the reconstructed and original complex data show that the proposed interpolations tend to reduce the amplitude of the signal. This is apparent in Fig. 66, where the ratio  $\beta$  of the energy of the reconstructed signal to the energy of the original signal, defined as

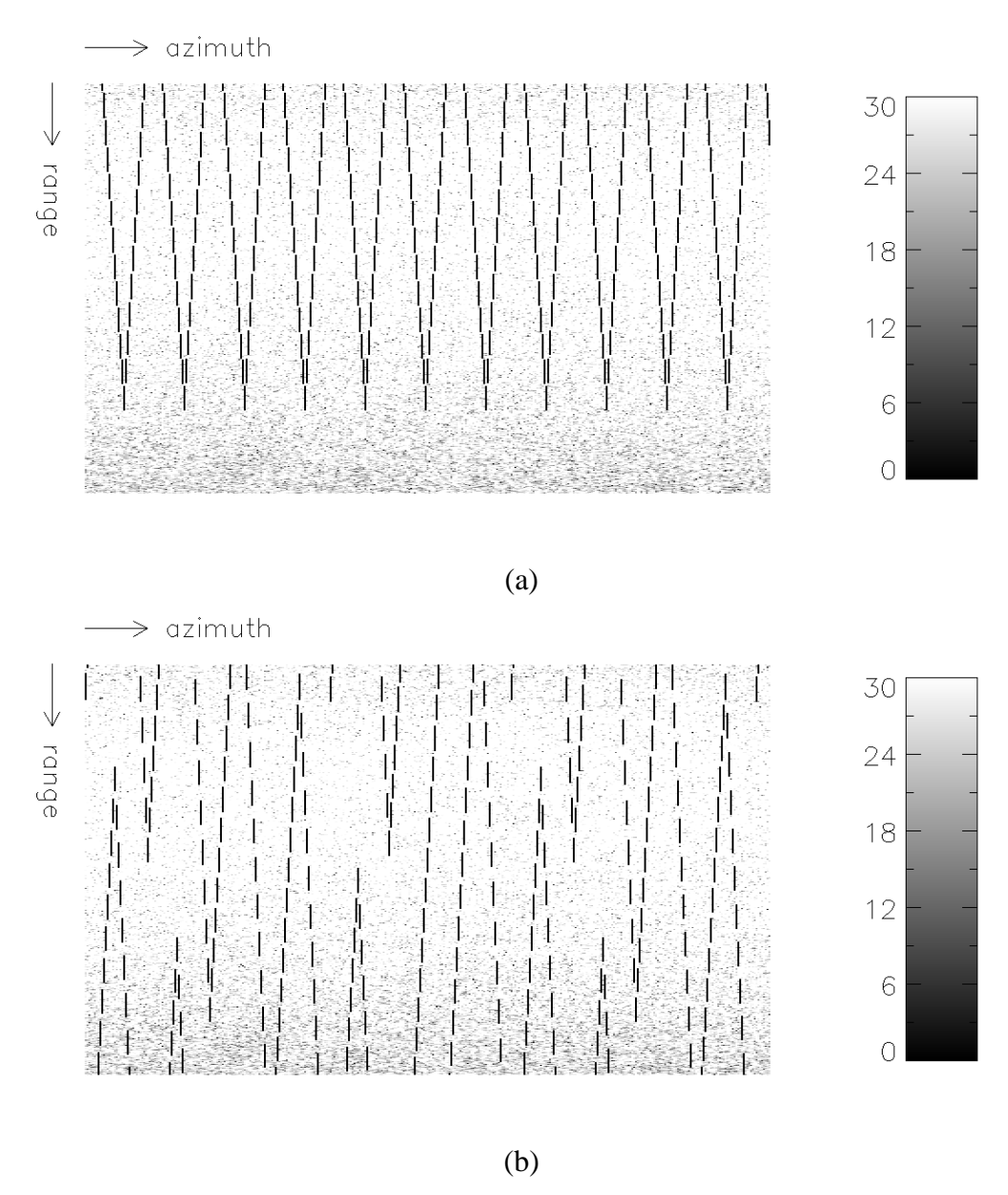


Fig. 64. Portions (375 range lines) of raw staggered SAR data sets. The periodic pattern of missing samples is visible. (a) Sequence 1. (b) Sequence 2.

$$\beta = \frac{\sum_{p=0}^{N_{az}-1} |\hat{u}_{dem}[q, p]|^2}{\sum_{p=0}^{N_{az}-1} |u_{dem}[q, p]|^2}$$
(83)

is displayed in logarithmic scale for each valid azimuth line of the data set, for the two sequences of *PRIs*, the two interpolation methods and the three considered scaling factors. As is apparent, however, the two-point linear interpolation is seen to introduce a higher bias than the BLU interpolation. Moreover, the achieved relative radiometric accuracy for two-point linear interpolation could not meet the typical requirements.

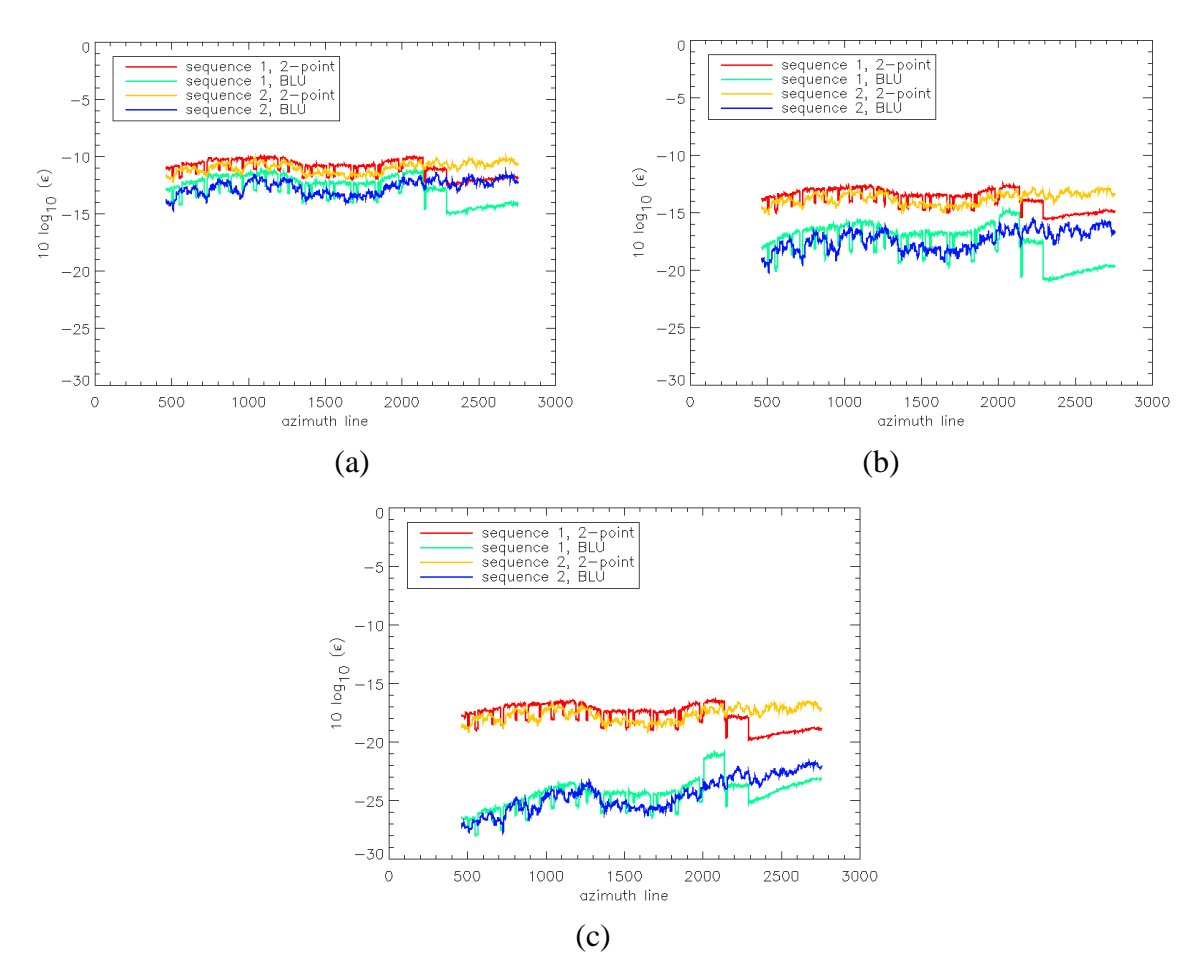


Fig. 65. Relative error ε, as defined in (82), in logarithmic scale for each valid azimuth line of the data set, for the two sequences of *PRIs*, the two interpolation methods, and the three considered mean *PRFs* on transmit. (a) Mean *PRF* on transmit = 360 Hz (low azimuth oversampling). (b) Mean *PRF* on transmit = 450 Hz (medium azimuth oversampling). (c) Mean *PRF* on transmit = 600 Hz (high azimuth oversampling).

#### 6.1.3 Data Focusing and Impulse Response Analysis

The reference decimated data set and all data sets, obtained by resampling the staggered SAR data to a uniform grid, have been processed using the operational F-SAR processor to obtain focused data with an azimuth resolution of 0.675 m [28]. In order to obtain this azimuth resolution a PBW equal to 175 Hz, i.e., by a factor of 4.5 smaller than that of the satellite design example, has been processed. The same processing was carried out for the simulated data sets.

Focused data are displayed in Fig. 67, Fig. 68, Fig. 69, and Fig. 70, after an amplitude presumming in azimuth by a factor of 8 and using a 50 dB-log-intensity scale, to highlight the differences in the low backscatter areas, such as part of the Bärensee lake in the right-hand part of the image. For each staggered SAR image, the difference between the image itself and the reference image is shown as well. This allows a first quantitative assessment of the impact of sequence, interpolation method, and oversampling rate on image quality.

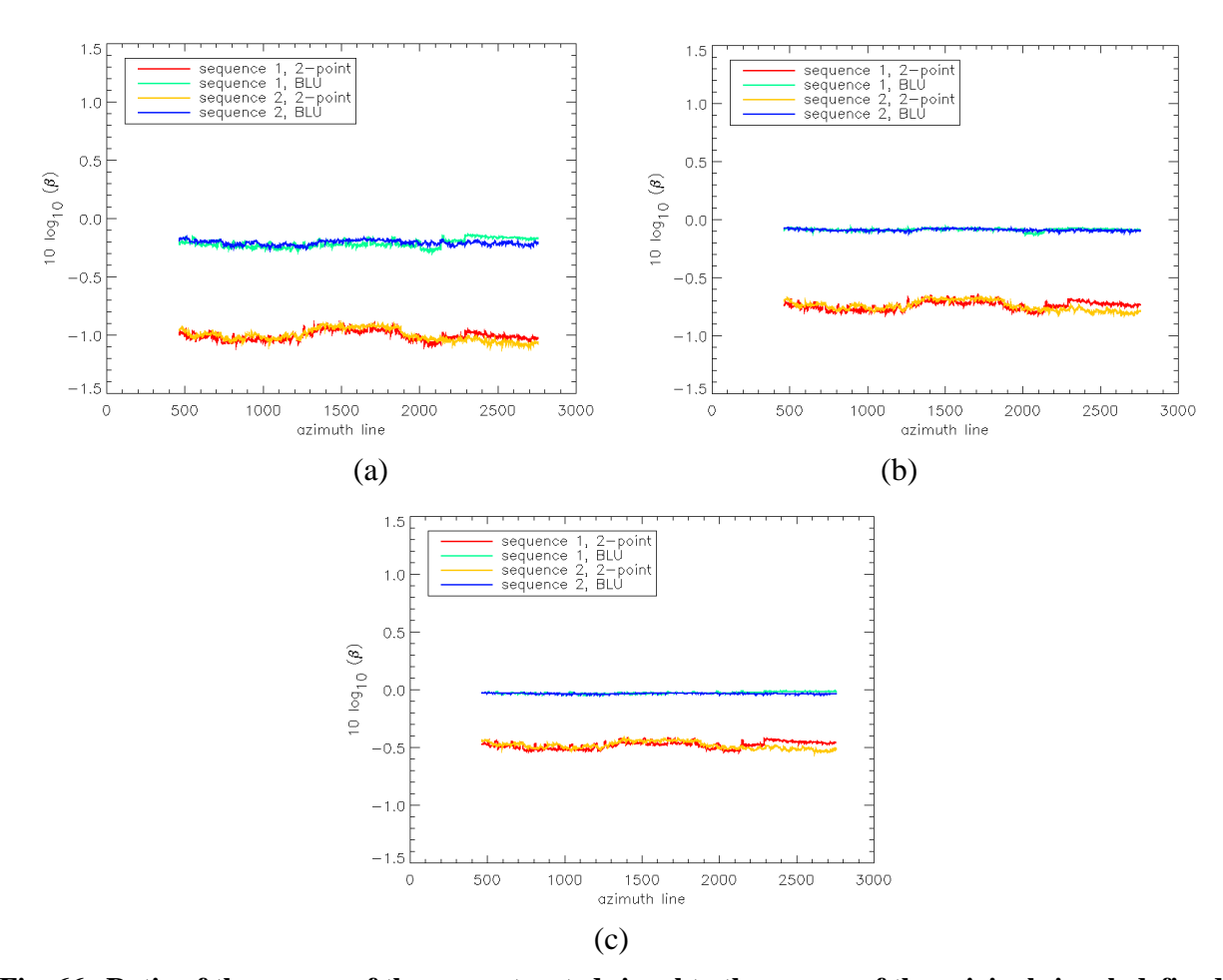


Fig. 66. Ratio of the energy of the reconstructed signal to the energy of the original signal, defined as in (83), in logarithmic scale for each valid azimuth line of the data set, for the two sequences of *PRIs*, the two interpolation methods and the three considered mean *PRFs* on transmit. (a) Mean *PRF* on transmit = 360 Hz (low azimuth oversampling). (b) Mean *PRF* on transmit = 450 Hz (medium azimuth oversampling). (c) Mean *PRF* on transmit = 600 Hz (high azimuth oversampling).



Fig. 67. Focused image (log-intensity) for the reference (decimated and upsampled) data.

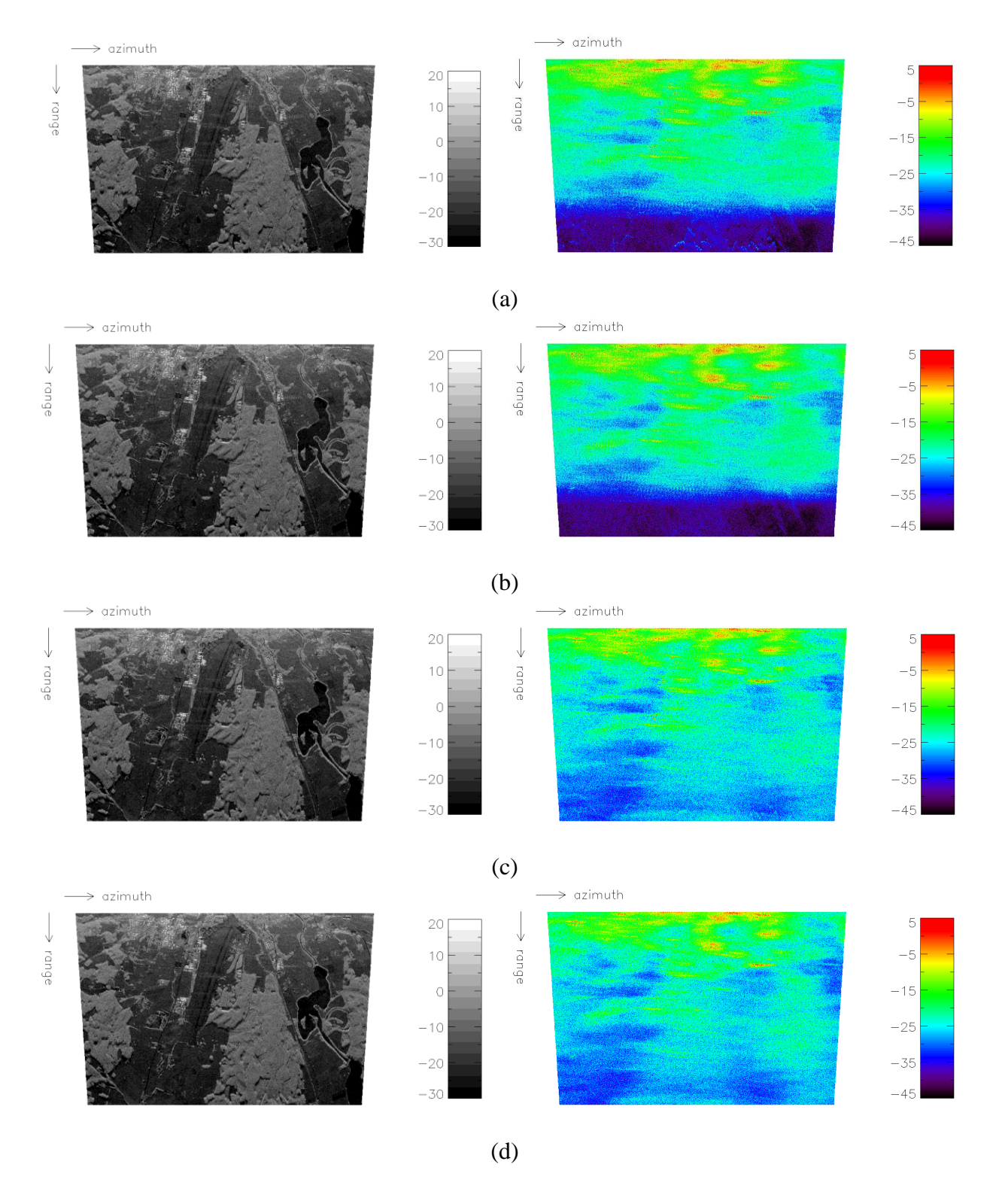


Fig. 68. Focused images (log-intensity) for a mean *PRF* on transmit of 360 Hz (low azimuth oversampling) (left) and differences with the reference image with uniform *PRI* (right). (a) Sequence 1, two-point linear interpolation. (b) Sequence 1, BLU interpolation. (c) Sequence 2, two-point linear interpolation. (d) Sequence 2, BLU interpolation.

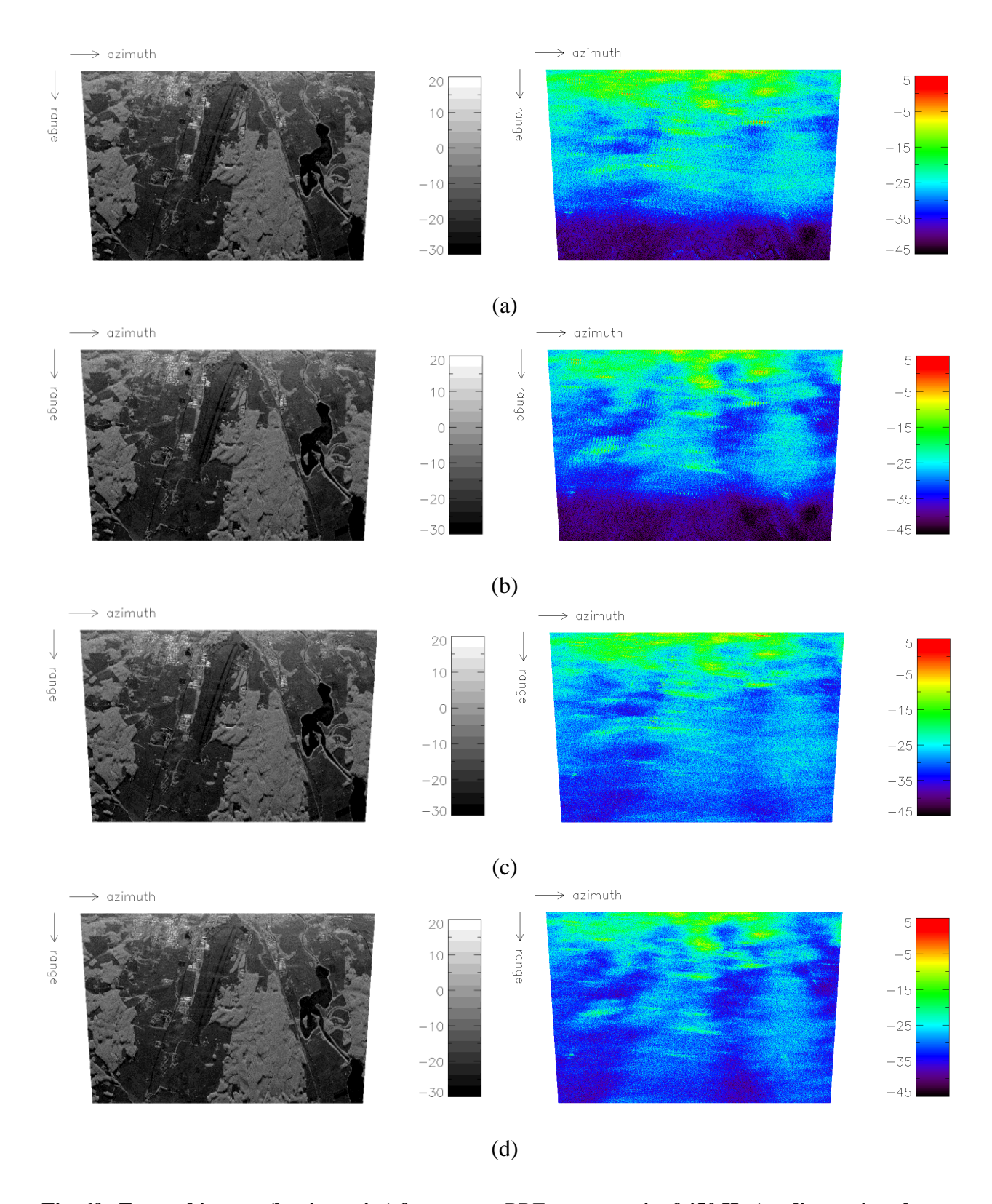


Fig. 69. Focused images (log-intensity) for a mean *PRF* on transmit of 450 Hz (medium azimuth oversampling) (left) and differences with the reference image with uniform *PRI* (right). (a) Sequence 1, two-point linear interpolation. (b) Sequence 1, BLU interpolation. (c) Sequence 2, two-point linear interpolation. (d) Sequence 2, BLU interpolation.

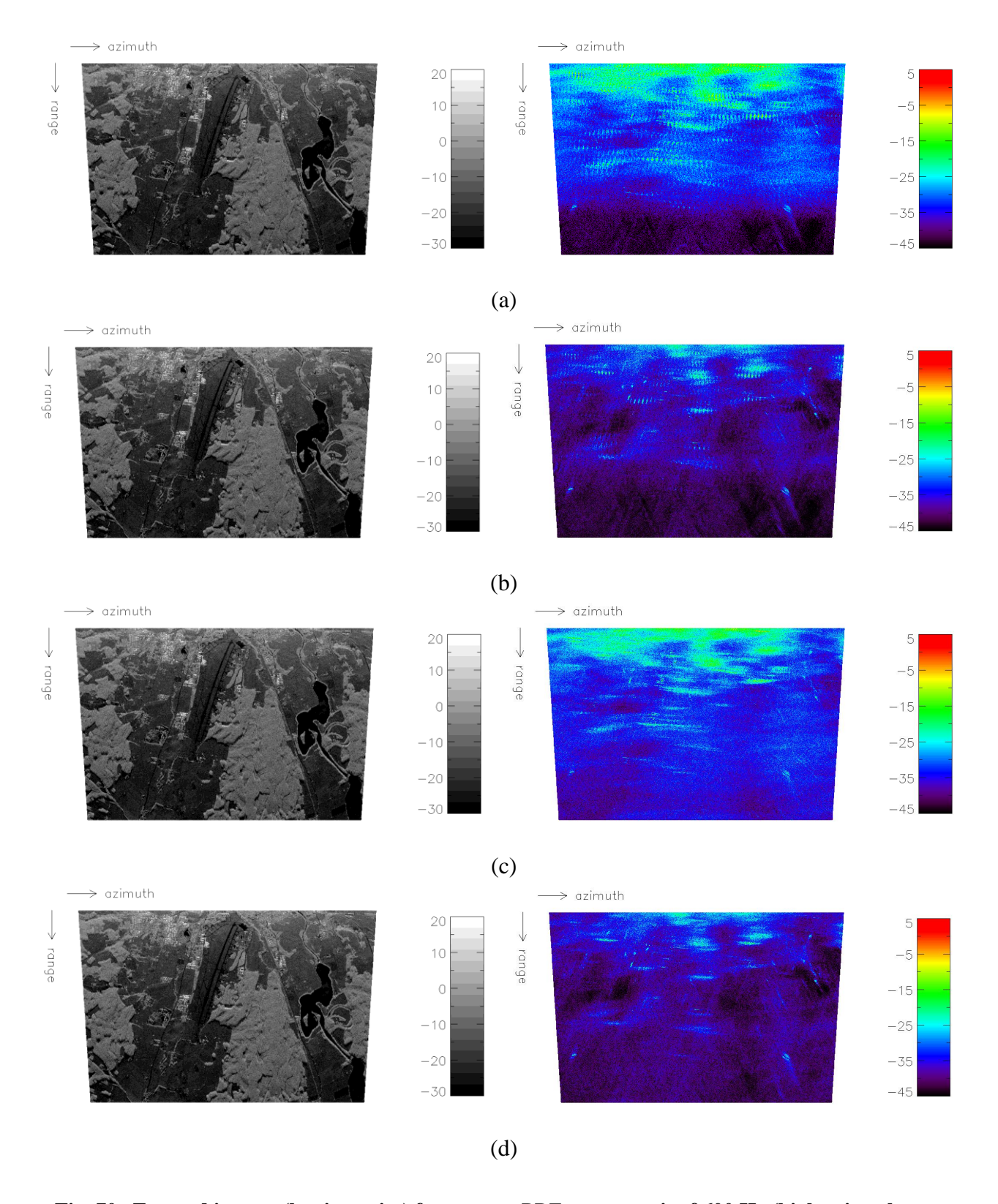


Fig. 70. Focused images (log-intensity) for a mean *PRF* on transmit of 600 Hz (high azimuth oversampling) (left) and differences with the reference image with uniform *PRI* (right). (a) Sequence 1, two-point linear interpolation. (b) Sequence 1, BLU interpolation. (c) Sequence 2, two-point linear interpolation. (d) Sequence 2, BLU interpolation.

Although the relative increase of the intensity in these low backscatter areas is significant, these changes are due to the very high dynamic range of backscatter of F-SAR data and would not be noticeable in a satellite scenario given the much lower *SNR* expected.

It can be also observed that for low azimuth oversampling rates (cf. Fig. 68) strong targets give rise to image artefacts.

The relative increase of the intensity in low backscatter areas and the aforementioned image artifacts can be explained by looking at the differences between the impulse response in conventional SAR with uniform *PRI* and staggered SAR. For that the simulated focused data are shown, in case only the twelve corner reflectors are present in the scene. Fig. 71 shows the location of the corner reflectors, while the simulated focused data are shown in Fig. 72, Fig. 73, Fig. 74, and Fig. 75, together with a zoom in the vicinity of one of the corner reflectors. The color scale has been chosen to highlight azimuth ambiguities. As already mentioned in Section 2.3.4, azimuth ambiguities arise in SAR images from the finite sampling of the Doppler spectrum at the *PRF* and may give rise to visible artifacts due to the large dynamics of SAR reflectivity.

While, for the conventional SAR system with constant *PRI*, first-order azimuth ambiguities appear as stripes, displaced in range and azimuth, in the staggered SAR case the energy of ambiguities is spread over a much wider area. The local power of the ambiguous signal for a conventional SAR system is therefore determined by the local power of the signal in some specific areas, while for a staggered SAR system it is related to the average signal power over a much larger area. For the low backscatter areas of this scene (e.g., the lake in the bottom-left hand part of the image), the local power of the signal in the above mentioned specific areas (namely the field in the upper central part of the image) is lower than the average signal power over the larger areas surrounding the ambiguities, where forested areas with higher backscatter are also present.

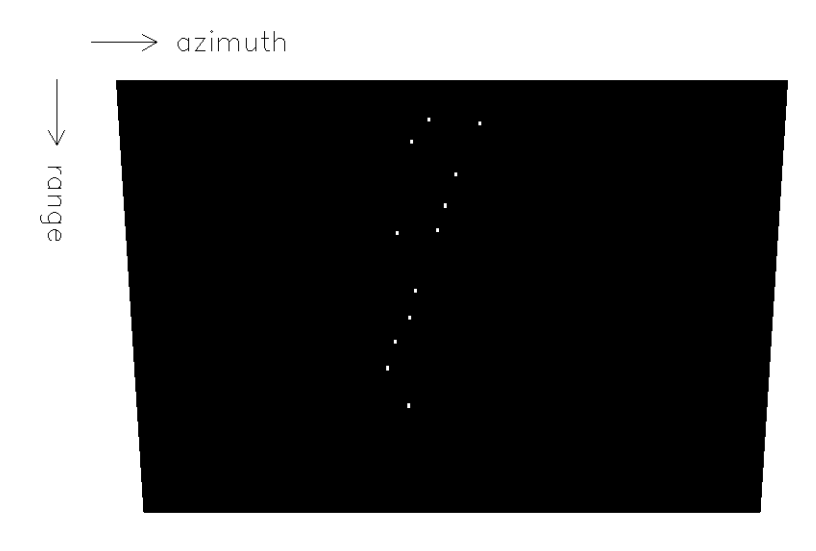


Fig. 71. Location of the twelve corner reflectors present in the scene.

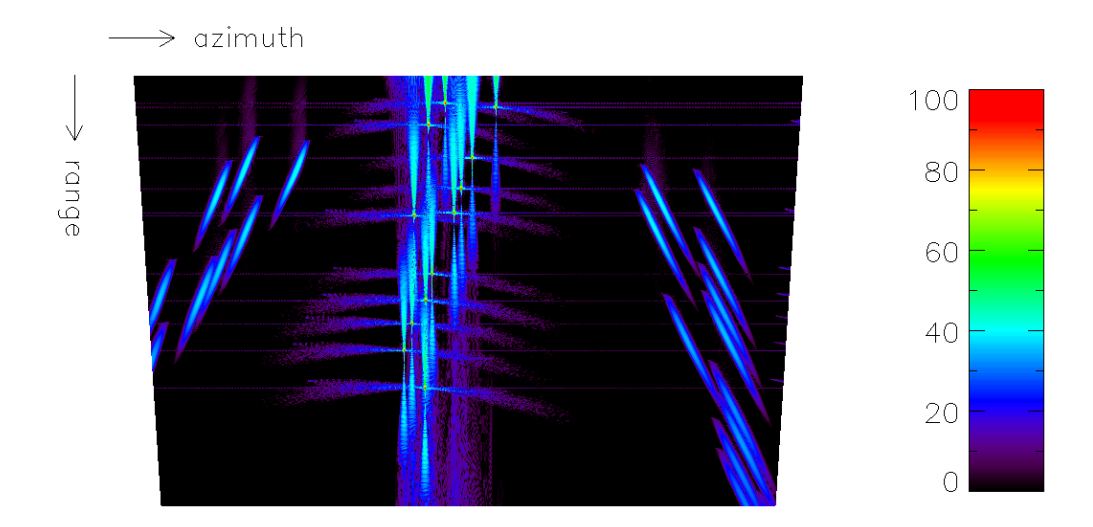


Fig. 72. Simulated focused image (log-intensity) assuming that only the twelve corner reflectors are present in the scene. Reference (decimated and upsampled) data.

From the simulated focused images the AASR can be evaluated as illustrated in Section 5.1, i.e., as difference of 2-D ISLRs. Table 8 displays the achieved AASR for different oversampling rates, sequences of PRIs, and interpolation methods. For the constant PRI example, an AASR = -33.9 dB is achieved. As apparent, the AASR gets significantly better as the oversampling increases and if BLU interpolation is used. The performance difference between BLU interpolation and two-point linear interpolation becomes significant for higher oversampling rates, as also apparent from the performance assessment on raw data (cf. Fig. 65). Moreover, the more elaborate sequence (sequence 2) leads to slightly better performance than the sequence with fast PRI change (sequence 1). In Section 6.1.1 a mean PRF on transmit  $PRF_{mean\ TX} = 600$  Hz has been selected for the F-SAR data set in order to have the same oversampling rate as in the L-band design example of Section 5.1 at near range. The AASR in the F-SAR case (-34.2 dB) is very similar to the AASR in the L-band design example (-33.6 dB at near range in Fig. 36 (g)). The slight difference is due to the different shapes of the azimuth antenna patterns.

The F-SAR processor also allows a fast analysis of the image quality through the automatic evaluation of some relevant parameters on the basis of corner reflectors present in the calibration site. The azimuth resolution is displayed in Fig. 76. As is apparent, using BLU interpolation, the azimuth resolution for staggered SAR is practically the same as for conventional SAR, while two-point linear interpolation leads to slight losses.

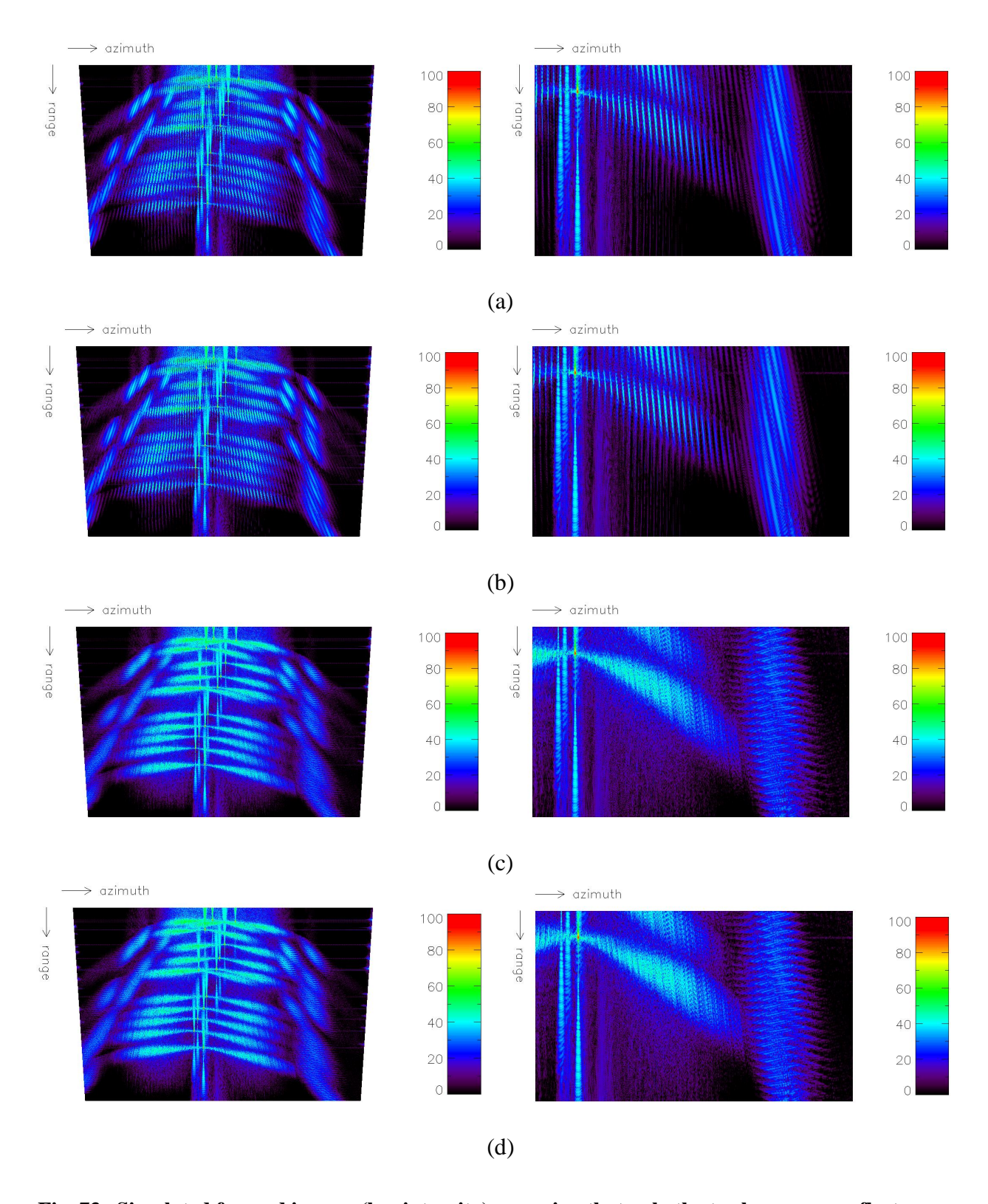


Fig. 73. Simulated focused images (log-intensity) assuming that only the twelve corner reflectors are present in the scene for a mean *PRF* on transmit of 360 Hz (low azimuth oversampling). The full images are shown on the left, while zooms containing the point scatterer on the lower right are shown on the right. (a) Sequence 1, two-point linear interpolation. (b) Sequence 1, BLU interpolation. (c) Sequence 2, two-point linear interpolation. (d) Sequence 2, BLU interpolation.

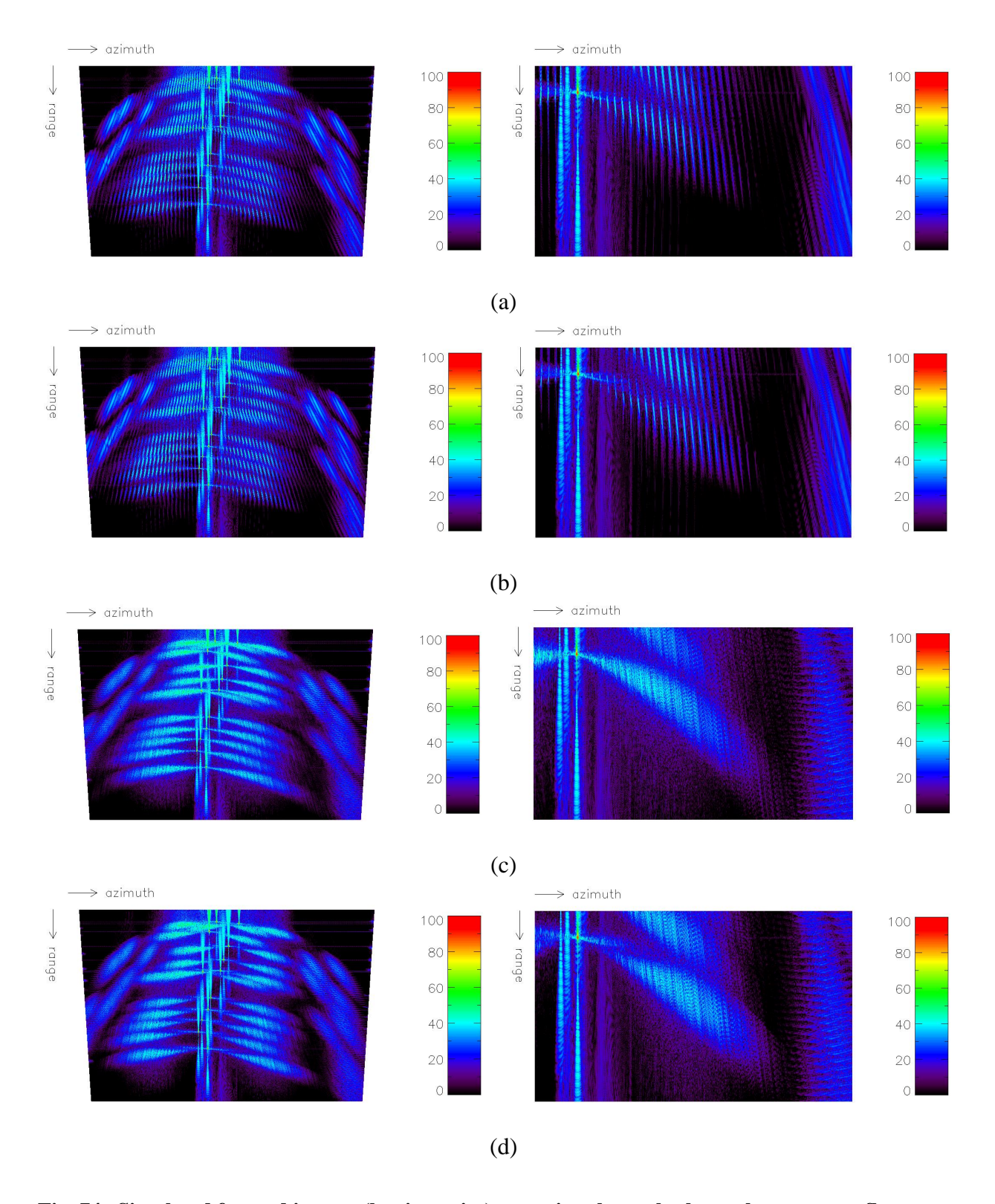


Fig. 74. Simulated focused images (log-intensity) assuming that only the twelve corner reflectors are present in the scene for a mean *PRF* on transmit of 450 Hz (medium azimuth oversampling). The full images are shown on the left, while zooms containing the point scatterer on the lower right are shown on the right. (a) Sequence 1, two-point linear interpolation. (b) Sequence 1, BLU interpolation. (c) Sequence 2, two-point linear interpolation. (d) Sequence 2, BLU interpolation.

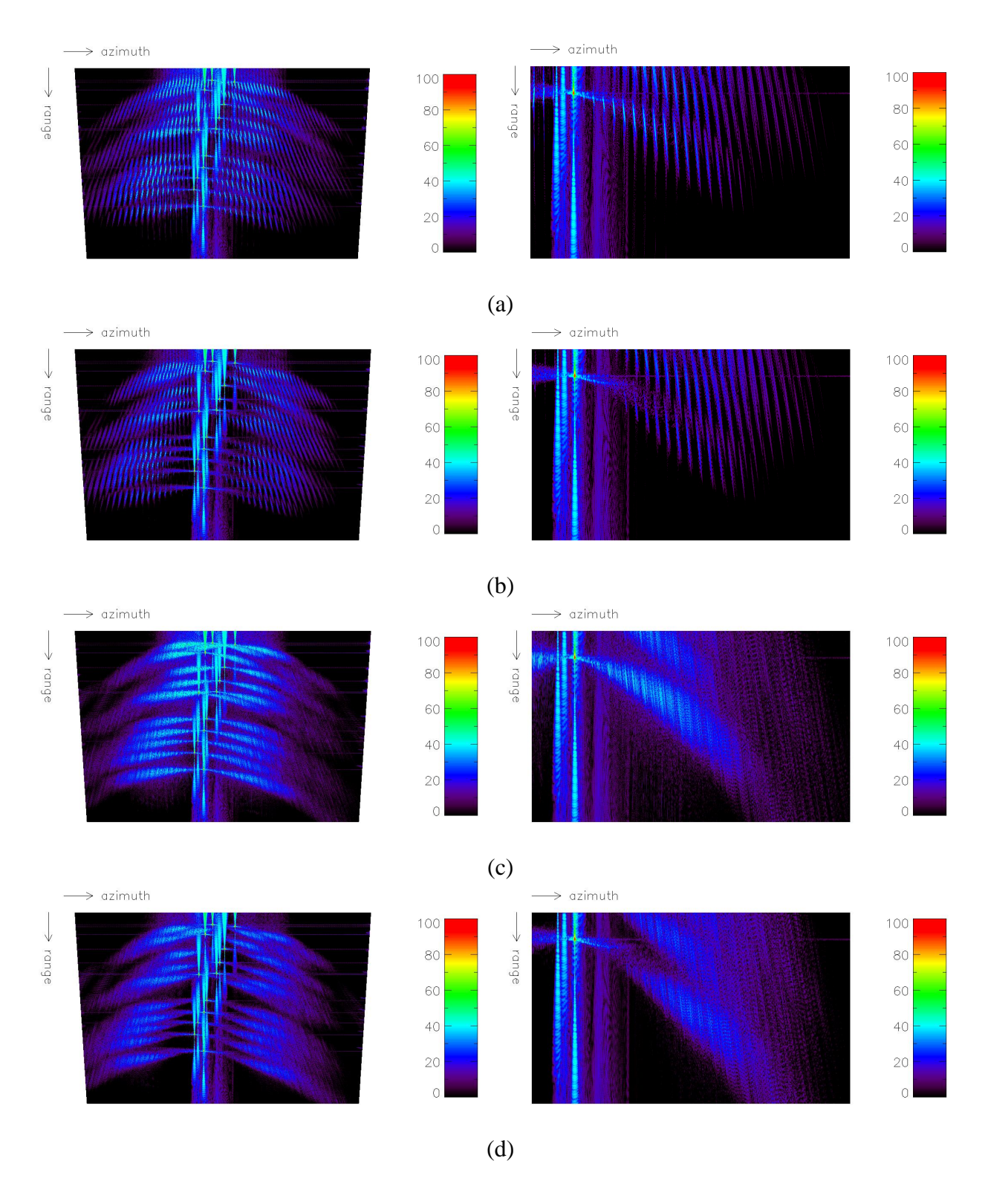


Fig. 75. Simulated focused images (log-intensity) assuming that only the twelve corner reflectors are present in the scene for a mean *PRF* on transmit of 600 Hz (high azimuth oversampling). The full images are shown on the left, while zooms containing the point scatterer on the lower right are shown on the right. (a) Sequence 1, two-point linear interpolation. (b) Sequence 1, BLU interpolation. (c) Sequence 2, two-point linear interpolation. (d) Sequence 2, BLU interpolation.

	Mean PRF on	Mean PRF on	Mean PRF on
	TX = 360 Hz	TX = 450 Hz	TX = 600 Hz
Sequence 1, 2-point	-16.9 dB	-20.6 dB	-25.6 dB
Sequence 1, BLU	-17.5 dB	-22.3 dB	-33.3 dB
Sequence 2, 2-point	-18.1 dB	-21.9 dB	-27.2 dB
Sequence 2, BLU	-18.7 dB	-23.4 dB	-34.2 dB

Table 8. AASR evaluated from F-SAR simulated focused data for different oversampling rates, sequences of PRIs, and interpolation methods.

The analysis of the azimuth resolution degradation is also important to better assess the effects of RCM and their implication on the two-dimensional signal reconstruction. In Section 4.3 a theoretical argument was put forward to establish that there are no effects related to the differential range curvature (all samples received from the same range have the same range curvature, as they are acquired in monostatic geometry) and that the relative range offset is negligible. As an uncompensated RCM implies resolution degradation, the fact that measurements on real data

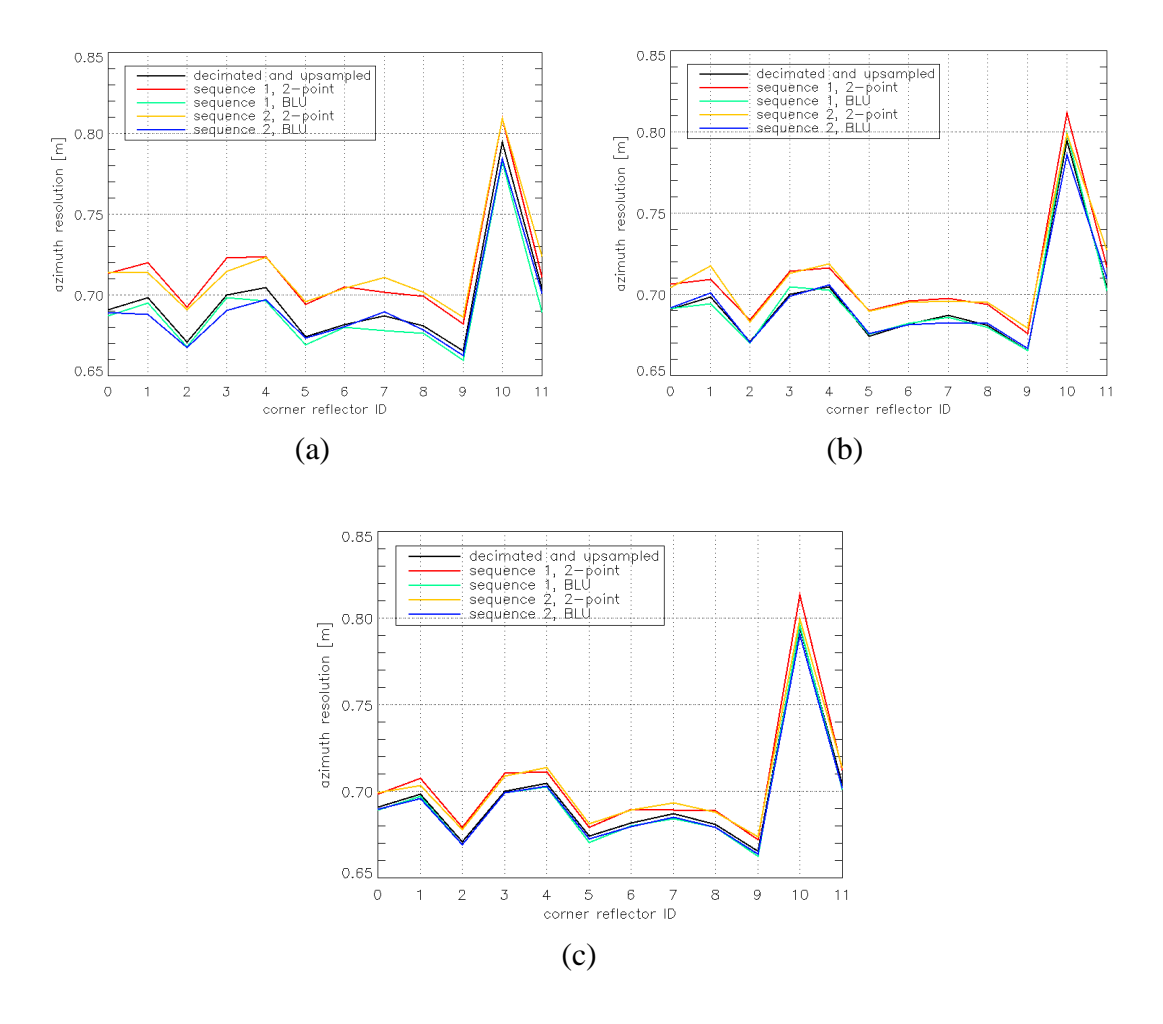


Fig. 76. Azimuth resolution evaluated on the twelve corner reflectors present in the calibration site. (a) Mean *PRF* on transmit of 360 Hz (low azimuth oversampling). (b) Mean *PRF* on transmit of 450 Hz (medium azimuth oversampling). (c) Mean *PRF* on transmit of 600 Hz (high azimuth oversampling).

show only negligible resolution degradation, especially if BLU interpolation is used, is a further proof that RCM effects are negligible.

Fig. 77 shows the *PSLR* as an alternative quality measure. The evaluation of the *PSLR* on real data is probably impaired by the clutter surrounding some of the corner reflectors. Nonetheless, *PSLR* measurements in simulated data suggest that the *PSLR* could even be better for staggered SAR data sets.

Finally, Fig. 78 shows the absolute phase of staggered SAR relative to the absolute phase of the reference evaluated on the twelve corner reflectors present in the calibration site. As is apparent, using BLU interpolation and at least a medium azimuth oversampling, the maximum displacement of the absolute phase with respect to the reference is of the order of few degrees.

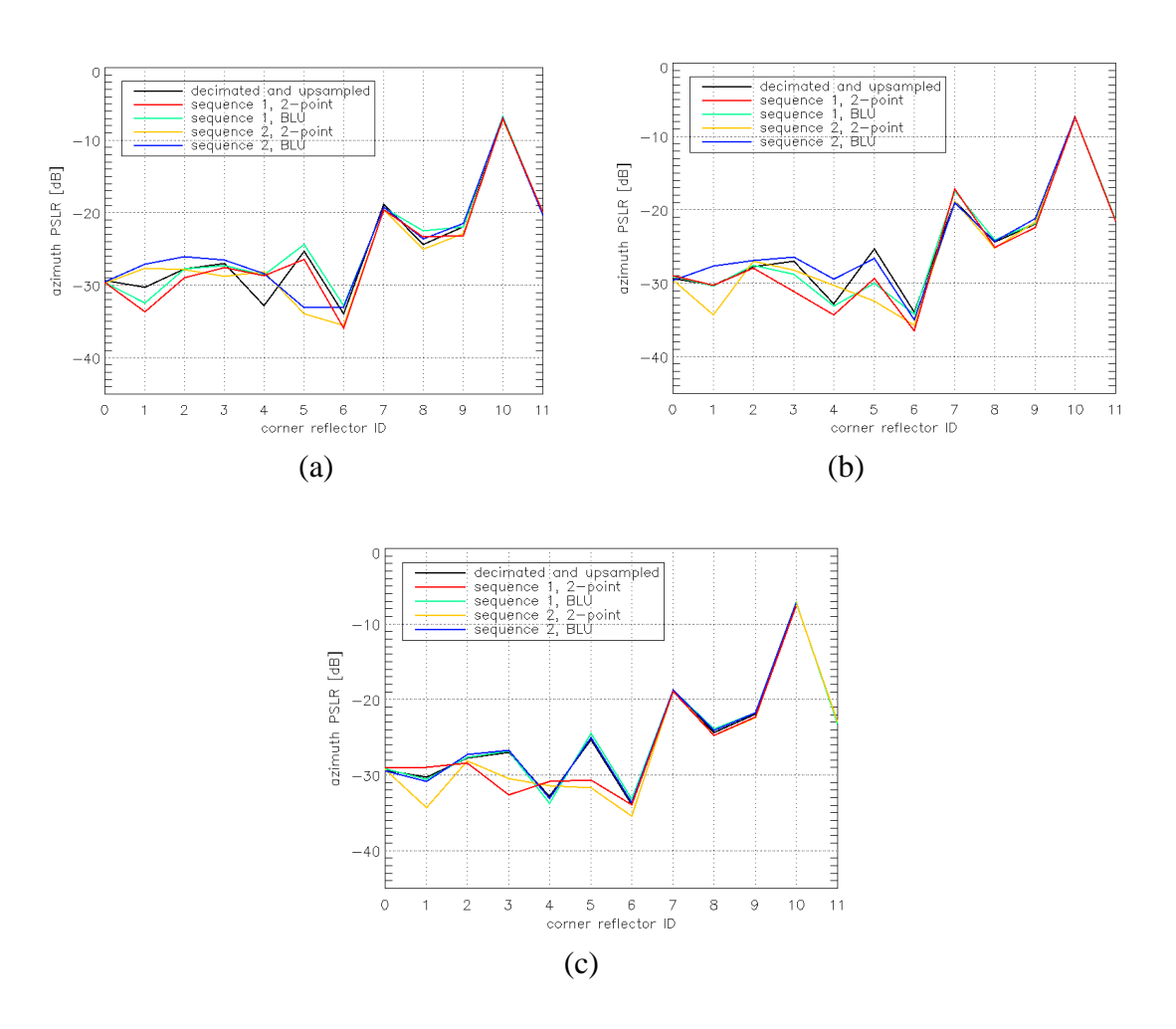


Fig. 77. Azimuth *PSLR* evaluated on the twelve corner reflectors present in the calibration site. (a) Mean *PRF* on transmit of 360 Hz (low azimuth oversampling). (b) Mean *PRF* on transmit of 450 Hz (medium azimuth oversampling). (c) Mean *PRF* on transmit of 600 Hz (high azimuth oversampling).

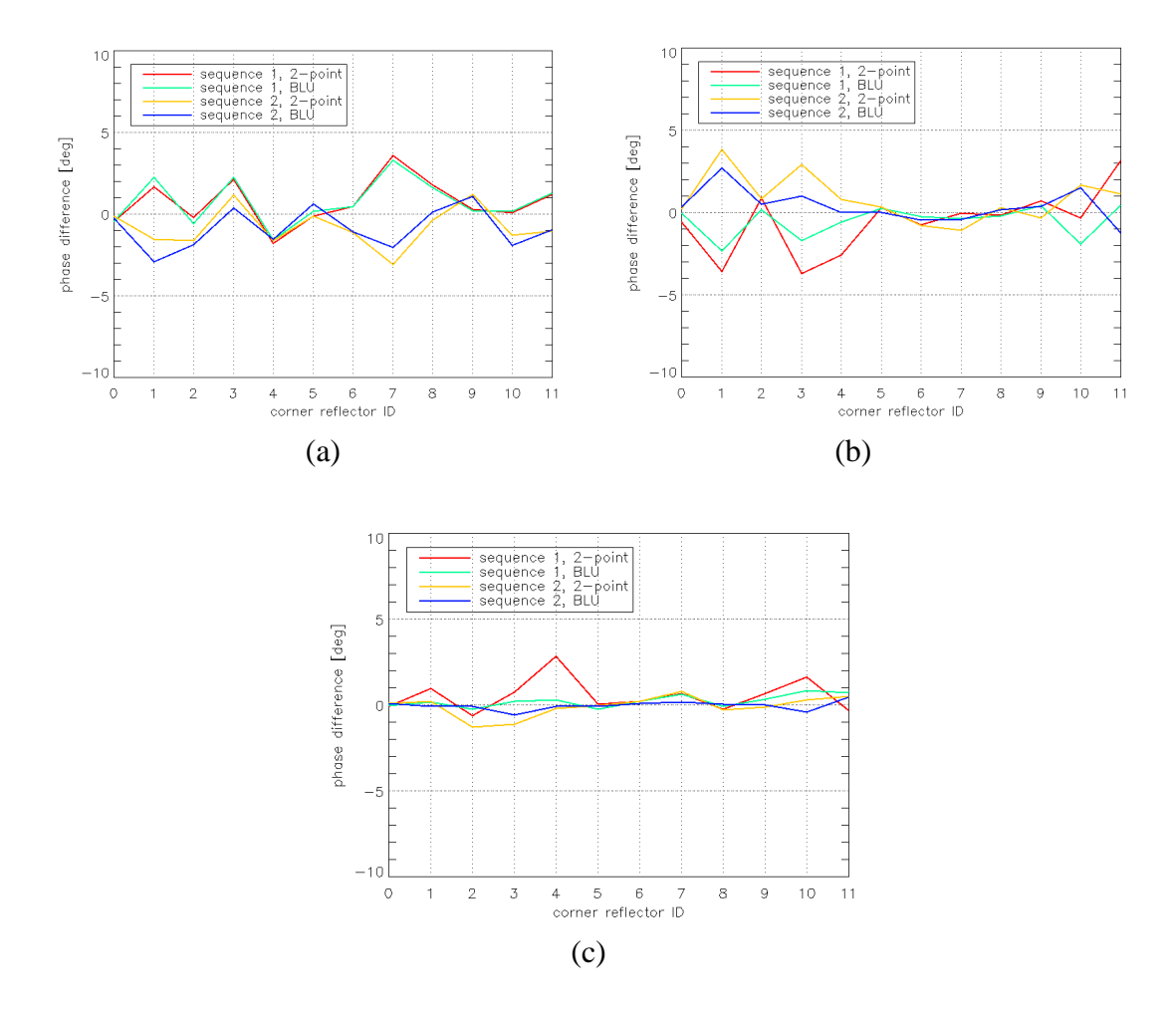


Fig. 78. Phase difference evaluated on the twelve corner reflectors present in the calibration site.
(a) Mean *PRF* on transmit of 360 Hz (low azimuth oversampling). (b) Mean *PRF* on transmit of 450 Hz (medium azimuth oversampling). (c) Mean *PRF* on transmit of 600 Hz (high azimuth oversampling).

# 6.2 TerraSAR-X Experiment

#### 6.2.1 Characteristics of TerraSAR-X and Experiment Definition

TerraSAR-X is a versatile SAR satellite with a large variety of acquisition modes (among which the stripmap, ScanSAR, and spotlight modes depicted in Fig. 12) and high operational flexibility. Since its launch on June 15, 2007, it serves the scientific community and users from the industrial sector and governmental institutions [30], [36], [37]. A nearly identical twin satellite, TanDEM-X, was launched on June 21, 2010 with the goal of generating a global digital elevation model (DEM) of the Earth's surface with unprecedented accuracy and resolution [31], [46].

Although TerraSAR-X is a conventional SAR system, such as the one described in Section 2, i.e., it cannot map simultaneously multiple subswaths using DBF on receive, it has 512 different *PRIs* available and can be commanded to transmit pulses according to a sequence of *M* distinct *PRIs*, which then repeat periodically, as described in Section 4.1, i.e., it can be operated in staggered SAR mode. TerraSAR-X provides therefore a unique opportunity to demonstrate the staggered SAR concept, although without the simultaneous mapping of multiple swaths.

The lake Constance, situated in Germany, Switzerland, and Austria, has been chosen as test site for the demonstration. A lake, surrounded by cities, is the ideal site to observe the effect of azimuth ambiguities, which are peculiar in staggered SAR: The azimuth ambiguities of the strong scatterers present in the urban areas, in fact, will be well visible in the water, characterized by much lower backscatter. Moreover, the size of lake Constance (maximum width of 14 km) is well suited to observe the azimuth ambiguities in the TerraSAR-X case: While from the impulse response of Fig. 34, relative to a L-band design example, it might seem that a 80 km extension in the azimuth direction is needed, in this case, due to the much lower wavelength at X-band, a much smaller azimuth extension is needed, as the azimuth displacement of azimuth ambiguities is proportional to the wavelength, as apparent in (24). Fig. 79 shows the test site; the red rectangle delimits the area, where data have been acquired.

In order to reduce the effect of range ambiguities a steep incidence angle has been selected for the experimental acquisition (cf. *RASR* plots in Section 5, where the performance is much better at near range rather than at mid- or far range), while an untapered elevation beam, usually employed in spotlight acquisitions, has been chosen to achieve a better *NESZ* (-26.5 dB at the center of the swath) at the expense of reducing the imaged swath.

A sequence of PRIs has then to be selected. In this case, the PRIs to be employed have to be chosen among the 512 available PRIs of TerraSAR-X. These PRIs span between PRI = 0.149 ms

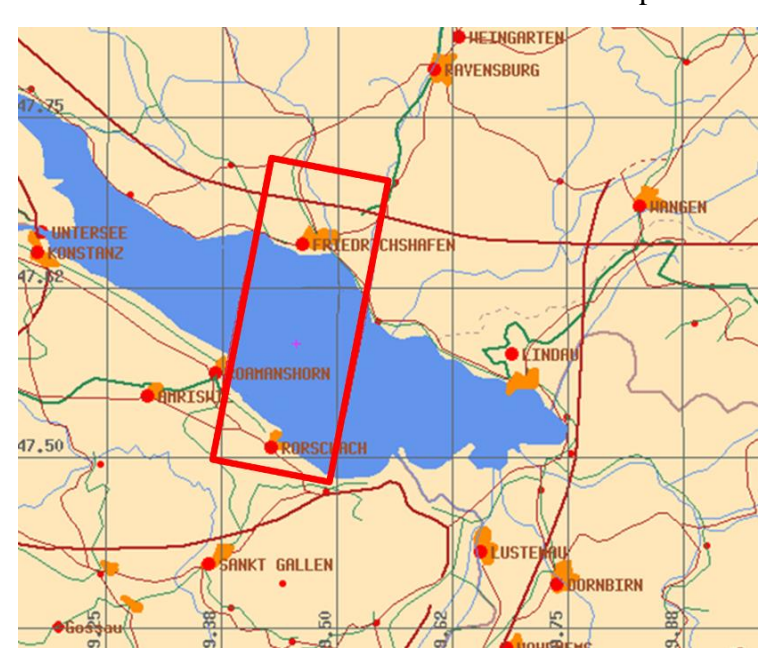


Fig. 79. The lake Constance test site for the TerraSAR-X staggered SAR demonstration. The red rectangle delimits the area, where data have been acquired.

(corresponding to a PRF = 6708 Hz) and PRI = 0.5 ms (corresponding to a PRF = 2000 Hz), the minimum difference between two PRIs is  $\Delta PRI_{\min} = 0.291$  µs, and the difference between two arbitrary PRIs is always an integer multiple of  $\Delta PRI_{\min}$ . In particular, there are two intervals, where the PRIs are uniformly spaced at  $\Delta PRI_{\min}$ , namely:

- There are 83 PRIs uniformly spaced at  $\Delta PRI_{min}$  in the interval comprised between 0.149 ms and 0.172 ms (corresponding to PRFs between 6708 Hz and 5814 Hz), from now on referred to as interval 1;
- There are 364 *PRIs* uniformly spaced at Δ*PRI*<sub>min</sub> in the interval comprised between 0.217 ms and 0.322 ms (corresponding to *PRFs* between 4608 Hz and 3106 Hz), from now on referred to as interval 2.

The minimum difference between two PRIs  $\Delta PRI_{min}$  is not small enough to design sequences with slow PRI change (which lead anyway to poor performance, as shown in Section 5.2.1) or more elaborated sequences. However, the quite dense and uniform distribution of PRIs in the aforementioned intervals is well suited to design sequences with fast PRI change. As the Doppler bandwidth of TerraSAR-X (of the order of 3200 Hz, using (20) with L = 4.8 m and  $v_S = 7675$  m/s) is approximately four times larger than that of the L-band design example of Section 5 (ranging between 750 Hz at mid-range to 850 Hz at near range), the interval 1, i.e., the one with smaller PRIs (higher PRFs), allows a higher oversampling rate (although not as high as in the L-band design example of Section 5) and is therefore to be preferred.

The formulas provided in Section 4.2 can be useful to select a sequence of PRIs, where two consecutive azimuth samples are never missing. Assuming  $PRI_0 = 0.172$  ms, i.e., the largest PRI of the interval 1,  $R_{0\text{min}} = 550$  km, and  $R_{0\text{max}} = 577.2$  km (minimum and maximum slant range for the analysis), we have to fix a value for the pulse length  $\tau$ , compute  $k^*$  using (49), and  $\Delta_{\min}$  using (47). Then  $\Delta$  has to be chosen as the smaller integer multiple of  $\Delta PRI_{\min}$  larger than  $\Delta_{\min}$ ,  $k^*$  has to be recomputed using (50) and M has then to be computed using (52). In this way, a sequence of PRIs is obtained, where two consecutive samples are never missed within the swath of interest. If the smallest PRI of the obtained sequence is smaller than the smallest PRI of the interval 1, i.e., 0.149 ms, a smaller value for the pulse length  $\tau$  has to be chosen and the procedure has to be repeated until a minimum PRI equal or larger than 0.149 ms is obtained. As an example, if a pulse length  $\tau = 10$   $\mu$ s is fixed, we obtain  $k^* = 23$ ,  $\Delta_{\min} = 0.145$  ms < 0.149 ms. If a pulse length  $\tau = 6.5$   $\mu$ s is fixed, we obtain  $k^* = 22$ ,  $\Delta_{\min} = 0.290$   $\mu$ s,  $\Delta = 0.291$   $\mu$ s =  $\Delta PRI_{\min}$ , recomputed  $k^* = 22$ , M = 45, and  $PRI_{\min} = 0.159$  ms > 0.149 ms. A larger M can be also used, as apparent in (52), therefore all 83 PRIs of the interval 1 are used, in order to achieve a larger oversampling rate.

Fig. 80 shows for such a sequence the PRI trend, the location of missing samples in the raw data, the percentage of missing samples and the maximum, mean and minimum pulse separation, while the other system parameters used in the simulation are listed in Table 9. Fig. 81 depicts the 2-D IRF and the 1-D IRF obtained by simulation for a slant range  $R_0 = 560$  km. As is apparent from the sidelobes of the IRF, very good performance is expected. The AASR, evaluated as difference of ISLRs, is for this slant range equal to -31.6 dB.

Parameter	Value	
Radar wavelength	0.0311 m (X-band)	
Wave polarization	НН	
Orbit height	520 km	
Minimum slant range	550 km	
Maximum slant range	577.2 km	
Antenna type	Planar	
Antenna size	$4.8 \text{ m (length)} \times 0.8 \text{ m (height)}$	
Chirp bandwidth	100 MHz	
Range sampling frequency	110 MHz	
Sequence of <i>PRIs</i>	Sequence with fast PRI change	
Resampling method	BLU on raw data (after range	
	compression)	
PBW	2800 Hz	
Azimuth processing window	Generalized Hamming with $\alpha = 0.6$	
Compensation of the azimuth pattern	Yes	
Range processing window	Generalized Hamming with $\alpha = 0.6$	

Table 9. System and processing parameters for the staggered SAR TerraSAR-X experiment. The minimum and maximum slant ranges refer to the selected beam.

The sequence of Fig. 80 would lead to excellent performance in terms of azimuth ambiguities, but, due to a system limitation of TerraSAR-X, an acquisition with such a sequence of *PRIs* is unfortunately not possible. The pulse length in TerraSAR-X, in fact, has to be equal or larger than 15  $\mu$ s. Moreover, two time guards between receive and transmit and transmit and receive, equal to 5.2  $\mu$ s and 3.271  $\mu$ s, respectively, have to be considered. This means that the minimum value of  $\tau$  to be used for the design of a sequence of *PRIs* according to the criteria of Section 4.2 is equal to 23.271  $\mu$ s.

While it is not possible to choose a sequence of PRIs in the interval 1, such that two consecutive azimuth samples are never missed and the pulse length is equal or larger than the minimum required one, it is possible to choose such a sequence, using larger PRIs, most of them included in the interval 2, e.g., choosing  $PRI_{max} = 0.335$  ms,  $\Delta = 4.08 \, \mu s = 14 \times \Delta PRI_{min}$ , and M = 28. The maximum value of  $\tau$  (including guards), which can be used for this sequence, is 46.9  $\mu s$ , therefore larger than the minimum required one. Fig. 82 shows the PRI trend, the location of missing samples in the raw data, the percentage of missing samples and the maximum, mean and minimum pulse separation, for this sequence. Fig. 83 depicts the 2-D IRF and the 1-D IRF obtained by simulation for a slant range  $R_0 = 560$  km, always assuming the system parameters of Table 9. Due to the non-sufficient azimuth oversampling (the mean PRF on transmit is here 3570 Hz for a Doppler bandwidth of 3200 Hz, while in the L-band design example of Section 5.1 a mean PRF on transmit of 2700 Hz was employed for a Doppler bandwidth comprised between 750 and 850 Hz), bad performance is achieved (cf. high sidelobes in Fig. 83). The AASR, evaluated as difference of ISLRs, is for this slant range equal to -9.1 dB.

Although the expected performance is not good, the experiment has been nevertheless performed, in order to compare the real data with the expected performance.

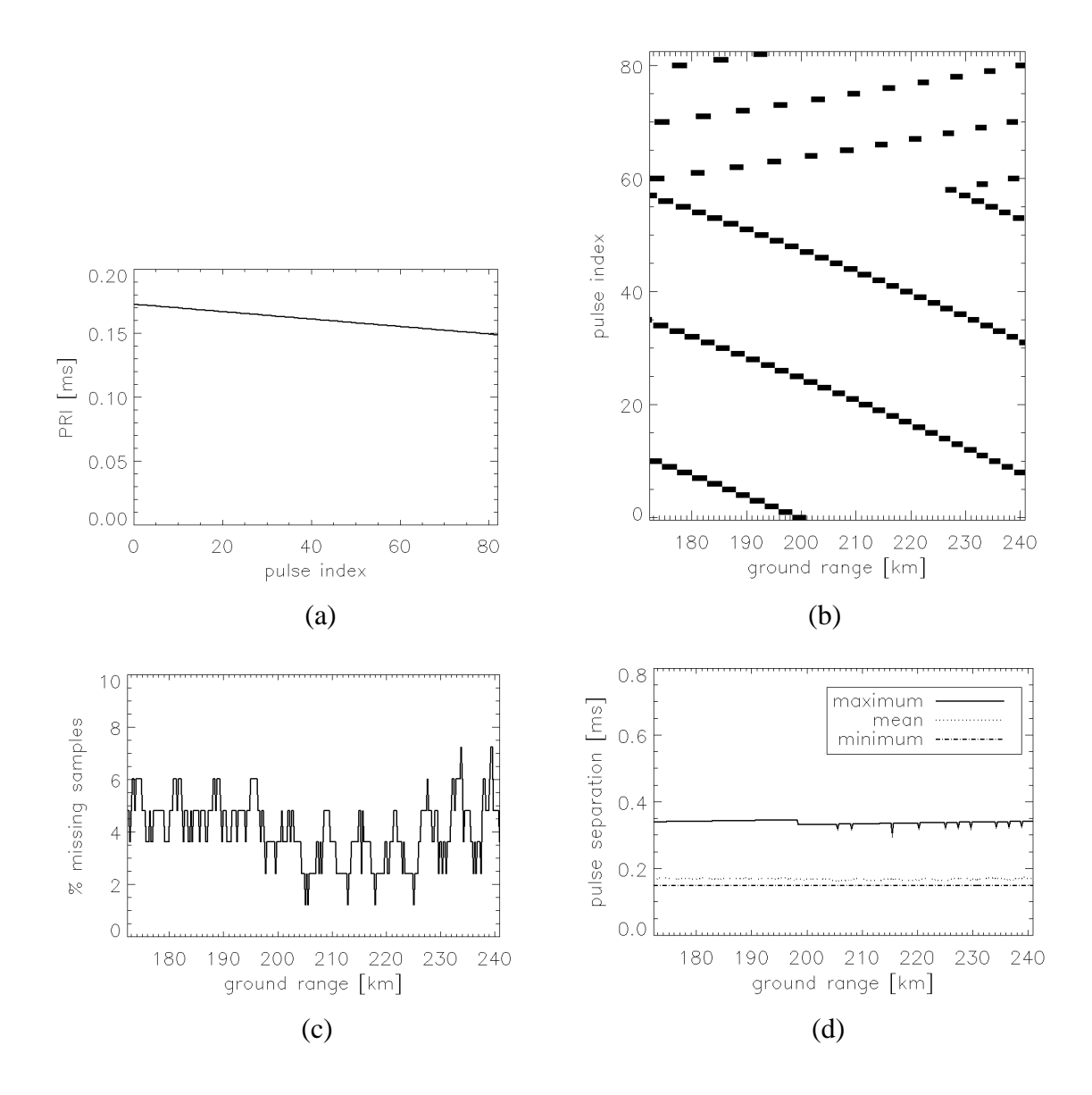


Fig. 80. Ideal sequence with fast *PRI* change to be used for the TerraSAR-X staggered SAR experiment ( $PRI_{max} = 0.172$  ms,  $R_{0min} = 550$  km,  $R_{0max} = 577.2$  km,  $\tau = 6.5$   $\mu$ s). (a) *PRI* trend. (b) Location of missing samples in the raw data. (c) Percentage of missing samples in the raw data versus ground range. (d) Maximum, mean and minimum pulse separation versus ground range.

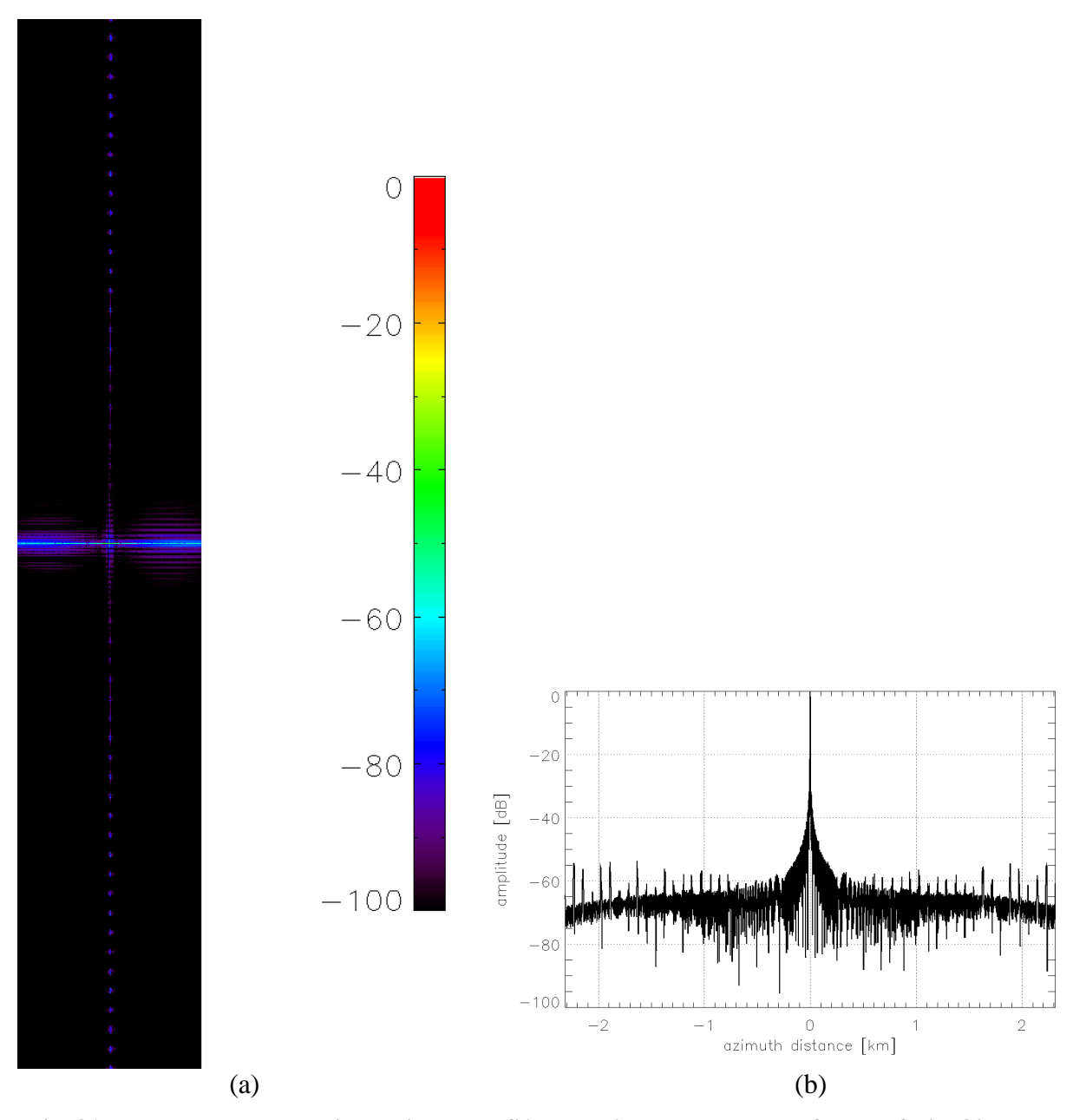


Fig. 81. Expected IRFs obtained with TerraSAR-X using the sequence of *PRIs* of Fig. 80 and the system parameters of Table 9. (a) 2-D IRF obtained by 2-D simulation. The horizontal and vertical axes represent slant range (1.4 km) and azimuth (4.6 km), respectively. (b) 1-D IRF obtained by 1-D simulation.

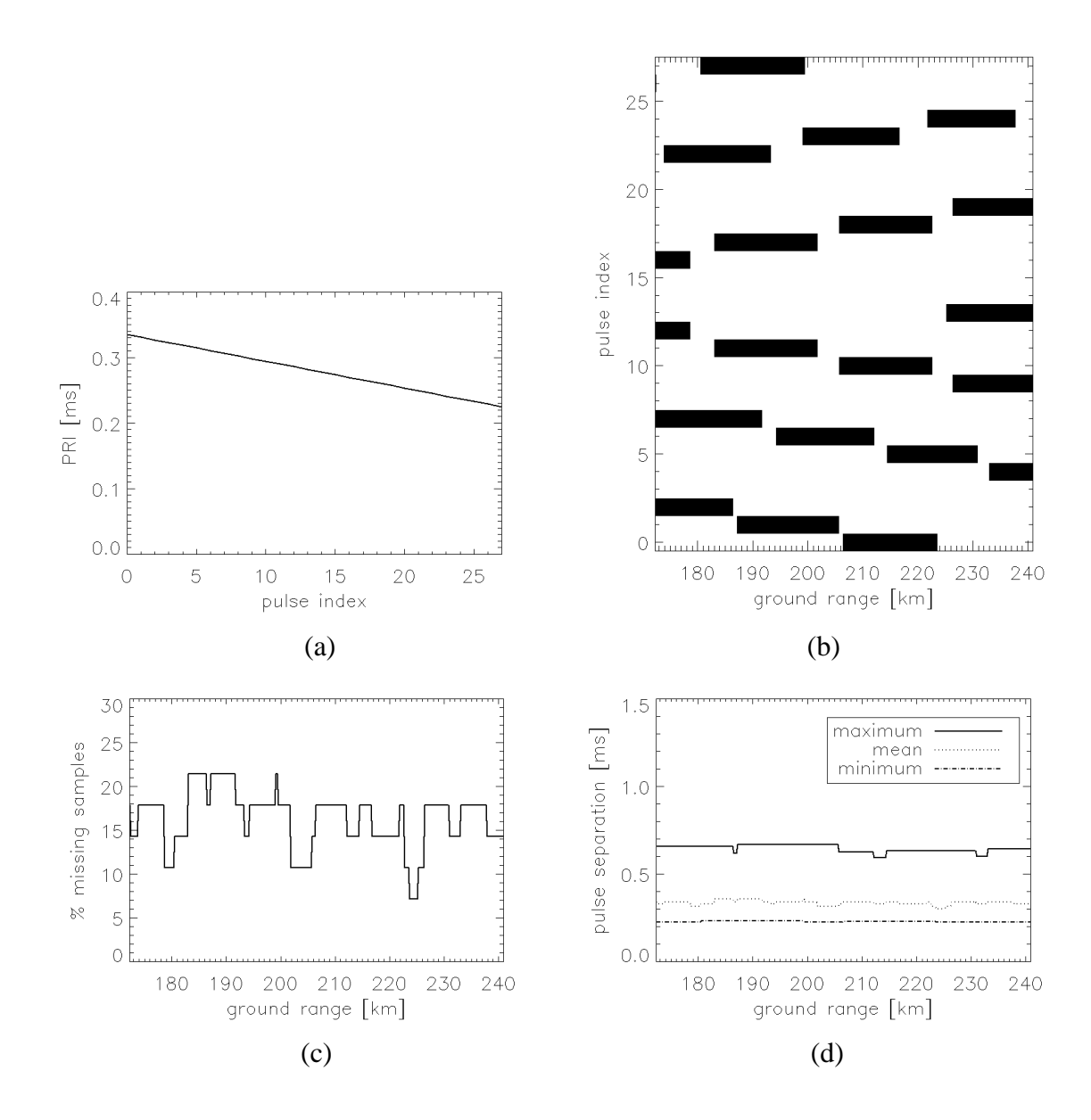


Fig. 82. Actual sequence with fast *PRI* change used for the TerraSAR-X staggered SAR experiment ( $PRI_{max} = 0.335 \text{ ms}$ ,  $R_{0min} = 550 \text{ km}$ ,  $R_{0max} = 577.2 \text{ km}$ ,  $\tau$  (including guards) = 46.9  $\mu$ s). (a) *PRI* trend. (b) Location of missing samples in the raw data. (c) Percentage of missing samples in the raw data versus ground range. (d) Maximum, mean and minimum pulse separation versus ground range.

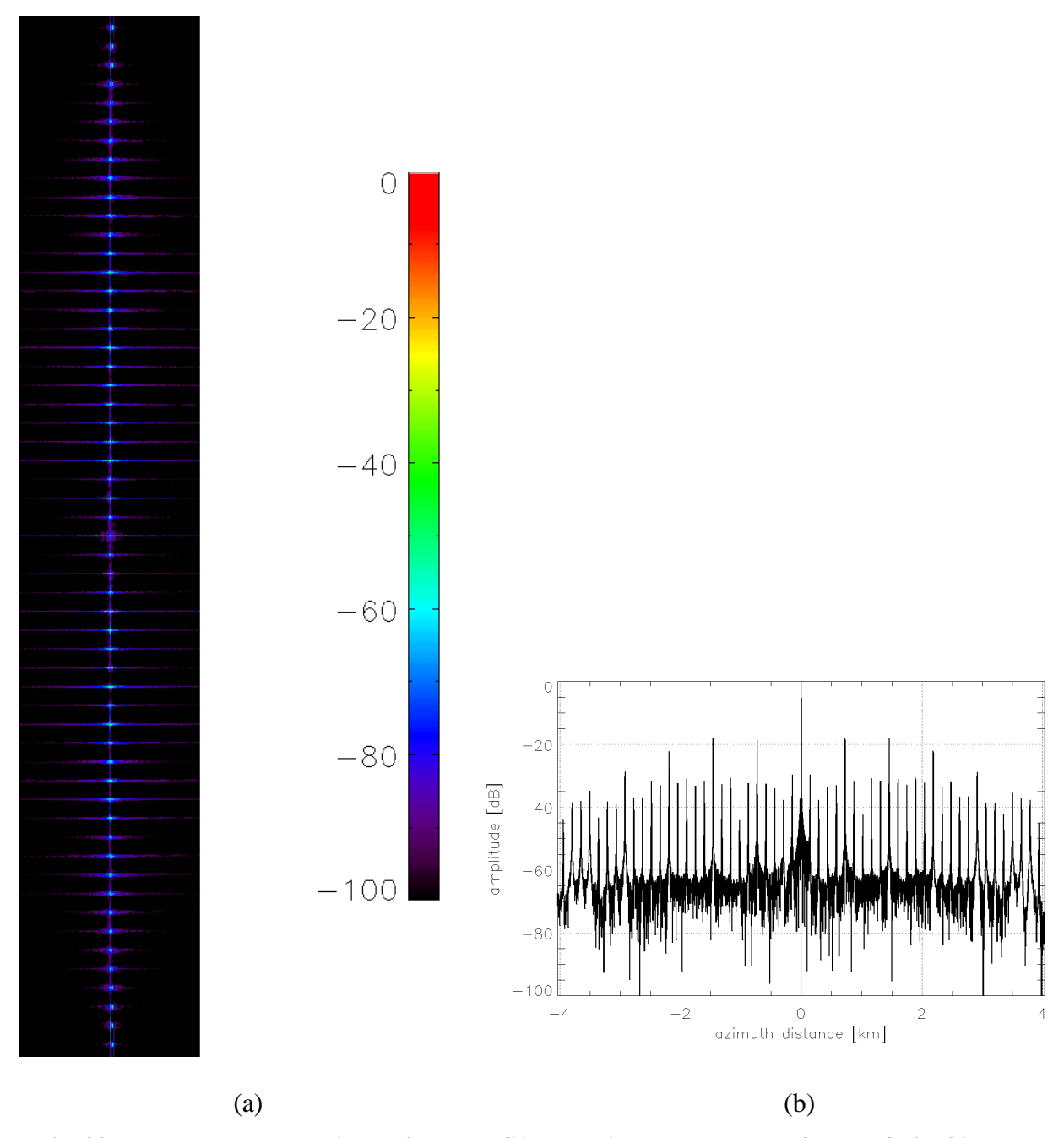


Fig. 83. Expected IRFs obtained with TerraSAR-X using the sequence of *PRIs* of Fig. 82 and the system parameters of Table 9. (a) 2-D IRF obtained by 2-D simulation. The horizontal and vertical axes represent slant range (1.4 km) and azimuth (8 km), respectively. (b) 1-D IRF obtained by 1-D simulation.

#### 6.2.2 TerraSAR-X Data Processing and Analysis of the Results

The TerraSAR-X staggered SAR acquisition over the Lake Constance has been performed on January 6, 2014.

The echoes, received by the radar between consecutive transmitted pulses, have different duration, as M = 28 different (decreasing) PRIs are employed. Fig. 84 (a) displays 100 consecutive received echoes, where the decreasing length of the radar echoes over a cycle of 28 transmitted pulses is visible. Unlike in a SAR with constant PRI, the first samples of the received echoes correspond in a staggered SAR system to different slant ranges. Those echoes have to be therefore rearranged in a two-dimensional matrix with coordinates slant range and azimuth, associating each sample of the radar echo to the corresponding transmitted pulse. Fig. 84 (b) shows the rearranged echoes, i.e., 100 range lines of the raw data, where the backscatter variation associated to the antenna pattern in elevation is visible. Missing samples are visible as well and their pattern over one cycle (highlighted by a red rectangle in Fig. 84 (b)) can be compared to the diagram of missing pulses of Fig. 82 (b).

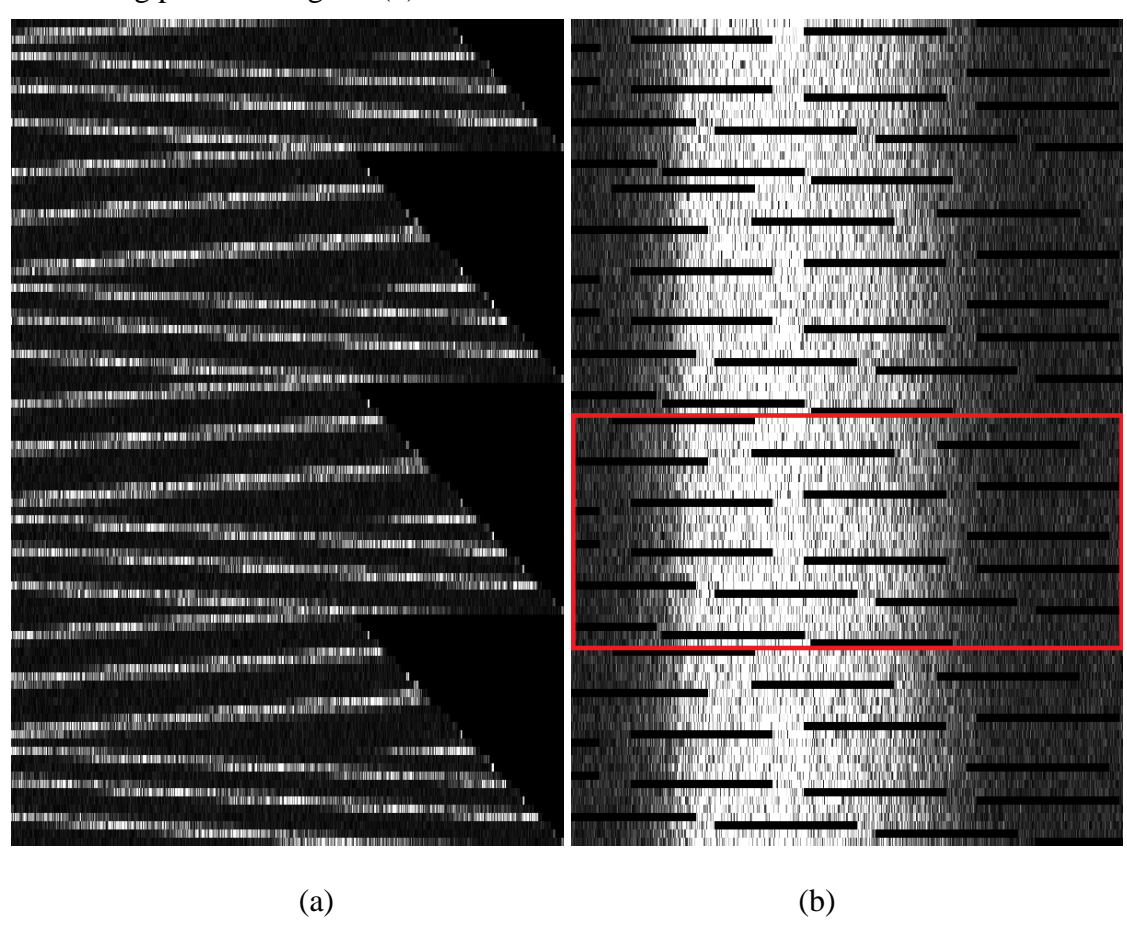


Fig. 84. (a) 100 consecutive received echoes (corresponding to 100 consecutive pulses). The horizontal axis represents slant range. (b) Rearranged echoes (i.e., 100 range lines of the raw data). The horizontal and vertical axes represent slant range (27.2 km) and azimuth (0.2 km), respectively. One cycle is highlighted with a red rectangle, so that it can be compared to the diagram of missing pulses of Fig. 82 (b).

Raw data with gaps have to be then resampled to a uniformly spaced grid. Fig. 85 shows 100 range lines of the resampled data, obtained using both two-point linear interpolation (Fig. 85 (a)) and BLU interpolation (Fig. 85 (b)). It can be noticed that for BLU interpolation, some of the areas where samples are missing are still dark. This is due to the non-sufficient azimuth oversampling rate and is more visible for the missing samples at the beginning of the sequence, where the distances to the preceding and succeeding azimuth samples are larger. If the neighbouring samples are weakly correlated to the sample to be estimated, BLU interpolation associates to these neighbouring samples low weights and the complex outcome of the estimate is likely to be characterised by lower amplitude. In the extreme case, where there are no correlated samples, the outcome of the estimation is zero. Two-point linear interpolation, in contrast, tends to keep the amplitude, as apparent in Fig. 85 (a), but the phase of the signal is likely to be wrongly estimated and this will result in a bad image quality of the focused SAR image.

The resampled staggered SAR raw data can be then focused with a conventional SAR processor. Fig. 86 shows the focused data obtained using the experimental TanDEM-X interferometric processor (TAXI) [120] and the data resampled using BLU interpolation. A zoom of the strongest scatterer in the scene, highlighted by a red rectangle in Fig. 86, is provided in Fig. 87

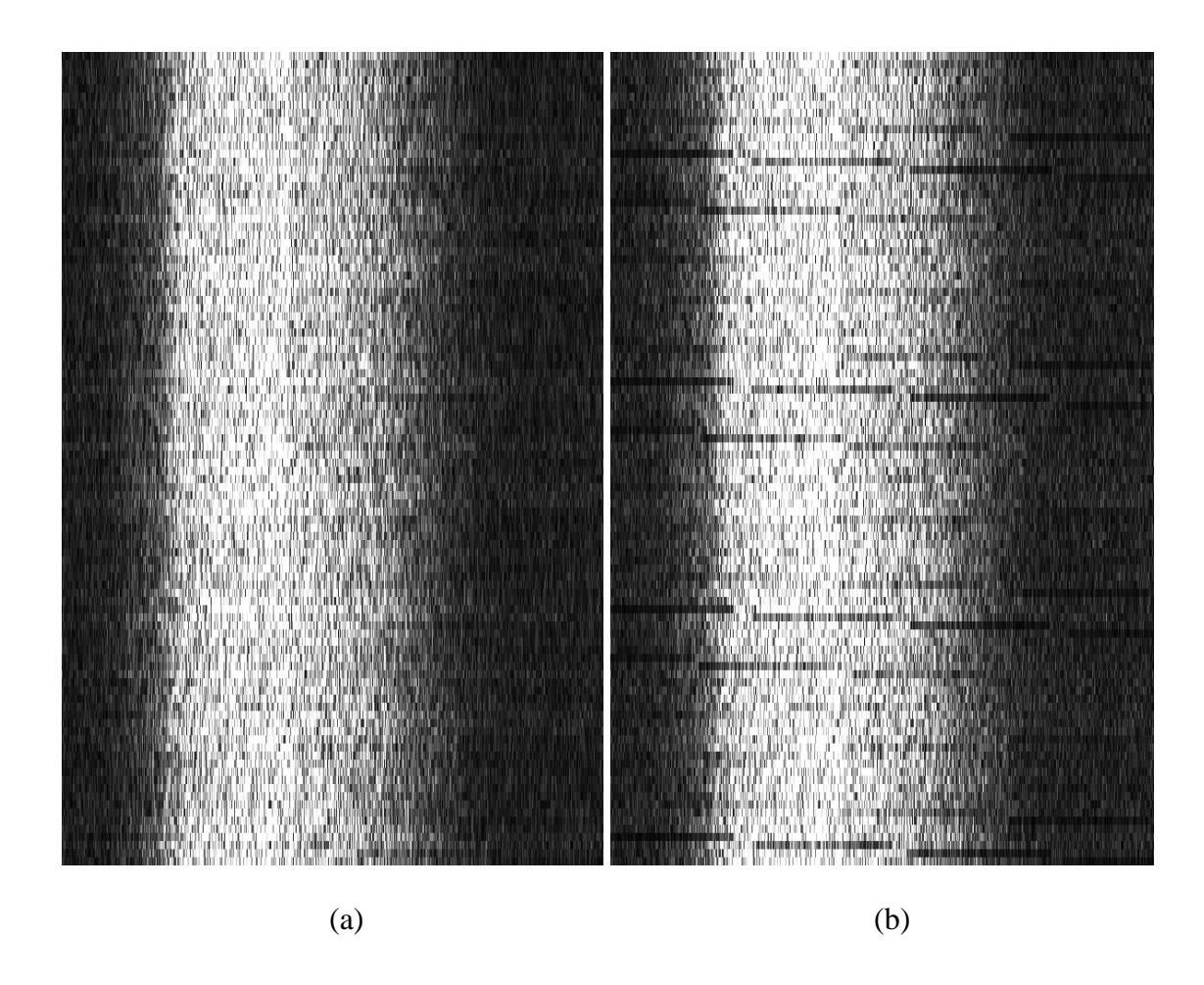


Fig. 85. Resampled data (100 range lines). (a) Using two-point linear interpolation. (b) Using BLU interpolation. The horizontal and vertical axes represent slant range (27.2 km) and azimuth (0.2 km), respectively.

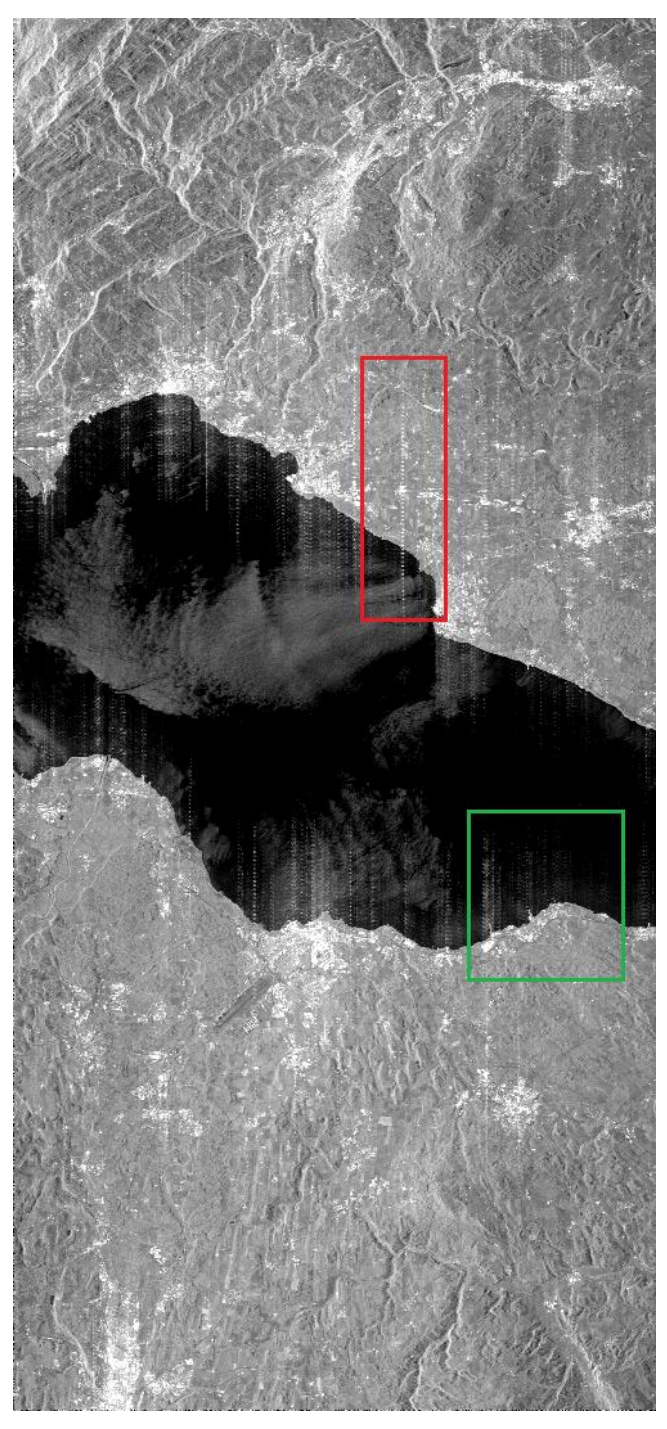


Fig. 86. Focused image, acquired by TerraSAR-X over the Lake Constance in staggered SAR mode. The horizontal and vertical axes represent slant range (9.5 km) and azimuth (49.1 km), respectively. Data are displayed in dB using a 20 dB dynamic scale. The red rectangle highlights the strongest scatterer in the scene and its sidelobes, while the green rectangle highlights a part of the image used to show how the image would look like, if the ideal sequence of Fig. 80 were used.

using a 50 dB-log-intensity scale for data resampled using both two-point linear interpolation and BLU interpolation. There are no visible differences between the two interpolation methods in this case. The same sidelobe structure as in the 2-D IRF of Fig. 83 (a) can be observed.

Fig. 88 shows two azimuth profiles obtained integrating the energy of the zoomed areas of Fig. 87 over slant range, relative to the resampled data obtained using two point linear interpolation and BLU interpolation, respectively. The azimuth profile of Fig. 88 (b) can be compared to the 1-D IRFs of Fig. 83 (b), taking into account that the azimuth profiles of Fig. 88 also include the energy of the background. From a visual comparison, it can be observed that the level of the azimuth sidelobes is in the real data corresponding to a strong scatterer comparable to the expected IRF obtained from simulation.

Although the sidelobe level is pretty high, due to a system limitation which only allowed the execution of the experiment with non-optimal parameters, measurements on real data are in good agreement with the expected performance from simulation.

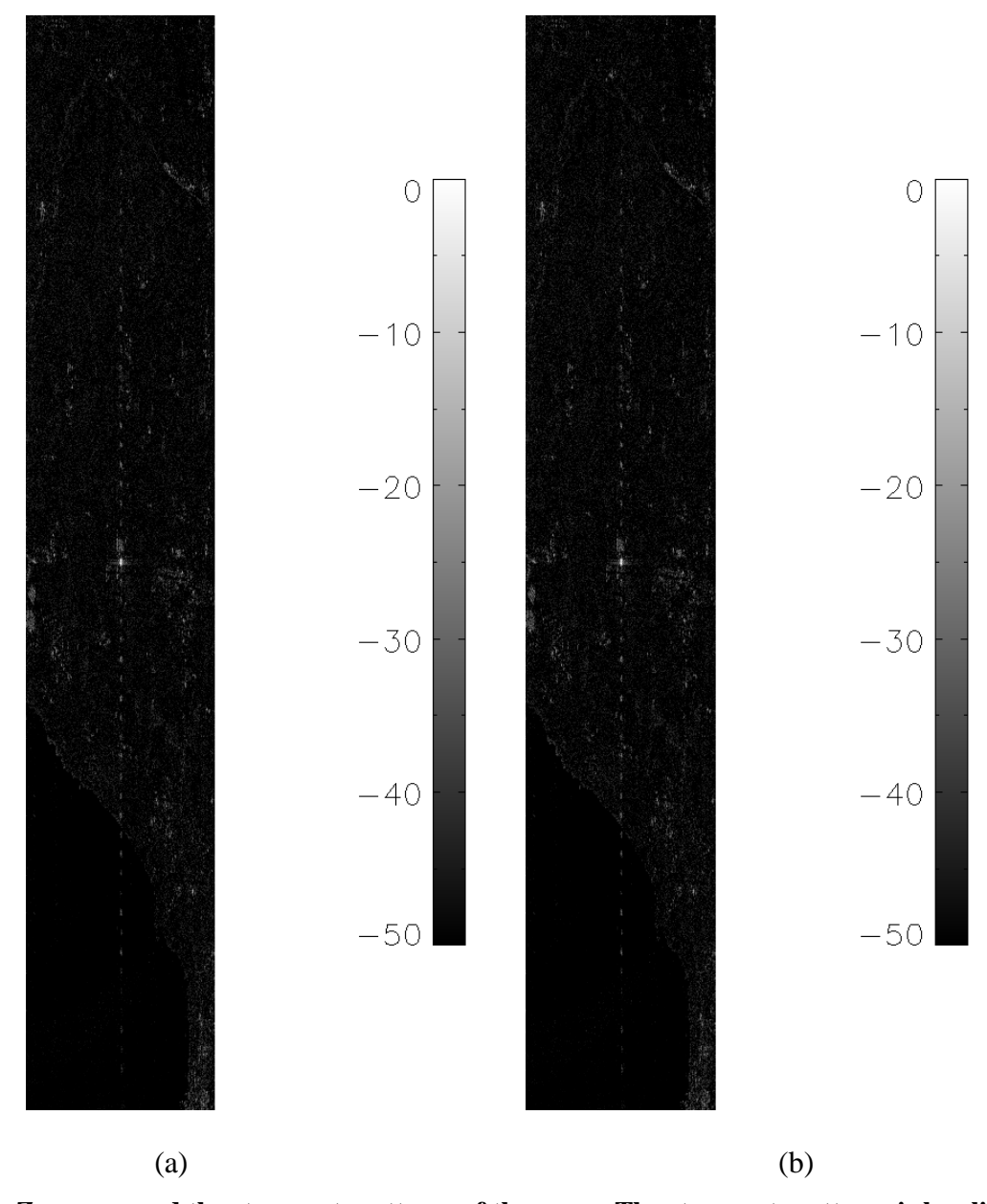


Fig. 87. Zoom around the strongest scatterer of the scene. The strongest scatterer is localized at the center of the displayed area. (a) Using two-point linear interpolation. (b) Using BLU interpolation. The horizontal and vertical axes represent slant range (1.4 km) and azimuth (8 km), respectively.

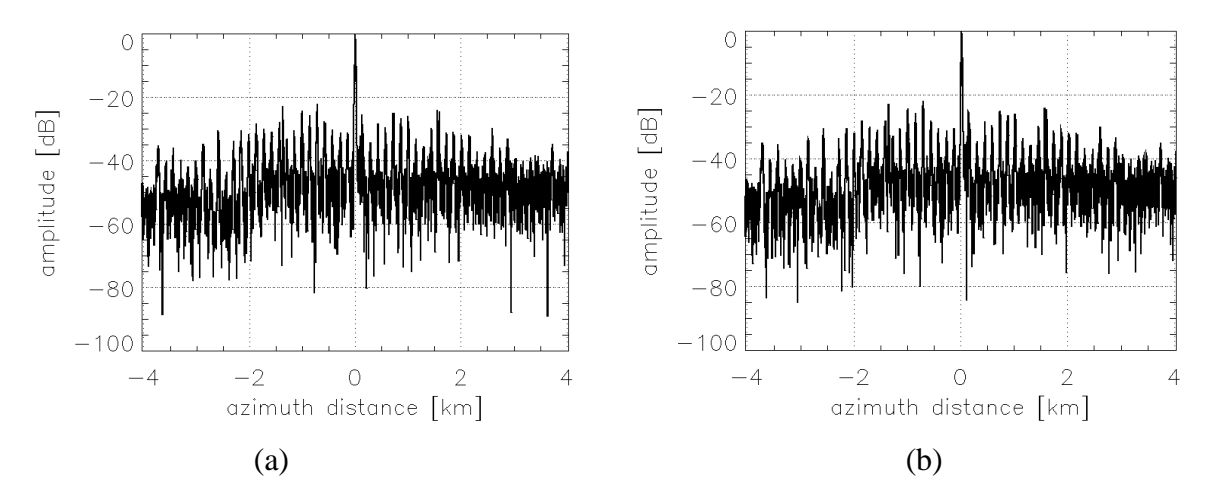


Fig. 88. Azimuth profiles obtained by integrating the energy of the zoomed areas of Fig. 87 over slant range. (a) Using two-point linear interpolation. (b) Using BLU interpolation. This azimuth profile can be compared to the 1-D IRFs of Fig. 83 (b).

In order to give the reader a feeling of how staggered SAR data acquired over the Lake Constance would look, if the ideal sequence of Fig. 80 were used, a simulated image for this case has been generated starting from uniform *PRI* SAR data, acquired over the same test site. Fig. 89 shows a portion of the focused image of Fig. 86 (namely the area highlighted by the green rectangle) and a simulated image as it would be obtained with the ideal sequence, generated by means of convolution of the uniform *PRI* SAR data (assumed ambiguity-free) and the expected 2-D impulse response. As is apparent, the sidelobes are very low and not visible, if the image is displayed in dB using a typical 20 dB dynamic scale.

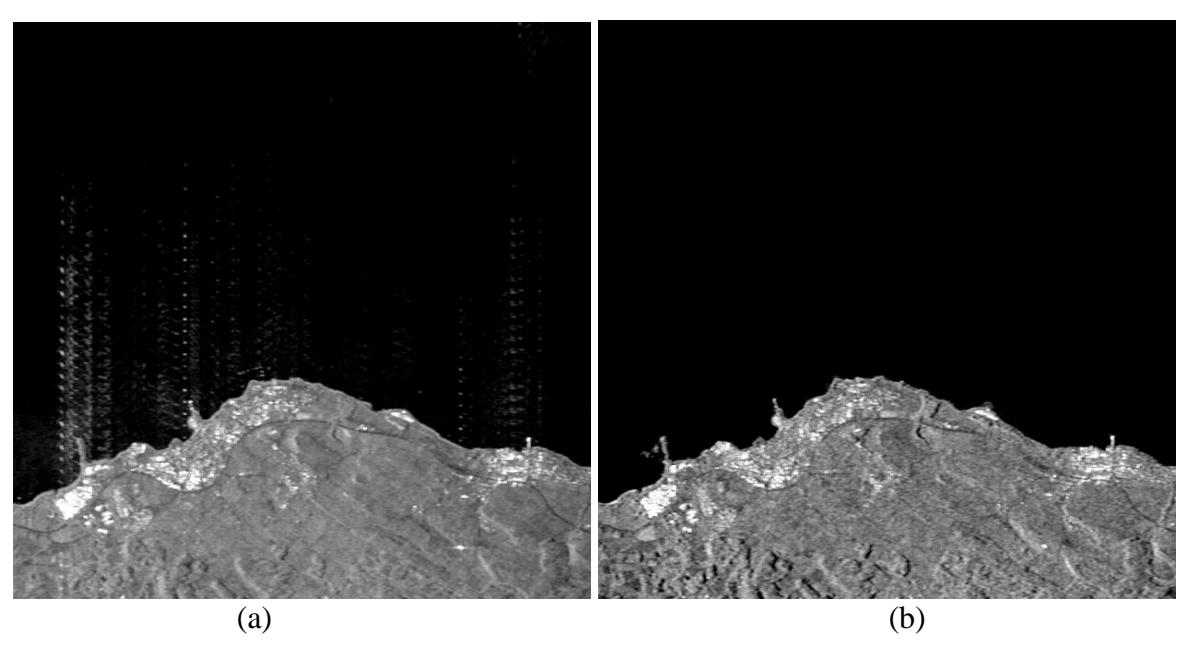


Fig. 89. (a) Portion of the focused staggered SAR image (green rectangle in Fig. 86). (b) Staggered SAR image that would have been obtained, in case the ideal sequence of Fig. 80 were used. Simulation from uniform *PRI* data. The horizontal and vertical axes represent slant range (5.6 km) and azimuth (7 km), respectively. Data are displayed using in both cases a 20 dB dynamic scale.

# 7 Data Volume Reduction

In order to meet typical azimuth ambiguity requirements, a staggered SAR system needs to employ a high mean *PRF* on transmit, i.e., data are to be oversampled in azimuth. This causes an increased data volume, which can be, however, reduced by on-board Doppler filtering and decimation [121]-[123].

## 7.1 HRWS Systems and Azimuth Oversampling

Due to their resolution and coverage requirements, HRWS systems are inherently associated with a huge data volume, thereby increasing the demands for internal data storage, downlink, ground processing and archiving. Recent studies from the Tandem-L mission quantify the volume of the acquired data as 8 TB/day [50].

Moreover, in order to comply with azimuth ambiguity requirements, a *PRF* much higher than the required PBW is often desirable. For a HRWS SAR system with constant *PRI* and multiple elevation beams using a reflector antenna, the ratio of the required *PRF* to the PBW is typically even larger than 2. If the system is operated in staggered SAR mode, the ratio of the mean *PRF* on transmit to the PBW can be even larger than 3. This determines a further increase of the data volume to be downlinked with a direct impact on the cost of the mission.

As an example, the staggered SAR system of the L-band design example of Section 5.1 has a mean PRF on transmit equal to 2700 Hz and a PBW  $B_p = 780$  Hz. Due to the azimuth oversampling, the data volume to be downlinked increases by almost 250%. The system, in fact, downlinks data included in the Doppler frequency interval  $[-PRF_{mean\ TX}/2, PRF_{mean\ TX}/2]$ , while only data in the Doppler frequency interval  $[-B_p/2, B_p/2]$  are needed to achieve the desired azimuth resolution. The information contained in the Doppler frequency intervals  $[-PRF_{mean\ TX}/2, -B_p/2]$  and  $[-B_p/2, PRF_{mean\ TX}/2]$  is useless and discarded in the SAR processing. Even considering the case of a SAR system with constant PRI and multiple elevation beams, a PRF = 1800 Hz would be anyway selected to achieve a good AASR. For a PBW  $B_p = 780$  Hz, this corresponds to an increase of the data volume to be downlinked by more than 130%.

120 7 Data Volume Reduction

### 7.2 On-Board Doppler Filtering and Decimation

Let us first consider the case of a SAR system with constant PRI. If data were just decimated prior to downlink (e.g., by a factor of 2 in the latter example where PRF = 1800 Hz and  $B_p = 780$  Hz), a considerable degradation of the AASR would occur. Fig. 90 (a) shows the PSD of the azimuth SAR signal at near range for the reflector used in the L-band design examples of Section 5. The PSD is the joint transmit-receive antenna pattern displayed as a function of Doppler frequency (the relationship between azimuth angle and Doppler frequency is given in (14)). The unambiguous energy, the ambiguous energy, and the additional ambiguous energy due to the decimation are highlighted in green, red, and blue, respectively. As is apparent, the additional ambiguous energy due to decimation is significant, i.e., the total ambiguous energy is the same obtained for PRF = 1800 Hz / 2 = 900 Hz. However, if Doppler filtering is performed before decimation, the additional ambiguous energy due to decimation can be substantially reduced, as shown in Fig. 90 (b)<sup>7</sup> [121]-[123].

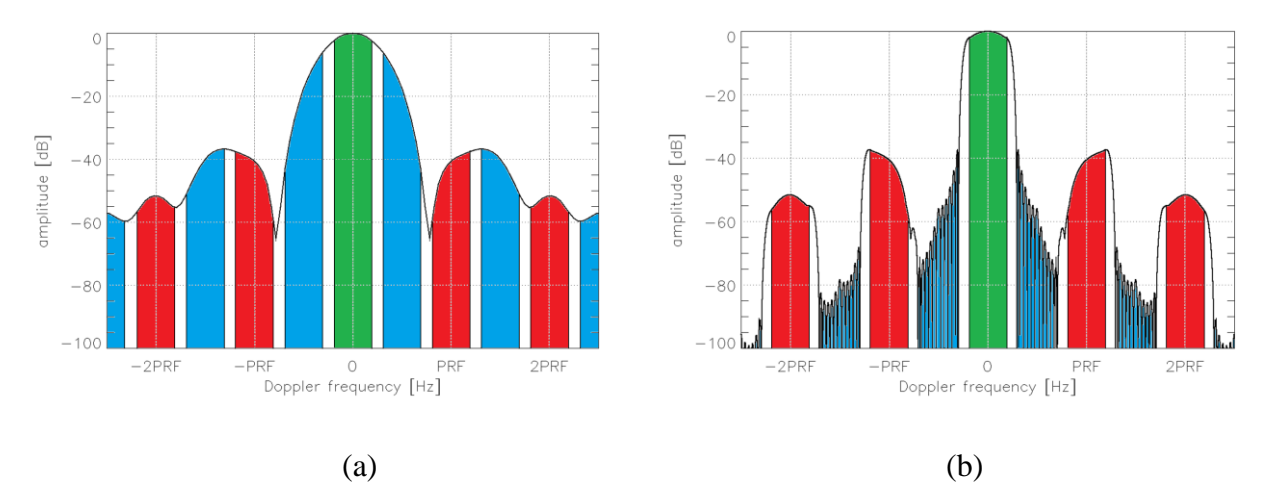


Fig. 90. PSD of the azimuth SAR signal at near range for the reflector used in the L-band design examples of Section 5. The energy of the unambiguous component, the ambiguous components, and the additional ambiguous components due to decimation are highlighted in green, red and blue, respectively. (a) Only decimation (no Doppler filtering). (b) Doppler filtering and decimation.

Due to the large amount of data, acquired by typical HRWS systems, the number of on-board operations per sample has to be minimized, while avoiding a degradation of the impulse response. The Doppler filtering can be therefore performed in time domain using a finite impulse response (FIR) filter with a relatively small number of taps. The filter will introduce a distortion of the Doppler spectrum of the signal, which can be compensated for in the SAR processing (on ground). The case of decimation by an integer factor is analyzed in the following, as this is associated with a straightforward implementation and a much lower computational cost, but the proposed strategy can be also used in case of a rational decimation factor.

<sup>&</sup>lt;sup>7</sup> The azimuth presumming, used so far in airborne SAR, can be considered as a Doppler filtering operation and represents the easiest way of data reduction.

In a staggered SAR system, the Doppler filter has to be applied to raw data resampled to a uniform *PRI*, but, in practice, resampling, Doppler filtering, and decimation can be also jointly performed, as explained in the following. Fig. 91 shows the block diagrams of the proposed data volume reduction strategy for a system with constant *PRI* and a staggered SAR system.

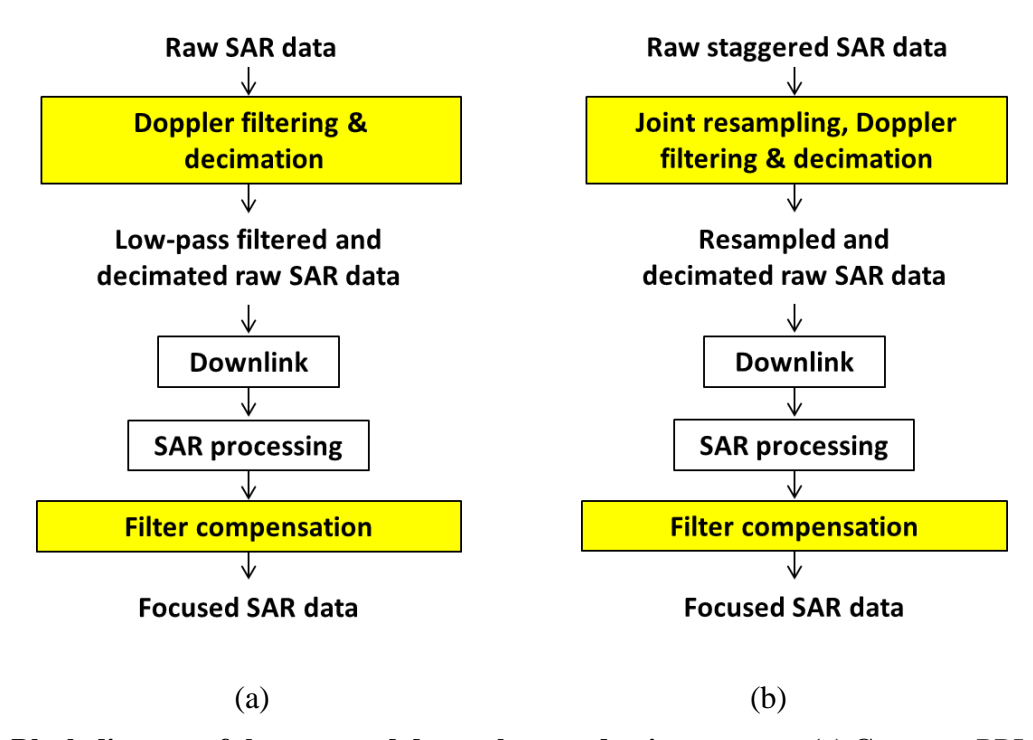


Fig. 91. Block diagram of the proposed data volume reduction strategy. (a) Constant *PRI* SAR. (b) Staggered SAR.

Fig. 92 (a) shows how in the staggered SAR case the filtering has to be applied on resampled data, which are obtained from the raw staggered SAR (non-uniformly sampled) data through BLU interpolation. Each sample of the resampled data is obtained as a linear combination of some of the samples of the raw staggered SAR data, while each sample of the filtered data is obtained as a linear combination of some of the resampled data. This means that each sample of the filtered data can be obtained directly as a linear combination of some of the staggered SAR data (Fig. 92 (b)). Moreover, there is no need to compute the samples, which would anyway be discarded by the decimation operation [123].

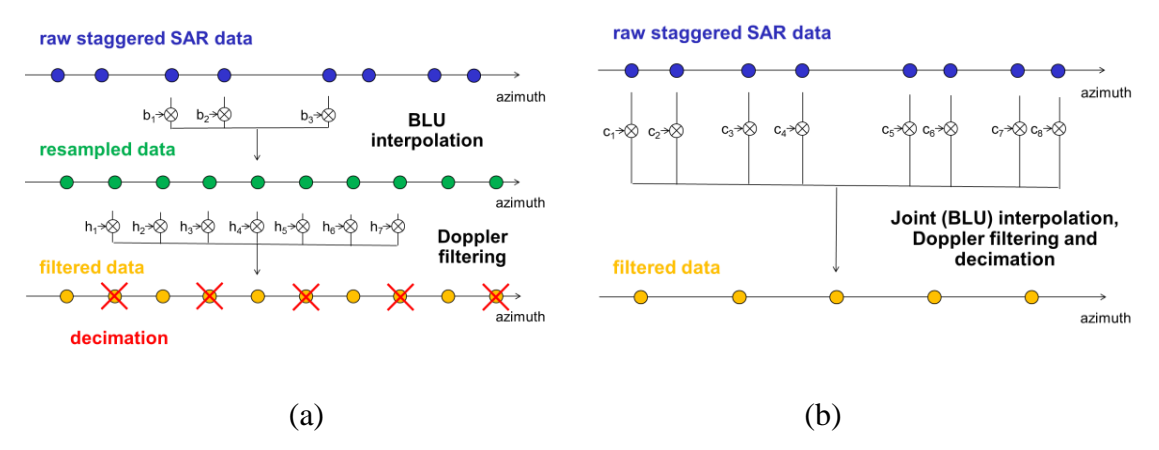


Fig. 92. (a) Interpolation, Doppler filtering and decimation in the staggered SAR case. (b) Equivalent scheme, where interpolation, Doppler filtering and decimation are jointly performed.

### 7.3 FIR Filter Design

The FIR filter can be designed as a Wiener filter, i.e., exploiting the knowledge of the PSD of the useful and disturbance signals [109]. In this case, the disturbance signal is given by the frequency components, which fold back to the main part of the spectrum after decimation. The coefficients of the *P*-tap FIR Wiener filter are given by

$$\mathbf{h}_{\mathbf{DVR}} = \mathbf{R}_{\mathbf{s}}^{-1} \mathbf{r}_{\mathbf{us}} \tag{84}$$

where  $\mathbf{R}_s$  is the correlation matrix of the overall signal and  $\mathbf{r}_{us}$  is the correlation vector of the useful signal, given by

$$\mathbf{R}_{s} = \begin{bmatrix} R_{s}[0] & R_{s}[-1] & \cdots & R_{s}[1-P] \\ R_{s}[1] & R_{s}[0] & \cdots & R_{s}[2-P] \\ \vdots & \vdots & \ddots & \vdots \\ R_{s}[P-1] & R_{s}[P-2] & \cdots & R_{s}[0] \end{bmatrix}$$
(85)

and

$$\mathbf{r_{us}} = \begin{bmatrix} R_{us} \left[ -\frac{P-1}{2} \right] \\ \vdots \\ R_{us} \left[ 0 \right] \\ \vdots \\ R_{us} \left[ \frac{P-1}{2} \right] \end{bmatrix}$$
(86)

respectively. For a decimation factor equal to 2,  $R_s[n]$  and  $R_{us}[n]$  are related to the two-way power pattern in azimuth  $G^2(f)$  through the following relation

7.3 FIR Filter Design 123

$$R_{s}[n] = R_{us}[n] + R_{d}[n] = \frac{2}{PRF} \int_{f=0}^{B_{p}/2} G^{2}(f) \cos\left(\frac{2\pi n}{PRF}f\right) df + \frac{2}{PRF} \int_{f=(PRF-B_{p})/2}^{PRF/2} G^{2}(f) \cos\left(\frac{2\pi n}{PRF}f\right) df$$
(87)

where a symmetric antenna azimuth pattern has been assumed and all back-folded components of second and higher order have been ignored.  $R_d[n]$  is the correlation of the disturbance signal due to backfolding.

Fig. 93 shows the filter coefficients, i.e., the impulse response, and the transfer function of the 25-tap FIR Wiener filter obtained for PRF = 1800 Hz and  $B_p = 780$  Hz, assuming the azimuth antenna pattern at near range of the reflector used for the L-band design example of Section 5 and that data are decimated by a factor of 2. It can be noticed how the filter attenuates the frequency components in the Doppler frequency interval  $[PRF/2-B_p/2, PRF/2]$ . For this decimation factor, in fact, a low-pass filter is needed.

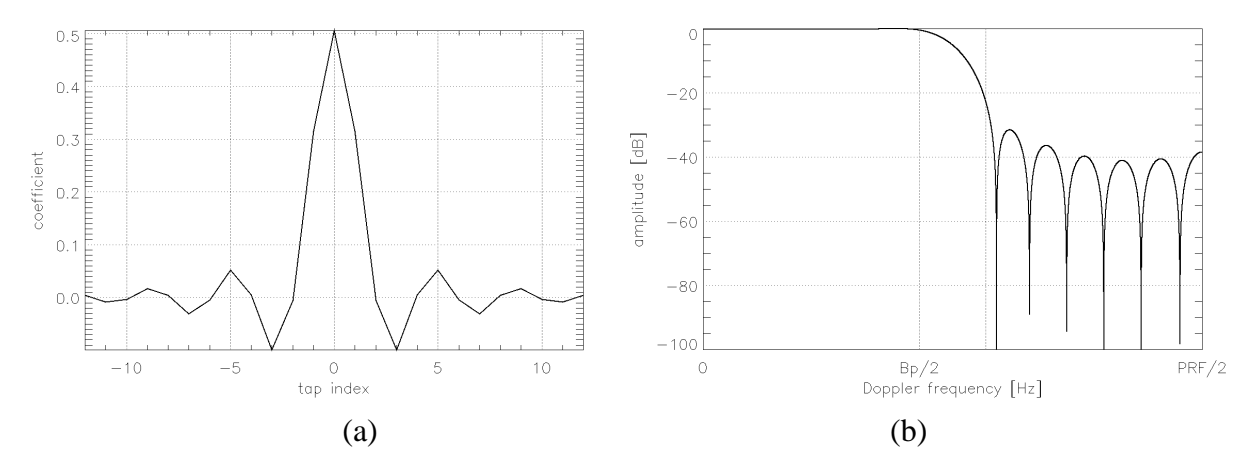


Fig. 93. 25-tap Wiener filter used for data volume reduction by a factor of 2. (a) Impulse response (filter coefficients). (b) Transfer function.

An alternative to design the FIR Wiener filter is given by the MVDR or Capon beamformer [112], where only the knowledge of the PSD of the disturbance signal is exploited. The coefficients of the Wiener filter are given by

$$h_{DVR} = R_d^{-1} \mathbf{1} \tag{88}$$

where  $\mathbf{R_d}$  is the correlation matrix of the disturbance signal, given by

$$\mathbf{R_{d}} = \begin{bmatrix} R_{d}[0] & R_{d}[-1] & \cdots & R_{d}[1-P] \\ R_{d}[1] & R_{d}[0] & \cdots & R_{d}[2-P] \\ \vdots & \vdots & \ddots & \vdots \\ R_{d}[P-1] & R_{d}[P-2] & \cdots & R_{d}[0] \end{bmatrix}$$
(89)

124 7 Data Volume Reduction

and 1 is a steering vector, whose components are all ones. The relationship between  $R_d[n]$  and the two-way antenna pattern  $G^2(f)$  is given for a decimation factor equal to 2 in (87). Fig. 94 shows the filter coefficients and the transfer function of the 9-tap MVDR filter obtained for the same antenna pattern and parameters.

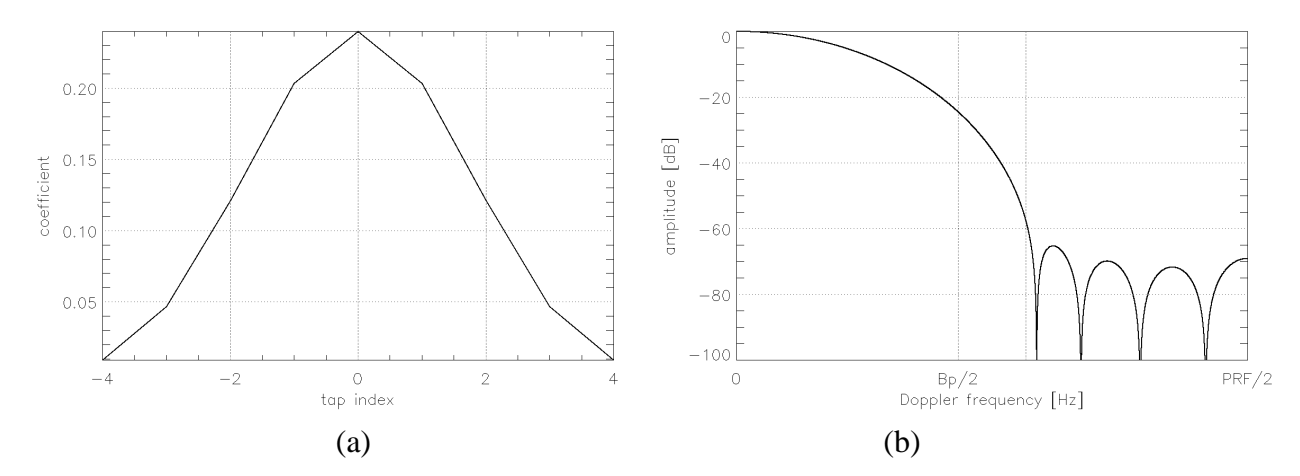


Fig. 94. 9-tap MVDR filter used for data volume reduction by a factor of 2. (a) Impulse response (filter coefficients). (b) Transfer function.

While the Wiener filter is characterized by a flat response in the Doppler frequency interval  $[0, B_p/2]$  and requires more taps (i.e., 25 in the example of Fig. 93) to provide a sufficient attenuation in the interval  $[PRF/2-B_p/2, PRF/2]$ , the MVDR achieves a very good suppression of the higher frequencies with a much smaller number of taps (i.e., 9 in the example of Fig. 94). As a drawback, the MVDR filter introduces a significant attenuation in the interval  $[0, B_p/2]$  as well (up to 20 dB in the example of Fig. 94), which can be however compensated in the processing, as explained in the following.

For a staggered SAR system the same formulas for the design of the filter hold, where in place of the PRF, the uniform PRF to which non-uniformly sampled data are resampled is to be used. The latter PRF can be selected equal to the mean PRF on transmit of the system, as done in the following example, but it can also be different, therefore allowing in a straightforward way to obtain a decimation by an arbitrary non-integer decimation factor. With reference to the staggered SAR system of the L-band design example of Section 5.1, where the mean PRF on transmit is equal to  $PRF_{mean\ TX} = 2700$  Hz and the PBW to  $B_p = 780$  Hz, data could be resampled to a uniform  $PRF = PRF_{mean\ TX}$ , filtered, and finally decimated by a factor of 3 to 900 Hz.

For a decimation factor equal to 3,  $R_s[n]$  and  $R_u[n]$  are related to the two-way power pattern in azimuth  $G^2(f)$  through the following relation

$$R_{s}[n] = R_{us}[n] + R_{d}[n] = \frac{2}{PRF} \int_{f=0}^{B_{p}/2} G^{2}(f) \cos\left(\frac{2\pi n}{PRF}f\right) df + \frac{2}{PRF} \int_{f=PRF/3-B_{p}/2}^{PRF/3+B_{p}/2} G^{2}(f) \cos\left(\frac{2\pi n}{PRF}f\right) df$$
(90)

always assuming a symmetric antenna azimuth pattern centered about zero Doppler and ignoring back-folded high-frequency components. Fig. 95 shows the filter coefficients and the transfer function so obtained. As apparent, the filter for data volume reduction for a decimation factor equal to 3 is no longer a low-pass filter, but instead a band-stop filter.

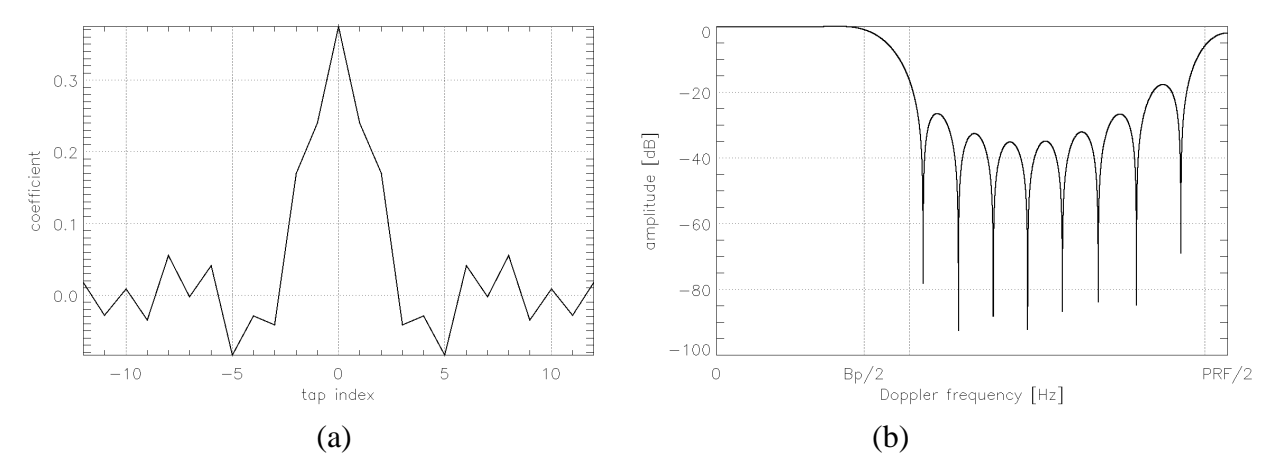


Fig. 95. 25-tap Wiener filter used for data volume reduction by a factor of 3. (a) Impulse response (filter coefficients). (b) Transfer function.

### 7.4 Performance Analysis

The performance of a system, where the described data volume reduction strategy is implemented, is evaluated and compared with a reference system, where the data volume reduction strategy is not applied, i.e., all data are downlinked. Some considerations of the joint effects of Doppler filtering and quantization are also reported.

The azimuth resolution and the azimuth PSLR remain unchanged with respect to the reference case, provided that the distortion of the Doppler spectrum of the signal, introduced by the Doppler filtering, is compensated for in the processing. This is done by multiplying the azimuth spectrum of the processed data by C(f), where

$$C(f) = \begin{cases} \frac{1}{H_{DVR}(f)} &, |f| \le B_p/2 \\ 0 &, B_p/2 \le |f| \le PRF/2 \end{cases}$$

$$(91)$$

where  $H_{DVR}(f)$  is the transfer function of the employed FIR filter.

As far as azimuth ambiguities are concerned, the *AASR* for a SAR system with constant *PRI*, where the described data volume reduction strategy is applied, for an integer decimation factor p and assuming that  $PRF \ge pB_p$ , can be analytically expressed as

126 7 Data Volume Reduction

$$AASR = \frac{\sum_{\substack{k=-\infty\\k\neq 0}}^{k=\infty} \int_{B_{p}/2}^{B_{p}/2} G^{2}(f+kPRF)Q^{2}(f)df}{\int_{-B_{p}/2}^{B_{p}/2} G^{2}(f)Q^{2}(f)df}$$

$$+ \frac{\sum_{\substack{k=-\infty\\k=-\infty}}^{k=\infty} \sum_{h=1}^{p-1} \int_{-B_{p}/2}^{B_{p}/2} G^{2}(f+kPRF)Q^{2}(f)\frac{H_{DVR}^{2}(f+\frac{h}{p}PRF)}{H_{DVR}^{2}(f)}df}{\int_{-B_{p}/2}^{B_{p}/2} G^{2}(f)Q^{2}(f)df}$$
(92)

where Q(f) accounts for the amplitude weighting of the Doppler spectrum applied in the processing (e.g., generalized Hamming window and compensation of the azimuth antenna pattern), not including the compensation of the Doppler filter. The AASR is composed of two terms, where the first term is the AASR of a system, where no data volume reduction is performed, while the second one represents the AASR degradation due to the on-board filtering [123].

Fig. 96 (a) shows the AASR as a function of ground range for a SAR with constant PRI and multiple elevation beams, the reflector used for the L-band design example of Section 5, PRF = 1800 Hz, and  $B_p = 780$  Hz, assuming that data volume reduction is not performed. The AASRs in case data are decimated by a factor of 2, using both the Wiener filter of Fig. 93 and the MVDR filter of Fig. 94, are superimposed. As apparent, the proposed strategy based on Doppler filtering and decimation allows a significant reduction of the data volume at the expense of a negligible AASR degradation. The AASR degradation, defined as the difference of the AASRs obtained with and without data volume reduction, i.e., defined as the second term of (92), is displayed in Fig. 96 (b). This is smaller than -49 dB for the 25-tap Wiener filter and smaller than -64 dB for the 9-tap MVDR filter.

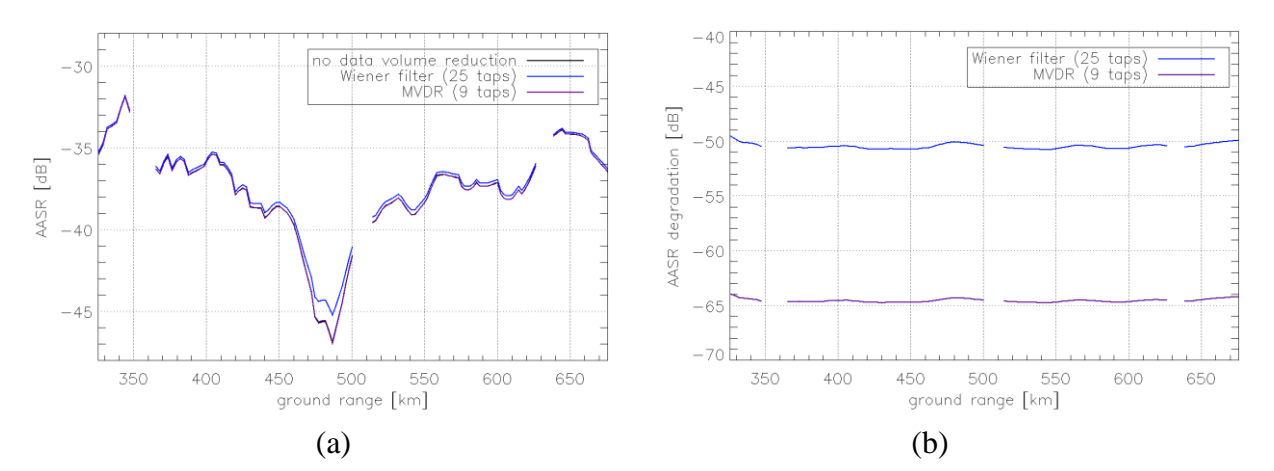


Fig. 96. (a) AASR vs. ground range for a constant PRI SAR in case data volume reduction is not performed and in case data volume reduction by a factor of 2 is performed using the Wiener filter of Fig. 93 and the MVDR filter of Fig. 94. (b) AASR degradation due to data volume reduction.

This AASR degradation is reflected in the 2-D impulse response through additional azimuth ambiguities, which, in case of decimation by a factor of 2, are located at half the azimuth distance of the first-order azimuth ambiguities, as can be observed in Fig. 97, where the 2-D impulse responses at near range are shown in case data volume reduction is not performed (Fig. 97 (a)) and in case the 25-tap Wiener filter of Fig. 93 is used (Fig. 97 (b)). The additional azimuth ambiguities are due to decimation, while the Doppler filter significantly reduces their energy.

In the staggered SAR case the AASR can be evaluated by simulation as the difference of ISLRs. Fig. 98 (a) shows the AASR as a function of ground range for the staggered SAR of the design example of Section 5.1, where  $PRF_{mean\ TX} = 2700$  Hz, and  $B_p = 780$  Hz, assuming that data volume reduction is not performed. The AASR for the case where the data are decimated by a factor of 3, using the Wiener filter of Fig. 95, is superimposed and the AASR degradation due to data volume reduction is shown in Fig. 98 (b). As apparent, even in the staggered SAR case the proposed strategy based on Doppler filtering and decimation allows a significant reduction of the data volume at the expense of a negligible AASR degradation (smaller than -55 dB). It has therefore to be considered as a completing part of the staggered SAR concept.

This *AASR* degradation is reflected in the 2-D impulse response even in the staggered SAR case through localized additional azimuth ambiguities, as it can be observed in Fig. 99, where the 2-D impulse responses at near range are shown in case data volume reduction is not performed (Fig. 99 (a)) and in case the 25-tap Wiener filter of Fig. 95 is used (Fig. 99 (b)).

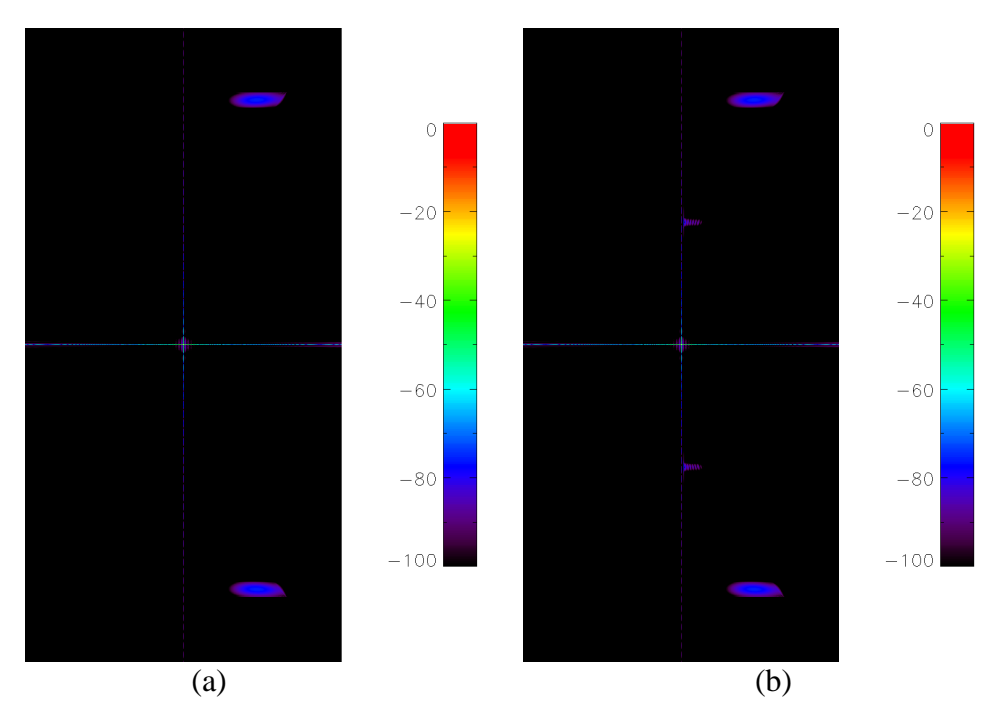


Fig. 97. Effect of data volume reduction on the 2-D IRF for a constant *PRI* SAR. The horizontal and vertical axes represent slant range and azimuth, respectively. The size (slant range × azimuth) is 1.7 km × 60.9 km. (a) 2-D IRF in dB, in case no data volume reduction is performed. (b) 2-D IRF in dB, in case data are decimated by a factor of 2, after having filtered them with the 25-tap Wiener filter of Fig. 93. The additional azimuth ambiguities due to decimation are visible.

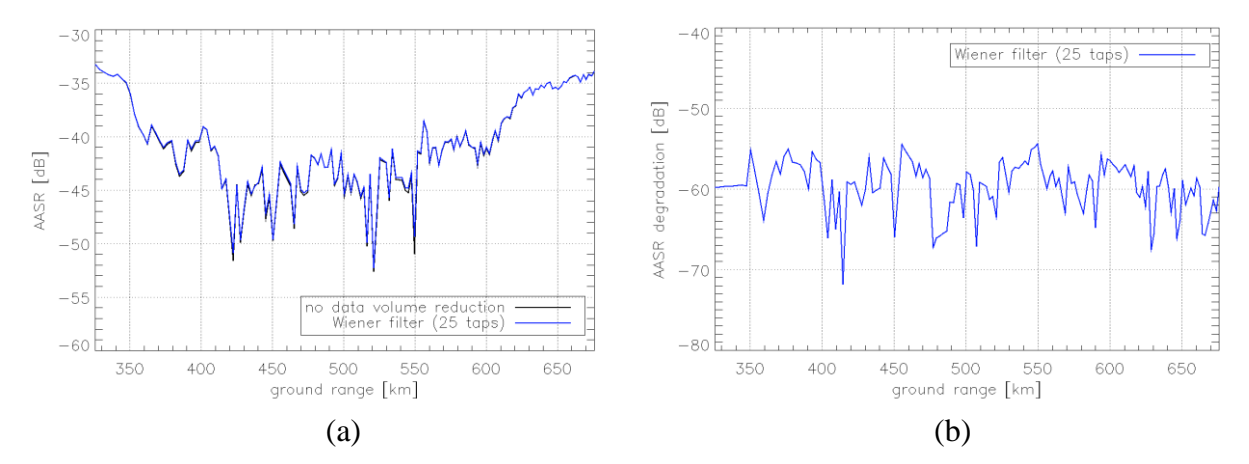


Fig. 98. (a) AASR vs. ground range for a staggered SAR in case data volume reduction is not performed and in case data volume reduction by a factor of 3 is performed using the Wiener filter of Fig. 95. (b) AASR degradation due to data volume reduction.

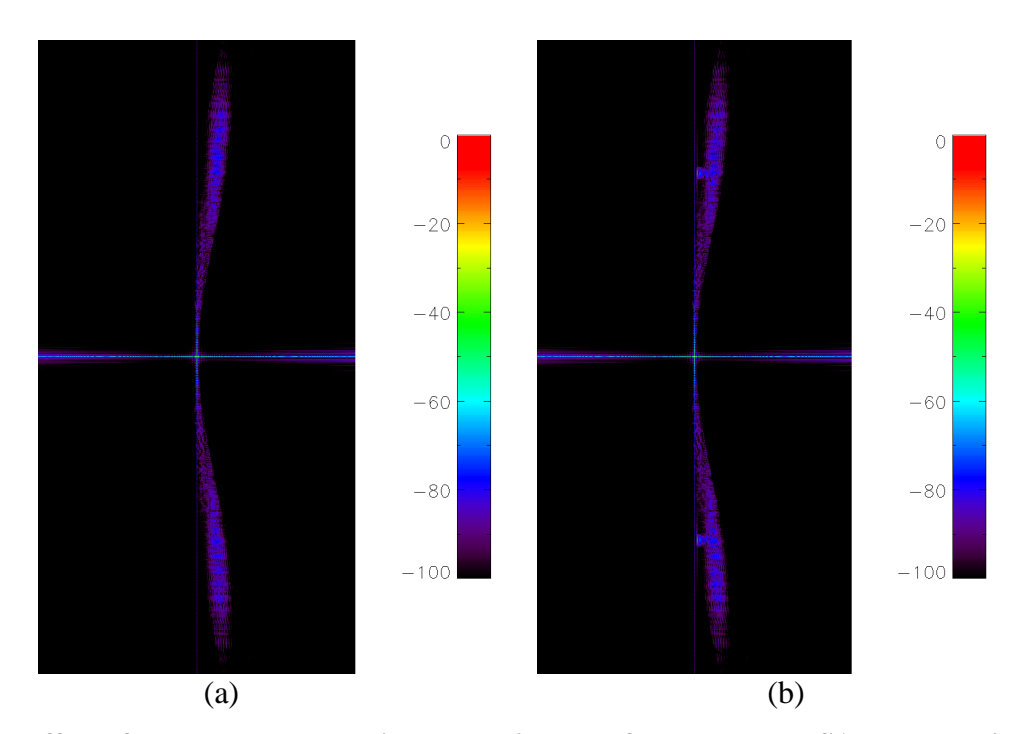


Fig. 99. Effect of data volume reduction on the 2-D IRF for a staggered SAR. The horizontal and vertical axes represent slant range and azimuth, respectively. The size (slant range  $\times$  azimuth) is 1.7 km  $\times$  40.6 km. (a) 2-D IRF in dB, in case all data are downlinked. (b) 2-D IRF in dB, in case data are decimated by a factor of 3, after having filtered them with the 25-tap Wiener filter of Fig. 95. The additional localized azimuth ambiguities due to decimation are visible.

## 7.5 Joint Effects of Doppler Filtering and Quantization

In the context of data volume reduction, the on-board Doppler filtering is likely to be followed by a quantization stage prior to downlink [124]. In the following, the joint effects of on-board Doppler filtering and block adaptive quantization (BAQ) are analyzed [125], [126]. SAR raw data acquired by the German satellite TerraSAR-X are used for the analysis [127].

Block adaptive data quantization in spaceborne SAR systems allows a drastic reduction of the data volume at the cost of a usually acceptable image degradation. In particular, an increase of the quantization noise determines a degradation, among others, of the *NESZ*, which includes all error contributions induced by the system, such as antenna pattern, instrument thermal noise, and processing filters.

If data are Doppler filtered and decimated prior to quantization, the resulting *NESZ* in general varies. Moreover, when compensating for the transfer function of the Doppler filter in the SAR processing, the quantization noise might be amplified. Filters characterized by a flat response within the processed Doppler bandwidth, such as the Wiener filter of Fig. 93, are expected to be robust to this problem, while for other filters, such as the MVDR filter of Fig. 94, a further degradation of the *NESZ* is expected.

SAR raw data acquired by the German satellite TerraSAR-X over the Amazon rainforest are used for the analysis. The calibrated radar brightness (beta nought) for the test scene is represented in Fig. 100. The PRF for the considered acquisition is 3785 Hz, and the processed Doppler bandwidth has been set to 1514 Hz, resulting in a ratio  $PRF/B_p$  equal to 2.5.

The original raw data set, output of an 8-bit analog-to-digital (A/D) converter, has been quantized using a compression rate of 4 bit/sample<sup>8</sup>. Furthermore, the original (8-bit) raw data have been also filtered using a 25-tap Wiener filter and a 9-tap MVDR filter, decimated by a factor of 2, and quantized using a compression rate of 4 bit/sample. Note that the Wiener and MVDR filters have been computed with reference to the TerraSAR-X antenna pattern and they therefore differ from the filters of Fig. 93 and Fig. 94.

For each of the six available data sets (8-bit not-filtered, 4-bit not-filtered, 8-bit Wiener-filtered, 4-bit Wiener-filtered, 8-bit MVDR-filtered, and 4-bit MVDR-filtered) SAR processing has been performed, the transfer function of the filter (where applied) has been compensated for and the *NESZ* has been evaluated.

The procedure for the evaluation of the *NESZ* is sketched in Fig. 101. It consists of identifying water areas (where the backscatter is assumed to be negligible compared to noise) by using an intensity threshold and evaluating the noise intensity – which corresponds to the NESZ – as a function of incidence angle on these areas using a median filter.

<sup>&</sup>lt;sup>8</sup> This is also the standard compression rate assumed for the Tandem-L mission.

7 Data Volume Reduction

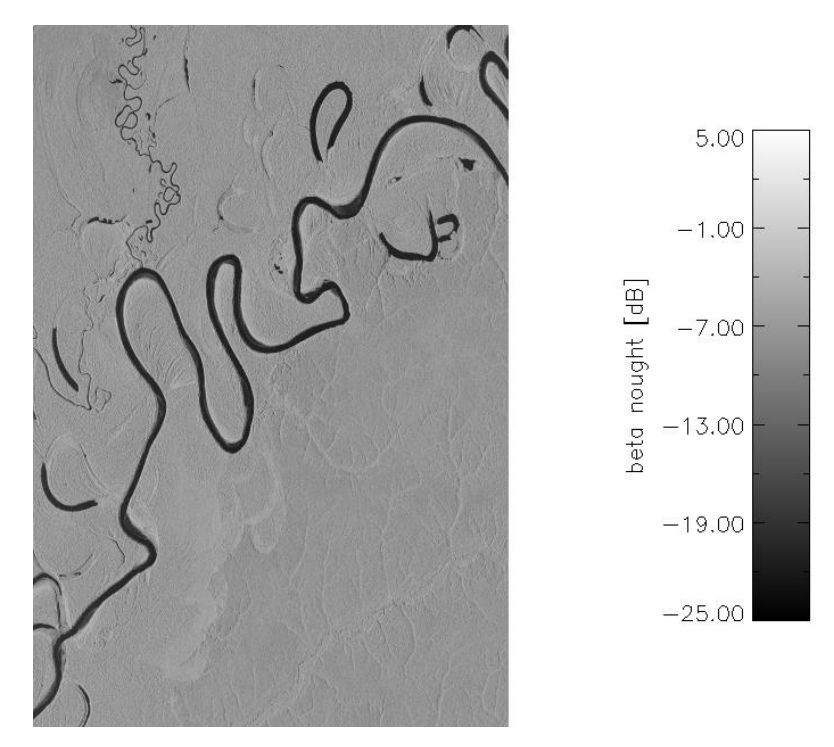


Fig. 100. Beta nought in dB for the test scene, located in the Amazon rainforest.

The *NESZ* as a function of the incidence angle is displayed for the six data sets in Fig. 102. The 8-bit and 4-bit data sets are represented with dashed and solid lines, respectively. An average *NESZ* degradation of approximately 0.5 dB is observed for the 4-bit data sets with respect to the 8-bit data sets. While there is no appreciable difference between the three 8-bit data sets (the three curves overlap almost perfectly), a slight additional degradation of the *NESZ* can be observed for the 4-bit filtered data sets with respect to the 4-bit non-filtered data set. This additional degradation for a compression rate of 4 bit/sample is equal to 0.1 dB and 0.2 dB for Wiener filter and the MVDR filter, respectively, and can be larger for higher compression rates (e.g., 2 bit/sample). The Wiener filter has therefore to be preferred, but the additional degradation for the MVDR filter is also small and could be accepted, if the on-board computational capacity only allows using a filter with a smaller number of taps.

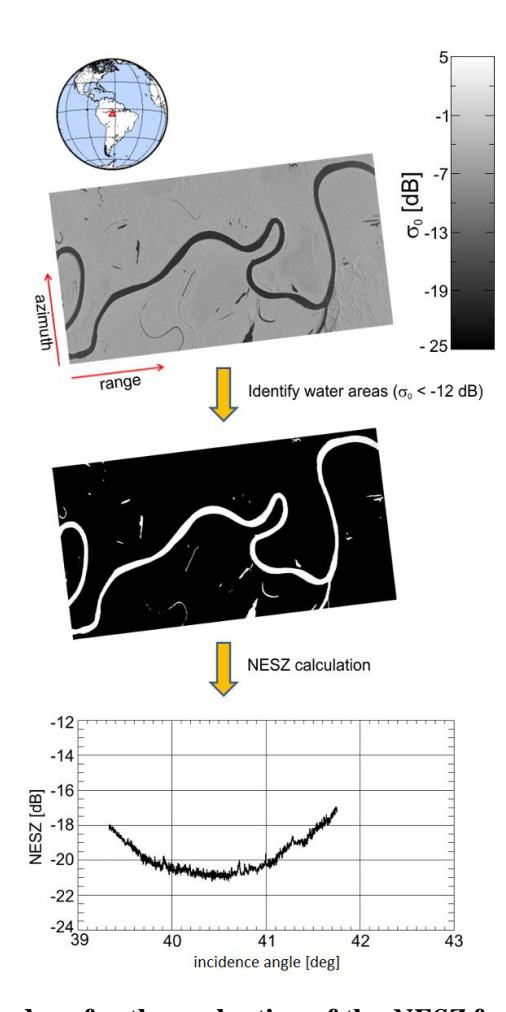


Fig. 101. Procedure for the evaluation of the NESZ from water areas.

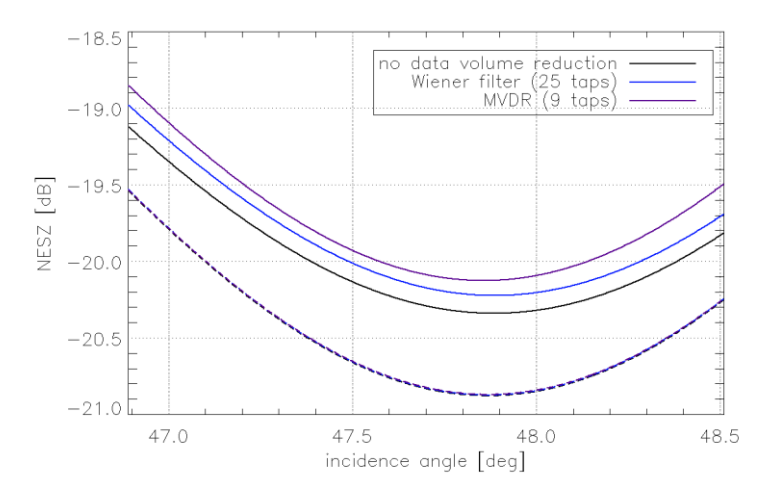


Fig. 102. NESZ for each of the six available data sets. The three 8-bit data sets are represented with dashed lines, which overlap almost perfectly. The three 4-bit data sets are represented with solid lines.

# 8 Staggered SAR with Displaced Phase Centers

The staggered SAR concept can be further extended to include a continuous variation of the phase center in addition to the continuous *PRI* variation. A range-dependent variation of the phase center on receive allows transmitting pulses according to a sequence of different *PRIs* and directly acquiring uniformly-sampled data without the need of any interpolation. This concept has been recently patented [128]-[129].

## 8.1 Concept

The staggered SAR concept provides an effective solution to the problem of blind ranges in a SAR system with multiple elevation beams through the continuous variation of the *PRI*, therefore allowing high-resolution imaging of a wide continuous swath without the need of a long antenna with multiple subapertures. This solution, however, requires that data have to be significantly oversampled in azimuth in order to keep the *AASR* under control. As the *RASR* has to be controlled as well, the design of the antenna could become in some cases challenging. Alternative solutions, including variants of the staggered SAR concept, which lead to a reduction of the antenna height at the expense of an increase of the antenna length, could be therefore of interest.

In particular, it can be noticed that in a SAR system a change of the phase center at which a pulse is transmitted or received is equivalent to a change of the sampling time for that pulse within the synthetic aperture equal to the ratio of the displacement of the phase center to the speed of the platform. From the implementation point of view, different phase centers on transmit and on receive can be achieved by using separate antennas, but also by activating different tiles of the same antenna. The change of the phase center in reflector antennas is instead discussed in [130].

The introduction of a continuous variation of the phase center in a staggered SAR system could be therefore exploited to change the effective locations of the samples in staggered SAR data and achieve equivalent uniformly sampled data without the need of any interpolation. It has to be remarked that the variation of the phase center has to compensate not only for the *PRI* variation, but also for the missing samples. As the missing samples are different for each range, a pulse-to-pulse variation of the phase center on transmit and/or on receive is not enough to achieve equivalent uniformly sampled data; a range-dependent variation of the phase center on

receive within the same pulse is instead required. A sketch of this architecture is provided in Fig. 103.

In the following, it is explained how a staggered SAR with displaced phase centers can be designed, starting from a staggered SAR system without displaced phase centers.

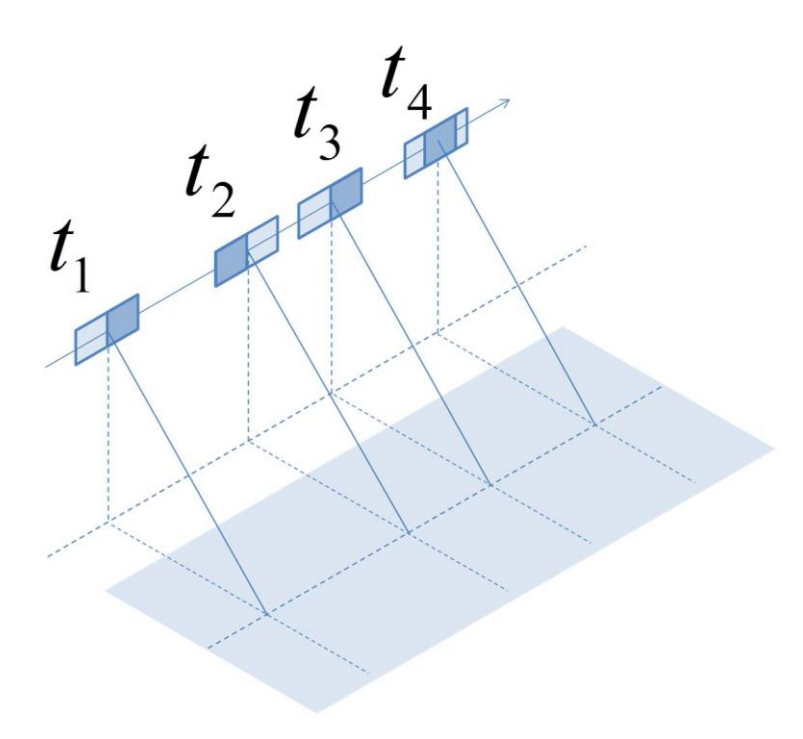


Fig. 103. Staggered SAR with displaced phase centers. Different tiles of the antenna are activated on receive to achieve a variation of the phase center. Moreover, the variation of the phase center has to be range dependent.

## 8.2 System Design

In Section 5.4 a C-band staggered SAR system based on a planar antenna has been presented, capable of mapping a 400 km wide swath with 5 m azimuth resolution. The relevant parameters were listed in Table 5, while the ambiguity performance was shown in Fig. 56. In particular, the system is characterized by an antenna length of 10 m and an antenna height of 1.5 m and achieves an *ASR* better than -22 dB by adopting a mean *PRF* on transmit equal to 2800 Hz (cf. Fig. 56 (c)).

Let us assume that the phase center on receive can be continuously varied with range within the same pulse and can be arbitrarily selected<sup>9</sup>. For a given sequence of *PRIs* and pulse length (or

<sup>&</sup>lt;sup>9</sup> In practice, for most of the system architectures the phase center cannot be arbitrarily selected, but only chosen within a set of available phase centers, e.g., if the phase center variation is achieved activating different tiles of the same antenna.

8.2 System Design 135

mean duty cycle) it is of interest to evaluate the maximum span of variation of the phase center on receive required to obtain equivalent uniformly-sampled data for each range within the imaged swath. Fig. 104 (a) shows the PRI trend of the more elaborated sequence of M = 217 PRIs used for the considered C-band design example, where a duty cycle equal to 6% is assumed. Fig. 104 (b) shows instead for a slant range  $R_0 = 728.6$  km (near range) the time distance between the 208 available samples of a cycle of PRI variation (9 are missing at that range, because the radar is transmitting) and 208 uniformly-spaced samples, which spans at this range over a 2.27 ms interval. The time distance span for all ranges of the imaged swath is displayed in Fig. 104 (c). From the maximum time distance span, in this example equal to 2.69 ms, the maximum span of variation of the phase center on receive can be obtained. This is equal to 20.2 m and directly corresponds to the required increase of the antenna length, which would therefore be 30.2 m long!

While the achieved total antenna length seems to be extremely large compared to the one of the reference staggered SAR without displaced phase centers, one could notice that a sequence with fast *PRI* change, obtained as described in Section 4.2.2, with the same mean *PRF* on transmit and duty cycle as the most elaborated one of Fig. 104 (a), leads to a maximum time distance span of only 0.67 ms, corresponding to an increase of the antenna length of 5 m. Fig. 105 shows for this sequence with fast *PRI* change the *PRI* trend, the time distance between the 29 available samples at near range of a cycle of *PRI* variation and 29 uniformly spaced samples, and the time distance span for all ranges of the imaged swath.

A staggered SAR with displaced phase centers, which employs the sequence of *PRI* of Fig. 105 (a), would be characterized by an antenna 5 m longer than for the reference staggered SAR without displaced phase centers (15 m instead of 10 m) and would achieve an *AASR* better than the one achieved by the reference staggered SAR without displaced phase centers. Under the assumption that the phase center could be arbitrarily selected, in fact, the *AASR* for the staggered SAR with displaced phase centers is the same as for a SAR with constant *PRI* with a *PRF* equal to the effective *PRF*, i.e., the product of the mean *PRF* on transmit and the ratio of the available samples at a given range to the number of pulses of the sequence. As the number of available (or missing) samples per cycle of *PRI* variation is in general different for each range, the effective *PRF* will be in general different for each range as well. Fig. 106 shows for the latter example (i.e., for the sequence of *PRIs* of Fig. 105 (a)) the number of available samples per cycle of *PRI* variation, the corresponding effective *PRF*, and the achieved *AASR* and *RASR* as a function of ground range.

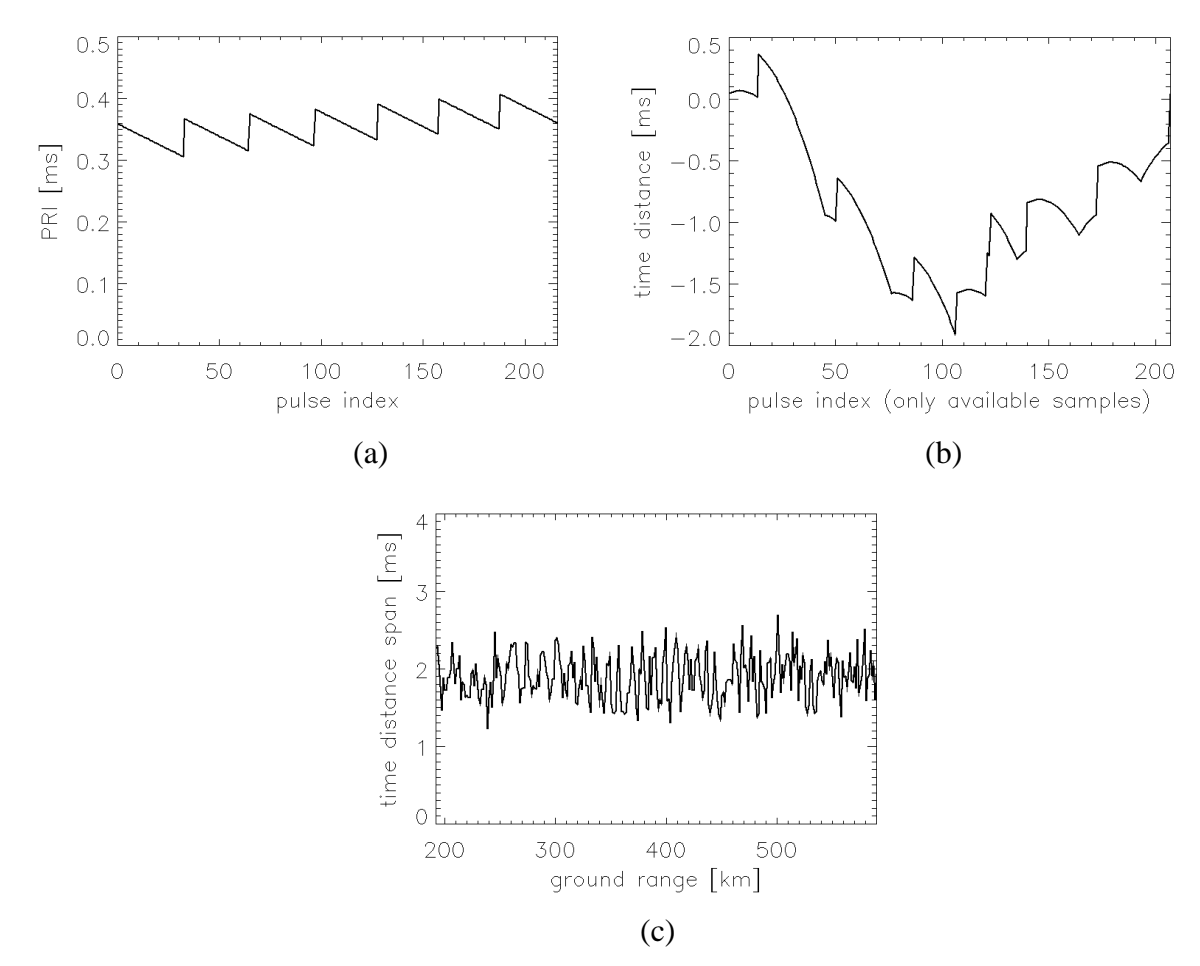


Fig. 104. (a) *PRI* trend for the more elaborated sequence used for the C-band design example. (b) Time distance between the 208 available samples at near range and 208 uniformly spaced samples. (c) Time distance span vs. ground range.

8.2 System Design

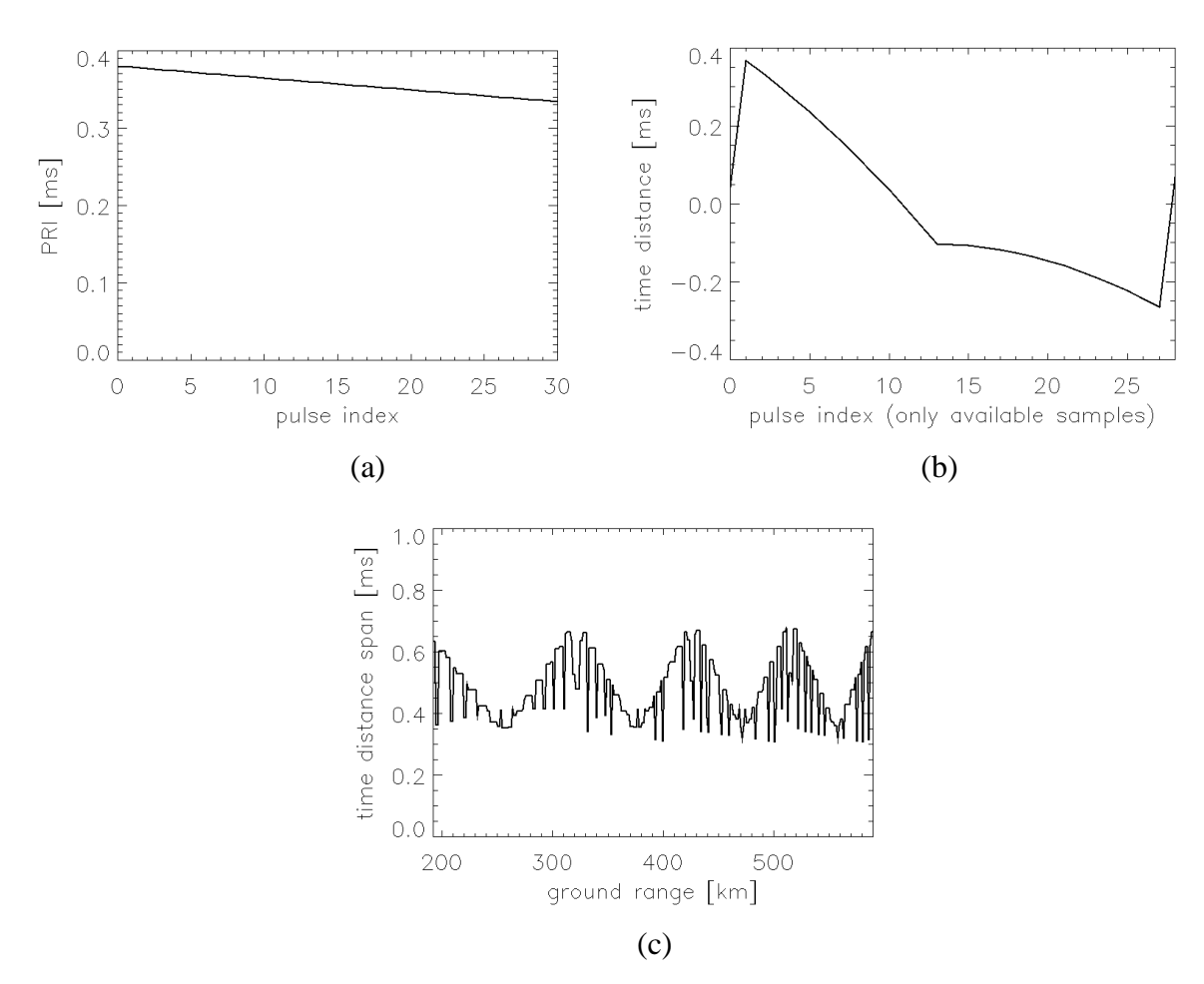


Fig. 105. (a) *PRI* trend for a sequence with fast *PRI* change, which is better suited for a staggered SAR with displaced phase centers. (b) Time distance between the 29 available samples at near range and 29 uniformly spaced samples. (c) Time distance span vs. ground range.

The achieved AASR has been evaluated assuming that a 10 m long antenna has been used in both transmit and receive and a uniform azimuth processing window has been adopted, as specified in Table 5. The AASR is better than -26 dB, while it was only better than -24 dB for the staggered SAR without displaced phase centers (cf. Fig. 56 (a)). As far as range ambiguities are concerned, the RASR can be evaluated using the same formula as for staggered SAR without displaced phase centers, i.e., (80). As the mean PRF on transmit is the same, the RASR remains almost unchanged (the slight improvement with respect to Fig. 56 (b) is due to the use of a sequence with fast PRI change rather than a more elaborated sequence).

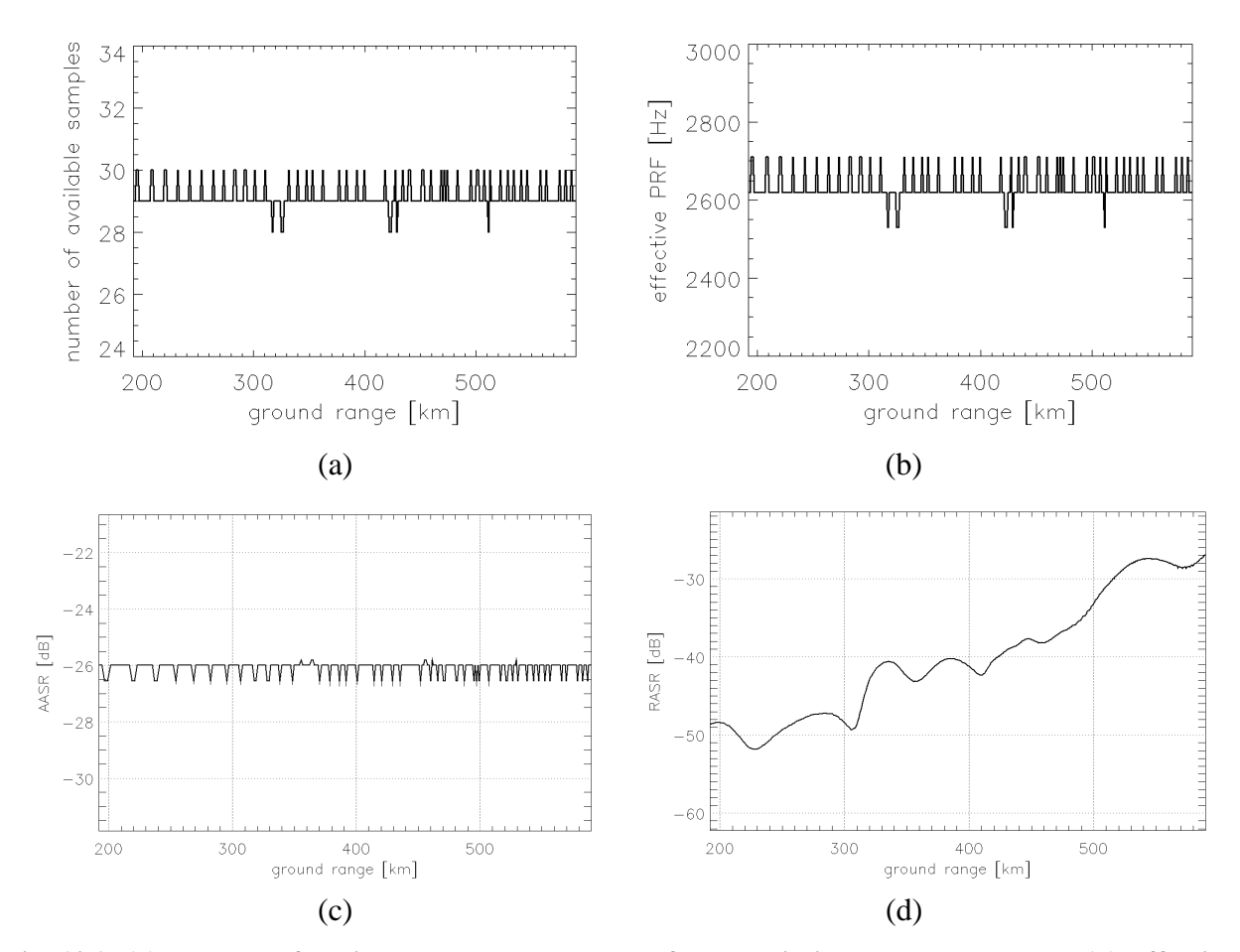


Fig. 106. (a) Number of available samples per cycle of *PRI* variation vs. ground range. (b) Effective *PRF* vs. ground ranges. (c) *AASR* vs. ground range for a staggered SAR with displaced phase centers. (d) *RASR* vs. ground range for a staggered SAR with displaced phase centers.

The basic idea of the staggered SAR with displaced phase centers is, however, that the same performance of a staggered SAR without displaced phase centers can be obtained by reducing the antenna height at the expense of an increase of the antenna length. In order to reduce the antenna height without a significant degradation of the *RASR*, the mean *PRF* on transmit has to be reduced as well. Fig. 107 (a) shows the worst *AASR* achieved over the 400 km swath as a function of the mean *PRF* on transmit, assuming that a sequence with fast *PRI* change is used. Under the same assumption, Fig. 107 (b) shows the antenna length increase as a function of the mean *PRF* on transmit. The total length of the antenna is obtained by adding 10 m. It can be noticed that reducing the mean *PRF* on transmit implies increasing the antenna length, but that the increase is not that significant. In order to keep the *AASR* under -24 dB a mean *PRF* on transmit of 2030 Hz can be selected, corresponding to an antenna length increase of 6.75 m and a total antenna length of 16.75 m. The *AASR* as a function of ground range is shown in Fig. 108 (a).

8.2 System Design 139

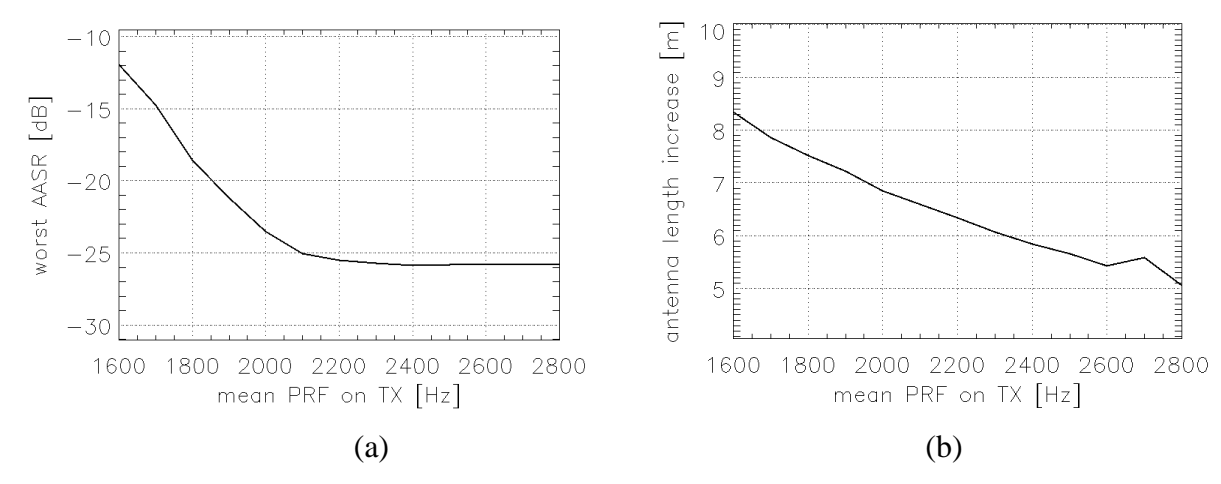


Fig. 107. (a) Worst *AASR* achieved over the swath for a sequence with fast *PRI* change as a function of the mean *PRF* on transmit. (b) Antenna length increase required for a sequence with fast *PRI* change as a function of the mean *PRF* on transmit.

Once the antenna length and the mean *PRF* on transmit have been selected, the antenna height has to be selected in order to comply with the *RASR* (or *ASR*) requirement. Fig. 108 (b) shows the *RASR* achieved for three different values of the antenna height, namely 1.5 m, 1.05m, and 0.9 m. The *ASR* is displayed in Fig. 108 (c) and is better than -22 dB for an antenna height equal to 1.05 m. A staggered SAR with displaced phase centers is therefore able to achieve the same ambiguity performance of a staggered SAR without displaced phase centers with a smaller antenna height (1.05 m instead of 1.5 m) at the expense of an increased antenna length (16.75 m instead of 10 m). The antenna area of the staggered SAR with displaced phase centers is 17 % larger than that of the staggered SAR without displaced phase centers.

Finally, it is important to remark that these results were obtained under the assumption that the phase center could be arbitrarily selected. If the phase center could be only chosen within a set of available phase centers, a degradation of the *AASR* would be observed. On the other hand, here a system design procedure has been presented, where the antenna size of a staggered SAR with displaced phase centers is derived starting from a staggered SAR system without displaced phase centers. An optimized design, involving for instance the use of sequences of *PRIs*, which minimize the antenna length, could lead to better performance or more compact systems.

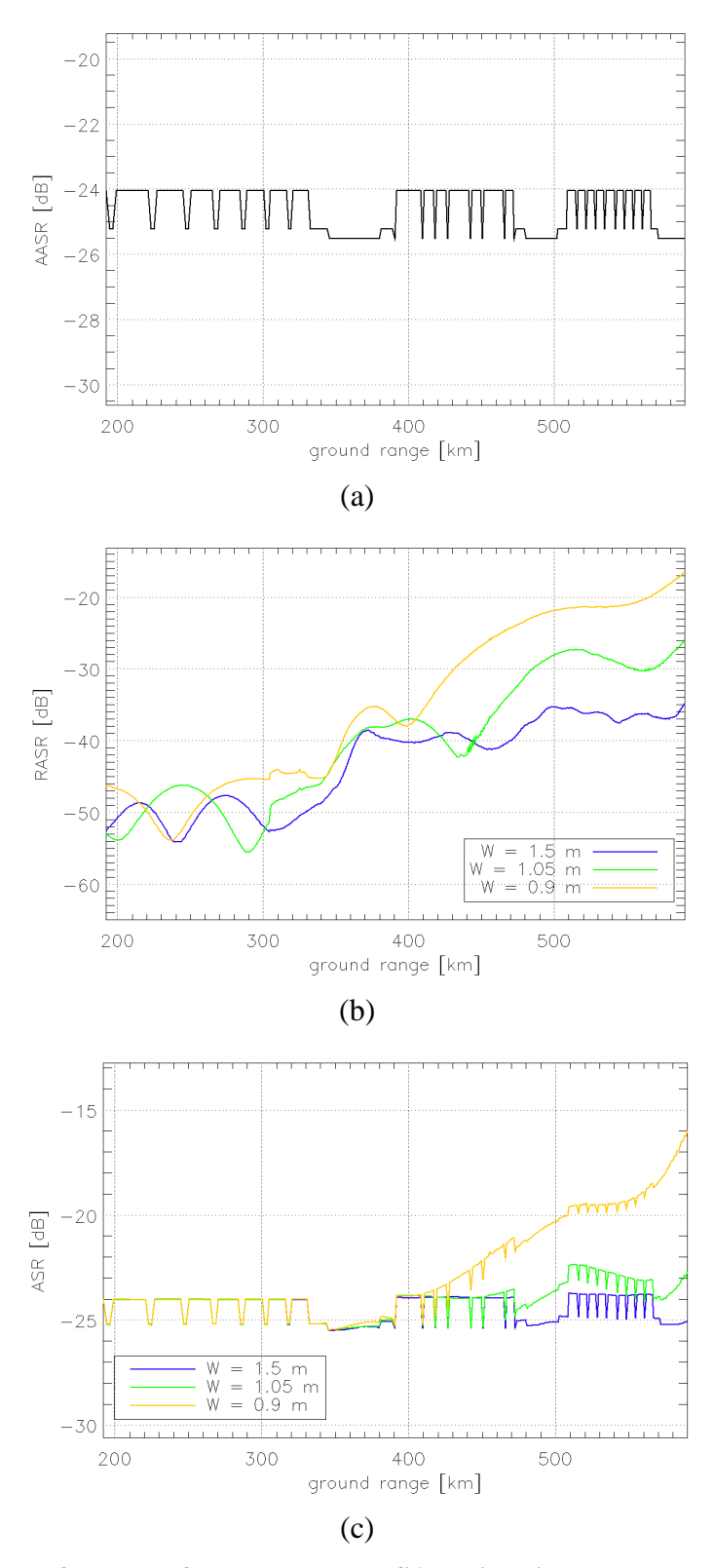


Fig. 108. Ambiguity performance for the staggered SAR with displaced phase centers for different antenna heights. (a) AASR. (b) RASR. (c) ASR.

# 9 Conclusions

This thesis analyzes in detail the staggered SAR concept and proposes design methods, which allow a staggered SAR system to achieve outstanding image quality performance. The overall research work is discussed and the results are listed. An outlook for further research is provided.

#### 9.1 Discussion

SAR can provide a significant contribution in understanding the dynamic processes within the Earth system, but for that frequent and high-resolution imaging of the whole Earth's surface is required. In order to meet the requirements of different applications, in fact, a SAR sensor able to image the whole Earth's surface twice per week with a resolution below 10 m is needed. This observation frequency requires a swath width on ground of approximately 350 km.

Conventional SAR sensors, among which all current spaceborne SAR sensors in operation, are however inherently limited, in that they can provide either high-resolution or wide-swath imaging, as the selected *PRI* of the system imposes simultaneously a lower bound to the azimuth resolution and an upper bound to the swath width. In particular, a ground swath on ground of the order of 100 km can be imaged with 10 m azimuth resolution.

In the last few decades new concepts for HRWS imaging have been devised to overcome this inherent limitation, based on multiple receive subapertures and DBF on receive. Three main architectures have been proposed:

- A system with multiple receive subapertures in azimuth, described in Section 3.2, which uses DBF on receive to increase the sensitivity;
- A ScanSAR system with multiple subapertures in azimuth, described in Section 3.3.1;
- A system with a single azimuth aperture, which uses DBF in elevation to simultaneously map multiple subswaths through multiple elevation beams, described in Section 3.3.2.

The problem of the first architecture is that a very long antenna - of the order of 40 m and therefore difficult to deploy in space - is required to map a 350 km swath. The drawback of the second architecture is the complexity of the overall system in relation to the achieved performance. Moreover, some of the imaged targets are characterized by a rather high Doppler centroid. The last one would be the ideal architecture for the aforementioned swath and resolution

9 Conclusions

requirements, in particular if implemented with a reflector, fed by a multi-channel array, but "blind ranges" are present across the swath, as the radar cannot transmit while it is receiving. Blind ranges could be imaged on a second acquisition with a different *PRI*, but this would be inefficient for global coverage and even not acceptable for some applications.

As the location of the blind ranges is related to the selected *PRI*, the continuous variation of the *PRI* in a system with multiple elevation beams, i.e., staggered SAR, was already suggested as a possible solution. If the system is operated in staggered SAR mode, the locations of the blind ranges change from pulse to pulse. Therefore, there remain no ranges which cannot be imaged, since at each range only some of the samples are missing (Section 4.1).

However, the continuous variation of the *PRI* is not just a minor modification of the system; on the contrary, it has several implications, each of which has to be carefully considered in order to avoid an unacceptable degradation of the image quality. The main problem is that missing samples in the raw data cause sidelobes in the 2-D IRF or, in other words, additional ambiguous energy in the focused SAR image.

This thesis thoroughly addresses the relevant issues related to the design of a staggered SAR system and proposes innovative methods for sequence design and data processing, which allow a staggered SAR system to meet outstanding image quality requirements with state-of-the-art antenna technology.

In particular, the sequence of *PRIs* has to be designed such that two consecutive azimuth samples are never missed within the imaged swath, as explained in Sections 4.2.2 and 4.2.3. Moreover, data have to be averagely oversampled in azimuth. The maximum distance between consecutive available azimuth samples is therefore bounded such that BLU interpolation, described in Section 4.3.3, can be used to recover uniformly sampled data, which, after SAR focusing, are still characterized by an acceptable level of azimuth ambiguities. Another essential point is that data have to be resampled before range compression, as discussed in Sections 4.1.1, 4.2.2, and 5.2.3. As data are oversampled in azimuth, range ambiguous echoes come from directions closer to that of the desired signal in comparison to a SAR system with constant *PRI*, but their energy is incoherently integrated and partially filtered out during the SAR processing (Section 5.1). Finally, on-board Doppler filtering and decimation allows a drastic reduction of the volume of data to be downlinked (Section 0).

This thesis also provides new insights into SAR ambiguities and introduces a formula for the *RASR* in staggered SAR and a general method for the evaluation of the *AASR*, which is also applicable to staggered SAR, while the conventional formula for the *RASR* provides inaccurate results for a staggered SAR and the conventional formula for the *AASR* is not even applicable to a staggered SAR. The development of a methodology for an accurate evaluation of the *RASR* and the *AASR* has been fundamental to understand the impact of the different system and processing parameters on the SAR imaging performance. Several design examples have been presented, mainly related to the Tandem-L mission proposal, but also to a HRWS C-band system, where the performance has been shown using the same figures as in a SAR with constant *PRI* (Section 5).

The acquisition of a dedicated airborne data set, characterized by a high oversampling in azimuth, has allowed the synthesis of equivalent raw staggered SAR data, their focusing, and a further check of the image quality, already assessed through the evaluation of the AASR (Section

6.1). Moreover, the experiment with TerraSAR-X, commanded to acquire data in staggered SAR mode, although with non-optimal settings, demonstrates that staggered SAR operation can be performed without particular complications and that the results are in good agreement with expectations from simulations (Section 6.2).

The advances of this thesis have contributed to the selection of staggered SAR as the baseline acquisition mode of Tandem-L, a proposal for an innovative satellite mission to monitor dynamic processes over the Earth's surface with unprecedented accuracy and resolution.

## 9.2 Summary of Results

In the following the results achieved within this thesis are listed in detail.

Chapter 2 consists of a general review of SAR remote sensing, but it also introduces a novel formula – namely (29) – for the *RASR* in a constant *PRI* SAR, which takes into account the 2-D antenna pattern and is therefore more accurate if the 2-D pattern is not separable as the product of an azimuth and an elevation pattern (e.g., for reflector antennas). Although not described in detail in this thesis, further contributions to the general theory of SAR are the novel method for the estimation of the local *AASR* in SAR images, mentioned in Section 2.3.4 and described in detail in [86], the analysis of the impact of azimuth ambiguities on interferometric performance, which will be mentioned in Section 9.3 and is described in detail in [87], [88], and the novel method for the estimation of the *NESZ* in polarimetric data, used in Section 6.1.1 to check the *NESZ* of the F-SAR airborne data and described in detail in [119].

Chapter 3 recalls how swath width and resolution constrain the *PRF* in a conventional SAR and presents the main architectures for HRWS imaging. This thesis stresses that the areas where after range compression targets are imaged with degraded azimuth resolution is larger twice as much as the areas where samples are missing in the raw data.

The contributions concerning staggered SAR start with Section 4. The concept is presented, highlighting the additional tasks that the system designer has to tackle when dealing with a staggered SAR rather than with a SAR with constant *PRI* and multiple elevation beams. These are:

- The selection of a suitable sequence of *PRIs*;
- The choice of the interpolation method to be used to resample staggered SAR data to a regular grid;
- The definition of a processing strategy, i.e., whether data have to be resampled before or after range compression.

The design of sequences with slow *PRI* change, proposed in [65], is reviewed and new sequences, referred to as sequences with fast *PRI* change and more elaborated sequences, based on the criterion for which two consecutive azimuth samples are never missed within the imaged swath, are proposed. The design of the latter sequences is optimized on the basis of the other parameters of the system and generalized for fully polarimetric staggered SAR systems.

As far as the interpolation method is concerned, this thesis recalls two-point interpolation, explains how the multi-channel reconstruction, used in SAR systems with multiple subapertures, can be used in staggered SAR systems as well, and proposes BLU interpolation as a technique

9 Conclusions

which makes use of the spectral properties of the signal within the interpolation. Moreover, this thesis points out for the first time the advantages of performing the resampling before range compression.

Chapter 5 is devoted to the performance analysis. A formula for the NESZ in staggered SAR is provided in (79), a further formula for the RASR in staggered SAR is given in (80), which accounts for the incoherent integration of the range ambiguous echoes, and a new method for the evaluation of the AASR is proposed, which is more general than the conventional one and is applicable to staggered SAR systems as well. It has to be remarked that before the latter developments the RASR and the AASR of a staggered SAR system could not be evaluated. Therefore, it was difficult to compare the performance of a staggered SAR system to that of a system with constant PRI and multiple elevation beams. Using these formulas and methods, it is shown how the novel proposed sequences of PRIs, together with BLU interpolation and the processing strategy based on the resampling of the raw data, lead to much better ambiguity performance and make the system compliant with typical ambiguity requirements. The mean PRF on transmit, which results in the same level of AASR and RASR in a staggered SAR, is much larger than the PRF, which results in the same level of AASR and RASR in a SAR with constant PRI and multiple elevation beams. The achieved AASR and RASR in staggered SAR are worse by a couple of dB compared to that achieved by a SAR with constant PRI with the same antenna. However, the staggered SAR system allows imaging of a continuous swath rather than multiple subswaths and the energy of range and azimuth ambiguities is spread over large areas: Ambiguities therefore appear in the image as a noise-like disturbance rather than localized artifacts. It is also explained how the system designer can trade resolution, ambiguities, and NESZ by properly selecting the processed Doppler bandwidth and the mean duty cycle.

The presented system design examples integrate the performance analysis. It is shown how a 350 km continuous swath can be imaged at L-band in single- and dual-polarization with 10 m or even 7.5 m azimuth resolution and outstanding ambiguities using a reflector antenna with a diameter of 15 m, like the one considered for the Tandem-L mission proposal. A 175 km swath can be instead imaged in fully-polarimetric mode. Moreover, a planar antenna with a length of 10 m and a height of 2.6 m can image at C-band a 400 km wide continuous swath (280 km in fully-polarimetric mode) with 5 m azimuth resolution (Section 5.4) and excellent ambiguity performance (*ASR* better than -30 dB in single- and dual-polarimetric mode). This means that staggered SAR is also an appealing candidate for a HRWS Sentinel follow-on mission.

The experiments with real data of Section 6 confirm and enforce the results of the performance analysis, showing several sample images corresponding to different *AASR* levels. A further proof-of-concept is the experiment with TerraSAR-X, the first acquisition in staggered SAR mode from space. Although the settings were not optimal, it was possible to demonstrate the technique and observe a very good agreement between results and expectations from simulation.

Section 7 presents a strategy for data volume reduction, which is an integral part of the staggered SAR concept, as the high oversampling in azimuth would otherwise require a huge downlink capacity. The concept is presented for both SAR with constant *PRI* and staggered SAR. Two methodologies for the design of the filters are presented, based on the Wiener filter and the MVDR beamformer, respectively. The performance is assessed and an analytical formula for the

9.3 Outlook 145

AASR degradation due to data volume reduction in a SAR with constant *PRI* is provided, while the *AASR* degradation in staggered SAR is evaluated by simulation. The *AASR* degradation is in both cases negligible, even using a filter with a relatively small number of taps. The joint effects of Doppler filtering and quantization are furthermore assessed using real TerraSAR-X data.

Section 1 presents a further extension of the staggered SAR concept, the staggered SAR with displaced phase centers, where a range-dependent variation of the phase center on receive allows transmitting pulses according to a sequence of different *PRIs* and directly acquiring uniformly sampled data without the need of any interpolation. This concept has been also patented [128]-[129].

#### 9.3 Outlook

A robust and optimized staggered SAR concept has been presented in this thesis, based on novel sequences of *PRIs*, interpolation methods, and processing strategies, which allow a staggered SAR system to meet outstanding ambiguity requirements with state-of-the-art antenna technology. Further developments, however, could lead to even better performance and/or reduced system complexity and costs.

The design of the antenna and the selection of the weights used for digital beamforming could be for instance optimized to minimize the energy of range and azimuth ambiguities. While algorithms for the suppression of jammers from known DoAs are well established, the inaccurate knowledge of the antenna pattern on-board makes this issue challenging.

Furthermore, within this thesis the most general assumption concerning the statistics of the SAR image has been made, i.e., that the observed scene is a zero-mean complex random process with PSD proportional to the azimuth antenna power pattern. While this assumption allows preserving the information relative to distributed scatterers and is therefore very important for SAR interferometry, the observed scene includes in practice different areas, characterized by different statistics. Depending on the application, the exploitation of higher order statistics could allow relaxing the requirement on the oversampling rate in azimuth, i.e., using a lower mean *PRF* on transmit. In this way, the same *RASR* could be obtained with a lower antenna.

Furthermore, there is an inherent characteristic of systems with multiple elevation beams, including staggered SAR systems, which can be exploited for range ambiguities suppression, i.e., the most annoying range ambiguities for a given imaged subswath are the desired signals for the other imaged subswaths. Since the signals from all multiple beams are anyway downloaded to the ground to map multiple subswaths, it is possible to use this additional information "a posteriori" to mutually suppress range ambiguities. This advanced technique for range ambiguity suppression is referred to as cross elevation beam range ambiguity suppression (CEBRAS) [131]. While several approaches have been already devised in [131], the application of this technique becomes challenging, if raw staggered SAR data are on-board filtered and decimated prior to downlink, according to the data volume reduction strategy proposed in Section 0.

If a staggered SAR system is used for single-pass SAR interferometry, where one satellite transmits pulses and receives their echoes, while a second satellite (in a bistatic configuration)

9 Conclusions

only receives the echoes, the receive-only satellite can receive even when the other satellite is transmitting. While one of the two SAR images used for interferometry will have missing samples, because the satellite cannot transmit, while it is receiving, the second one will not have any missing sample. If the coherence (or complex correlation) between the two images is high enough, the samples of the second image can be used to recover the missing samples in the first image. This was already done for TanDEM-X data, where some samples were missing due to synchronization of the two satellites [108]. This could also allow relaxing the requirement on the oversampling in azimuth and obtaining the same *RASR* with a lower antenna. Moreover, unlike in SAR systems with constant *PRI* (see e.g., [87], [88]), the azimuth ambiguities of the two SAR images are unlikely to be coherent.

A major step forward in the design of HRWS systems could come from the combination of the staggered SAR concept, based on the simultaneous mapping of multiple subswaths and the continuous variation of the *PRI*, and multiple azimuth channels. A staggered SAR with multiple azimuth channels could allow further increasing the azimuth resolution, while keeping the wide continuous swath, i.e., a 350 km continuous swath could be imaged with 3 m azimuth resolution. Multiple azimuth feeds allow mapping a wider Doppler spectrum, therefore achieving a higher resolution, but an algorithm to unambiguously reconstruct the aliased signals is still under investigation [132].

- [1] M.I. Skolnik, "The Nature of Radar," in *Introduction to Radar Systems*, Third Edition. New York, USA: McGrawHill, 2001, ch. 1, pp. 8–14.
- [2] J.C. Maxwell, "A Dynamical Theory of the Electromagnetic Field," *Philosophical Transactions of the Royal Society of London*, vol. 155, pp. 459–512, January 1865.
- [3] C. Hülsmeyer, "Verfahren, um entfernte metallische Gegenstände mittels elektrischer Wellen einem Beobachter zu melden," German Patent DE 165546, November 21, 1905.
- [4] C. Hülsmeyer, "Hertzian-wave Projecting and Receiving Apparatus Adapted to Indicate or Give Warning of the presence of a Metallic Body, Such as a Ship or a Train, in the Line of Projection of Such Waves," British Patent 13,170, September 22, 1904.
- [5] G. Marconi, "Radio telegraphy," *Proceedings of the IRE*, vol. 10, no. 4, pp.215–238, August 1922.
- [6] A.H. Taylor, L.C. Young, and L.A. Hyland, "System for Detecting Objects by Radio," U.S. Patent 1,981,884, November 27, 1934.
- [7] G. Breit and M.A. Tuve, "A Test of the Existence of the Conducting Layer," *Physical Review*, vol.28, no. 3, pp. 554–575, September 1926.
- [8] A. Moreira, P. Prats-Iraola, M. Younis, G. Krieger, I. Hajnsek, and K.P. Papathanassiou, "A tutorial on synthetic aperture radar," *IEEE Geoscience and Remote Sensing Magazine*, vol. 1, no. 1, pp. 6–43, March 2013.
- [9] C.A. Wiley, "Pulsed Doppler radar methods and apparatus," U.S. Patent 3196436, July 20, 1965.
- [10] C.A. Wiley, "Synthetic aperture radars," *IEEE Transactions on Aerospace and Electronic Systems*, vol. 21, no. 3, pp. 440–443, May 1985.
- [11] (2015, July) NASA, JPL, Missions Seasat, [Online], Available: http://www.jpl.nasa.gov/missions/seasat/
- [12] (2015, July) ESA, ERS Earth Online ESA, [Online], Available: https://earth.esa.int/web/guest/missions/esa-operational-eo-missions/ers
- [13] (2015, July) JAXA EORC, Japanese Earth Resources Satellite, [Online], Available: http://www.eorc.jaxa.jp/JERS-1/en/

[14] (2015, July) CSA, RADARSAT-1, [Online], Available: <a href="http://www.asc-csa.gc.ca/eng/satellites/radarsat1/">http://www.asc-csa.gc.ca/eng/satellites/radarsat1/</a>

- [15] (2015, July) NASA, JPL, SIR-C/X-SAR Images, [Online], Available: <a href="http://www.jpl.nasa.gov/radar/sircxsar/">http://www.jpl.nasa.gov/radar/sircxsar/</a>
- [16] (2015, July) NASA, JPL, Shuttle Radar Topography Mission, [Online], Available: <a href="http://www2.jpl.nasa.gov/srtm/">http://www2.jpl.nasa.gov/srtm/</a>
- [17] (2015, July) ESA, Envisat Earth Online ESA, [Online], Available: <a href="https://earth.esa.int/web/guest/missions/esa-operational-eo-missions/envisat">https://earth.esa.int/web/guest/missions/esa-operational-eo-missions/envisat</a>
- [18] (2015, July) JAXA EORC, About ALOS PALSAR, [Online], Available: <a href="http://www.eorc.jaxa.jp/ALOS/en/about/palsar.htm">http://www.eorc.jaxa.jp/ALOS/en/about/palsar.htm</a>
- [19] J.-S. Lee and E. Pottier, *Polarimetric Radar Imaging: From Basics to Applications*. Boca Raton, USA: CRC Press, 2009.
- [20] S.R. Cloude, *Polarisation: Applications in Remote Sensing*. New York, USA: Oxford Univ. Press, 2009.
- [21] P.A. Rosen, S. Hensley, I.R. Joughin, F.K. Li, S.N. Madsen, E. Rodriguez, and R.M. Goldstein, "Synthetic aperture radar interferometry," *Proceedings of the IEEE*, vol. 88, no. 3, pp. 333–382, March 2000.
- [22] R. Bamler and P. Hartl, "Synthetic aperture radar interferometry," *Inverse Problems*, vol. 14, no. 4, pp. R1–R54, August 1998.
- [23] S.R. Cloude and K.P. Papathanassiou, "Polarimetric SAR interferometry," *IEEE Transactions on Geoscience and Remote Sensing*, vol. 36, no. 5, pp. 1551–1565, September 1998.
- [24] A. Reigber and A. Moreira, "First demonstration of airborne SAR tomography using multi-baseline L-band data," *IEEE Transactions on Geoscience and Remote Sensing*, vol. 38, no. 5, pp. 2142–2152, September 2000.
- [25] D. Massonnet, M. Rossi, C. Carmona, F. Adragna, G. Peltzer, K. Feigl, and T. Rabaute, "The displacement field of the Landers earthquake mapped by radar interferometry," *Nature*, vol. 364, pp. 138–142, July 1993.
- [26] A. Ferretti, C. Prati, and F. Rocca, "Permanent scatterers in SAR interferometry," *IEEE Transactions on Geoscience and Remote Sensing*, vol. 39, no. 1, pp. 8–30, January 2001.
- [27] (2015, July) DLR, Microwaves and Radar Institute E-SAR The Airborne SAR System of DLR, [Online], Available: <a href="http://www.dlr.de/hr/en/desktopdefault.aspx/tabid-2326/3776">http://www.dlr.de/hr/en/desktopdefault.aspx/tabid-2326/3776</a> read-5679/
- [28] A. Reigber, R. Scheiber, M. Jäger, P. Prats-Iraola, I. Hajnsek, T. Jagdhuber, K. Papathanassiou, M. Nannini, E. Aguilera, S. Baumgartner, R. Horn, A. Nottensteiner, and A. Moreira, "Very-high-resolution airborne synthetic aperture radar imaging: Signal processing and applications," *Proceedings of the IEEE*, vol. 101, no. 3, pp.759–783, March 2013.
- [29] (2015, July), Catalogue of satellite instruments, CEOS EO Handbook. [Online]. Available: <a href="http://www.eohandbook.com">http://www.eohandbook.com</a>
- [30] (2015, July), DLR Portal, TerraSAR-X Germany's radar eye in space. [Online]. Available: <a href="http://www.dlr.de/dlr/en/desktopdefault.aspx/tabid-10377/565\_read-436/#/gallery/350">http://www.dlr.de/dlr/en/desktopdefault.aspx/tabid-10377/565\_read-436/#/gallery/350</a>

[31] (2015, July), DLR Portal, TanDEM-X - the Earth in three dimensions. [Online]. Available: <a href="http://www.dlr.de/dlr/en/desktopdefault.aspx/tabid-10378/566\_read-426/#/gallery/345">http://www.dlr.de/dlr/en/desktopdefault.aspx/tabid-10378/566\_read-426/#/gallery/345</a>

- [32] (2015, July), CSA, RADARSAT-2. [Online]. Available: <a href="http://www.asc-csa.gc.ca/eng/satellites/radarsat2/">http://www.asc-csa.gc.ca/eng/satellites/radarsat2/</a>
- [33] (2015, July), ASI, CosmoSkyMed. [Online]. Available: <a href="http://www.asi.it/en/activity/observation-earth/cosmo-skymed">http://www.asi.it/en/activity/observation-earth/cosmo-skymed</a>
- [34] (2015, July), ESA, Sentinel-1. [Online]. Available: <a href="http://www.esa.int/Our\_Activities/Observing">http://www.esa.int/Our\_Activities/Observing</a> the Earth/Copernicus/Sentinel-1
- [35] (2015, July) JAXA EORC, Advanced Land Observing Satellite-2 "DAICHI-2" (ALOS-2). [Online]. Available: <a href="http://global.jaxa.jp/projects/sat/alos2/">http://global.jaxa.jp/projects/sat/alos2/</a>
- [36] R. Werninghaus and S. Buckreuss, "The TerraSAR-X Mission and System Design," *IEEE Transactions on Geoscience and Remote Sensing*, vol. 48, no. 2, pp. 606–614, February 2010.
- [37] D. Miller and W. Pitz, "The TerraSAR-X satellite," *IEEE Transactions on Geoscience and Remote Sensing*, vol. 48, no. 2, pp. 615–622, February 2010.
- [38] J. Mittermayer, S. Wollstadt, P. Prats-Iraola, and R. Scheiber, "The TerraSAR-X Staring Spotlight Mode Concept," *IEEE Transactions on Geoscience and Remote Sensing*, vol. 52, no. 6, pp. 3695–3706, June 2014.
- [39] U. Steinbrecher, T. Kraus, G. Castellanos Alfonzo, C. Grigorov, D. Schulze, and B. Bräutigam, "TerraSAR-X: Design of the new operational WideScanSAR mode," *Proceedings of the EUSAR*, Berlin, Germany, 2014.
- [40] J. Mittermayer and H. Runge, Conceptual Studies for Exploiting the TerraSAR-X Dual Receiving Antenna, *Proceedings of the IGARSS*, Toulouse, France, 2003.
- [41] A. Moreira, "TerraSAR-X Upgrade to a Fully Polarimetric Imaging Mode," *Proceedings of the POLINSAR*, Frascati, Italy, 2003.
- [42] (2015, July), DLR Portal, TerraSAR-X Image of the Month: The Drygalski Glacier in Antarctica. [Online]. Available: <a href="http://www.dlr.de/en/desktopdefault.aspx/tabid-4237/6774">http://www.dlr.de/en/desktopdefault.aspx/tabid-4237/6774</a> read-16350/
- [43] (2015, July), DLR Earth Observation Picture Gallery, Mato Grosso, Brazil radar documents logging in the Central Brazilian rainforest. [Online]. Available: <a href="http://www.dlr.de/eo/en/DesktopDefault.aspx/tabid-6695/10983">http://www.dlr.de/eo/en/DesktopDefault.aspx/tabid-6695/10983</a> read-10126/gallery-1/gallery\_read-Image.1.3752/
- [44] V. Herrera-Cruz and F. Koudogbo, "TerraSAR-X rapid mapping for flood events," *Proceedings of the ISPRS*, Hannover, Germany, 2009.
- [45] (2015, July), DLR Portal, TerraSAR-X Image of the Month: Mexico City. [Online]. Available: <a href="http://www.dlr.de/en/desktopdefault.aspx/tabid-4237/6774\_read-24560/">http://www.dlr.de/en/desktopdefault.aspx/tabid-4237/6774\_read-24560/</a>
- [46] G. Krieger, A. Moreira, H. Fiedler, I. Hajnsek, M. Werner, M. Younis, and M. Zink, "Tan-DEM-X: A satellite formation for high resolution SAR interferometry," *IEEE Transactions on Geoscience and Remote Sensing*, vol. 45, no. 11, pp. 3317–3341, November 2007.

[47] A. Freeman, W. T. K. Johnson, B. Honeycutt, R. Jordan, S. Hensley, P. Siqueira, and J.C. Curlander, "The "Myth" of the Minimum SAR Antenna Area Constraint," *IEEE Transactions on Geoscience and Remote Sensing*, vol. 38, pp. 320–324, no.1, January 2000.

- [48] K. Tomiyasu, "Conceptual performance of a satellite borne, wide swath synthetic aperture radar," *IEEE Transactions on Geoscience and Remote Sensing*, vol. 19, no. 2, pp. 108–116, April 1981.
- [49] G. Krieger, I. Hajnsek, K.P. Papathanassiou, M. Younis, and A. Moreira, "Interferometric synthetic aperture radar (SAR) missions employing formation flying," *Proceedings of the IEEE*, vol. 98, no. 5, pp. 816–843, May 2010.
- [50] A. Moreira, G. Krieger, I. Hajnsek, K.P. Papathanassiou, M. Younis, P. Lopez-Dekker, S. Huber, M. Villano, M. Pardini, M. Eineder, F. De Zan, and A. Parizzi, "Tandem-L: A Highly Innovative Bistatic SAR Mission for Global Observation of Dynamic Processes on the Earth's Surface," *IEEE Geoscience and Remote Sensing Magazine*, vol. 3, no. 2, pp. 8–23, June 2015.
- [51] I. Hajnsek, M. Shimada, M. Eineder, K.P. Papathanassiou, T. Motohka, M. Watanabe, M. Ohki, F. de Zan, F. Lopez-Dekker, G. Krieger, and A. Moreira, "Tandem-L: Science requirements and mission concept," *Proceedings of the EUSAR*, Berlin, Germany, 2014.
- [52] A. Moreira, G. Krieger, I. Hajnsek, K. Papathanassiou, M. Younis, F. Lopez-Dekker, S. Huber, M. Eineder, M. Shimada, T. Motohka, M. Watanabe, M. Ohki, A. Uematsu, and S. Ozawa, "Tandem-L/ALOS-Next: A highly innovative SAR mission for global observation of dynamic processes on the Earth's surface," *Proceedings of the IGARSS*, Milan, Italy, 2015.
- [53] A. Currie and M.A. Brown, "Wide-swath SAR," *IEE Proceedings F (Radar Signal Processing)*, vol. 139, no. 2, pp. 122–135, April 1992.
- [54] G.D. Callaghan and I.D. Longstaff, "Wide swath spaceborne SAR using a quad element array," *IEE Proceedings F (Radar Signal Processing)*, vol. 146, no. 3, pp. 159–165, June 1999.
- [55] M. Suess, B. Grafmüller, and R. Zahn, "A novel high resolution, wide swath SAR system," *Proceeding of the IGARSS*, Sidney, Australia, 2001.
- [56] M. Suess and W. Wiesbeck, "Side-looking synthetic aperture system," European Patent 1 241 487 A1, September 18, 2002.
- [57] J.T. Kare, "Moving Receive Beam Method and Apparatus for Synthetic Aperture Radar", U.S. Patent 6,175,326 B1, Jan 16, 2001.
- [58] M. Younis, C. Fischer, and W. Wiesbeck, "Digital beamforming in SAR systems," *IEEE Transactions on Geoscience and Remote Sensing*, vol. 41, no. 7, pp. 1735–1739, July 2003.
- [59] A. Freeman, G. Krieger, P. Rosen, M. Younis, W.T.K. Johnson, S. Huber, R. Jordan, and A. Moreira, "SweepSAR: Beam-forming on Receive using a Reflector-Phased Array Feed Combination for Spaceborne SAR," *Proceedings of the IEEE Radar Conference*, Pasadena, USA, 2009.
- [60] G. Krieger, N. Gebert, M. Younis, and A. Moreira, "Advanced Synthetic Aperture Radar Based on Digital Beamforming and Waveform Diversity," *Proceedings of the IEEE Radar Conference*, Rome, Italy, 2008.

[61] G. Krieger, N. Gebert, M. Younis, F. Bordoni, A. Patyuchenko, and A. Moreira, "Advanced Concepts for Ultra-Wide-Swath SAR Imaging," *Proceedings of the EUSAR*, Friedrichshafen, Germany, 2008.

- [62] G. Krieger, M. Younis, S. Huber, F. Bordoni, A. Patyuchenko, J. Kim, P. Laskowski, M. Villano, T. Rommel, P. Lopez-Dekker, and A. Moreira, "Digital Beamforming and MIMO SAR: Review and New Concepts," *Proceedings of the EUSAR*, Nuremberg, Germany, 2012.
- [63] W. Wiesbeck, L. Sit, M. Younis, G. Krieger, and A. Moreira, "Radar 2020: The Future of Radar Systems," *Proceedings of the IGARSS*, Milan, Italy, July 2015.
- [64] B. Grafmüller and C. Schaefer, "Hochauflösende Synthetik-Apertur Radarvorrichtung und Antenne," DE 10 2005 062 031.0 22.12.2005.
- [65] N. Gebert and G. Krieger, "Ultra-Wide Swath SAR Imaging with Continuous PRF Variation," *Proceedings of the EUSAR*, Aachen, Germany, 2010.
- [66] M. Villano, G. Krieger, and A. Moreira, "Staggered SAR: High-Resolution Wide-Swath Imaging by Continuous PRI Variation," *IEEE Transactions on Geoscience and Remote Sensing*, vol. 52, no. 7, pp. 4462–4479, July 2014.
- [67] M. Villano, G. Krieger, and A. Moreira, "A Novel Processing Strategy for Staggered SAR," *IEEE Geoscience and Remote Sensing Letters*, vol. 11, no. 11, pp. 1891–1895, November 2014.
- [68] M. Villano, "Student Research Highlight Staggered Synthetic Aperture Radar," *IEEE Aerospace and Electronic System Magazine*, vol. 30, no. 7, pp. 30–32, July 2015.
- [69] M. Villano, G. Krieger, and A. Moreira, "Ambiguities and Image Quality in Staggered SAR," *Proceeding of the APSAR*, Marina Bay Sands, Singapore, 2015.
- [70] M. Villano, M. Jäger, U. Steinbrecher, G. Krieger, and A. Moreira, "Staggered SAR: Imaging a Wide Continuous Swath by Continuous PRI Variation," *Proceedings of the Kleinheubacher Tagung*, Miltenberg, Germany, 2014.
- [71] M. Villano and G. Krieger, "Staggered SAR: From Concept to Experiments with Real Data," *Proceedings of the EUSAR*, Berlin, Germany, 2014.
- [72] M. Villano, G. Krieger, and A. Moreira, "The Staggered SAR concept: Imaging a wide continuous swath with high resolution," *Proceedings of the IRS*, Dresden, Germany, 2013.
- [73] M. Villano, G. Krieger, and A. Moreira, "Staggered SAR for High-Resolution Wide-Swath Imaging," *Proceedings of the IET RADAR*, Glasgow, UK, 2012.
- [74] M. Villano, G. Krieger, and A. Moreira, "Staggered SAR: A New Concept for High-Resolution Wide-Swath Imaging," *Proceedings of the IEEE GOLD*, Rome, Italy, 2012.
- [75] C. Elachi, Spaceborne Radar Remote Sensing: Applications and Techniques. New York, USA: IEEE Press, 1988.
- [76] J.C. Curlander and R.N. McDonough, *Synthetic Aperture Radar: Systems and Signal Processing*. New York, USA: Wiley, 1991.
- [77] F.M. Henderson and A.J. Lewis, Eds., *Manual of Remote Sensing: Principles and Applications*. New York: Wiley, 1998.
- [78] K. Tomiyasu, "Tutorial review of synthetic-aperture radar (SAR) with applications to imaging of the ocean surface," *Proceedings of the IEEE*, vol. 66, no. 5, pp. 563–583, May 1978.

[79] C. Oliver and S. Quegan, *Understanding Synthetic Aperture Radar Images*. Herndon, USA: SciTech Publishing, 2004.

- [80] G. Franceschetti and R. Lanari, *Synthetic Aperture Radar Processing*. Boca Raton, USA: CRC Press, 1999.
- [81] I.G. Cumming and F.H. Wong, *Digital Processing of Synthetic Aperture Radar Data: Algorithms and Implementation*. Norwood, MA: Artech House, 2005.
- [82] F.J. Harris, "On the Use of Windows for Harmonic Analysis with the Discrete Fourier Transform," *Proceedings of the IEEE*, vol. 66, no. 1, pp 51–83, January 1978.
- [83] F.K. Li and W.T.K. Johnson, "Ambiguities in Spaceborne Synthetic Aperture Radar Systems," *IEEE Transactions on Aerospace and Electronic Systems*, vol. 19, no. 3, pp. 389–397, May 1983.
- [84] R.K. Raney and G.J. Princz, "Reconsideration of azimuth Ambiguities in SAR", *IEEE Transactions on Geoscience and Remote Sensing*, vol. 25, no. 6, pp. 783–787, November 1987.
- [85] A. Moreira, "Suppressing the Azimuth Ambiguities in Synthetic Aperture Radar Images," *IEEE Transactions on Geoscience and Remote Sensing*, vol.31, no. 4, pp. 885–895, July 1993.
- [86] M. Villano and G. Krieger, "Spectral-Based Estimation of the Local Azimuth-Ambiguity-to-Signal Ratio in SAR Images," *IEEE Transactions on Geoscience and Remote Sensing*, vol. 52, no. 5, pp. 2304–2313, May 2014.
- [87] M. Villano and G. Krieger, "Accounting for Azimuth Ambiguities in Interferometric Performance Analysis," *Proceedings of the IGARSS*, Munich, Germany, 2012.
- [88] M. Villano and G. Krieger, "Impact of Azimuth Ambiguities on Interferometric Performance," *IEEE Geoscience and Remote Sensing Letters*, vol. 9, no. 5, pp. 896–900, September 2012.
- [89] F.T. Ulaby and M.C. Dobson, *Handbook of Radar Scattering Statistics for Terrain*. Dedham, USA: Artech House, Inc., 1989.
- [90] R.K. Moore, J.P. Claassen, and Y. H. Lin, "Scanning spaceborne synthetic aperture radar with integrated radiometer," *IEEE Transactions on Aerospace and Electronic Systems*, vol. 17, no. 3, pp. 410–420, May 1981.
- [91] W.G. Carrara, R.S. Goodman, and R.M. Majewski, *Spotlight Synthetic Aperture Radar: Signal Processing Algorithms (IPF)*. Norwood, USA: Artech House, 1995.
- [92] F. De Zan and A. Monti Guarnieri, "TOPSAR: Terrain observation by progressive scans," *IEEE Transactions on Geoscience and Remote Sensing*, vol. 44, no. 9, pp. 2352–2360, September 2006.
- [93] M. Villano, K.P. Papathanassiou, G. Krieger, and A. Moreira, "Imaging a Wide Swath with Full Polarimetry," *Proceedings of the POLINSAR*, Frascati, Italy, 2015.
- [94] G. Krieger, N. Gebert, and A. Moreira, "Unambiguous SAR Signal Reconstruction From Nonuniform Displaced Phase Center Sampling", *IEEE Geoscience and Remote Sensing Letters*, vol. 1, no.4, pp. 260–264, October 2004.

[95] G. Krieger, N. Gebert, and A. Moreira, "SAR Signal Reconstruction From Nonuniform Displaced Phase Center Sampling", *Proceedings of the IGARSS*, Anchorage, USA, 2004.

- [96] N. Gebert, G. Krieger, and A. Moreira, "Digital Beamforming on Receive: Techniques and Optimization Strategies for High-Resolution Wide-Swath SAR Imaging", *IEEE Transactions on Aerospace and Electronic Systems*, vol. 45, no. 2, pp. 564–592, February 2009.
- [97] A. Papoulis, "Generalized Sampling Expansion," *IEEE Transactions on Circuits and Systems*, vol. 24, no. 11, pp. 652–654, November 1977.
- [98] J.L. Brown, "Multi-Channel Sampling of Low-Pass Signals," *IEEE Transactions on Circuits and Systems*, vol. 28, no. 2, pp. 101–106, Febraury 1981.
- [99] N. Gebert, M. Villano, G. Krieger, and A. Moreira, "Errata: Digital Beamforming on Receive: Techniques and Optimization Strategies for High-Resolution Wide-Swath SAR Imaging," *IEEE Transactions on Aerospace and Electronics Systems*, vol. 49, no. 3, p. 2110, July 2013.
- [100] D. Cerutti-Maori, I. Sikaneta, J. Klare, and C.H. Gierull, "MIMO SAR Processing for Multi-channel High-Resolution Wide-Swath Radars," *IEEE Transactions on Geoscience and Remote Sensing*, vol. 52, no. 8, pp.5034–5055, August 2014.
- [101] I. Sikaneta, C.H. Gierull, and D. Cerutti-Maori, "Optimum Signal Processing for Multichannel SAR: With Application to High-Resolution Wide-Swath Imaging," *IEEE Transactions on Geoscience and Remote Sensing*, vol. 52, no. 10, pp.6095–6109, October 2014.
- [102] N. Gebert, G. Krieger, and A. Moreira, "Multi-Channel Azimuth Processing in ScanSAR and TOPS Mode Operation," *IEEE Transactions on Geoscience and Remote Sensing*, vol. 48, no. 7, pp. 2994–3008, July 2010.
- [103] N. Gebert, M. Villano, G. Krieger, and A. Moreira, "Correction to Multichannel Azimuth Processing in ScanSAR and TOPS Mode Operation," *IEEE Transactions on Geoscience and Remote Sensing*, vol. 51, no. 8, p. 4611, August 2013.
- [104] M. Bara, R. Scheiber, A. Broquetas, and A. Moreira, "Interferometric SAR signal analysis in the presence of squint," *IEEE Transactions on Geoscience and Remote Sensing*, vol. 38, no. 5, pp. 2164–2178, September 2000.
- [105] G. Krieger, N. Gebert, and A. Moreira, "Multidimensional Waveform Encoding: A New Digital Beamforming Technique for Synthetic Aperture Radar Remote Sensing," *IEEE Transactions on Geoscience and Remote Sensing*, vol. 46, no. 1, pp. 31–46, January 2008.
- [106] G. Krieger, M. Younis, S. Huber, F. Bordoni, A. Patyuchenko, J. Kim, P. Laskowski, M. Villano, T. Rommel, P. Lopez-Dekker, and A. Moreira, "MIMO-SAR and the Orthogonality Confusion," *Proceedings of the IGARSS*, Munich, Germany, 2012.
- [107] J. Salzman, D. Akamine, L. Lefeuvre, and J. Kirk, "Interrupted Synthetic Aperture Radar," *IEEE Aerospace and Electronic Systems Magazine*, vol. 17, no. 5, pp. 33–39, May 2002.
- [108] M. Pinheiro and M. Rodriguez-Cassola, "Reconstruction methods of missing SAR data: analysis in the frame of TanDEM-X synchronization link," *Proceedings of the EUSAR*, Nuremberg, Germany, 2012.
- [109] S. M. Kay, Fundamentals of Statistical Signal Processing: Estimation Theory. Englewood Cliffs, USA: Prentice Hall, 1993.

[110] S. Barbarossa, "Detection and imaging of moving objects with synthetic aperture radar. Part 1. Optimal detection and parameter estimation theory," *IEE Proceedings – F (Radar Signal Processing)*, vol. 139, no. 1, pp. 79–88, January 1992.

- [111] S. Huber, M. Younis, A. Patyuchenko, G. Krieger, and A. Moreira, "Spaceborne Reflector SAR Systems with Digital Beamforming," *IEEE Transactions on Aerospace and Electronic Systems*, no. 48, vol. 4, pp. 3473–3493, October 2012.
- [112] J. Capon, "High resolution frequency-wavenumber spectrum analysis," *Proceedings of the IEEE*, vol. 57, no. 8, pp. 1408–1418, August 1969.
- [113] (2015, October), GRASP TICRA. [Online]. Available: <a href="http://www.ticra.com/products/software/grasp">http://www.ticra.com/products/software/grasp</a>
- [114] D. D'Aria, D. Giudice, A. Monti Guarnieri, P. Rizzoli, and J. Medina, "A Wide Swath, Full Polarimetric, L-Band Spaceborne SAR", *Proceedings of the IGARSS*, Boston, USA, 2008.
- [115] H.L. Van Trees, Optimum Array Processing. New York, USA: Wiley, 2002.
- [116] D. Giuli and L. Facheris, "Performance of interpulse Signal Coding in Interleaved-pulse Polarimetric SAR", *European Transactions on Telecommunications and Related Technologies*, vol. 4, no. 5, pp. 555–567, September October 1993.
- [117] J. Dall and A. Kusk, "Azimuth phase coding for range ambiguity suppression in SAR," *Proceedings of the IGARSS*, Anchorage, USA, 2004.
- [118] M.J. Sanjuan-Ferrer, P. Lopez-Dekker, I. Hajnsek, F. Bordoni, G. Adamiuk, R. Hanssen, F. van Leijen, H. Skriver, R. Danielson, T. Nagler, L.T. Pedersen, O. Lang, A. Gabriele, M. Ludwig, and A. Lecuyot, "High resolution wide swath SAR applications study: an overview," Proceedings of the ARSI & KEO, Noordwijk, The Netherlands, 2014.
- [119] M. Villano, "SNR and Noise Variance Estimation in Polarimetric SAR Data," *IEEE Geoscience and Remote Sensing Letters*, vol. 11, no. 1, pp.278–282, Jan. 2014.
- [120] P. Prats, M. Rodriguez-Cassola, L. Marotti, M. Naninni, S. Wollstadt, D. Schulze, N. Tous-Ramon, M. Younis, G. Krieger, and A. Reigber, "Taxi: A versatile processing chain for experimental TanDEM-X product evaluation," *Proceedings of the IGARSS*, Honolulu, USA, 2010.
- [121] M. Villano, G. Krieger, and V. Del Zoppo, "On-Board Doppler Filtering for Data Volume Reduction in Spaceborne SAR Systems," *Proceedings of the IRS*, Gdansk, Poland, 2014.
- [122] V. Del Zoppo, M. Villano, and G. Krieger, "A data volume reduction strategy based on onboard Doppler filtering," *Proceedings of the IEEE GOLD*, Berlin, Germany, 2014.
- [123] M. Villano, G. Krieger, and A. Moreira, "Data Volume Reduction in High-Resolution Wide-Swath SAR Systems," *Proceeding of the APSAR*, Marina Bay Sands, Singapore, 2015.
- [124] M. Villano, M. Martone, V. Del Zoppo, and G. Krieger, "Joint effects of on-board Doppler filtering and quantization in spaceborne SAR systems," *Proceedings of the IEEE GOLD*, Berlin, Germany, 2014.
- [125] R. Kwok and W.T.K. Johnson, "Block Adaptive Quantization of Magellan SAR Data," *IEEE Transactions on Geoscience and Remote Sensing*, vol. 27, no. 4, pp. 375–383, July 1989.
- [126] D. Lancashire, B. Barnes, and S. Udall, "Block adaptive quantization," U.S. Patent 6 255 987 B1, July 3, 2001.

[127] M. Martone, B. Bräutigam, and G. Krieger, "Quantization Effects in TanDEM-X Data," *IEEE Transactions on Geoscience and Remote Sensing*, vol. 53, no. 2, pp. 583–597, February 2015.

- [128] M. Villano, G. Krieger, and A. Moreira, "Synthetik-Apertur-Radarverfahren," German Patent Application DE 10 2012 219 255.5, filed October 22, 2012. Patent Pending.
- [129] M. Villano, G. Krieger, and A. Moreira, "Synthetik-Apertur-Radarverfahren," European Patent Application 13187738.3 1811, filed October 8, 2013. Patent Pending.
- [130] S. Bertl, P. Lopez-Dekker, M. Younis, and G. Krieger, "Equivalency of Multiple Beams and Multiple Phase Centres for Digital Beamforming SAR Systems," *Proceedings of the EUSAR*, Berlin, Germany, 2014.
- [131] G. Krieger, S. Huber, M. Villano, M. Younis, T. Rommel, P. Lopez-Dekker, F. Queiroz de Almeida, and A. Moreira, "CEBRAS: Cross Elevation Beam Range Ambiguity Suppression for High-Resolution Wide-Swath and MIMO-SAR Imaging," *Proceedings of the IGARSS*, Milan, Italy, 2015.
- [132] F. Queiroz de Almeida and G. Krieger, "Multichannel Staggered SAR Azimuth Sample Regularization," *accepted to the EUSAR*, Hamburg, Germany, 2016.

# A Spherical SAR Geometry

In this Appendix the basic relationships between the main variables in a spherical SAR geometry are recalled. The spherical Earth model is needed for the design of spaceborne SAR systems, while the flat Earth one is still fine for the design of airborne SAR systems, due to their much lower altitude [79].

Fig. 109 shows the plane defined by the Earth's center O, a point scatterer P, and the radar S at the closest approach  $R_0$  to the point scatterer P.  $R_E$  is the mean Earth radius,  $\alpha_L$  is often referred to as the look angle, while  $\gamma$  is the angle formed by the two line segments  $\overline{OS}$  and  $\overline{OP}$ .

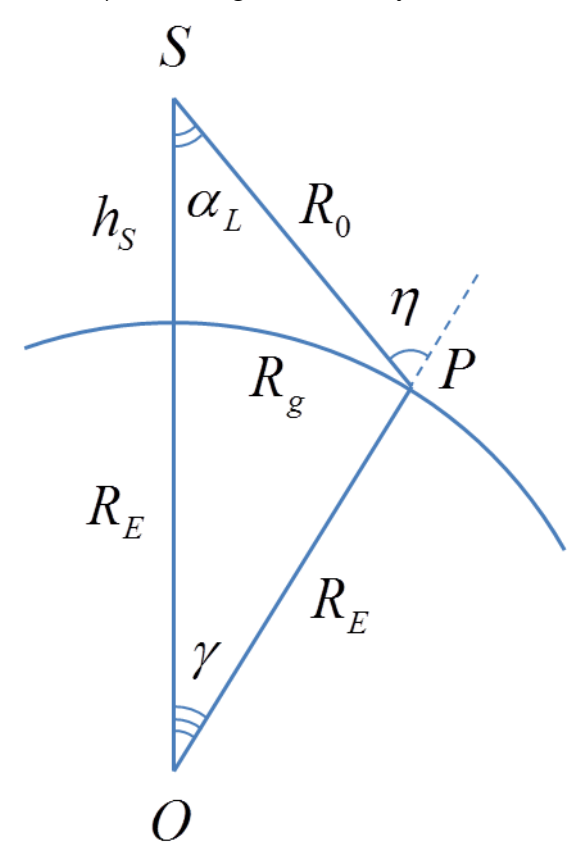


Fig. 109. Spherical SAR geometry, shown in a plane defined by the Earth's center, a point scatterer P, and the radar at the closest approach  $R_0$  to that point scatterer.

The following relations can be easily derived from the laws of sines and cosines

$$R_0 = \left(R_E + h_S\right) \frac{\sin \gamma}{\sin \eta} \tag{93}$$

$$R_0^2 = R_E^2 + (R_E + h_S)^2 - 2R_E(R_E + h_S)\cos\gamma$$
(94)

$$\gamma = \eta - \alpha_L \tag{95}$$

$$\sin \alpha = \frac{R_E}{R_E + h_S} \sin \eta \tag{96}$$

Fig. 110 shows instead the plane defined by the radar track, assumed circular in the spherical SAR geometry, and the point scatterer *P*. The relationships between the main variables in this plane are important to simulate the azimuth signal for both a SAR with constant *PRI* and a staggered SAR.

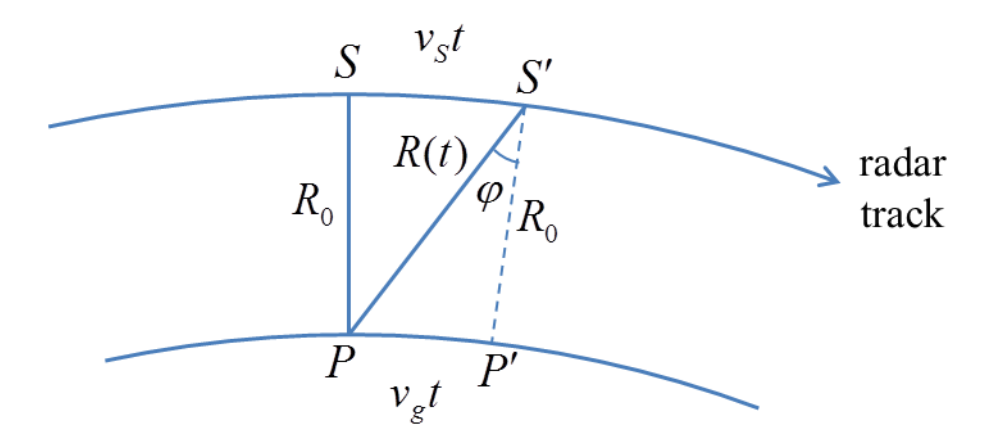


Fig. 110. Spherical SAR geometry, within the plane defined by the radar track and the point scatterer *P*.

In particular, if *S* is the position of the radar at the closest approach to the scatterer P (t = 0), at time t, the radar will have moved by  $v_S t$  along the radar track and will occupy the position S'. Defining as  $v_g$  the speed of the radar beam on ground, which can be approximated as t = 0

$$v_g \cong v_S \frac{R_E}{R_E + h_S} \tag{97}$$

the range of the radar to the point scatterer R(t) can be expressed as

Equation (97) is strictly valid only for nadir.

$$R(t) \cong \sqrt{R_0^2 + (v_r t)^2} \cong R_0 + \frac{(v_r t)^2}{2R_0}$$
 (98)

where the effective speed  $v_r$  is the geometric mean of  $v_s$  and  $v_g$  [81]

$$v_r = \sqrt{v_S v_g} \tag{99}$$

The azimuth angle  $\varphi$  can be instead obtained from the following expression

$$\tan \varphi = \frac{v_g t}{R_0} \tag{100}$$

Having the knowledge of the azimuth antenna pattern, the amplitude and the phase of the azimuth raw signal received at time t can be obtained from the range R(t) and the azimuth angle  $\varphi$ .

# Curriculum Vitae

#### Personal data

Name: Michelangelo Villano

Date of birth: June 8, 1984

Place of birth: Vallo Della Lucania (SA), Italy

Nationality: Italian

## **Education and Professional Experience**

<b>Doctoral Degree (DrIng.)</b> , Ele	Electrical Engineering and Information
---------------------------------------	--

Technology (summa cum laude). Karlsruhe Institute of Technology,

Karlsruhe, Germany.

Since 2013 Guest Editor of the Special Issues "Advances in Antenna Array Pro-

cessing for Radar 2014" and "Advances in Antenna Array Processing for Radar 2016" of the International Journal of Antennas and Propagation.

Since 2009 Research Scientist at the Microwaves and Radar Institute. German Aero-

space Center (DLR), Oberpfaffenhofen, Germany.

2008-2009 Young Graduate Trainee. European Space Agency (ESA/ESTEC),

Noordwijk, The Netherlands.

**2008 Master of Science**, Telecommunications Engineering (*summa cum laude*).

Sapienza University of Rome, Rome, Italy.

2006 Bachelor of Science, Telecommunications Engineering (summa cum

laude). Sapienza University of Rome, Rome, Italy.

#### **Awards**

2015

2015	<b>IEEE Geoscience and Remote Sensing Society Letters Prize Paper</b>
	Award 2015.
2015	Student Paper Award at the APSAR 2015 Conference.

2015 Student Paper Award at the AFSAN 2013 Connecence.

**2014** First Place Student Paper Award at the EUSAR 2014 Conference.

**2014 Certificate of Merit** at the Kleinheubacher Tagung 2014.

2012 Shortlisted among the Five Best Student Papers at the IET Radar 2012

Conference.

2009 Accenture Graduation Prize for the best MSc Thesis in Engineering.
 2003-2008 Fellowship at the University College "Lamaro - Pozzani" of the National

Federation of "Cavalieri del Lavoro."

**2003 Silver Medal** at the 19<sup>th</sup> Italian Mathematical Olympiad.